A TRACE/PARCS Coupling, Uncertainty Propagation and Sensitivity Analysis Methodology for the IAEA ICSP on Numerical Benchmarks for Multi-Physics Simulation of Pressurized Heavy Water Reactor Transients

A TRACE/PARCS Coupling, Uncertainty Propagation and Sensitivity Analysis Methodology for the IAEA ICSP on Numerical Benchmarks for Multi-Physics Simulation of Pressurized Heavy Water Reactor Transients

By Kai Groves, B. Eng

A Thesis Submitted to the School of Graduate Studies in Partial Fulfillment of the Requirements for the Degree Master of Applied Sciences

Descriptive Note

McMaster University MASTER OF APPLIED SCIENCES (2020) Hamilton, Ontario (Engineering Physics)

TITLE: A TRACE/PARCS Coupling, Uncertainty Propagation and Sensitivity Analysis Methodology for the IAEA ICSP on Numerical Benchmarks for Multi-Physics Simulation of Pressurized Heavy Water Reactor Transients

Lay Abstract

This thesis documents McMaster's contribution to an International Atomic Energy Agency Benchmark on Pressurized Heavy Water Reactors that closely resemble the CANDU design. The Benchmark focus is on coupling of thermal-hydraulics and neutron physics codes, and simulation of postulated accident scenarios. This thesis contains some select results from the Benchmark, comparing the results generated by McMaster to other participants. This thesis also documents additional work that was performed to propagate fundamental nuclear data uncertainty through the coupled transient calculations and obtain an estimate of the uncertainty in key figures of merit. This work was beyond the scope of the Benchmark and is a unique contribution to the open literature. Finally, sensitivity studies were performed on one of the accident scenarios defined in the Benchmark, the loss of coolant accident, to determine which input parameters have the largest contribution to the variability of key figures of merit.

Abstract

The IAEA ICSP on Numerical Benchmarks for Multiphysics Simulation of Pressurized Heavy Water Reactor Transients was initiated in 2016 to facilitate the development of a set of open access, standardized, numerical test problems for postulated accident scenarios in a CANDU styled Reactor. The test problems include a loss of coolant accident resulting from an inlet header break, a loss of flow accident caused by a single pump trip, and a loss of regulation accident due to inadvertently withdrawn adjusters. The Benchmark was split into phases, which included stand-alone physics and thermal-hydraulics transients, coupled steady state simulations, and coupled transients. This thesis documents the results that were generated through an original TRACE/PARCS coupling methodology that was developed specifically for this work. There is a strong emphasis on development methods and step by step verification throughout the thesis, to provide a framework for future research in this area. In addition to the Benchmark results, additional studies on propagation of fundamental nuclear data uncertainty, and sensitivity analysis of coupled transients are reported in this thesis. Two Phenomena and Key Parameter Identification and Ranking Tables were generated for the loss of coolant accident scenario, to provide feedback to the Benchmark Team, and to add to the body of work on uncertainty/sensitivity analysis of CANDU style reactors.

Some important results from the uncertainty analysis work relate to changes in the uncertainty of figures of merit such as integrated core power, and peak core power magnitude and time, between small and large break loss of coolant accidents. The analysis shows that the mean and standard deviation of the integrated core power and maximum integrated channel power, are very close between a 30% header break and a 60% header break, despite the peak core power being much larger in the 60% break case. Furthermore, it shows that there is a trade off between the uncertainty in the time of the peak core power, and the magnitude of the peak core power, with smaller breaks showing a smaller standard deviation in the magnitude of the peak core power, but a larger standard deviation in when this power is reached during the transient, and vice versa for larger breaks. From the results of the sensitivity analysis study, this thesis concludes that parameters related to coolant void reactivity and shutoff rod timing and effectiveness have the largest impact on loss of coolant accident progressions, while parameters that can have a large impact in other transients or reactor designs, such as fuel temperature reactivity feedback and control device incremental cross sections, are less important.

Acknowledgements

I would like to thank my Supervisor Dr. Novog, for all his support throughout my research process. There is no doubt I would not have been able to complete this dissertation without him. Through numerous discussions and meetings, I learned a tremendous amount about nuclear reactor modelling, computational physics, international collaboration, and Benchmark studies. I believe the knowledge I gained through this process will be useful for the rest of my career in the nuclear engineering industry. I would also like to thank other professors in McMaster University's Department of Engineering Physics, particularly Dr. Adriaan Buijs, Dr. Benjamin Rouben, and Dr. John Luxat for their support throughout my academic journey, both in academic courses, and research related work.

Furthermore, I would like to thank the members of my research group including Garik Patterson, Liz Macconnachie, Kendall Boniface, Chris Hollingshead, Devan Wager, and Mitchell Kurnell. Special recognition is given to both Michael Tucker, for endless hours of discussion and collaboration, and Simon Younan, for general support, and collaboration. Without these talented individuals, I would not have been able to reach this point in my academic career. I would also like to thank my parents, for their constant encouragement.

Finally, I would like to thank the International Atomic Energy Agency, for their support of Benchmark activities, and Canadian Nuclear Laboratories, for their hard work organizing the Benchmark. Special Recognition is given to Mattias Krause of the International Atomic Energy Agency, and Alexandre Trottier and Nusret Aydemir of Canadian Nuclear Laboratories, for endless hours of discussion and support.

Table of Contents

List of Figures

List of Tables

List of Acronyms

CANDU – CANada Deuterium Uranium

IAEA – International Atomic Energy Agency

ICSP – International Collaborative Standard Problem

PHWR – Pressurized Heavy Water Reactor

OECD – Organization for Economic Co-operation and Development

NEA – Nuclear Energy Agency

UAM – Uncertainty in Analysis and Modelling

LWR – Light Water Reactor

PWR – Pressurized Water Reactor

LWR – Light Water Reactor

LOR – Loss of Regulation (synonymous with "Adjuster Rod Withdrawal" in this work)

LOF – Loss of Flow (synonymous with "Pump Rundown" or "Pump Trip" in this work)

LOCA – Loss of Coolant Accident (synonymous with "Header Break" in this work)

AECL – Atomic Energy of Canada Limited

ADJ – Adjuster Rod

LQZC – Liquid Zone Controller

MCA – Mechanical Control Absorber

SOR – Shutoff Rod

SDS-1 – Shutdown System 1

SDS-2 – Shutdown System 2

RRS – Reactor Regulating System

PIRT – Phenomena Identification and Ranking Table

PKPIRT – Phenomena and Key Parameter Identification and Ranking Table

IST – Industry Standard Toolset

BEAU/BEPU – Best Estimate And Uncertainty/Best Estimate Plus Uncertainty

PDCSC – Partial Derivative Cross Section Coefficients

CNL - Canadian Nuclear Laboratories

CNEA - Comision National de Energia Atomica (Argentina)

TH – Thermal-Hydraulics

RP – Reactor Physics

FOM – Figure of Merit

IHD# - Inlet Header # (e.g. IHD4 = Inlet Header 4)

OHD# - Outlet Header # (e.g. OHD7 = Outlet Header 7)

P# - Pump # (e.g. P2 = Pump 2)

SG# - Steam Generator # (e.g. SG2 = Steam Generator 2)

Declaration of Academic Achievement

The basis of this research is a collaboration between myself, my supervisor Dr. David Novog, and the International Atomic Energy Agency. It was through this collaboration that a methodology for coupled TRACE/PARCS transient simulations was developed and tested. The International Atomic Energy Agency provided specifications for various postulated transients, which were used to develop the models described in this dissertation. The scope of the Benchmark was also expanded upon in this work, through a collaboration between myself and Dr. Novog, to perform uncertainty and sensitivity analysis of selected transients. To this end, propagation of fundamental nuclear data uncertainty was performed with the SAMPLER module of the SCALE code package, and Phenomena and Key Parameter Identification and Ranking Tables were generated for the loss of coolant accident scenario defined in the Benchmark.

Dr. Novog provided guidance on how to perform this research, including the selection of TRACE, PARCS and SCALE as the primary analysis tools, the development of the individual code models and coupling methodology, and the application of uncertainty propagation and sensitivity analysis methods to the selected transients. However, the preparation of all input files, calibration to the Benchmark standard, execution of all coupled transients and uncertainty propagation and sensitivity analysis runs, and interpretation and plotting of results, was original work. The first draft of this dissertation was prepared by myself, and review and revision was performed by myself and Dr. Novog.

1. Introduction

The IAEA ICSP on Numerical Benchmarks for Multiphysics Simulation of Pressurized Heavy Water Reactor (PHWR) Transients, hereafter referred to as the IAEA ICSP Benchmark (or just "the Benchmark"), was initiated in 2016 to facilitate the development of a set of open access, standardized, numerical test problems for postulated accident scenarios in a PHWR [1]. No test problems currently exist in open literature for verification, validation, or even high-level comparison of PHWR transients, and the associated coupling methods. Conversely, there are several similar Benchmarks that are completed, or currently being performed for Light Water Reactors designs, such as the OECD NEA's UAM Benchmark [2], which is focussed on uncertainty analysis of coupled LWR transients (PWR – Three Mile Island I, BWR – Peach Bottom 2, and VVER-1000 – Kozloduy-6, Kalinin-3), and builds upon previously completed Benchmarks on PWR Main Steam Line Breaks [3], BWR Turbine Trips [4] and VVER-1000 Coolant Transients [5], among others. As such, the goal of the IAEA ICSP Benchmark is to address this gap in PHWR analysis by developing a set of standardized test problems that could be investigated by future researchers and/or form the basis of follow up Benchmarks on validation or uncertainty/sensitivity analysis of numerical transients.

The current Benchmark focus is on coupling of reactor physics (neutronics) and thermal-hydraulics codes, and to that end, neutron diffusion and one-dimensional system thermal-hydraulics codes were selected as the analysis tools to be coupled, although provisions were also made for Monte Carlo based neutron transport codes on the reactor physics side of the problem. This follows a standard approach for coupled CANDU safety analysis, where the 3-dimensional core power distribution predicted by a diffusion code is passed to a systems thermal-hydraulics code, which calculates the local thermal-hydraulic conditions in the reactor core, which are then passed back to the diffusion code [6]. It was assumed that participants were familiar with this analysis methodology, and had experience using the selected analysis tools in stand-alone or coupled PHWR safety analysis applications. As such, at the outset of the Benchmark, a key region of interest was the methodologies used to couple the codes together, with stand-alone code performance being a secondary region of interest. Previous work at McMaster by David Hummel [7], Frederic Salaun [8], Andrew Morreale [9] and others investigated reactor physics/thermal-hydraulics coupling with various codes, and laid a strong foundation for McMaster's participation in the Benchmark.

The IAEA ICSP Benchmark Specifications defines 4 test problems [10] which are applicable to PHWR designs:

1. Steady State (Null Transient)
2. Adjuster Rod Withdrawal (Loss of Regulation – LOR)
3. Primary Heat Transport Pump Rundown (Loss of Flow – LOF)
4. Inlet Header Break (Loss of Coolant Accident – LOCA)

The reactor design considered in the IAEA ICSP most closely resembles the CANDU-6, although there are many simplifications and approximations which limit the applicability of the results to any operating CANDU-6 reactor. For example, there is no Reactor Regulating System (RRS) model defined in Specifications and at the start of the transients a pressurizer boundary condition which is used to control system pressure is isolated, leading to a complete lack of pressure control during the transients, which significantly alters system behaviour. Other changes of this type were implemented in the Specifications

to isolate thermal-hydraulic and reactor physics phenomena. However, the major features of the CANDU-6 design are still retained, and the Benchmark exercises can still be an effective way to compare coupling methods for CANDU related safety analysis.

Participant countries included Canada (Canadian Nuclear Laboratories, McMaster, and SNC Lavalin), Argentina, Romania, Pakistan, India, China, and South Korea, although the later two countries did not participate in the final submission. As such, this Benchmark and the associated Technical meeting served as a forum for international collaboration from members of academia, industry, and research institutions.

This thesis documents McMaster's contribution to the Benchmark, and additional work performed to understand the role of uncertainties in output Figures of Merit (FOMs). McMaster joined the Benchmark in 2016, during the 2nd technical meeting, and has been working closely with the Benchmark Team since. All problems and requested results have been submitted for inclusion in the final IAEA TECDOC, which was in development at the time of writing. Fundamental nuclear data uncertainty was propagated through lattice physics calculations and coupled transients, to determine the uncertainty in core power for all transients. Finally, two Phenomena and Key Parameter Identification and Ranking Tables (PKPIRTs) were developed for the loss of coolant accident scenario, to determine the sensitivity of selected parameter and phenomena to two FOMS: 1. maximum integrated channel power and 2. Peak core power.

2. Literature Review and Background

In the sections to follow, a high-level overview of the CANDU-6 design, thermal-hydraulic feedback, the specific analysis tools used in this work, and the accident scenarios defined above, will be provided. In addition, a short literature review on code coupling techniques, uncertainty/sensitivity analysis and Phenomena Identification and Ranking Tables (PIRTs) will be discussed.

2.1. CANDU-6 Reactor Design

The CANDU-6 reactor is a 2000 MW_{TH}, 600 MW_e nuclear power plant that was designed by AECL, in Canada. CANDU-6 reactors currently operate internationally in Argentina, Romania, China, and South Korea. As such, the CANDU-6 design is a good choice for the basis of the PHWR model used in the IAEA ICSP Benchmark. A diagram showing the major components of the CANDU-6 reactor relevant to this dissertation can be seen in Figure 1. This Figure shows components of the primary side of the CANDU-6 reactor, specifically, the reactor core and primary heat transport system, the later of which uses heavy water as the working fluid. The secondary side of the CANDU-6 is similar to the typical steam-water turbine cycle of any large-scale power plant and won't be reviewed here.

The reactor core consists of 380 fuel channels containing 12 fuel bundles, which are made up of 37 natural uranium fuel elements enclosed in a large Calandria tank, filled with a heavy water moderator. The fuel elements are approximately 50 cm long and consists of a stack of 2 cm long uranium dioxide (UO_2) pellets surrounded by Zircaloy-4, a zirconium-based alloy. The CANDU fuel bundle design is shown in Figure 2. While not shown in Figure 1, the reactor core also contains reactivity control devices which penetrate the Calandria tank from the top and from the side, some of which are inserted into the core during normal operation, and some of which sit out of the core, poised for insertion if additional reactivity control is required. The in-core devices consist of 14 adjustable light water compartments, called Liquid Zone Controllers (LQZCs), which can adjust local and global reactivity by varying the amount of light water in the compartments, and 21 moveable stainless steel absorbing rods, called Adjuster Rods (ADJs), which are fully inserted during normal operation to flatten the power distribution. 4 additional cadmium absorbing rods, called Mechanical Control Absorbers (MCAs) sit outside of the core and are used for rapid reduction of reactor power, without causing shutoff. Finally, 28 cadmium Shut-off Rods (SORs) also sit outside of the core and are strictly used for reactor shutdown This shutdown system is referred to as Shutdown System 1 (SDS 1). A second independent shutdown system is also present in CANDU-6 reactors, which injects gadolinium nitrate poison directly into the moderator through injection nozzles. This shutdown system is referred to as SDS-2. The movement of these control devices, and the actuation of SDS-1 and SDS-2, is controlled by the Reactor Regulating System (RSS).

The primary heat transport system consists of 380 pressure tubes made of zirconium alloy, Zr-2.5Nb, and holds the 12 fuel bundles mentioned above. Each pressure tube is connected to an inlet and outlet end fitting, which allow for online re-fuelling. Each end fitting connects to an inlet and outlet feeder, which are smaller diameter pipes that connect to the reactor headers. There are 8 headers in a CANDU-6 reactor, 4 inlet and 4 outlet, that distribute low temperature coolant to the fuel channel inlet feeders and collect and mix high temperature coolant from the outlet feeders. Each outlet header is connected to a steam generator via 2 riser lines. The riser lines feed into an inlet plenum which distributes the coolant to thousands of U-tubes, where heat is transferred to the secondary side fluid via conduction through the U-tube walls. The PHTS coolant then re-accumulates in the steam generator outlet plenum,

which is connected to a single pump suction line that feeds the primary heat transport pump. There are 4 primary heat transport pumps, which are each connected to a single inlet header via 2 pump discharge lines. A pressurizer is also connected to two outlet headers and uses electrical heaters and cold-water sprays to control the pressure of the PHTS. All CANDU reactors are fuelled and cooled bi-directionally, meaning that adjacent fuel channels will be fuelled in opposite directions and will have coolant running in opposite directions. The core is split in half to create two loops, such that 1 quarter of all channels are connected to a single steam generator and pump. Balance lines between steam generators are used to equalize the pressure throughout the PHTS.

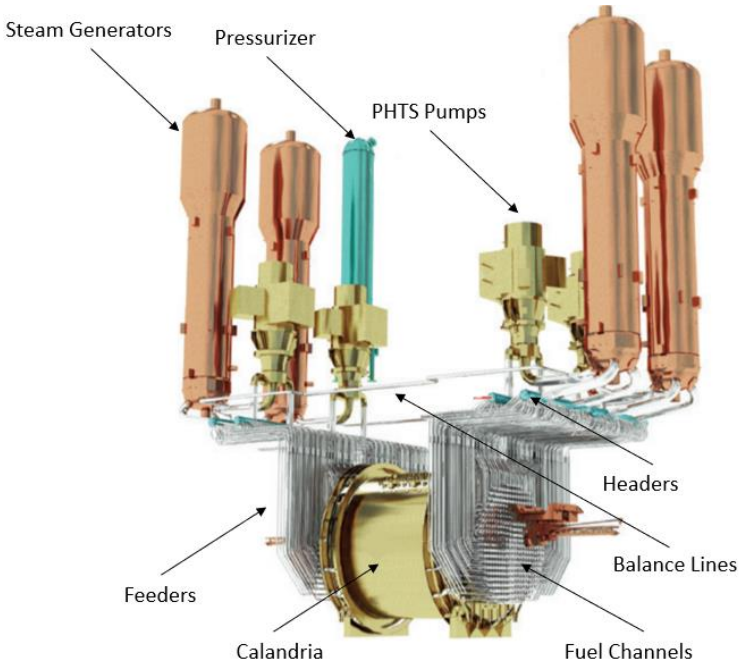

Figure 1. CANDU-6 Primary Heat Transport System and Reactor Core

Figure 2. CANDU Fuel Bundle Photograph: Assembled Bundle, Single Fuel Element, and Single Fuel Pellet [11]

2.2. CANDU Thermal-Hydraulic Feedback Phenomena

All reactor designs experience some type of reactivity feedback due to changes in thermal-hydraulic conditions and temperatures. Of importance to this thesis are the feedbacks due to fuel temperature changes and coolant density changes or voiding. The CANDU design is subject to particularly strong coolant voiding feedback, and weak fuel temperature feedback, compared to other reactor designs such as LWRs, which are undesirable from an accident control perspective. However, due to the use of natural uranium fuel and a heavy water moderator, the CANDU design is advantageous in its neutron kinetics, with a longer reactor period and large delayed neutron fraction [12], and with the application of good safety and control systems, can mitigate potential accident scenarios. These two TH feedback phenomena will be discussed here briefly as they form an important phenomenon in this research. Other thermal-hydraulic parameters, such as coolant temperature, moderator temperature and density, and moderator boron concentration, have a more minor impact on reactivity feedback, and additional discussion on these parameters can be found in [6]. The two feedback effects discussed below help show the need for coupled transient simulations of postulated accident scenarios.

2.2.1. Fuel Temperature Feedback – Doppler Broadening

Fuel temperature feedback is dominated by the change in the absorption and fission cross sections with changing fuel temperature. As shown in Figure 3 and Figure 4, large resonances in microscopic cross sections occur at intermediate energies for important nuclides such as U-235, U-238 and Pu-239. Figure 3 plots the microscopic neutron capture cross section, and Figure 4 plots the microscopic fission cross section. At these specific energies, neutron interaction is very likely. Due to the motion of atoms in the fuel lattice, there is a range of relative speeds between incident neutrons and fuel nuclides, such that neutrons with energies (speeds) slightly different than the resonance energy can still interact with a high probability. As the fuel temperature increases, this range of relative speeds increases, and the resonance peaks become "broader", analogous to doppler broadening. While this phenomena occurs with both capture and fission cross sections, given the large fraction of U-238 present in nuclear fuel, and its small fission cross section at thermal energies, nuclear fuel tends to become more absorbing as the temperature increases and so an increase in fuel temperature results in a negative reactivity insertion. However, Pu-239 has a large low energy fission resonance peak around 0.3 eV, which can be seen in Figure 4 and is within the energy range of thermal neutrons. For CANDU reactors, which produce significant amounts of Pu-239 over the course of reactor operation (as shown in Figure 23), this causes a gradual decrease in the negative fuel temperature reactivity co-efficient with fuel burnup. The impact of Pu-239 is less pronounced in LWRs fuelled with enriched U-235, as the amount of Pu-239 is small compared to the amount of U-235. Regardless, negative fuel temperature feedback is an important consideration in safety analysis applications.

2.2.2. Coolant Density Feedback - Coolant Void Reactivity

Coolant density feedback is extremely important in CANDU reactor analysis. The term Coolant Void Reactivity (CVR) refers specifically to the hypothetical scenario where all the coolant is voided and the change in reactivity is inferred, and coolant density feedback is a more general term for any feedback due to coolant density change. In an LWR, the use of an integral coolant and moderator (the coolant also acts as a moderator in LWRs) means that a decrease in coolant density will lead to a decrease in moderation, and a reduction in core reactivity. Therefore, for LWRs, the coolant density reactivity co-

efficient is negative. However, in CANDUs, the coolant is physically separate from the moderator, and so a loss of coolant does not mean a loss of moderation and in fact, reactivity increases substantially when coolant is lost. This is due to a couple of reactivity effects. First, consider fast neutrons that were born from fission in the fuel and are moving through the fuel channel towards the moderator.

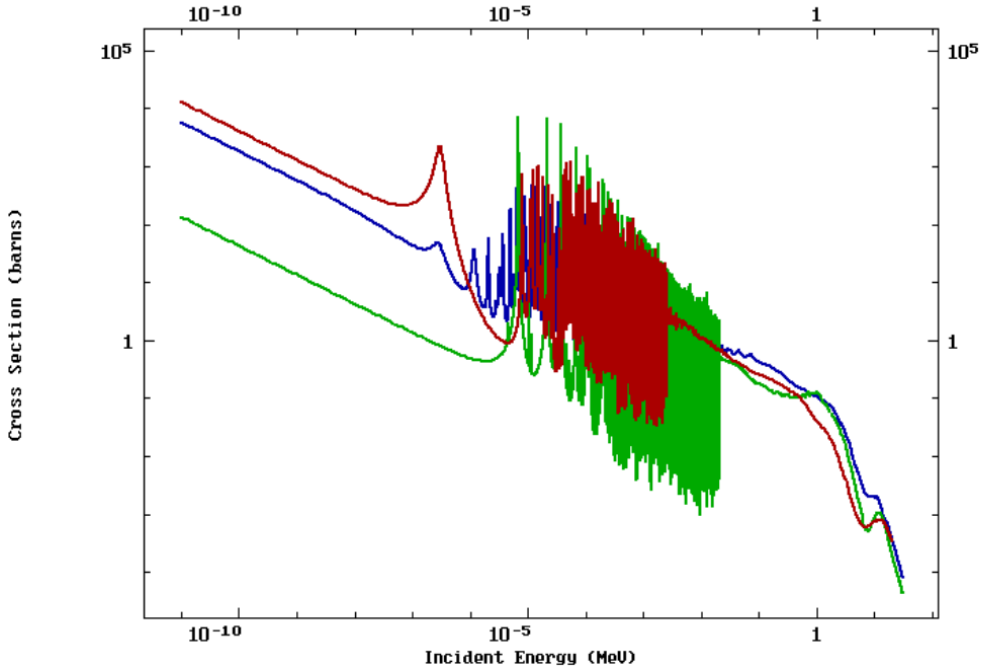

Figure 3. U-235 (blue), U-238 (green) and Pu-239 (red) Microscopic Capture Cross Section

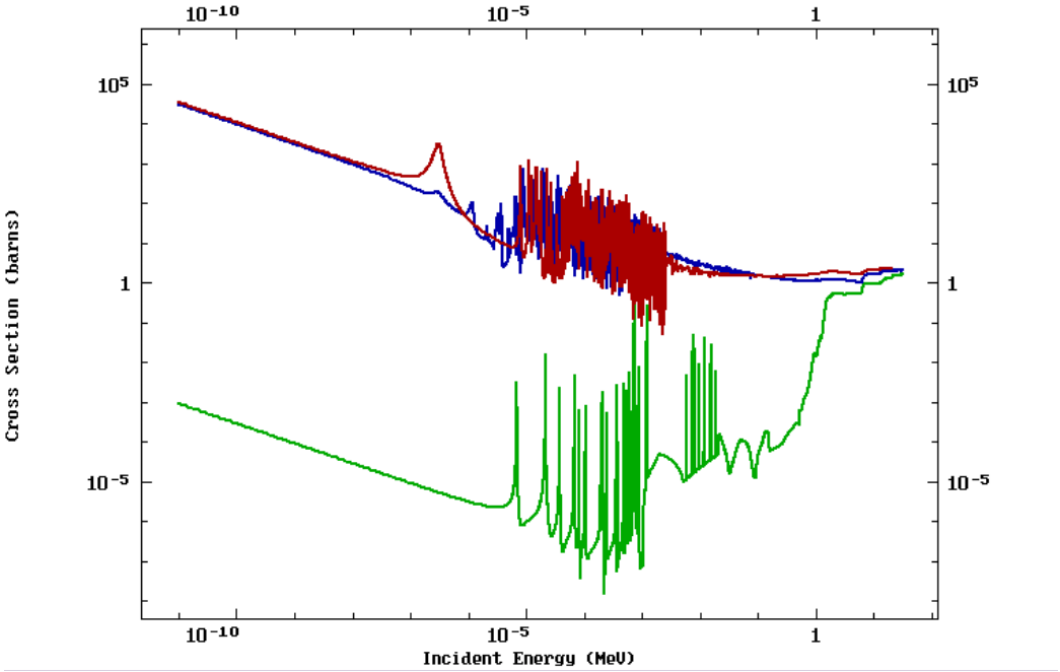

Figure 4. U-235 (Blue), U-238 (Green) and Pu-239 (Red) Microscopic Fission Cross Sections

When coolant is present, some fraction of fast neutrons will be scattered into the resonance energy range and captured parasitically. Without coolant, more fast neutrons will escape resonance capture and reach the moderator to be thermalized or additional fuel where they may participate in fission, leading to increased fast fission events and decreased neutron capture. Both factors tend to increase reactivity. Now, consider the opposite situation, of thermal neutrons entering back into a fuel channel from the moderator to participate in fission. When coolant is present, some fraction of thermal neutrons will be scattered by hot coolant to higher energies and captured in the resonance energy range of au-238. Without coolant, up scattering does not occur, and so more neutrons can participate in fission. This leads to an increase in reactivity from U-238, as fewer neutrons are absorbed parasitically, but a decrease in reactivity from Pu-239, as fewer neutrons reach the 0.3 eV resonance peak for fission. The result is a net increase in reactivity, that decreases as fuel burnup increases.

2.3. Overview of IAEA ICSP Benchmark Accident Scenarios

The sections below describe the 3 accident scenarios that were postulated for the IAEA ICSP Benchmark. Details of the accident scenarios are defined in the IAEA ICSP Benchmark Specifications [10]. In all transients, the pressurizer boundary condition is isolated from the system just before the transient is initiated. This significantly changes the expected results of the transient, such that the results generated by Benchmark participants may not reflect that behaviour described below.

2.3.1. Loss of Regulation

In a loss of regulation accident, RRS is assumed to lose control of the liquid zone controllers, adjuster rods, or both, causing the liquid zone compartments to drain, and adjusters to be removed from the core [6]. This results in an insertion of positive reactivity, leading to a reactor power rise and an in balance between core power and core flow, which can cause fuel overheating and system pressurization. This accident progression can be terminated by a bulk power trip, and reactor shutdown via SDS 1. Long term removal of heat is via forced flow from the PHTS pumps. In some cases, however, flux distortions can lead to local cases of fuel dry out (loss of liquid contact to the fuel sheath), while the bulk reactor power remains below the trip set-point. Consider, for example, the slow removal of a single adjuster rod in a low powered core region, or perhaps worse, the slow removal of a single adjuster, halfway out of the reactor. The neutron flux and power will increase in fuel channels that were previously adjacent to the adjuster rod and flow mismatch could cause local dryout in some fuel channels, particularly those with low burnup. This type of accident scenario forms the basis of Regional OverPower (ROP) setpoint analysis, which aims to determine trip set points for spatially distributed flux detectors, which measure local power, as opposed to bulk reactor power. In the IAEA ICSP Benchmark, two adjuster rods (ADJ 7 and 14) on the right side of the core are postulated to be removed simultaneously over the course of about 50 seconds, at a rate of 10.2 cm/s. The duration of the transient is defined to be 25 seconds, so the expected result is an asymmetric increase in reactivity over the course of the transient, an increase in reactor power and system pressure, and subsequent increase in fuel and cladding temperatures. Due to the system pressurization, little to no void formation is anticipated.

2.3.2. Loss of Flow

A loss of flow accident typically involves a malfunction, or loss of power to one or more primary heat transport pumps. Complete loss of class IV electrical power can lead to all 4 pumps tripping simultaneously, causing them to run-down and stop [6]. Pump rundown refers to the gradual reduction in impeller rotation, due to the large inertia of the pump, and the resultant gradual reduction in coolant flow. The pump rundown curve (impeller speed vs. time after pump trip) is an important aspect in safety analysis of loss of flow events, as it significantly impacts the rate at which flow is lost, the subsequent mismatch in core power/flow, fuel and cladding temperature rise, and coolant voiding. The pump rundown curve defined in the IAEA ICSP Benchmark Specifications can be seen in Figure A-5 in Appendix A. In this accident scenario, reactor shutdown can occur via SDS-1 through a bulk reactor power setpoint, or a high-pressure set-point. Like the LOR case, the in balance between core power and flow can cause the PHTS to pressurize, if the pressurizer cannot overcome the swell in coolant volume. For example, if loss of forced flow occurs at lower power (say 70% FP), and one or more pumps trip, a mismatch between flow and power can still occur, but given the low initial core power, it will take more time for the bulk power setpoint to be reached, and a high pressure signal could be generated instead. In the IAEA ICSP Benchmark, a single pump trip (P2) is postulated, and the pump runs down over the course of approximately 90 seconds. Again, the duration of the transient is defined to be 25 seconds, so the expected result is an asymmetric increase in reactivity over the course of the transient, an increase in reactor power and system pressure, and subsequent increase in fuel and cladding temperatures. In this case, coolant voiding in the tripped loop is anticipated.

2.3.3. Loss of Coolant Accident

Loss of coolant accidents are typically the result of a break in some component of the PHTS. The size of the break determines the categorization of the LOCA as small, medium, or large. A large LOCA is defined as a break at least twice as large as the diameter of a feeder pipe [6], and as such, can only occur above the fuel channel/feeder elevation. In the IAEA ICSP, a 60% inlet header break is postulated, and is therefore considered a large break LOCA. The accident progression between a small and large break LOCA can be significantly different, and so the focus of this discussion will be on large break LOCAs. In conservative analysis, is it often assumed that the pipe breaks instantaneously, which is not possible in reality, but leads to the fastest rate of system de-pressurization, and coolant void reactivity insertion. This assumption has been put into question, and current analysis practise is to assume a realistic break opening time. In the IAEA ICSP Benchmark, the break is postulated to occur over the course of 0.1 seconds, and the break opens linearly (meaning the break flow area increases from 0 to its maximum value, at a constant rate, over the course of 0.1 seconds). A typical accident progression is outlined here:

- Following the break, a rapid de-pressurization of the PHTS occurs, as it is now open to near atmospheric pressure. This in turn causes a rapid decrease in saturation pressure and temperature.
- The coolant in fuel channels downstream of the break rapidly vaporizes causing a large positive reactivity insertion.
- Reactor power increases due to the positive void co-efficient of CANDU reactors, leading to fuel and cladding temperature rise.

- Flow reversal in the broken pass occurs, while forward flow is maintained in the in-tact pass. In both passes, the flow begins to decrease both due to a decrease in pressure gradient, and due to a physical loss of coolant.
- The bulk core power reaches the overpower set point, and the reactor is shutdown via SDS-1.
- Due to low coolant inventory, fuel and cladding temperatures can continue to increase after shutdown.

The reactor shutdown phase of the accident occurs very quickly, and the reactor is completely shutdown 2 seconds after the break occurs. Long term cooling of the fuel after reactor shutdown is maintained initially by steam cooling, and eventually through Emergency Core Cooling (ECC) systems, which pump cold light water from a reservoir directly into the PHTS. In the IAEA ICSP Benchmark, SDS-1 is actuated when the core power reaches 120 %FP. There is a 0.25 second delay before the rods begin to move, after the trip has been actuated. The tips of the shut-off rods are defined to sit just above the reflector nodes, and so shutoff rod insertion begins immediately after the 0.25 second delay. The shut-off rods traverse the core in 1.5 seconds, at a rate of 294 cm/s.

2.4. Overview of Analysis Tools and Methods

2.4.1. Lattice Physics Transport Calculations

A typical lattice physics calculation consists of the following steps:

A. An evaluated nuclear data library, such as ENDF or JEFF, is prepared by a national research laboratory (e.g. Oak Ridge National Laboratory). Here, an experienced team will consider previous data sets and perform and analyze new experiments, to determine microscopic cross sections, decay rates, and other important parameters for all pertinent nuclides. In some cases, analytical solutions are integrated with experimental data. The final data set is given the term, "evaluated" to indicate the review process that was performed. This results in a pointwise, near continuous library of data, as a function of neutron energy.
B. A nuclear data processing code, such as NJOY, is used to collapse the point-wise data into a relatively course group structure (as compared to the continuous representation), using a generic flux spectrum. Ideally, this generic flux spectrum would be specific to the reactor for which the analysis is being performed. The output is known as a multi-group library and is typically performed by lattice physics code developers. It is important to note that the group width (i.e. the range of energy over which a parameter is held constant) is not fixed and is of crucial importance. In the SCALE 6.2 code distribution, several multi-group libraries are available, among the most recent being the ENDF-B VII 238 and 252 group libraries.
C. The multi-group library is then used to solve a simplified version of the neutron transport equation in a deterministic code (NEWT/TRITON in SCALE, WIMS, etc.). This step is often given the term "lattice physics calculation" and is often the only step in this process performed by a researcher. In the context of a multi-physics simulation, the output of this step is a set of homogenized cross sections that can be used in diffusion code.

An overview of this progression is shown in Figure 5. Additional discussion on this method, particularly on steps A and B, can be found in [13]. Step C is typically performed with either a 2 or 3-dimensional,

deterministic transport code, or a 3-dimensional Monte-Carlo based transport code. These options will be review in the following Sections.

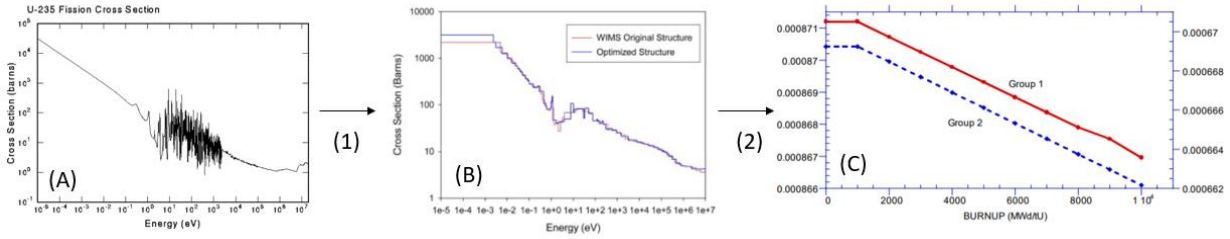

Figure 5. Lattice Physics Calculation Progression: (A) - Continuous Energy U-235 Fission Cross Section, (B) - ENDF-B VII 252 Group U-235 Fission Cross Section Library, (C) 2 Group U-235 Fission Macroscopic Cross Sections. Step (1) NJOY, Step (2) Lattice Physics Code

2.4.1.1. 2-Dimensional Deterministic Transport Codes

2-dimensional transport codes such as NEWT[14] and POLARIS [15] from the SCALE [16] code package, WIMS-AECL [17], DRAGON [18] and HELIOS can all be used to solve a simplified version of the neutron transport equation over an arbitrary 2-dimensional geometric domain. DRAGON also has the ability to perform 3-dimensional deterministic transport calculations. The SCALE code package is a U.S. N.R.C product that is increasingly being used in the CANDU analysis industry, at companies such as Kinectrics. WIMS-AECL was developed in Canada specifically to support industry-based analysis of CANDU reactors, while DRAGON, which was also developed in Canada, is an open source code used frequently in academia that also forms a component of the Industry Standard Toolset (IST). A full description of the calculation methods employed in a 2-dimensional transport codes is beyond the scope of this dissertation. Additional discussion can be found in [19]. Of the codes mentioned above, only NEWT was used in this work. Briefly, NEWT solves the transport equation using discrete ordinates approach, where the space, time and energy dependencies are treated using the finite difference method, and angular behaviour is treated by considering several discrete directions in space. This approach is the preferred method in modern lattice physics codes, compared to other methods such as integral transport, or collision probability, where simplifying assumptions are required [14]. NEWT uses an "Extended Step Characteristic" (ESC) approach, which allows for arbitrary polygons to be defined. POLARIS on the other hand, uses the method of characteristics, which drastically reduces run time, but was incompatible with CANDU fuel bundle geometry until recently and was not used for that reason.

2.4.1.2. 3-Dimensional Monte Carlo Codes

The Monte Carlo method has also been used extensively for transport calculations. Some examples of Monte Carlo based transport codes include SERPENT [20], MCNP [21], which are stand alone codes and KENO [22], from the SCALE code package. These codes have the advantage of allowing more complicated, arbitrary geometries compared to deterministic solvers, but have a drawback of being more computationally intensive. Furthermore, except for SERPENT, Monte Carlo transport codes typically do not have the ability to produce homogenized, 2 group cross sections, which, in the context of coupled diffusion/system-thermal hydraulics coupling, is a necessary feature. In this sense, lattice physics calculations are a necessary pre-cursor to diffusion calculations, as they provide the input data needed to perform the simulation. However, with increasing computational power, full core 3-

dimensional Monte Carlo based transport solutions are becoming more common, often taking advantage of core symmetry to reduce the computational effort.

2.4.2. Full Core Diffusion Calculations

Diffusion calculations have been used historically for full core analysis of nuclear power plants due to their low computational cost, flexibility, and proven track record. In a typical diffusion calculation, the core is subdivided into nodes, with one node representing one fuel bundle (in CANDU space) or assembly (in LWR space). For accurate calculations, reflector nodes must also be defined. Other input requirements include defining in-core device positions, burnup distributions and thermal-hydraulic parameter distributions. Often, a separate code is used to format the cross-section data output from a lattice physics code into the format required by the diffusion code. This is a step that is often forgotten but can play an important role in the overall data processing, as different codes have different, and sometimes incompatible, input requirements. Once defined, the diffusion equation is solved over the entire reactor domain. The output is typically a normalized power and flux distribution, which can then be used directly for core analysis, or passed to a thermal-hydraulics code in a coupled calculation. Most diffusion codes can solve the time in-dependent and time dependent versions of the diffusion equation. The time dependent version is used for transient simulations of accident scenarios or experiments, while the steady state time-independent implementation is useful for re-fuelling studies, among other applications. Some examples of diffusion codes include PARCS [23], RFSP, and NESTLE-C. PARCS is a U.S. NRC tool, while NESTLE-C and RFSP were developed for CANDU applications in academia and industry, respectively. Given the link between diffusion codes and lattice physics codes, the two are often developed together to facilitate efficient data transfer. For example, WIMS is intended to be used with RFSP, and PARCS is compatible with a large variety of lattice physics codes, including NEWT and HELIOS, through the processing utility GenPMAX [24].

A simplified version of the time independent, 2 group diffusion equation is shown in Equation 2-3a and 2-3b.

$$-\nabla \cdot D_1(r)\nabla\phi_1(r) + \left(\Sigma_{a1}(r) + \Sigma_{1\to2}(r)\right)\phi_1(r) = \left(\frac{\nu\Sigma_{f2}(r)}{k_{eff}} + \Sigma_{2\to1}(r)\right)\phi_2(r) \qquad (2-3a)$$

$$-\nabla \cdot D_2(r)\nabla\phi_2(r) + \left(\Sigma_{a2}(r) + \Sigma_{2\to1}(r)\right)\phi_2(r) = \Sigma_{1\to2}(r)\phi_1(r) \qquad (2-3b)$$

Where:

- r is the spatial location
- $D_1(r)$ and $D_2(r)$ are the group 1 and 2 diffusion coefficients
- $\phi_1(r)$ and $\phi_2(r)$ are the group 1 and 2 fluxes
- $\Sigma_{1\to2}$ is the group 1 to 2 (down-scattering/moderation) cross section'
- $\Sigma_{2\to1}$ is the group 2 to 1 (up-scattering) cross section
- Σ_{a1} and Σ_{a2} are the group 1 and 2 absorption cross sections
- Σ_{f2} is the group 2 fission cross section
- k_{eff} is the neutron multiplication factor

These equations assume that all fission occur with group 2 neutrons, all fissions are prompt, and all prompt neutrons are emitted in group 1. Although these equations are simplified from the versions

employed in a diffusion code, they are useful for the purposes of illustration. In both equations, the left hand side of the equation describes a loss of neutrons from the group (equation 2-1a tracks group 1 neutrons, and equation 2-1b tracks group 2 neutrons) and the right hand side describes a gain of neutrons into the group. Term 1 on the left-hand side of both equations describes a loss of neutrons due to leakage, and term 2 describes a loss due to absorption and scattering out of the group. The right-hand side of both equations represents a gain of neutrons into the group via fission, or scattering. After applying the finite difference method to this equation, it can be used to determine the group 1 and group 2 flux in each node of a reactor model.

In general, the cross sections shown above are a function of their position in the reactor and will change continuously with spatial location. However, when the equations and core model are discretized, the cross sections become dependent on the local conditions of the fuel bundle. In the context of this work, the cross sections are only dependent on the burnup of the fuel, the local thermal-hydraulic conditions, and the presence of any control devices.

$$\Sigma_x\left(B, T_f, D_c, T_c, CR_1 \dots CR_N\right) =$$

$$\Sigma_{x_0}(B) + \frac{\partial \Sigma_x}{\partial \sqrt{T_f}}(B)\left(\sqrt{T_f} - \sqrt{T_{f_0}}\right) + \frac{\partial \Sigma_x}{\partial D_c}(B)\left(D_c - D_{c_0}\right) + \frac{\partial \Sigma_x}{\partial T_c}(B)\left(T_c - T_{c_0}\right) + \sum_i^N CR_i \qquad (2-4)$$

Where:

- Σ_x is any cross section in node
- Σ_{x_0} is the reference cross section
- B is the local burnup
- T_f, T_c and D_c are the local fuel temperature, coolant temperature and coolant density
- T_{f_0}, T_{c_0} and D_{c_0} are the reference fuel temperature, coolant temperature and coolant density
- $\frac{\partial \Sigma_x}{\partial \sqrt{T_f}}$, $\frac{\partial \Sigma_x}{\partial T_c}$ and $\frac{\partial \Sigma_x}{\partial D_c}$ are the fuel temperature, coolant temperature and coolant density Partial Derivative Cross Sections Coefficients (PDCSCs)
- CR_i are the control rod incremental cross sections
- N is the number of control rod devices

What is important to note about equation 2-2 is the dependence of the partial derivative cross section coefficients on the local burnup, which allows for thermal-hydraulic feedback to be modelled at any level of fuel burnup. Note that control rod incremental devices are not a function of burnup in equation 2-2, although this is typically due to their low sensitivity to burnup, not due to a fundamental limitation in modelling [25] [26].

2.4.3. Full Core Thermal-Hydraulic System Calculations

While lattice physics and diffusion calculations are inherently linked as described above, a system thermal-hydraulics code is a standalone code that can determine the overall thermal-hydraulic behaviour of the system in question on its own. There are many different formulations of full core-system codes, but for the work describe in this thesis, the 6-equation formulation is most relevant. These codes solve the momentum, energy, and mass balance equations for both liquid and vapour phases. As such, these are often called two fluid, 6 equation codes. This set of partial differential equations can accurately model two-phase flow and heat transfer phenomena in the length scales of

interest (on the order of 1 bundle length). Additionally, 2 more equations can be added to the solution algorithm, to account for non-condensable gas species, and boron dissolved in the coolant.

System thermal-hydraulics codes are essentially one dimensional (some aspects of the calculation, such as conduction in fuel elements is in 2-D, but largely, the equations are solved in one dimension), and require the user to model the reactor as a series of nodes that are linked in a specific configuration. Each node contains information such as flow area, hydraulic diameter, roughness, volume, length, and elevation change. The nodalization scheme that is chosen is very important to the solution accuracy and can be different for each new component in the system. Some examples include TRACE [27], RELAP [28], CATHENA [29] and TUF. Both TRACE and RELAP are U.S. NRC codes, though RELAP has been used extensively in Canadian analysis, while TRACE was recently adopted as part of the Canadian IST and is being modified for use in CANDU analysis. CATHENA and TUF are both part of the Canadian IST, with TUF being used more frequently in industry and CATHENA being used in academia/research institutions.

2.5. Coupling Requirements

Avramova and Ivanov discussed in detail the requirements associated with 3D coupled neutronics (reactor physics)/thermal-hydraulics calculations in [30]. They list 6 components of any coupling methodology that must be considered in order to produce a valid simulation: 1. Methods of coupling (internal or external, the authors use the term "ways of coupling"), 2. Coupling approach (integration algorithm or parallel processing), 3. Spatial mesh overlays, 4. Coupled time step algorithms, 5. Coupling numerics (explicit, semi-implicit, and implicit) and 6. Coupling convergence. It is worth briefly reviewing these terms, given their relevance to the work that will be performed in this thesis.

First, the authors discuss the difference between internal and external coupling methods. In external coupling, a 3D kinetics model is coupled to T-H core boundary conditions in one code. This code would model the core thermal hydraulics using parallel channels, whose boundary conditions are obtained from a separate system code. The authors note that this a somewhat outdated method that was introduced due to limited computer resources at the time. The more sophisticated internal coupling method uses the full system model to generate core T-H conditions. The major differences are summarized in Figure 6. One can see that in the internal coupling method, the pertinent T-H variables are passed directly to the diffusion code, rather than using a simplified T-H model within the diffusion code to solve for these variables.

It is worth noting that the external method is rarely, if ever, used in multi-physics analysis today, and the terms internal and external coupling are now often used to distinguish between variables that are passed through memory and variables passed through a script-based interface. This second meaning of internal vs. external coupled is retained in the remainder of this dissertation. The authors instead define additional terminology in the context of coupling approaches. First, they discuss the difference between serial integration and parallel processing. In serial integration, the neutronics code is integrated into the T-H code as a routine (or vice versa) and uses the same dump/restart files. In synchronous processing, the neutronics and T-H codes are run separately, and data is exchanged during each time step of the calculation. Within the parallel processing approach, the authors define three different ways of passing data: Parallel virtual machine, message passing interface and static linked library. Briefly, both the parallel virtual machine and message passing interface pass information through computer memory,

while the static linked library writes the updated variables directly to the codes input file, which is then read into memory.

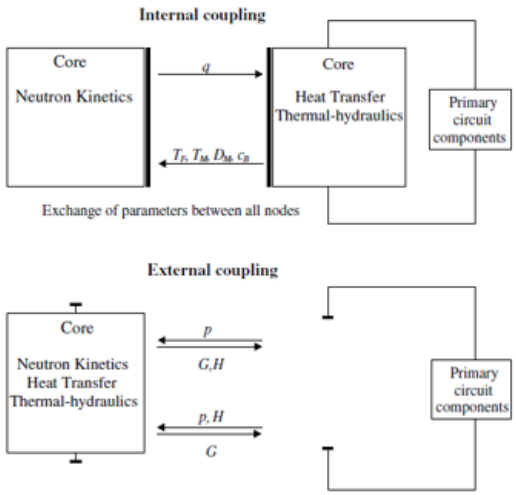

Figure 6. Summary of Differences between Internal and External Coupling Methods [30]

The authors then discuss in detail the impact of spatial meshing overlays on coupled multi-physics results. First, they define the difference between fixed and flexible coupling. In fixed coupling, there is a one to one mapping of T-H channels to neutronic assemblies (or channels in CANDU context), while in flexible coupling, the user has the choice to group several T-H channels together and map them to a corresponding set of neutronics assemblies (or vise versa, although this is never done in practise as the neutronics solvers are much less computationally expensive). The ideal approach (particularly for CANDU applications), is fixed coupling, however, even with advances in computer technology, this is often not feasible. The authors note that grouping T-H channels tends to smooth the power distribution and reduce feedback effects, particularly for local reactivity events such as a rod ejection accident in an LWR [31]. They go on to suggest a number of characteristics that can be used to group several neutronics assemblies into one T-H channel including relative power, coolant flow and burnup, and discuss studies that have been performed to determine the optimum arrangement for BWR and PWR cores. Currently, there are no such studies available in the open literature on CANDU analysis.

The authors then discuss coupling time-step algorithms. In summary, they note advantages and disadvantages of: 1. using a single code's time step selection algorithm to drive the time steps for both codes, 2. use of variable time step algorithms that take into account information from both codes simultaneously, and 3. the multiple time step marching scheme, where one code (typically the neutronics code) is allowed to take one large time step, while the other marches forward in smaller time steps that eventually meet up (say 10 T-H time steps are equal to one neutronics time step). They also suggest a small algorithm that can be used to determine the neutronics time step based on the T-H time step and the rate of change and accumulation of the local and global power errors. In this work, the terms "information exchange time step" and "internal time step" are used to distinguish between how often information is exchanged between codes, and the calculation time step of each code, respectively.

Finally, the authors briefly touch on coupling numerics, ie. the difference between explicit, semi-implicit and implicit schemes. An explicit scheme calculates the state of the system at a given time step with

information from previous time steps, and an implicit scheme uses information from both the previous and current time steps. In a semi-implicit scheme, parts of the calculation are implicit, and parts are fully explicit. The authors discuss a semi implicit scheme where the neutronics code calculates the nodal power distribution for the current time step using cross section feedback with fluid information from the current time step, but fuel rod temperatures from the previous time step. Within the context of coupling numerics, the authors also note that a major drawback of the current coupling methods is that the two codes are solved sequentially, as opposed to simultaneously, but do not provide any terminology to discuss these terms. However, in [32], the terms loose and tight coupling are defined which cover this gap. In a loose coupling scheme, the codes are run separately and pass information back and forth in what they call a Picard iteration until convergence is obtained, while in tight coupling, a single system of equations is solved that covers all the necessary physical phenomena.

It is worth noting that the terms described above are somewhat subjective, and as mentioned, there are often terms that can mean to different things, depending on the context of the situation (e.g. internal vs. external coupling). Hummel also provides a review of coupling requirements in [7], and defines similar terminology to that described above. In the context of the IAEA ICSP Benchmark, although participants were free to choose their own coupling technique for the Benchmark, several commonalities were identified over the course of the Benchmark. Using the terminology described above, the coupling methodology that was narrowed in on is fully explicit, and internal, with an integration algorithm approach (which implies loose coupling), flexible mesh overlay (28 T-H groups to 380 neutronics groups) and constant user defined time step (typically 0.1 or 0.05 seconds) for data transfer. The internal time step of each code is defined before the transient and was typically set to be 10 times smaller than the information exchange time step. No convergence scheme has been implemented at this time (i.e. the codes simply run sequentially). The T-H to neutronic map is provided in Figure A-1.

2.6. Multi-Physics Verification and Validation

Avramova and Ivanov discussed a qualification procedure for coupled multi-physics code systems in [33]. The qualification procedure that was described contains four elements: code and solution verification, model validation and predictive estimation of system responses with uncertainty quantification (sensitivity and uncertainty analysis). In general, the qualification procedure for a coupled system is based on qualification (verification and validation) of the individual codes used in the coupled model, and additional verification and validation of the coupling methodology. The extended verification procedure includes testing the data exchange between the codes, and the effectiveness of the coupling feedback, generally through code to code comparisons of well defined problems at different modeling levels (for example, stand alone neutronics simulations with and without T-H feedback allows thorough testing of the neutronics code without considering the impact of the T-H code). For example, the UAM LWR Benchmark is divided into three phases: neutronics phase, core phase, and system phase, which each contain three different exercises that pertain to one specific aspect of the phase (e.g. cell, lattice and core physics for the neutronics phase).

The extended validation procedure is simpler, in a sense, as it only involves comparing the coupling code system to available data and reference results (code to code comparison with a validated model). However, obtaining good agreement between best estimates calculations and experimental data is a challenging task on its own, and becomes even more complicated when uncertainty analysis is included

in the best estimate calculation. The authors presented the results of the OECD/NRC BWR Turbine Trip Benchmark, where participants best estimate results were compared against measured data for actual experiments performed at the Peach Bottom 2 nuclear reactor, as shown below in Figure 7. While good agreement is shown in both cases, it is worth noting that in the case of the axial power profile, the error bars shown for the average data is just the standard deviation of the participants results, not the uncertainty of a single participants results that was obtained through some form of uncertainty propagation. A similar type of validation study was performed for the OECD/DOE/CEA V1000CT Benchmark in [34], which looked at an experiment performed at Unit 6 of the Bulgarian KNPP, which is a VVER-1000 type reactor. Again, in this study, participants did not perform uncertainty propagation, and so there is no comparison of the uncertainty in the simulated model to the experimental uncertainty. One could argue that in both cases, no single participants model is truly validated, as that would require predictive estimation of the system response with uncertainty quantification, as described above. In fact, there is little to no work in the open literature on multi-physics validation studies that include uncertainty propagation to allow for a comparison of simulation uncertainty to measurement/experimental uncertainty. However, this type of analysis will be performed during phase 3 of the LWR-UAM Benchmark.

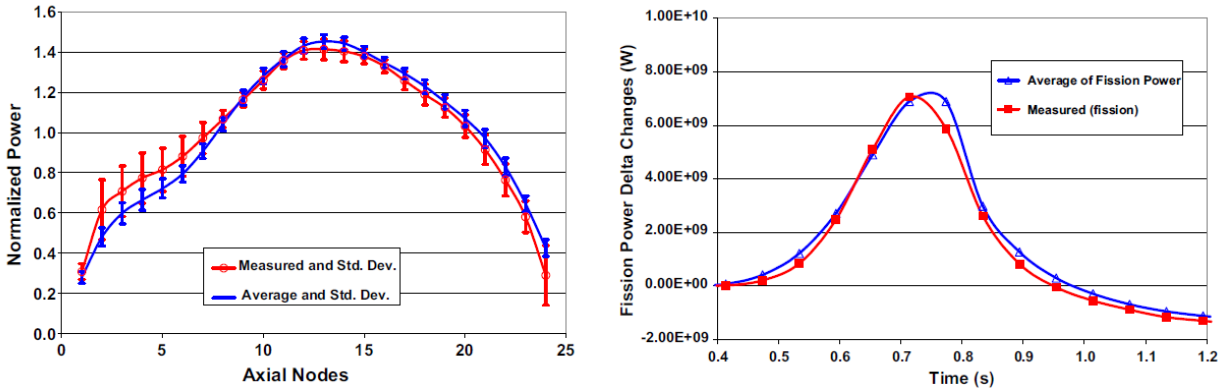

Figure 7. Comparison of the BWR Steady State Axial Power Profile (left) and Transient Fission Power (right) with Measured Data from the OECD/NRC BWR Turbine Trip Benchmark [30]

2.7. Overview of Uncertainty Analysis Methods

A high level overview of uncertainty analysis methods is provided in [35] by D'Auria et. al. The authors explain that an uncertainty analysis:

> *"consists of identification and identification and characterization of relevant input parameters (input uncertainty) as well as of the methodology to quantify the global influence of the combination of these uncertainties on selected output parameters (output uncertainty)."*

The authors then discuss 9 different uncertainty analysis methodologies, including the Canadian Best Estimate And Uncertainty (BEAU) method, the CSAU method (which the BEAU method is similar to) and the GRS method. They first define the difference between "propagation of input uncertainties", where uncertain input parameters with specific ranges or probability distributions are identified, and a number of simulations are performed, varying the uncertain parameters in each run, and "extrapolation of output uncertainties", where simulation results are compared against experiments to determine the

uncertainty in the output. The work in this dissertation focusses on the propagation of input uncertainties method, and so the extrapolation of output uncertainties method will not be discussed further. Within the propagation of input uncertainties, method, the authors distinguish between probabilistic and deterministic methods. In probabilistic methods, the "state of knowledge" of each input parameter is defined using a probability distribution. In deterministic methods, the state of knowledge is defined using reasonable uncertainty ranges and bounding values. All the methods listed above fall into the probabilistic category. Some features of each method are discussed below.

The CSAU method aims at determining the uncertainty associated with safety related parameters. The authors note that in demonstration cases, only single valued parameters (e.g. Peak Cladding Temperature – PCT, or integrated channel power, etc.) were assessed, with no examples of time dependent quantities. In the method, a PIRT is developed using experimental data and numerical transients to identify the most important phenomena and ranking is performed by expert judgement. High ranked parameters are then selected for inclusion in the uncertainty analysis and are perturbed based on uniform or normal distributions of their possible values. Output uncertainty is obtained by performing many calculations with the perturbed input data. The GRS method is similar, but allows for a larger number of input parameters, by randomly sampling from the combined probability distribution of the uncertain inputs. Furthermore, the GRS method employs the use of Wilks' formula to determine the number of runs required to obtain a given uncertainty band, for a given number of desired output parameters. Finally, the GRS method employs statistical methods to determine the sensitivity of key input parameter uncertainties, to key output result uncertainties. In many ways, the GRS method is just a more refined version of the CSAU method. The main difference between the Canadian BEAU method and the CSAU/GRS methods, is the use of a surrogate computer code, or response surface, to replace the computationally expensive tools that are traditionally used in Best Estimate analysis.

2.8. Role of Phenomena Identification and Ranking Tables in Multi-Physics Analysis

Phenomena Ranking and Identification Tables (PIRTs) and Phenomena and Key Parameter Ranking and Identification Tables (PKPIRTs) are a useful tool in multi-physics BEPU analysis. Starting in 1988, the United States Regulatory Commission allowed for the use of best estimate plus uncertainty methods for safety analysis of emergency core cooling systems. This led to the development of the "code scaling, applicability and uncertainty evaluation methodology" of which the PIRT process was a part of. In the context of that methodology, the PIRT process was used to support the BEPU licensing option by summarizing in a convenient format, the parameter which have the largest impact on the uncertainty and sensitivity of the simulation [36]. However, the PIRT process is also useful in multi-physics analysis, as a means of establishing the phenomenological requirements for such an analysis in their order of importance. This is an important step in multi-physics uncertainty propagation. Given the large number of input parameters which are uncertain, analysts must often choose which parameters to include, and which parameters to omit. The BEAU methodology described in [37] lists the 15 major steps to BEAU analysis. The PIRT/PKPIRT process is involved in 3 of the 15 steps.

Novog and Bao developed a PIRT for a loss of forced circulation accident in a CANDU style reactor in [38]. The metric of relevance for CANDU loss of forced circulation accidents is the dryout timing, given the impact dryout has on fuel temperatures, and fuel sheath failure. The parameter ranking was based

on the uncertainty of the parameters, the sensitivity of the dryout timing to the parameters, and the level of knowledge of the parameters. The methodology used to develop the PIRT can be summarized as follows:

Parameter Identification:

1. Relevant parameters and phenomena were identified using a hierarchical methodology by first identifying all major systems that play a major role in loss of flow accident and then selecting all components and processes within that system that are relevant to the accident progression. To ensure a complete and consistent list, the components were checked against station data (drawings, operating manuals etc.)
2. Based on the systems, components and processes that were defined in step 1, all relevant phenomena and parameters were identified through a review of the code input parameters, and mechanistic models, as described in the software theory manuals.
3. Finally, an interaction diagram was generated to show the relationship between the parameters and phenomena identified in step 2.

Parameter Ranking:

4. The uncertainty of the parameters and phenomena of interest was split into measurement uncertainty, simulation uncertainty and uncertainties due to physical changes in plant condition and operation. Measurement uncertainties were determined from instrumentation uncertainty calculations, and simulation uncertainties from code and model validation activities.
5. The sensitivity of the parameters and phenomena were determined by varying (perturbing) the values in both the positive and negative direction, and the slope in the conservative direction (i.e. that which reduced dryout timing) were reported.
6. The level of knowledge was determined though availability of reactor measurements, the applicability and coverage of supporting experiments and past experience. The parameters and phenomena were then given a rank between A to E, based on expert judgement.

The final ranking was then determined based on expert judgement of the combination uncertainty, sensitivity and level of knowledge. The results showed that channel power, CHF/dryout models and coolant flow are the parameters that have the largest impact on dryout timing.

A similar study was also performed in [37] for a large break loss of coolant accident in a Pickering B CANDU reactor. The Pickering units resemble the CANDU-6 design in many ways, with the same output power, and number of fuel channels. The figure of merit in this study was chosen to be the hot bundle enthalpy 5 second after the break. Like the Novog and Bao study, an initial PKPIRT was developed based on expert judgement to determine which parameters to include in the sensitivity analysis portion of the study. A linear response perturbation study was then performed, like the methodology used by Novog and Bao, to generate a final PKPIRT which could be compared back to the initial PKPIRT, to see if the initial ranking was accurate. A major difference in this study is that the ranking in the final PKPIRT was based solely off the sensitivity of the hot bundle enthalpy to various parameters and did not consider uncertainty or level of knowledge. The advantage here, however, is that it takes expert judgement out of the ranking and bases it entirely off quantitative results. Their results showed that coolant void reactivity had the highest impact on hot bundle enthalpy for a Large Break LOCA.

3. Model Development, and Coupling and Uncertainty Propagation Methods

3.1. TRACE System Model

3.1.1. Model Overview

The IAEA ICSP Benchmark Specifications [10] define thermal-hydraulic and neutronics parameters for coupled transients of a stylized CANDU-6 style reactor. On the thermal-hydraulics (TH) side of the problem, participants were provided with an ARIANT/CATHENA [29] system nodalization and channel power distribution and were asked to translate the nodalization into their code of choice and test the model using the channel powers provided. The TH model is limited to the Primary Heat Transport System (PHTS), and includes 28 fuel channel groups, 4 steam generators and primary heat transport pumps, a pressurizer, header to header balance lines and loop to loop interconnect lines. Heat transfer to the secondary side is captured using wall heat transfer models in the steam generator U-tubes, with constant secondary side temperatures and heat transfer coefficients defined at each U-tube node. Almost all control logic present in a real CANDU-6 plant, including steam generator and pressurizer level control, is removed from the model, and additional safety systems, such as Emergency Core Cooling (ECC), are not included. An overview of the system layout provided in the Benchmark Specifications is shown in Figure 8.

Two different channel power distributions were provided over the course of the Benchmark, and these are shown in Figure A-2, in Appendix A - IAEA ICSP Benchmark Thermal-Hydraulics Specifications. The distribution shown in the top of Figure A-2 was provided in an earlier version of the Specifications (December 2018) and was generated using a point kinetics model by the Benchmark Team. This channel power distribution is idealistic, with very little tilt in any direction and is useful for initial model development and testing. The distribution shown in the bottom of Figure A-2 was provided in the Final version of the IAEA ICSP Benchmark Specifications (March 2020), and was generated from a coupled ARIANT/NESTLE-C run, thus representing a realistic channel power distribution that one would obtain through steady state coupling, with a significant top-bottom tilt (more power in the bottom of the core) and a less significant left-right tilt (more power in right side of the core), which largely result from the specified burnup distribution shown in Figure B-1, in Appendix B. As such, this channel power distribution is useful for comparing system parameters between participants. The axial power distributions associated with the Final and December 2018 versions of the Specifications are shown in Figure A-3. There is only one axial power distribution defined in the December 2018 Specifications, while each channel has a unique axial power distribution in the Final Specifications. Figure A-3 shows the mean and standard deviation of the final axial power profiles. The final TRACE nodalization that was used to generate results that were submitted to the Benchmark is shown in Figure 14 and Figure 15. These Figures also show the fluid condition, relative to saturation, when the model was run with the channel power distribution from the December 2018 Specifications (Figure 14) and the Final Specifications (Figure 15).

The concept of a "channel group" is an important aspect of this thesis, and code coupling in general, as discussed in Section 2.5. A system thermal-hydraulics channel group refers to the grouping of several neutronics channels into one set of thermal-hydraulic components. Average properties (lengths,

elevation changes, flow areas etc.) are calculated for feeders, end fittings and fuel channels to create one representative geometry, which is then duplicated to capture the total properties of all the fuel channels represented in that group. The total channel power of all neutronics channels in that group is then written to a single power/heat structure component. The mapping between neutronics and system-thermal channels is shown in Figure A-1. This mapping is analogous to the "spatial meshing overlays" discussed in Section 2.5.

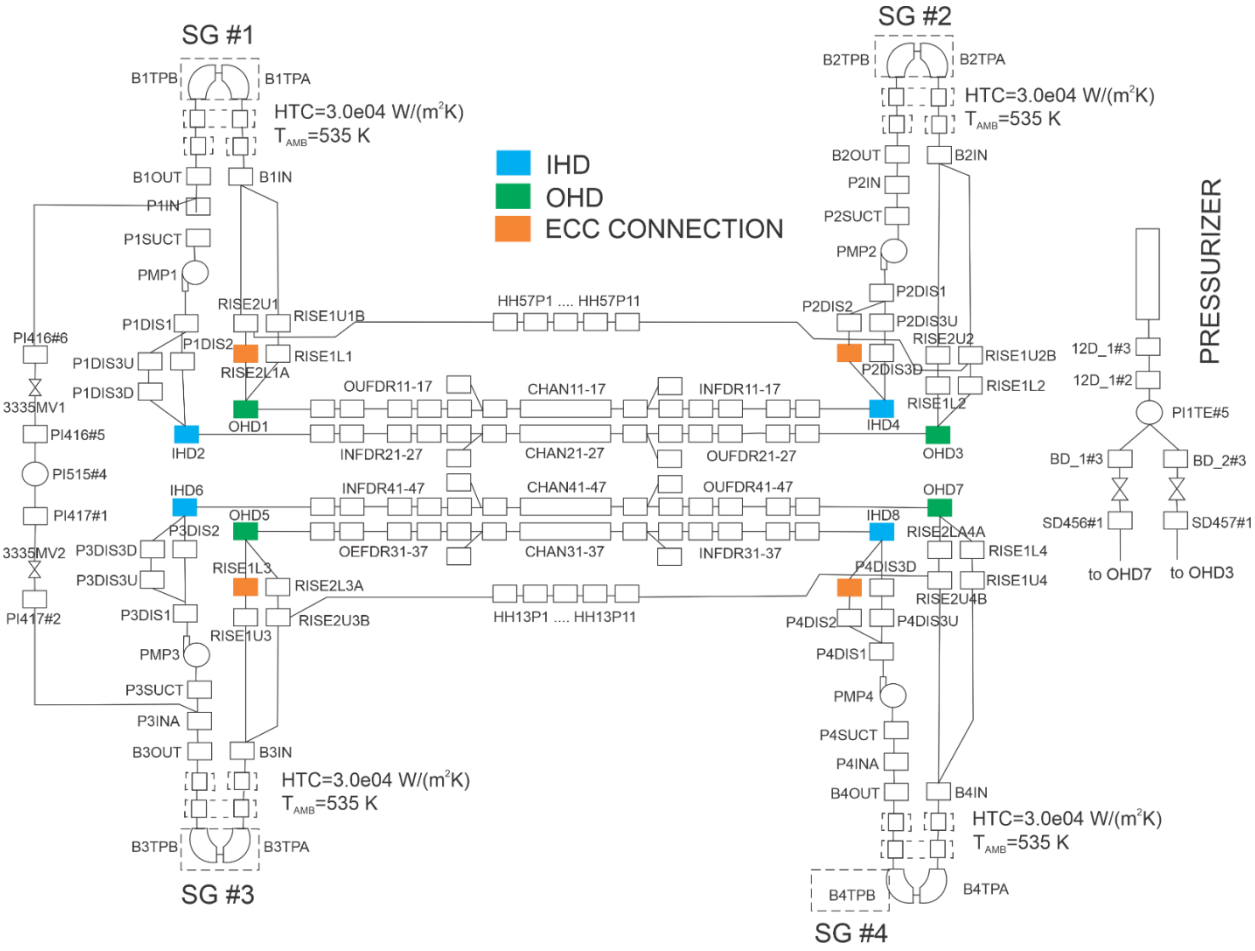

Figure 8. IAEA ICSP Benchmark System Thermal-Hydraulics Model Overview.

3.1.2. Model Development

The differences in input requirements between ARIANT and TRACE/RELAP are reviewed here. ARIANT is a "node and link" code, which means that a single flow area, hydraulic diameter, and K-factor are defined for each node, and a single velocity is calculated. TRACE and RELAP on the other hand are "node and 2 cell edge" codes, which means that 2 flow areas, hydraulic diameters and K-factors are defined for each cell edge, and 2 cell edge velocities are calculated. These differences are summarized in Figure 9. Note that in Figure 9, bolded quantities are calculated by the code, and un-bolded quantities are input parameters. Initial values for the bolded parameters are still required as input, which is why they are included in the Figure below.

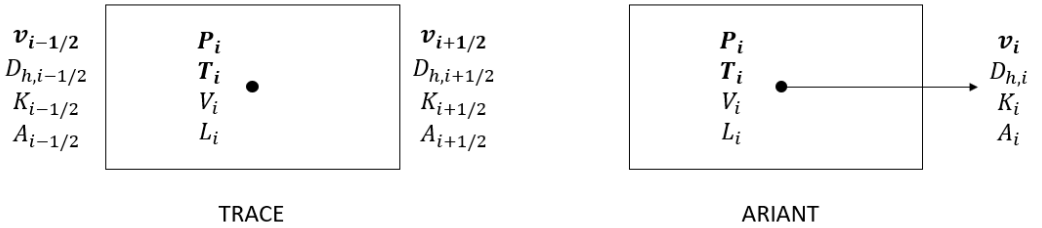

Figure 9. TRACE/RELAP Nodalization and Input Requirements (Left) vs. ARIANT/CATHENA Nodalization and Input Requirements (Right)

Where:

- v is the fluid velocity
- D_h is the cell or cell edge hydraulic diameter
- K is the cell or cell edge minor loss co-efficient or K-factor
- P is the fluid pressure
- T is the fluid temperature
- V is the cell volume
- L is the cell length
- A is the cell or cell edge flow area

Because of these differences in input requirements, a set of rules had to be developed to translate the ARIANT input deck into a TRACE input deck. These rules are summarized in Appendix C - ARIANT to TRACE Nodalization Conversion Rules and Calibration Methods, Section C-1. However, it was found that a direct implementation of these rules with no additional modifications or model calibration resulted in very poor pressure agreement throughout the system, but reasonable temperature agreement. This finding was documented in [39] and lead to a discussion in the third technical meeting for the IAEA ICSP Benchmark (September, 2018). It was realised that model modifications and/or calibration would be required to obtain comparable pressure distributions throughout the PHTS between participants, both due to differences in system code input requirements, as well as differences in modelling capabilities and closure relations. It was agreed at that time that participants should aim to match the ARIANT coolant pressure and temperature distributions, and fuel element temperature distributions provided in the IAEA ICSP Benchmark Specifications, by re-nodalizing components, modifying component geometry, or performing K-factor calibration, as necessary. This method allows for high-level verification of participants models, through comparison with ARIANT results, and provides confidence that the variables that will be passed to the diffusion codes are comparable among participants in the steady state. The ARIANT data discussed here will be referred to as the Reference ARIANT results in this dissertation.

Two different methods were investigated to improve the pressure agreement:

1. K-factor calibration
2. Model modifications with no K-factor calibration

In the first method, only K-factors were adjusted and no changes to model geometry were performed. In the second method, the opposite approach was taken, where defensible changes to the model geometry were made where possible, and only very minor K-factor adjustments were made. These

changes are described in Appendix C, Section C-2. It was found that the system results were very comparable between these two methods, and both agreed well with the Reference ARIANT results. It was decided that the method 2 model would be used moving forward, as the K-factor adjustments performed in method 1 were completely arbitrary and indefensible. This model will be referred to as the modified TRACE model in this dissertation. The un-modified (direct translation from the Benchmark specifications) and method 1 (K-factor calibration) models are also available for future investigation, if needed. The method 1 model will be referred to as the tuned model in this dissertation, although it was never used.

The pressure distribution obtained from running this model with the channel power distribution provided in the Final Specifications (Figure A-2, bottom), is shown on the top of Figure 11. One can see that in general the agreement with the Reference ARIANT results is good, although there are some areas which do not agree well:

1. Pressure drop between the pump discharge lines and inlet header (difficult to see in Figure 11)
2. Pressure drop between the outlet headers and the steam generator riser lines
3. Pressure drop between the steam generator outlet plenum, and the pump suction lines

3.1.2.1. Final Changes to the Modified Model

In all the cases identified above, poor pressure agreement resulted from a fundamental difference in TRACE and ARIANT modelling capabilities. ARIANT allows the user to turn off area change pressure drop calculations (often called the Bernoulli pressure drop term), while TRACE does not. This term arises from the conservation of mass flux imposed between adjacent nodes in a system thermal -hydraulics code, such that a change in flow area also causes a change in velocity and a corresponding change in pressure. In all the identified cases, a significant area change occurs, and the resulting pressure drop is larger in the TRACE results than in the ARIANT results. In the first two cases, removing the K-factors between the nodes was sufficient to improve the pressure agreement. However, in the last case, the K-factor was already set very close to 0, and so additional changes had to be made. Unfortunately, it was found that the only way to remove the pressure drop between these nodes is to modify the volume averaged flow area (volume of the component divided by its length) of one of the two components, forcing the area change pressure drop term to 0. In this work, the outlet plenum of the steam generator was modified by increasing its length, as one can see in Figure 10. This model will be referred to as the final or calibrated TRACE model in this thesis. The pressure drop distribution obtained with this model is shown in the bottom of Figure 11.

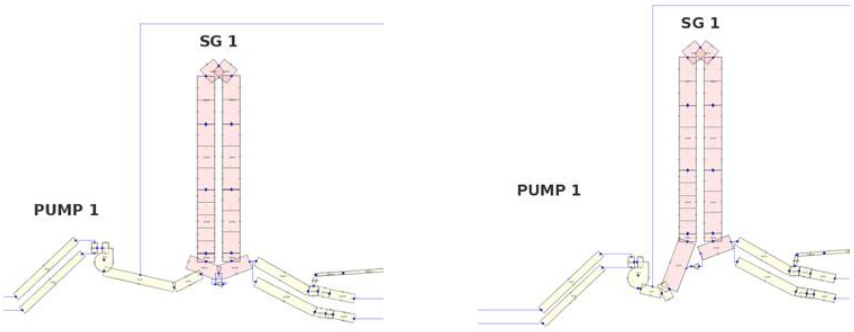

Figure 10. Specified Steam Generator Model (left) vs. Modified Steam Generator Model (right)

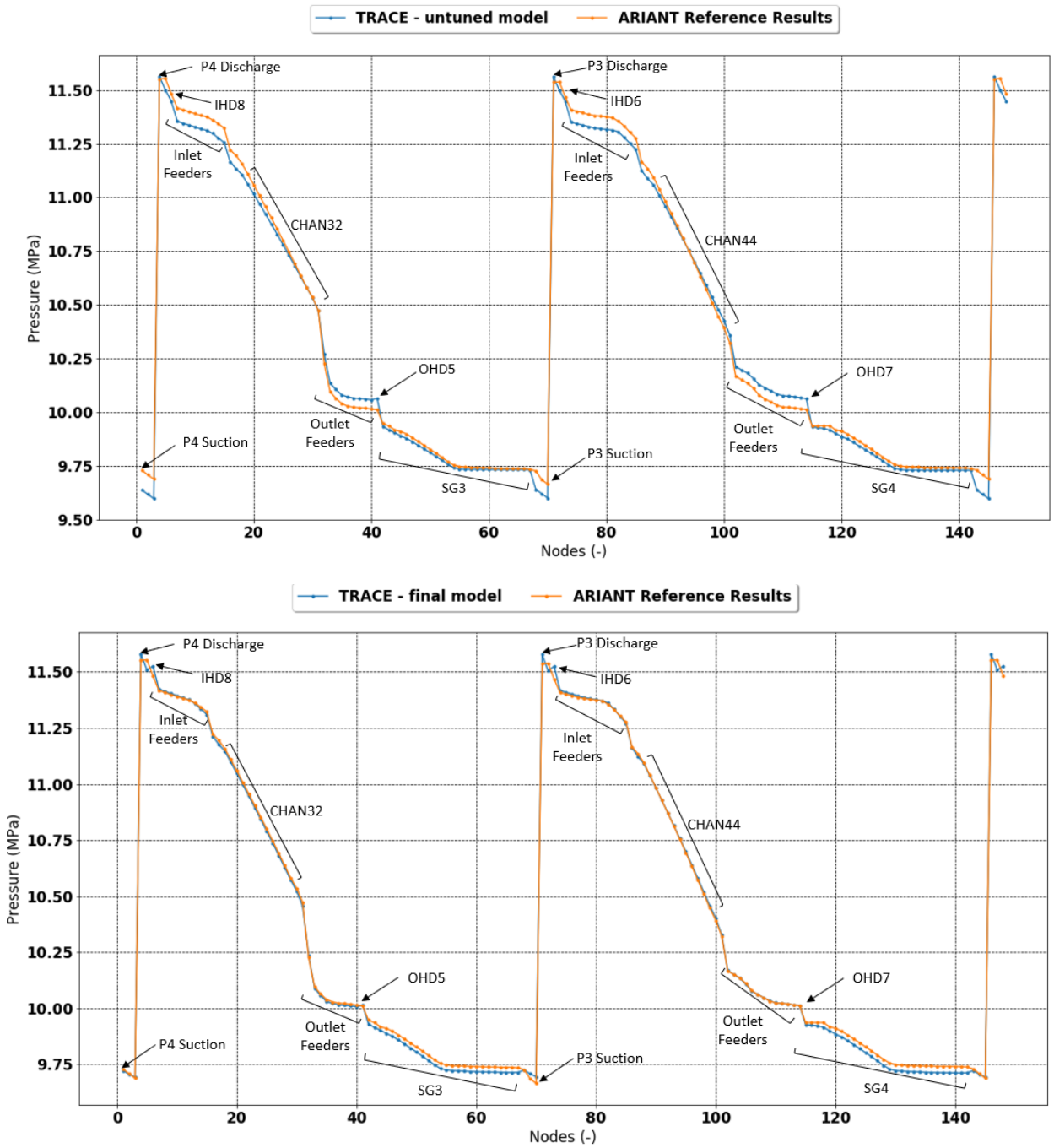

Figure 11. TRACE vs. ARIANT Pressure Profiles for Loop 2 of the System Model: Top – Modified Model Results, Bottom – Final Model Results

3.1.3. Model Verification

As discussed in the previous Section, a comparison of the steady state coolant pressure drop predicted by TRACE and ARIANT around loop 2 of the system model is shown in Figure 11, for the modified (top) and final (bottom) TRACE system models. Again, these results were generated using the channel power distribution from the Final Specifications (Figure A-2, bottom). One can see that the additional changes to the modified TRACE model greatly improved the pressure agreement, and that the TRACE and ARIANT results match very closely in the final model. Figure 12 shows the coolant temperature distribution around the same loop of the system There was little to no difference in the coolant temperature results between the modified and final TRACE models. Again, one can see that the agreement between TRACE and ARIANT is very good. These two Figures provide confidence that the final TRACE model is predicting coolant temperatures and densities that are comparable to the Reference ARIANT Results in the fuel channel nodes, as the coolant density is strictly a function of pressure and temperature in sub-cooled conditions, which as shown in Figure 15, is the case for the majority of the fuel channels.

Figure 13 shows the fuel element temperature distribution in Fuel Channel Group CHAN11, Bundle 6. The top plot shows the results of a fuel element model that does not contain a gas-gap, as a sensitivity case, and the bottom plots shows the results of the final model that does contain a gas-gap. The no gas-gap model was originally specified in the December 2018 Version of the IAEA ICSP Benchmark Specifications and was later replaced with a model that includes a small gas gap, which was retained in the Final Specifications, and final TRACE model. This is another departure from reality, since during normal operation the PHTS pressure causes the cladding to collapse onto the fuel pellets, removing any gas gap that was initial present. Material properties were defined for the fuel, and cladding. For a CANDU style reactor, the fuel is Uranium Dioxide, and the Cladding is Zircalloy-IV [10][40]. The gas gap heat transfer co-efficient was defined directly in the Specifications, as 10 000 $W/(m^2 K)$, and so the gas gap material does not have an impact on the temperature distribution in the fuel element. The widely used MATPRO Report [41] was used to determine the properties for the Uranium Dioxide and Zircaloy-IV materials.

In addition to the gas-gap, and no gas-gap models described above, a sensitivity study was also performed using the TRACE dynamic gas gap model, with no plastic deformation. When this option is selected (NFCI=1), a simplified FRAPCON 3.4 model is implemented which has the ability to determine gap heat transfer co-efficient, and cladding lift-off or collapse [27]. When using this model option, the user must also define a gap pressure, which was found to have a large impact on the temperature distribution in the bundle. In this work, a gap pressure of 3 MPa was selected, based on data provided in [40]. At this pressure, the cladding collapses onto the fuel, and the results are very comparable to the no gas gap model results.

From Figure 13, one can see that the results are comparable between ARIANT and TRACE, across all different versions of the fuel element model. This provides confidence that the material properties and TRACE fuel element models were defined correctly and are predicting comparable fuel temperatures to the Reference ARIANT Results, for a given channel power and axial distribution. From inspection of the results, one can see that the built-in material properties provided a closer match to the ARIANT results. It is unclear why this is the case, but it is not surprising that the TRACE material properties provide similar results, as they are also based largely off the same MATPRO Report.

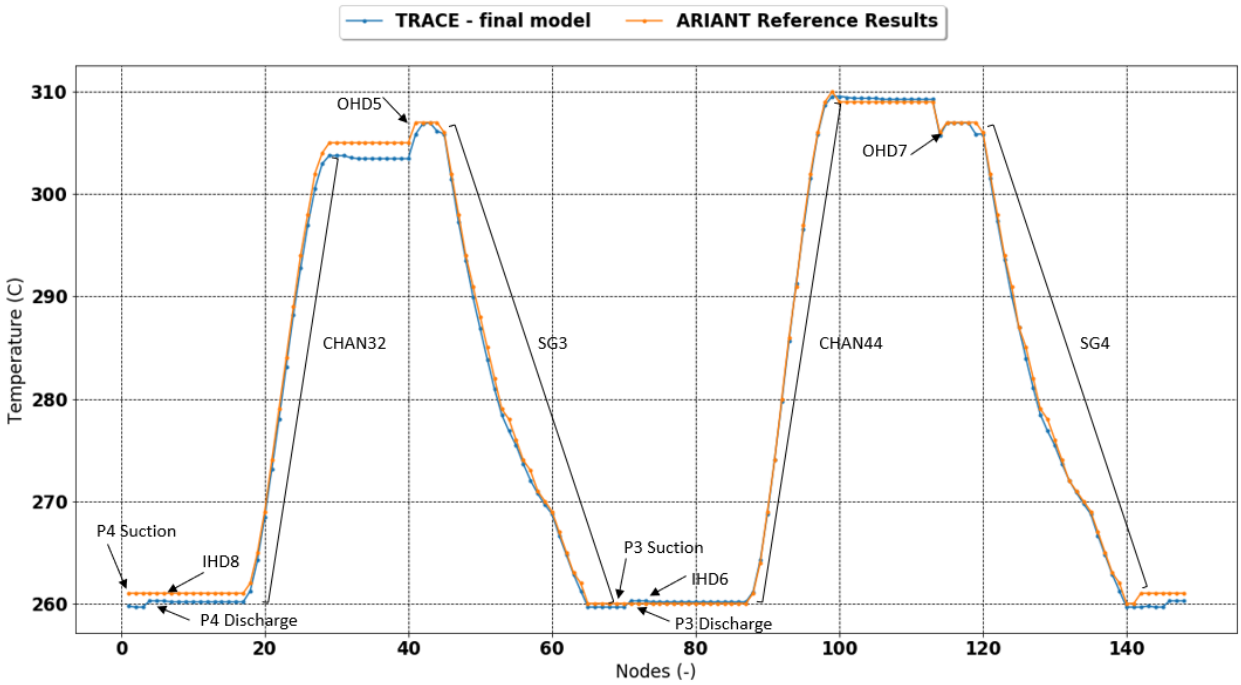

Figure 12. TRACE vs. ARIANT Coolant Temperature Profiles for Loop 2 of the System Model

3.1.4. Steady State and Null Transient Results

From Figure 15, one can see that Channel Groups CHAN17, CHAN27, CHAN37 and CHAN47 in the final TRACE model all have significant vapour formation in the fuel channel, when run with the channel power distribution defined in the Final Specifications. From Figure A-1, one can see that these channel groups reside near the bottom of the core, where there is a peak in core power (See Figure A-2, bottom). Furthermore, one can see that Channel Groups CHAN36, CHAN34 and CHAN46 all have some minor vapour formation in the outlet feeders, while the corresponding channels of the left side of the core, do not, indicating the presence of a small left-right tilt (which can again be seen in Figure A-2, bottom). Figure 14 shows the system response with the Channel Power Distribution defined in the December 2018 version of the Specifications (Figure A-2, top). In this case, there is no vapour formation in any channels, as expected for a CANDU-6 reactor.

All simulations described above were run in the steady state calculation mode, with a minimum time step of 1×10^{-6} seconds, and a maximum time step of 0.01 seconds. A steady state convergence criterion of 1×10^{-3} was used for all state variables. These are typical values recommended in the TRACE User Guidance Manual [42]. When the system was run using the channel power distribution from the December 2018 Specifications, the code converged in approximately 27 seconds of TRACE simulation time (which can be seen in Figure 14). However when the system was run with the channel power distribution from the Final Specifications, it was found that the code would never converge to a steady state error of 1×10^{-3}, due to the formation of vapour in some of the fuel channels. This was investigated by performing null transient runs (running the code in the transient calculation mode, but keeping all parameters constant), for various lengths of time. It was found that the major system parameters, such as header pressures and temperatures, and pump mass flow rates, converged to reasonable steady

state values after approximately 50 seconds of TRACE runtime. These results are shown in Figure 16 and Figure 17.

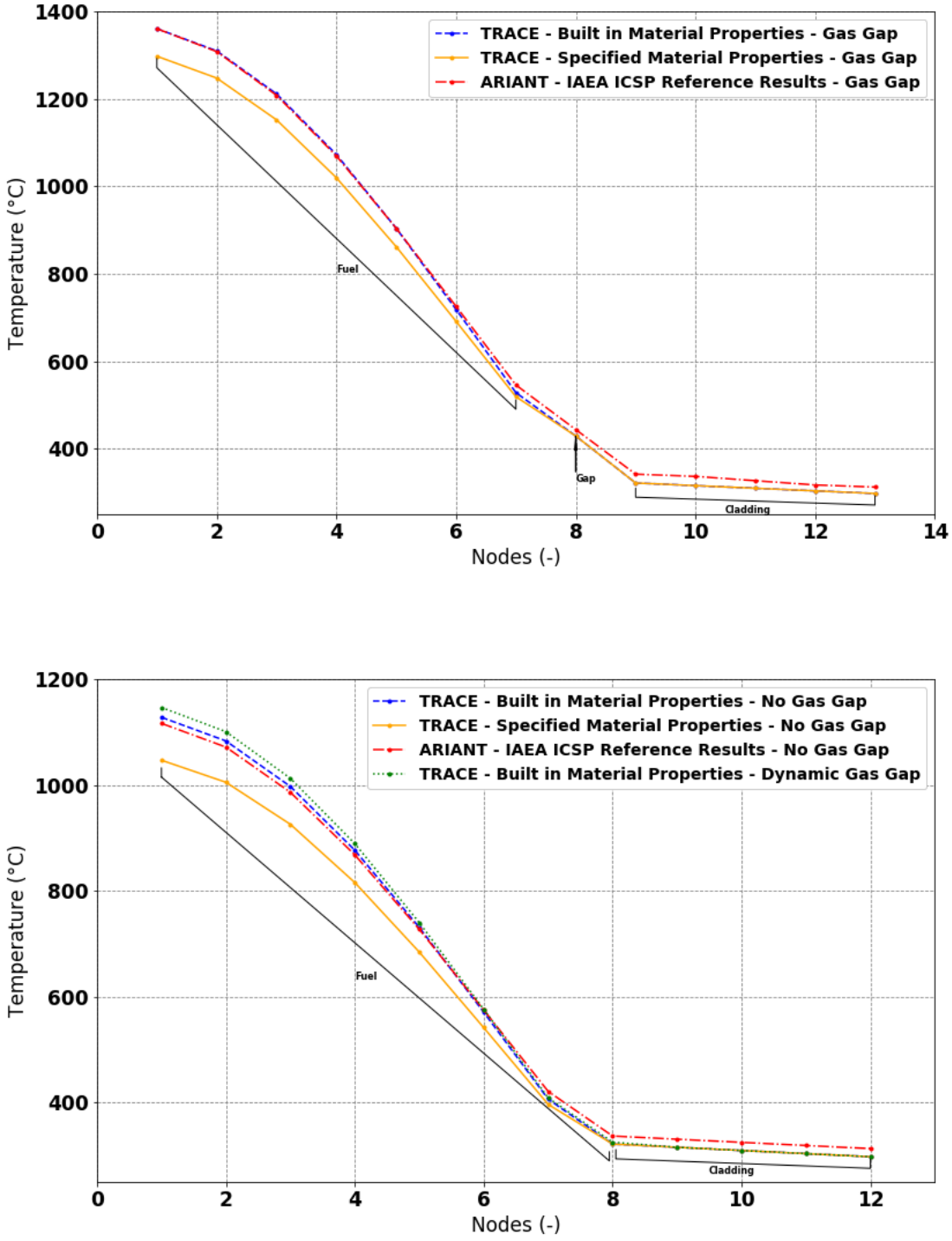

Figure 13. CHAN11, Bundle 6 Temperature Distribution: Top - Gas Gap, Bottom - No Gas Gap

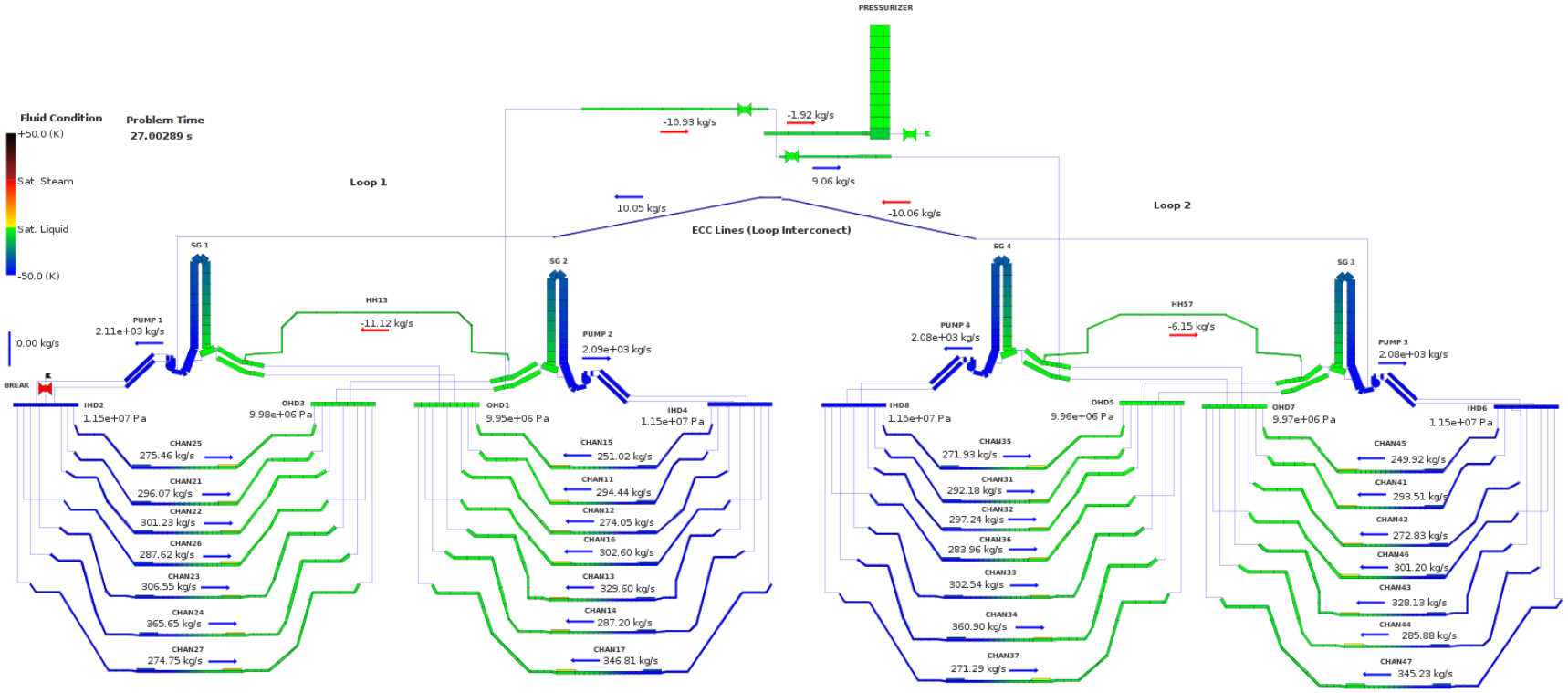

Figure 14. Final TRACE System Thermal-Hydraulics Model - Fluid Conditions (Generated with the Channel Power Distribution from the December 2018 IAEA ICSP Benchmark Specifications – Figure A-2, Top)

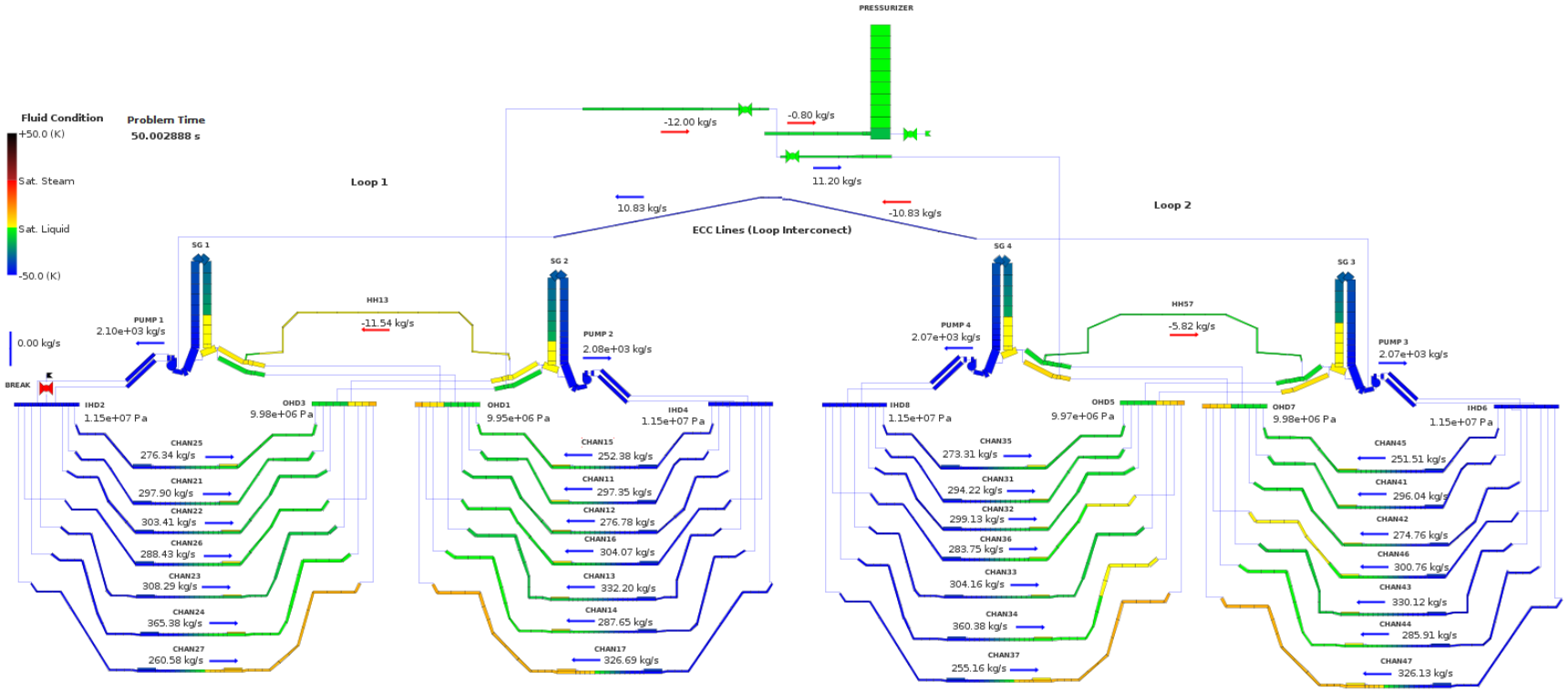

Figure 15. TRACE System Thermal-Hydraulic Model Fluid Condition Results (Generated with the Channel Power Distribution from the Final IAEA ICSP Benchmark Specifications – Figure A-2, Bottom)

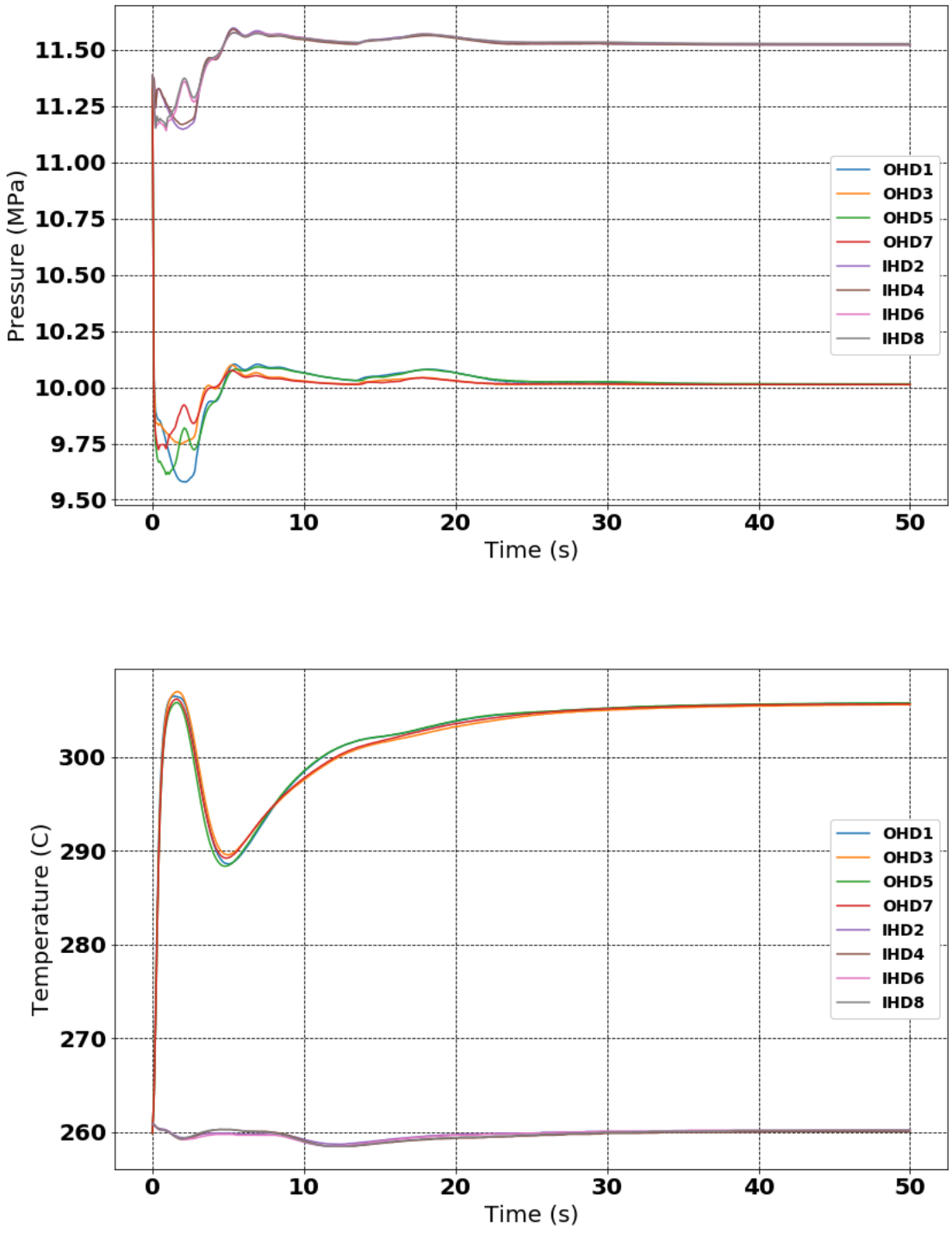

Figure 16. Stand-alone Null Transient Results with the Final Channel Power Distribution: Top - Header Pressures, Bottom - Header Temperatures

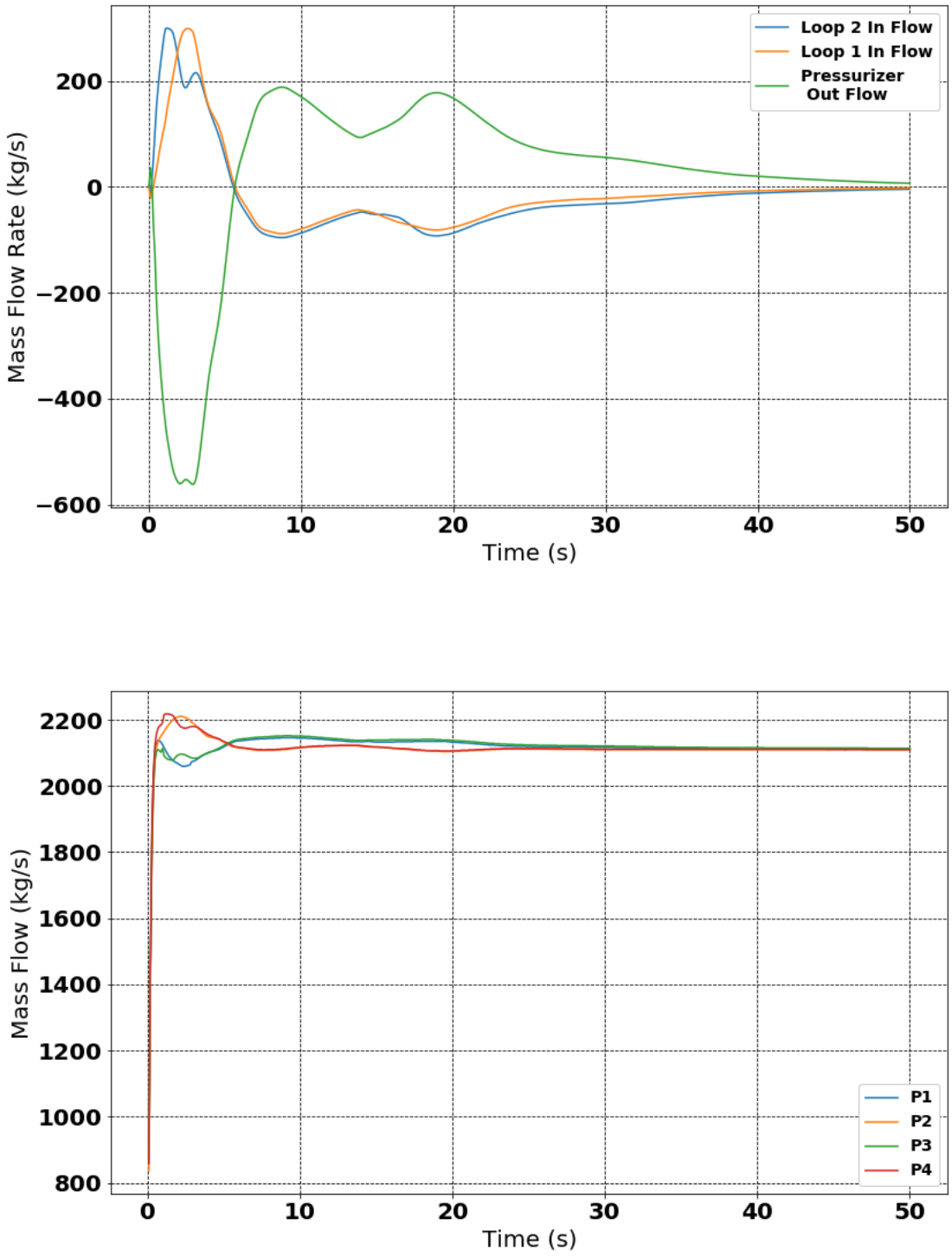

Figure 17. Stand-alone Null Transient Results with the Final Channel Power Distribution: Top - Loop Mass Transfer Flow Rate, Bottom - Pump Mass Flow Rate

3.2. Reference Lattice Physics Calculations

3.2.1. 2-Group Macroscopic Fuel Cross Sections and TH-Invariant Neutronics Data

Two group fuel and reflector reference cross sections, thermal-hydraulic branch partial derivative fuel cross section coefficients and TH invariant transient neutronics data were provided over a large burnup range in the IAEA ICSP Benchmark Specifications. This data will be referred to as the specified cross section data throughout this dissertation. This allowed participants to use a consistent set of cross sections, eliminating any differences that would result from generating this data with different lattice physics codes, or nuclear data libraries. However, to extend beyond the scope of the IAEA ICSP Benchmark and perform uncertainty analysis of selected transients, and to perform a high-level verification of the data provided by the Benchmark Team, the full set of input data was also generated using the SCALE [16] code system. The reflector calculations will not be discussed here.

In SCALE, a lattice physics transport calculation is performed by calling various sub modules that perform specific calculations in one input deck. In this work, a 2-D lattice cell calculations was performed, taking advantage of the uniform axial composition of a CANDU fuel bundle, using the NEWT [14] and TRITON [43] modules. NEWT solves a simplified version of the neutron transport equation over the defined geometrical domain, with TRITON performing isotopic depletion and cross section homogenization. The CENTRM and BONAMI Modules were used for self shielding calculations during the NEWT/TRITON run, with CENTRM performing self shielding in the resolved resonance region, and BONAMI performing self shielding for the thermal, fast and unresolved energy ranges [16]. Dancoff factors were also computed separately for each coolant density branch, using the MCDANCOFF Module. Here, MCDANCOFF must be run for each coolant density branch, and the resulting Dancoff factors for each fuel element ring must be manually written to the NEWT/TRITON input file. This methodology is consistent with past work done at McMaster for the Canadian Super Critical Water Reactor [8] and CANDU-9 analysis [44]. In this work, the 252 group ENDF-B VII library was used.

The CANDU bundle geometry that was defined in NEWT is shown in Figure 19, along with 2 group flux results, shown in Figure 20. Some details of the lattice physics calculations are provided in Table 2, and full details can be found in [45]. In this work, the key output of the lattice physics calculation is a set of homogenized, 2 group macroscopic cross sections as a function of burnup, that characterize a fuel bundle node during diffusion calculations. The homogenization region was defined over the entire cell geometry shown in Figure 19 and the group 2 energy cut-off was set at 0.0625 eV, and contains 39 of 252 groups. The 2 group specified cross section data provided by the Benchmark Team was generated using the HELIOS lattice physics codes with the same TH branch values shown in Table 2. However, in the actual data that was provided to participants, the TH branches were combined in some way to yield a single set of partial derivative cross section coefficients (PDCSCs) for each TH variable. As such, the original HELIOS data was obtained to facilitate a branch by branch comparison to the SCALE results.

A summary of PARCS input data requirements (equivalently SCALE output data, although SCALE provides much more than what is shown) is provided in Table 3. One can see that there are 24 different input parameters that are a function of both burnup, and TH variables (see Equation 2-4), in addition to the 17 TH independent input parameters, which are only a function of burnup. Given the 23 TH branches shown in Table 2, there are 569 (23x24 + 17) different burnup dependent input parameters that should be compared against the HELIOS data. As such, even high-level verification of this calculation is a difficult

task. In this work, a time-consuming visual comparison was performed by plotting all 569 parameters produced by HELIOS and SCALE as a function of burnup. The complete results of this type of verification is beyond the scope of this dissertation. However, Figure 21 shows a comparison of 3 important cross sections: the group 2 fission, absorption, and group 1 to 2 (fast to thermal) scattering cross sections. The results compare very well between codes, showing similar magnitudes and trends. The importance of these cross sections is clear from basic CANDU theory, where a large moderator volume causes most fast neutrons to be scattered to thermal energies, where they are either absorbed parasitically or participate in fission. This is also born out in the results of a simple sensitivity study that was performed very early on in this work, the results of which are shown in Table 1. In this study, each reference cross section was perturbed one at a time, by 1%, and the change in K-effective was determined by Equation 3-1. From Table 1, one can see that K-effective is most sensitive to the three cross sections mentioned above.

Table 1. Cross Section Perturbation Study Results

Cross Section	Relative Change in K-effective
$\Sigma_{tr,1}$	-0.138
$\boldsymbol{\Sigma_{a,1}}$	**1.797**
$\Sigma_{f,1}$	-0.851
$\Sigma_{tr,2}$	-0.171
$\boldsymbol{\Sigma_{a,2}}$	**8.490**
$\boldsymbol{\Sigma_{f,2}}$	**-8.917**
$\Sigma_{1\to1}$	0.0
$\Sigma_{1\to2}$	-1.108
$\Sigma_{2\to1}$	0.020
$\Sigma_{2\to2}$	0.0

$$\Delta k_{eff} = \frac{k_{eff,reference} - k_{eff,perturbation}}{k_{eff,reference}} \qquad (3-1)$$

Figures F-1 through F-9 in Appendix F show the TH PDCSCs for these cross sections. From inspection of these Figures, one can see that the agreement between SCALE and HELIOS is very good, with both codes showing the same trends as a function of burnup and similar magnitudes. There are several things that are worth pointing out about the PDCSC results:

- The HELIOS and SCALE PDCSC data compare very well for the following cases:
    1. Group 2 Absorption Coolant Density (Figure F-1)
    2. Group 2 Absorption and Fission Coolant Temperature (Figure F-4 and Figure F-5)
    3. Group 2 Absorption and Fission Fuel (Figure F-7 and F-8)
- For all TH Variables, the down scatter PDCSCs do not agree as well:
    1. Coolant Density: There is a clear bias present where SCALE predicts values that are consistently more negative than the HELIOS values. There is some noise present in both sets of data.
    2. Fuel Temperature: There is a clear bias present, where SCALE predicts values that are less positive than the HELIOS data for fuel temperatures greater than the reference

temperature, and more positive for fuel temperatures less than the reference temperature.

3. Coolant Temperature: The agreement is very poor here. However, it is worth recognizing that the coefficients are 2 orders of magnitude smaller than the coolant density and fuel temperature coefficients.

- For the Group 2 Fission Coolant Density PDCSCs, there is a clear trend where SCALE predicts less negative values than HELIOS, with the discrepancy growing as the coolant density becomes smaller. Despite this trend, the data still compares well.
- There is a known issue, which documented in [8], in SCALE branch calculations at low densities. This is evident in Figure F-1, F-2, and F-3 for the 0.001 g/cm^3 coolant density branch. This branch was removed from subsequent calculations.
- There is noise present in both the HELIOS and SCALE data for the 0.82120 g/cm^3 branch. This was also removed from subsequent calculations. s

In addition to direct comparison of the cross section data, comparison of integral parameters such as K-effective, and number densities of key isotopes such as U-235, Pu-239, and Xe-135 is an effective way to compare the outputs of a lattice physics calculation. The benefits of integral parameters are obvious; they allow one to compare a single number that is representative of the behaviour of the entire system. However, this can also be a drawback, as errors in less important or less sensitive parameters can be missed. Furthermore, none of the integral parameters mentioned above are actually passed to or used by a diffusion code, and so relying entirely on integral parameters to assess the accuracy of a lattice physics calculation can be misleading. The HELIOS and SCALE K-effective values and key isotope number densities as a function of burnup is provided in Figure 22 and Figure 23. Finally, a comparison of the HELIOS and SCALE CVR for various coolant density perturbations is shown in Figure 18. One can see that SCALE predicts consistently lower coolant void reactivity values than the corresponding branch in the HELIOS output. This result, while unexpected, could form a substantial finding, and helps explains the results that were obtained during stand-alone reactor physics and coupled transients. Further discussion on this issue is provided in Section 5.3 .

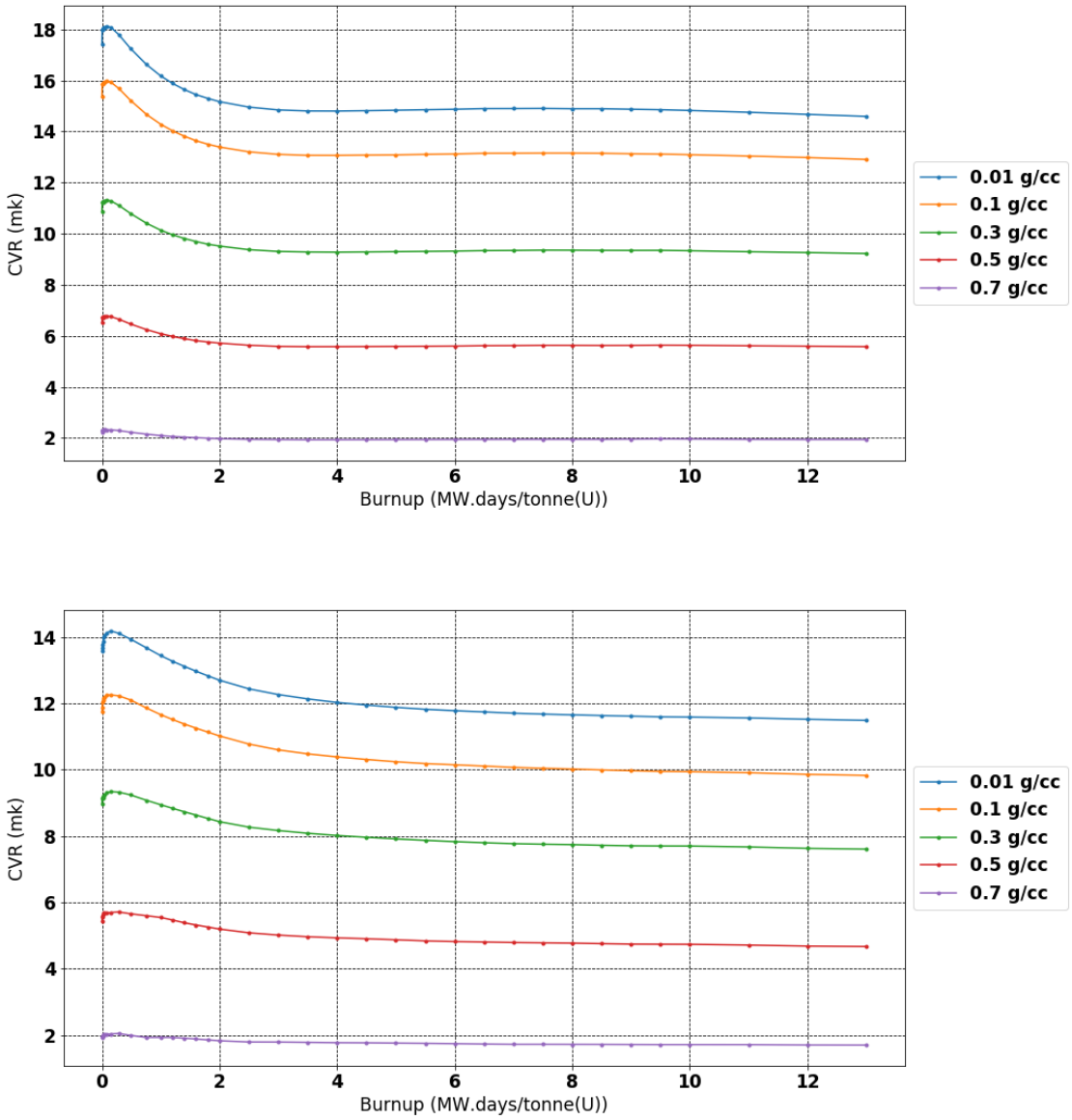

Figure 18. Comparison of Coolant Void Reactivity for various Coolant Density Perturbations: Top - HELIOS, Bottom - SCALE

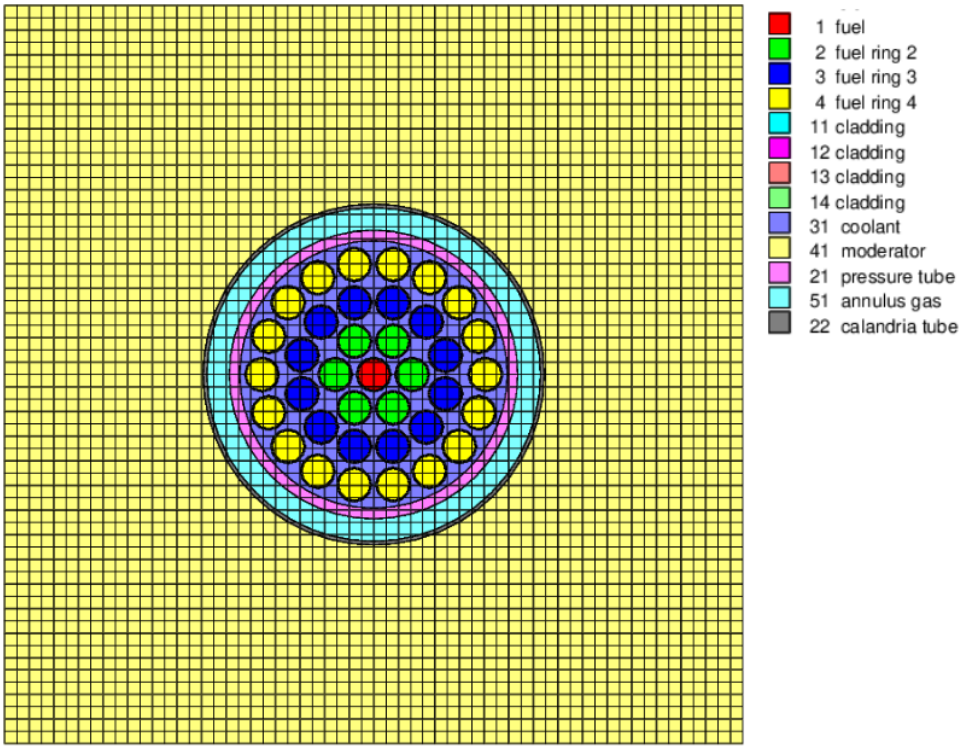

Figure 19. CANDU Fuel Bundle Geometric Domain in NEWT

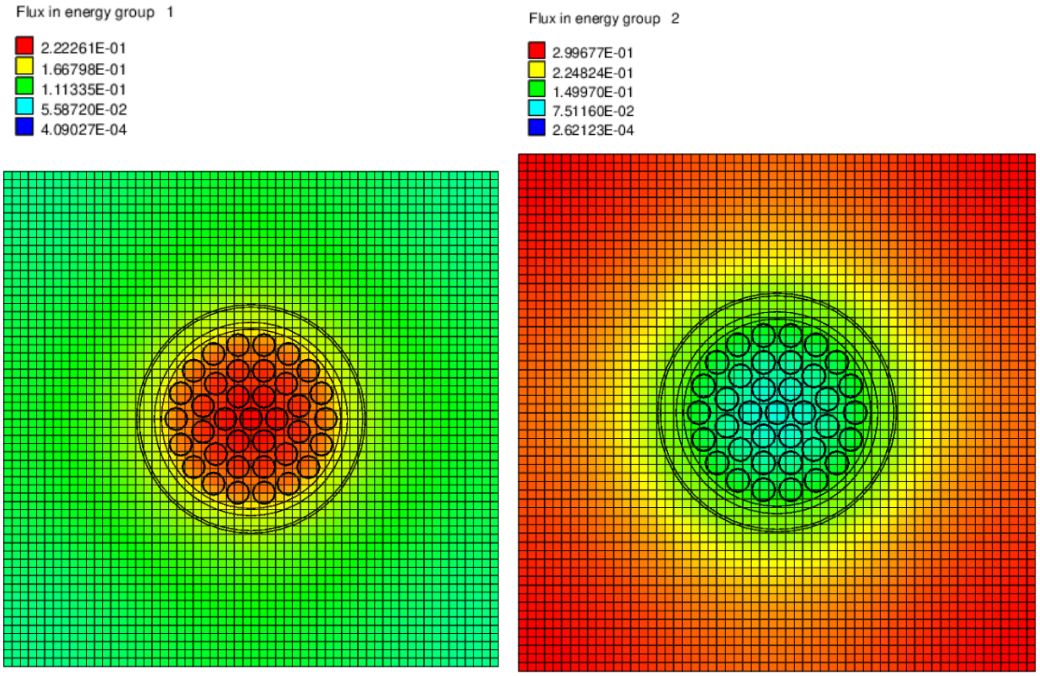

Figure 20. CANDU Fuel Bundle Flux Distribution: Left - Group 1 Flux, Right - Group 2 Flux (units – neutrons/barn*s)

Table 2. NEWT/TRITON Lattice Physics Parameters (bolded parameters indicate a reference value)

Parameter	Value(s)
Burnup	0, 0.0035, 0.01, 0.0185, 0.0318, 0.0519, 0.0854, 0.1524, 0.2865, 0.488, 0.7566, 1.0, 1.2, 1.4, 1.6, 1.8, 2.0, 2.5, 3.0, 3.5, 4.0, 4.5, 5.0, 5.5, 6.0, 6.5, 7.0, 7.5, 8.0, 8.5, 9.0, 9.5, 10.0, 11.0, 12.0, 13.0 MW.days/tonne.HM.
Fuel Temperatures (T_F)	50, 250, 290, 600, **687**, 900, 941, 1200, 1400, 1600, 1800, 2000 °C
Coolant Temperatures (T_C)	50, 250, **288.5**, 310 °C
Coolant Densities (D_C)	0.001, 0.01, 0.1, 0.3, 0.5, 0.7, **0.80623**, 0.8212 g/cm^3
Fuel Material and Density	Uranium Dioxide – 10.65 g/cm^3
Cladding Material and Density	Zircaloy-4 – 6.44 g/cm^3
Pressure Tube Material and Density	Zircaloy Zr-2.5Nb – 6.5 g/cm^3
Calandria Tube Material and Density	Zircaloy-2 – 6.44 g/cm^3
Coolant and Moderator Purities	98.39 wt.% D_2O – 99.935 wt.% D_2O
Specific Power	32.530 MW/MT(U)

Table 3. Summary of 2 Group Cross Section and TH Invariant Input Data for a PARCS Diffusion Calculation

Reference Macroscopic Cross Sections and TH Partial Derivative Cross Section Coefficients * For each cross section, Σ_x, there is a corresponding partial derivative cross section co-efficient for each TH branch: $\frac{\delta\Sigma_x}{\delta_{CD}}, \frac{\delta\Sigma_x}{\delta_{FT}}, \frac{\delta\Sigma_x}{\delta_{CT}}$	**Group 1 and 2 Fission:** $\Sigma_{F_1}(B)$and $\Sigma_{F_2}(B)$ – cm^{-1}
	Group 1 and 2 Absorption: $\Sigma_{A_1}(B)$ and $\Sigma_{A_2}(B)$ – cm^{-1}
	Group 1 and 2 Transport: $\Sigma_{T_1}(B)$ and $\Sigma_{T_2}(B)$ – cm^{-1}
	Group 1 and 2 Kappa-Fission: $\Sigma_{KF_1}(B)$ and $\Sigma_{KF_2}(B)$ – MeV/cm
	Group 1 and 2 Nu-Fission: $\Sigma_{NF_1}(B)$ and $\Sigma_{NF_2}(B)$ – cm^{-1}
	Within group and between group scattering: $\Sigma_{11}(B), \Sigma_{12}(B), \Sigma_{21}(B), \Sigma_{22}(B)$ – cm^{-1}
	Group 1 and 2 Xenon Microscopic Absorption: $\sigma_{Xe_1}(B)$ and $\sigma_{Xe_2}(B)$ – cm^2
	Group 1 and 2 Samarium Microscopic Absorption: $\sigma_{Sm_1}(B)$ and $\sigma_{Sm_2}(B)$ – cm^2
	Assembly Discontinuity Factors: $ADF_x(B)$ where $x = N, S, E, W, up$, or $down$
TH Invariant Data	**Xenon, Samarium and Promethium Yields**: $N_{Xe}(B)$, $N_{Sm}(B)$, and $N_{Pm}(B)$
	Group 1 and 2 Inverse Neutron Velocities: $v_{i,1}(B)$ and $v_{i,2}(B)$ – s/cm
	Delayed Neutron Precursor Fractions: $\beta_i(B)$, $i = 1 \ldots 6$
	Delayed Neutron Precursor Decay Rates: $\lambda_i(B)$, $i = 1 \ldots 6$

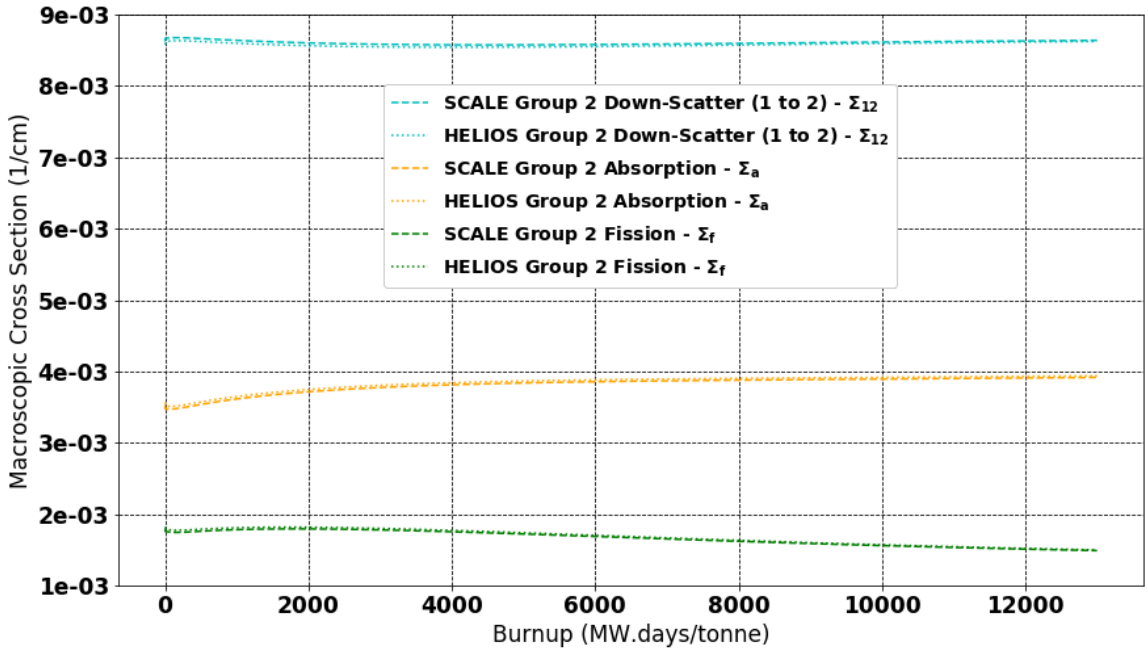

Figure 21. SCALE vs. HELIOS Lattice Physics Comparison: Down-scatter (Σ_{12}), Group 2 Absorption (Σ_{a2}) and Group 2 Fission (Σ_{f2}) Fuel Cross Sections

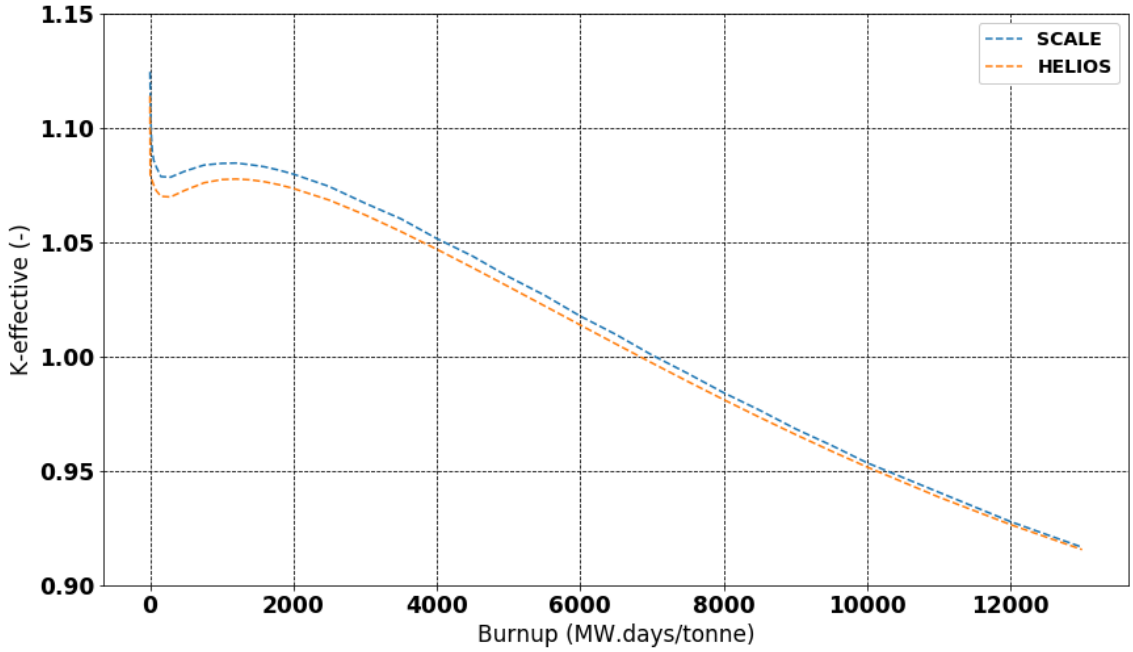

Figure 22. SCALE vs. HELIOS Lattice Physics Results Comparison: K-effective

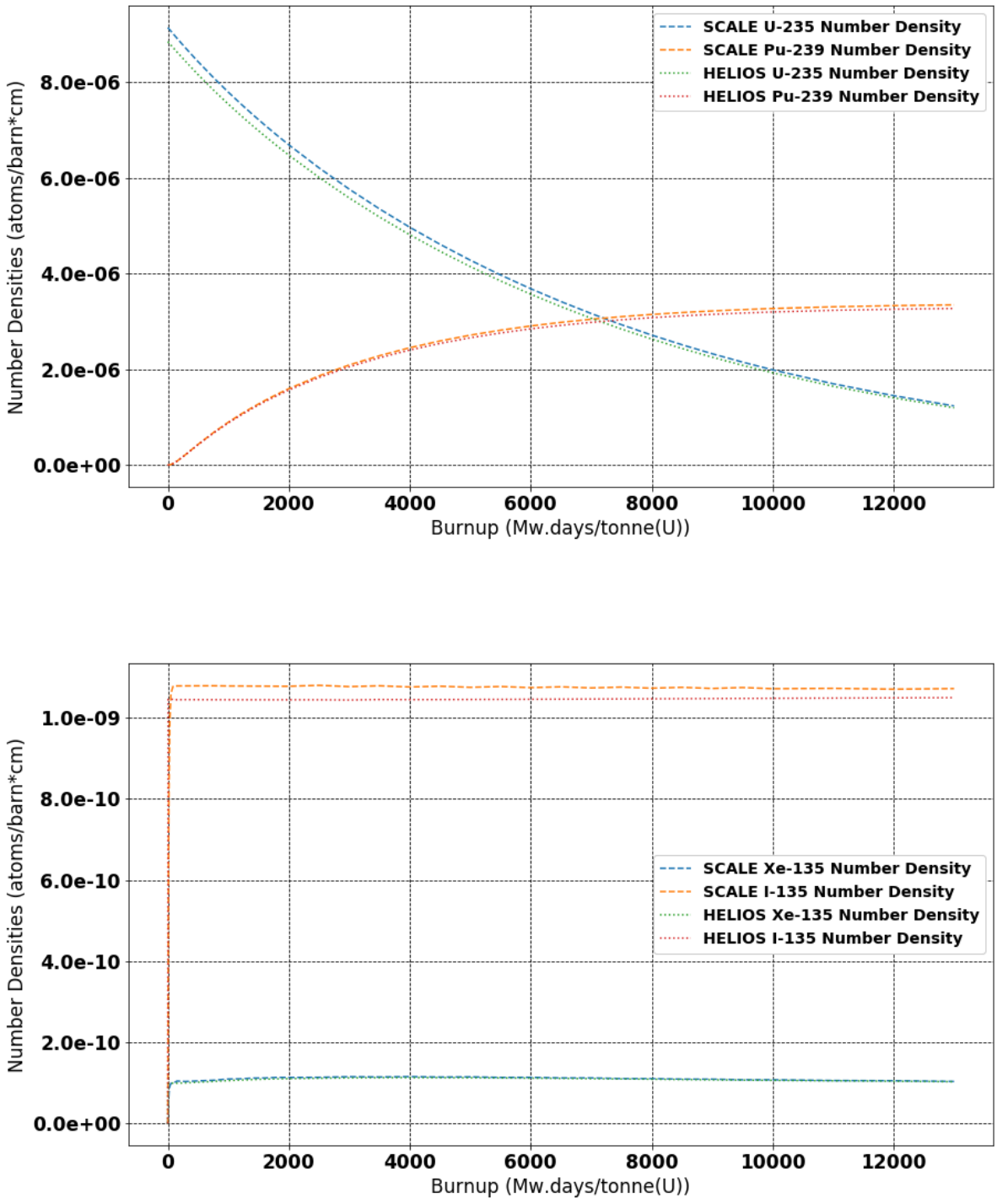

Figure 23. SCALE vs. HELIOS Lattice Physics Results - Number Density Comparison: Top - U-235 and Pu-239, Bottom - Xe-135 and I-135

3.2.2. Reactivity Device Incremental Cross Section Generation

Incremental control rod/liquid zone cross sections were provided in the IAEA ICSP Benchmark Specifications. These incremental cross sections were generated using the DRAGON lattice physics code, by the Benchmark Team [45]. There are three different types of Liquid Zone Controllers and Adjuster Rods in a CANDU-6 Reactor, each of which were modelled separately, in addition to the Shut-off Rods. Mechanical Control Absorbers were neglected in the IAEA ICSP Benchmark. Additional information on the differences between the Liquid Zone Controller and Adjuster Rod types can be found in [9]. This leaves 10 incremental cross sections:

- 3 Adjuster Rods (ADJ01, ADJ02, ADJ03)
- 3 Liquid Zone Controller Light Water Compartments (LQZ01, LQZ02, LQZ03)
- 3 Liquid Zone Controller Air Filled Compartments (ZCAIR01, ZCAIR02, ZCAIR03)
- 1 Shutoff Rod (SOR)

All 10 control rod device incremental cross sections were also re-generated in this work using SERPENT v2 [20]. While this was not entirely necessary to extend beyond the scope of the Benchmark and perform uncertainty analysis on the transient simulations, as it was for the fuel cross section data, it provided a way to verify the incremental cross sections provided by the Benchmark Team, and close a gap in McMaster's ability to simulate the transient cases without any cross section input data from the Benchmark Team. Details of the supercell geometry can be found in [45]. A sample SERPENT geometry is shown in Figure 24, for the adjuster rod calculation. The homogenization region is clearly shown with dashed lines. The results of the supercell calculations are discussed in more detail in Section 3.4, as a direct comparison of the incremental cross sections does not provide meaningful insight into their impact on full core diffusion calculations.

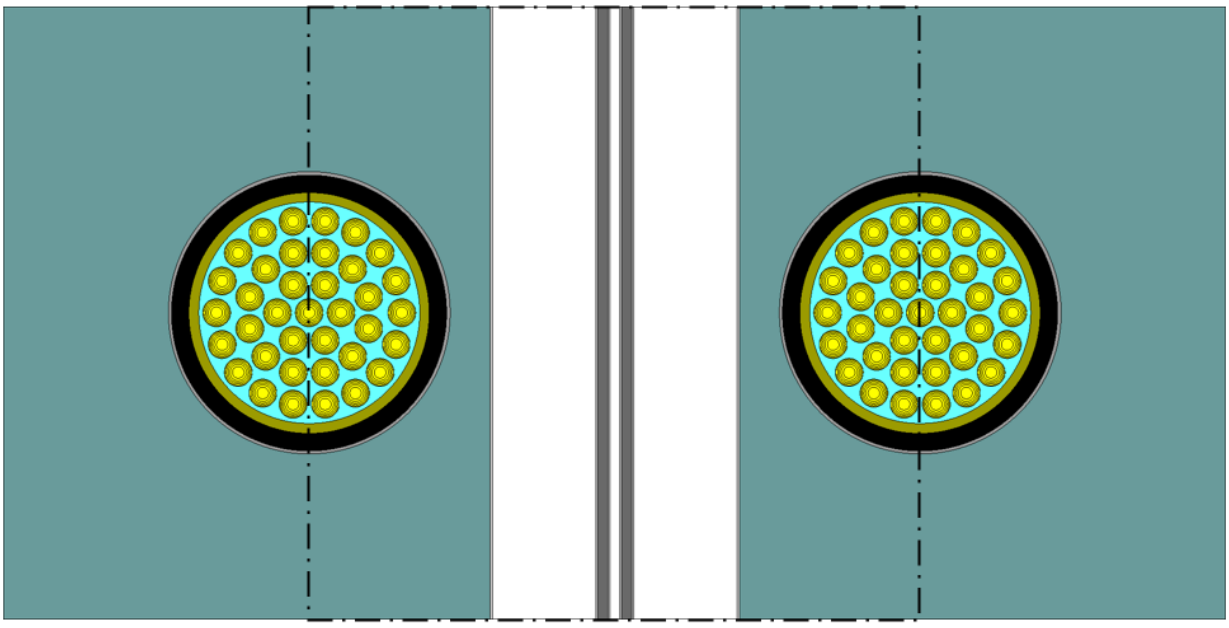

Figure 24. 2D Cross Sectional View of a 3D SERPENT Adjuster Rod Geometry

3.2.3. Lattice Physics Uncertainty Propagation

Fundamental nuclear data uncertainty was propagated through lattice physics calculations using the SAMPLER [46] module of the SCALE code package. SAMPLER is a Monte Carlo based uncertainty propagation tool which comes with a library of 1000 pre-calculated perturbation factors, which are applied directly to the multi-group library selected by the user. In this work, the 252 group ENDF-B VII library was used. The user also has the option to perturb geometry, and fission product poison yields. In an ideal world, multiple branch states for each thermal-hydraulic variable could be retained in the SAMPER run, and each perturbed cross section set would contain multiple branching points. However, even for the smallest possible perturbed cross section set (59 [35]), performing a lattice cell transport calculation for 36 burnup steps and 22 branches would be too computationally expensive. As such, a decision was made to choose a single branch state for each thermal-hydraulic variable that best captures the range of thermal-hydraulic values that could reasonably be expected in the desired transient. For the case of a loss of coolant accident in a CANDU style reactor, the expected behaviour is a decrease in coolant density, and an increase in both fuel and coolant temperatures before reactor shutdown (SCRAM) occurs, and a decrease in fuel and coolant temperatures after reactor shutdown. For this work, the following perturbations were chosen: FT = 900 °C, CT = 250 °C, and DC = 0.7 g/cm^3. The reference, un-perturbed SCALE run using only these branches and resulting 2 group cross sections will be referred to as the SCALE Uncertainty Propagation (UP) run/data.

In this work, 59 perturbations were performed, and both raw cross sections and fission product yields were perturbed. The mean K-eff value from the SAMPLER run, plus uncertainty bands of 2 standard deviations, are shown in Figure 25. The full set of 59 group 2 fission cross sections, and group 2 fission coolant density PDCSC are shown in Figure 26, with the reference case shown in red, the perturbed cases shown in grey, and the HELIOS reference case defined in the IAEA Benchmark Specifications shown in blue, for comparison.

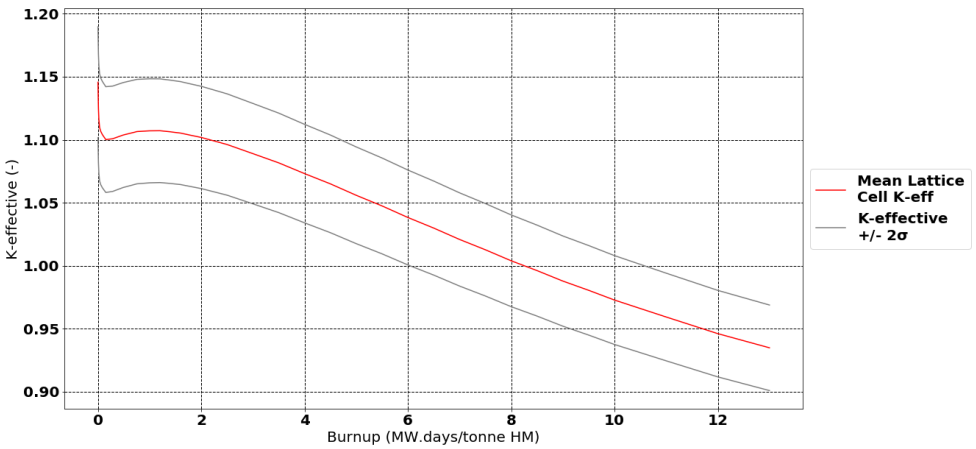

Figure 25. Mean K-effective and Standard Deviation from SAMPLER Lattice Physics Uncertainty Propagation Calculations

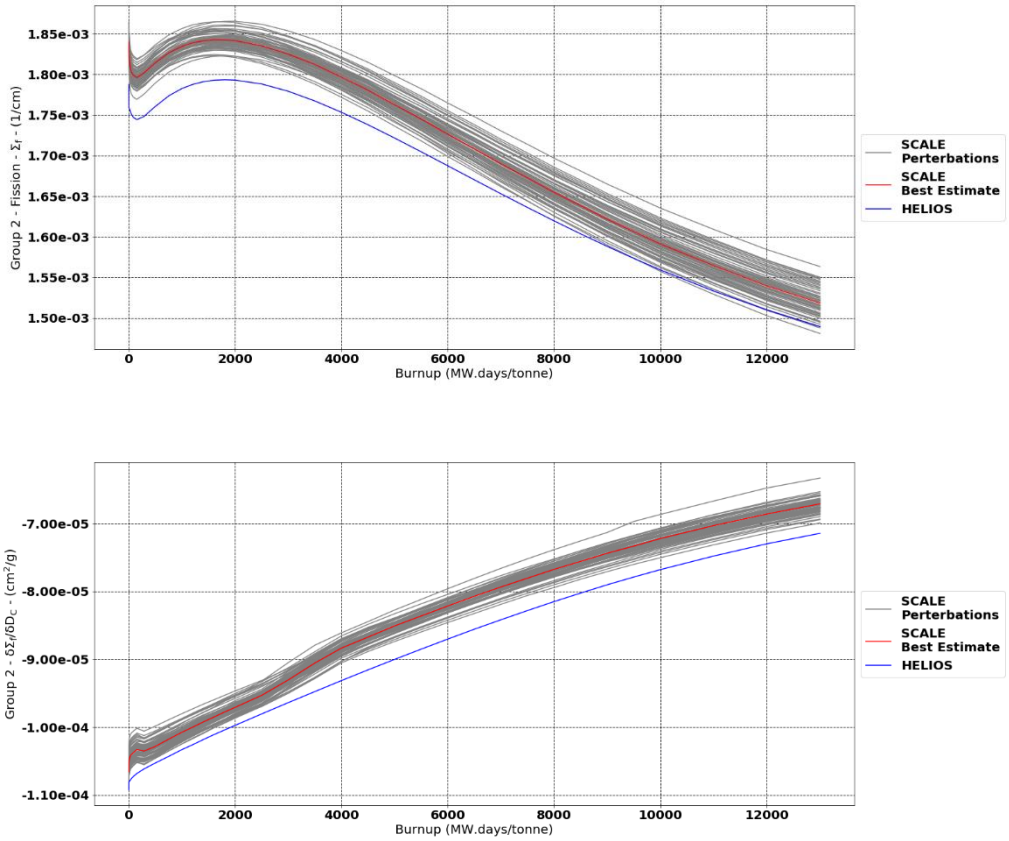

Figure 26. SAMPLER Uncertainty Propagation Results: Top - Group 2 Fission Cross Sections, Bottom - Group 2 Fission Coolant Density PDCSC

3.3. PMAX File Format and GenPMAX

3.3.1. Fuel PMAX Files – Reference, TH Branches and TH-Invariant Neutronics Data

The PMAX file format provides a link between lattice physics calculations, and the diffusion code. A PMAX file is nothing more than a formatted text file containing all the input data needed for a diffusion calculation, including, but not limited to 2 group reference cross section, TH branch partial derivative cross section coefficients, TH invariant diffusion data, and control device incremental cross sections. The preparation of the PMAX file is facilitated by a utility called GenPMAX [24]. In this work, the GenPMAX utility was only used to prepare the fuel portion of the PMAX file (everything except the incremental cross sections). To run GenPMAX, the user must prepare a short input file defining the burnup points, reference and branch TH parameters, and some details of the output format. One of the outputs of a NEWT/TRITON depletion run is a "txtfile16" data file, which contains a summary of the transport calculation, including all the data required to prepare a PMAX file. This file name is also defined in the GenPMAX input file.

The output of the GenPMAX run is a PMAX file that will be referred to as a branch structure type 0 PMAX file. In the NEWT/TRITON modules, there is no way to differentiate between coolant and

moderator. This is because many popular U.S. reactor designs, such as BWRs and PWRs, do not have a separate coolant and moderator, like a CANDU and the coolant also performs the moderation function. As such, the coolant temperature and density branches are defined as moderator branches in SCALE and are subsequently labelled this way in the type 0 PMAX file (i.e. DM/TM branches instead of DC/TC). While the diffusion calculation could be set up with this naming convention, in this work, the variables were changed to be consistent with their actual meaning using a short Python script. Note that only the variables were modified, and no changes to the actual cross section were performed. This modified PMAX file will be referred to as a branch structure type 1 PMAX file.

Unfortunately, the type 1 PMAX file cannot be used during externally coupled calculations with the version of PARCS used in this work (PARCS v32). This was originally discovered in previous work at McMaster on SCWR coupling [8]. In PARCS, nodewise data such as TH variables, Xenon/Samarium number densities, and control rod positions can all be defined using a "History" file (.hst file). In PARCS v32, 12 different TH variables can be defined:

1. CR – control rod fraction
2. DC – coolant density
3. PC – soluble poison concentration in the coolant
4. TF – fuel temperature
5. TC – coolant temperature
6. IC - impurity of the coolant
7. DM – density of the moderator
8. PM – poison concentration in the moderator
9. TM – temperature of the moderator
10. IM – impurity of the moderator
11. DN – density difference between neighbor and current assembly
12. BN – burnup difference between neighbor and current assembly

For each branch variable, there is a corresponding key word in the History file that defines what type of data is being written. However, for an unknown reason, the first 5 TH variables cannot be updated via the History file during a transient calculation, they can only be updated directly in memory. As such, variables 6 through 12 must be used instead when invoking external coupling such as that used here, treating them as though they are the first 5 variables. In this work, the DC, TF and TC branches were converted to DM, TM, and IM respectively. This final PMAX file will be referred to as branch structure type 2 file. This modification was also performed with a short Python script, and again, no changes to the actual cross sections were made, only changes to the variable names and file organization. However, this does require the user to make a change to the way data is written to the .hst file. In addition to updating the .hst file key words (this would also have to be done for branch type 1), all fuel temperature values must be converted to the square root of the fuel temperature. This is because the 2 group cross sections produced in SCALE are tabulated as a function of the square root of the fuel temperature. When using the TF branch, PARCS will automatically take the square root of the fuel temperature data, but this must be done manually when using any other branch variable to represent the fuel temperature. As such, there are two types of .hst files as well, type 1 and 2, that correspond to the PMAX files type.

3.3.2. Incremental Cross Sections

Due to computability issues between GenPMAX and SERPENT Version 2, a python script was used to extract the incremental cross sections from the SERPENT ". coe" output file and convert the data into PMAX format. An important finding from this step of the process is that, as stated in Section 7.3.2 of the GenPMAX input manual [24], the control rod incremental cross sections that are read from the PMAX file are multiplied by the control rod branch number before being used in PARCS. For example, for Control Rod Branch 10 (CR10), the value read by PARCS will by 10 times the incremental cross section defined in the PMAX file. As such, when writing the incremental cross sections produced by SERPRENT to a PMAX file, the values must be divided by the control rod branch number for them to be read correctly, as shown in Equation 3-2, where N is the control rod number.

$$\Sigma_{CRN,PMAX} = \frac{1}{N}\Sigma_{CRN,SERPENT} \qquad (3-2)$$

3.4. PARCS Diffusion Model

3.4.1. Model Overview

In addition to the fuel, reflector and incremental cross sections, the IAEA ICSP Benchmark Specifications define the core geometry, positions of the control rods and liquid zone controllers, and a reference burnup and thermal-hydraulic distribution. This allows participants to compare steady state results of like for like models. At a high-level, the Liquid Zone Controllers are filled halfway, the adjuster rods are fully inserted, and the shutoff rods are positioned outside of the core. The Reactor Regulating System (RRS) is not modelled, and there is no movement of Liquid Zone Levels, or adjuster rods, with the exception of the two rods which are withdrawn from the reactor at a fixed rate during the LOR transient. The core geometry is shown for one axial plane in Figure 27. All 12 axial planes are identical, and there are no axial reflectors included in the model. The locations of the control devices are shown in Figures C-5, C-6, and C-7, in Appendix C. For the Adjuster Rods and Liquid Zone Controllers, the locations in the X-Y plane are shown, and for the shutoff rods, the locations in the X-Z pane are shown. The Adjuster Rods are located in axial planes 5, 6/7 (starts at 6.5 and ends at 7.5), and 8 and the Liquid Zone Controllers are located in axial planes 4 and 9. Each shutoff rod extends the entire length of the core in the Y direction. The reference burnup and TH distributions are shown in Appendix C, Figure C-1 to C-4. The reference channel power distribution obtained with both SCALE and HELIOS cross section data are shown in Figure 28.

Some small modifications to the specified core geometry were performed to simplify the input. In the IAEA ICSP Benchmark Specifications, some fuel and reflector nodes are defined to be half a lattice pitch wide, despite the cross sections being generated for a full lattice pitch. While this could potentially be accommodated in PARCS, it greatly complicates the input, and so some small changes to the reflector region were made so that all nodes occupy one full lattice pitch. In the resulting PARCS model, all nodes have dimensions of 28.575 cm x 28.575 cm x 49.53 cm, except for the top, bottom, left and right most reflector nodes, which are 28.575 cm x 11.375 cm x 49.53 cm for the top and bottom reflector nodes, and 11.375 cm x 28.575 cm x 49.53 cm for the left and right most reflector nodes. In Figure 27, red cells correspond to void cells that were modified to reflector cells, and yellow cells correspond to reflector cells that were modified to void cells. From Figure 27, one can see that the PARCS model has a slightly larger reflector volume than the model defined in the Specifications.

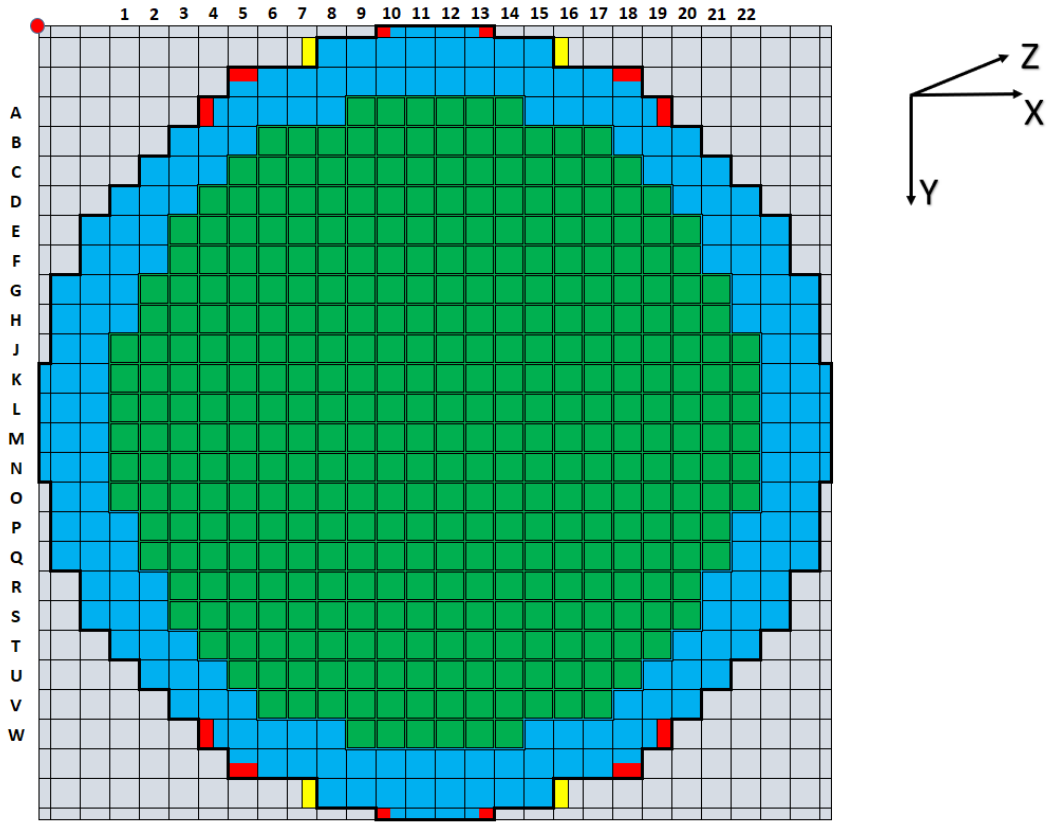

Figure 27. PARCS Core Geometry: Red = Void Cell modified to Reflector Cell, Yellow = Reflector Cell Modified to Void Cell

3.4.2. Steady State PARCS Model Results

High level verification of the lattice physics calculations and PARCS model was performed by running a series of requested steady state calculations, with both the HELIOS and SCALE input data. No reference results are provided in the Specifications, as was the case for thermal-hydraulics model, however, this set of calculations was performed by all participants and so verification was performed through final result comparison. The purpose of these tests was to determine the reactivity worth of each device, full/quarter core voiding, and a high fuel temperature case, using the specified burnup and TH distributions described above to generate a reference result to compare against. The control rod device worth's were determined by calculating the difference in the core reactivity when the rods are fully inserted and fully removed. The liquid zone controller reactivity worth was determined by calculating the difference in reactivity when the zones are filled entirely with liquid and entirely with air. The full core void reactivity was determined by setting all coolant density values to 0.001 g/cm^3, and the quarter core void reactivity was determined by setting all coolant density values in loop 1 pass 2 (CHAN21 to CHAN27) to 0.001 g/cm^3, and the high fuel temperature reactivity was determined by setting all fuel temperature values to 2000 °C and in each case, the difference in reactivity relative to the reference state was computed. The results are summarized in Table 4.

One can see that for all cases, the device worth's and fuel temperature reactivity are comparable between cross section sets, and participants, although CNL shows a notably smaller fuel temperature

reactivity. Furthermore, when using the specified cross section data, one can see that the McMaster coolant void reactivity obtained with PARCS and TRACE aligns with the CNL and CNEA results as well. Furthermore, from Figure 28, one can see that Channel S9 yields the highest power, which was also the case for all other participants. This provides confidence in the PARCS model, 2 group fuel/reflector cross sections, and incremental cross sections that were generated in this work. However, comparing the coolant void reactivity generated with the full TH branch SCALE data, one can see that the full core CVR is much smaller than that predicted using the specified data. This is a direct result of the smaller lattice level CVR shown in Figure 18, as the steady state coolant density distributions obtained with the SCALE and HELIOS data are almost identical. Smaller CVRs could also be obtained if the steady state core average coolant density is smaller in one case relative to the other. However, as shown in Figure 28, the channel power distributions obtained with the SCALE and HELIOS data are almost identical, which leads to almost identical coolant density distributions (the core average coolant density is 0.821 g/cc in both cases).

Table 4. High Level PARCS Verification Results - SCALE/SERPENT Cross Sections vs. HELIOS/DRAGON Cross Sections and CNL/CNEA Results

Cross Section Set	Base Reactivity (mk)	Adjuster Worth (mk)	Full Liquid Zone Worth (mk)	Shutoff Rod Worth (mk)	Full Core Void Reactivity (mk)	Quarter Core Void Reactivity (mk)	High Fuel Temperature Reactivity (mk)
SCALE/SERPENT - McMaster	3.90	16.29	7.36	77.70	12.63	3.61	-1.68
HELIOS/DRAGON (Specified) - McMaster	-1.60	16.93	7.10	79.13	16.69	5.02	-1.19
Specified Cross Sections - CNL	-0.35	15.81	7.84	N/A	16.58	4.85	-0.66
Specified Cross Sections – CNEA	0.76	14.51	7.00	N/A	16.16	4.84	-1.27

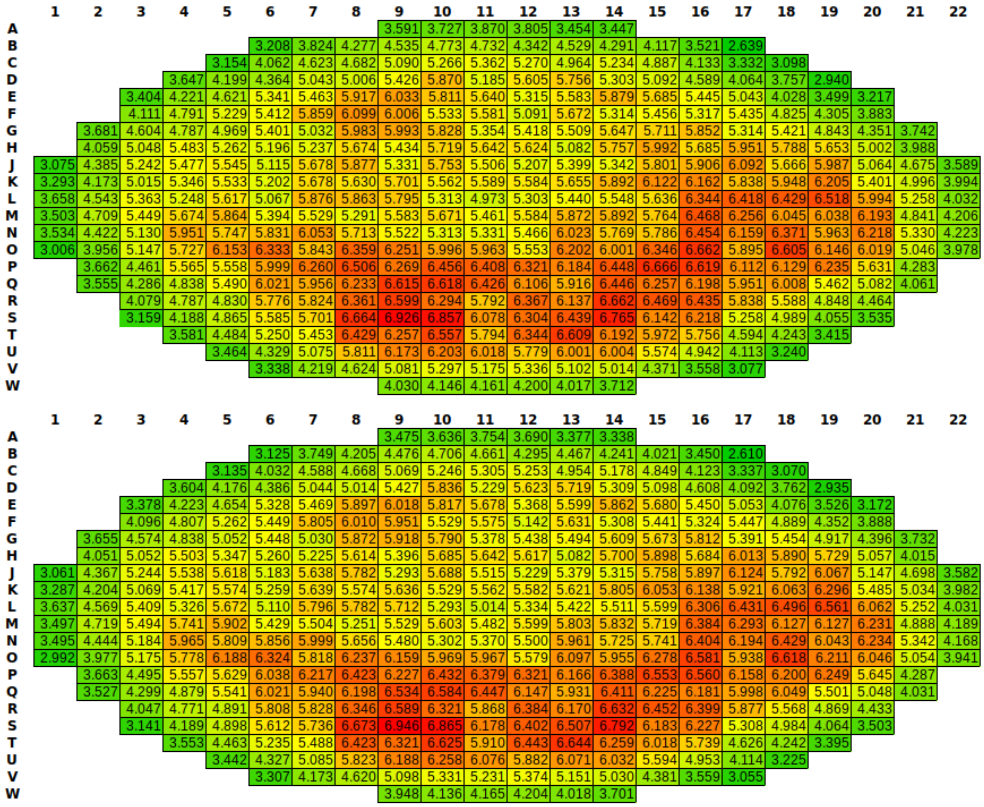

Figure 28. Channel Power Distribution Comparison with Reference Burnup and Thermal-Hydraulic Distribution: Top - SCALE/SERPENT, Bottom - HELIOS/DRAGON

3.4.3. Additional PARCS Verification

3.4.3.1. PMAX and History File Branch Structure Verification

Given the significant modifications that must be made to the PMAX and History files when using the type 2 branch structure, as described in Section 3.3, a simple test was performed to determine if the modifications were made correctly. In this test, the Reference TH and Burnup Distribution shown in Appendix C were written to type 1 and 2 History files, and the simulations were run with the corresponding PMAX files. The specified cross sections were used in this case. If the type 2 files were set up correctly, one would expect identical K-eff values and power distributions between the two runs. The results of the test are shown below in Figure 29. One can see that the two channel power distributions are identical to 3 decimal places in every node. Furthermore, the K-eff values come out to 0.998246 for the branch structure 1 calculation and 0.998251 in the branch structure 2 calculation, a difference of less than 0.001%. This also provides a comparison between the channel power distributions predicted with the SCALE and HELIOS cross sections (Figure 28) and the channel power distribution predicted using the specified cross section data. Converting the reactivity values shown in Table 4 to K-eff values, one obtains 0.998403 for the HELIOS cross section data, and 1.003911 for the SCALE cross section data. As expected, the HELIOS results compare very well with specified cross section data.

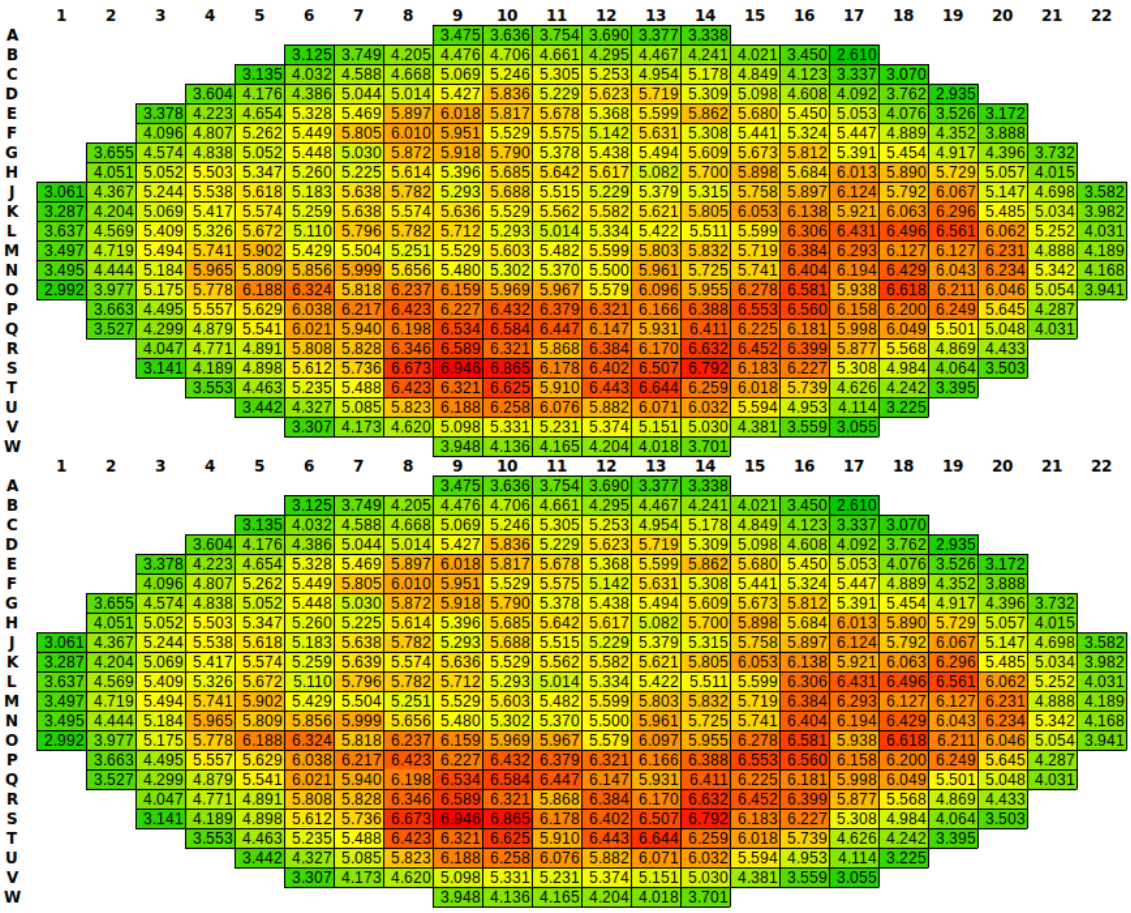

	1	2	3	4	5	6	7	8	9	10	11	12	13	14	15	16	17	18	19	20	21	22
A									3.475	3.636	3.754	3.690	3.377	3.338								
B						3.125	3.749	4.205	4.476	4.706	4.661	4.295	4.467	4.241	4.021	3.450	2.610					
C					3.135	4.032	4.588	4.668	5.069	5.246	5.305	5.253	4.954	5.178	4.849	4.123	3.337	3.070				
D				3.604	4.176	4.386	5.044	5.014	5.427	5.836	5.229	5.623	5.719	5.309	5.098	4.608	4.092	3.762	2.935			
E			3.378	4.223	4.654	5.328	5.469	5.897	6.018	5.817	5.678	5.368	5.599	5.862	5.680	5.450	5.053	4.076	3.526	3.172		
F			4.096	4.807	5.262	5.449	5.805	6.010	5.951	5.529	5.575	5.142	5.631	5.308	5.441	5.324	5.447	4.889	4.352	3.888		
G		3.655	4.574	4.838	5.052	5.448	5.030	5.872	5.918	5.790	5.378	5.438	5.494	5.609	5.673	5.812	5.391	5.454	4.917	4.396	3.732	
H		4.051	5.052	5.503	5.347	5.260	5.225	5.614	5.396	5.685	5.642	5.617	5.082	5.700	5.898	5.684	6.013	5.890	5.729	5.057	4.015	
J	3.061	4.367	5.244	5.538	5.618	5.183	5.638	5.782	5.293	5.688	5.515	5.229	5.379	5.315	5.758	5.897	6.124	5.792	6.067	5.147	4.698	3.582
K	3.287	4.204	5.069	5.417	5.574	5.259	5.638	5.574	5.636	5.529	5.562	5.582	5.621	5.805	6.053	6.138	5.921	6.063	6.296	5.485	5.034	3.982
L	3.637	4.569	5.409	5.326	5.672	5.110	5.796	5.782	5.712	5.293	5.014	5.334	5.422	5.511	5.599	6.306	6.431	6.496	6.561	6.062	5.252	4.031
M	3.497	4.719	5.494	5.741	5.902	5.429	5.504	5.251	5.529	5.603	5.482	5.599	5.803	5.832	5.719	6.384	6.293	6.127	6.127	6.231	4.888	4.189
N	3.495	4.444	5.184	5.965	5.809	5.856	5.999	5.656	5.480	5.302	5.370	5.500	5.961	5.725	5.741	6.404	6.194	6.429	6.043	6.234	5.342	4.168
O	2.992	3.977	5.175	5.778	6.188	6.324	5.818	6.237	6.159	5.969	5.967	5.579	6.096	5.955	6.278	6.581	5.938	6.618	6.211	6.046	5.054	3.941
P		3.663	4.495	5.557	5.629	6.038	6.217	6.423	6.227	6.432	6.379	6.321	6.166	6.388	6.553	6.560	6.158	6.200	6.249	5.645	4.287	
Q		3.527	4.299	4.879	5.541	6.021	5.940	6.198	6.534	6.584	6.447	6.147	5.931	6.411	6.225	6.181	5.998	6.049	5.501	5.048	4.031	
R			4.047	4.771	4.891	5.808	5.828	6.346	6.589	6.321	5.868	6.384	6.170	6.632	6.452	6.399	5.877	5.568	4.869	4.433		
S			3.141	4.189	4.898	5.612	5.736	6.673	6.946	6.865	6.178	6.402	6.507	6.792	6.183	6.227	5.308	4.984	4.064	3.503		
T				3.553	4.463	5.235	5.488	6.423	6.321	6.625	5.910	6.443	6.644	6.259	6.018	5.739	4.626	4.242	3.395			
U					3.442	4.327	5.085	5.823	6.188	6.258	6.076	5.882	6.071	6.032	5.594	4.953	4.114	3.225				
V						3.307	4.173	4.620	5.098	5.331	5.231	5.374	5.151	5.030	4.381	3.559	3.055					
W									3.948	4.136	4.165	4.204	4.018	3.701								

	1	2	3	4	5	6	7	8	9	10	11	12	13	14	15	16	17	18	19	20	21	22
A									3.475	3.636	3.754	3.690	3.377	3.338								
B						3.125	3.749	4.205	4.476	4.706	4.661	4.295	4.467	4.241	4.021	3.450	2.610					
C					3.135	4.032	4.588	4.668	5.069	5.246	5.305	5.253	4.954	5.178	4.849	4.123	3.337	3.070				
D				3.604	4.176	4.386	5.044	5.014	5.427	5.836	5.229	5.623	5.719	5.309	5.098	4.608	4.092	3.762	2.935			
E			3.378	4.223	4.654	5.328	5.469	5.897	6.018	5.817	5.678	5.368	5.599	5.862	5.680	5.450	5.053	4.076	3.526	3.172		
F			4.096	4.807	5.262	5.449	5.805	6.010	5.951	5.529	5.575	5.142	5.631	5.308	5.441	5.324	5.447	4.889	4.352	3.888		
G		3.655	4.574	4.838	5.052	5.448	5.030	5.872	5.918	5.790	5.378	5.438	5.494	5.609	5.673	5.812	5.391	5.454	4.917	4.396	3.732	
H		4.051	5.052	5.503	5.347	5.260	5.225	5.614	5.396	5.685	5.642	5.617	5.082	5.700	5.898	5.684	6.013	5.890	5.729	5.057	4.015	
J	3.061	4.367	5.244	5.538	5.618	5.183	5.638	5.782	5.293	5.688	5.515	5.229	5.379	5.315	5.758	5.897	6.124	5.792	6.067	5.147	4.698	3.582
K	3.287	4.204	5.069	5.417	5.574	5.259	5.638	5.574	5.636	5.529	5.562	5.582	5.621	5.805	6.053	6.138	5.921	6.063	6.296	5.485	5.034	3.982
L	3.637	4.569	5.409	5.326	5.672	5.110	5.796	5.782	5.712	5.293	5.014	5.334	5.422	5.511	5.599	6.306	6.431	6.496	6.561	6.062	5.252	4.031
M	3.497	4.719	5.494	5.741	5.902	5.429	5.504	5.251	5.529	5.603	5.482	5.599	5.803	5.832	5.719	6.384	6.293	6.127	6.127	6.231	4.888	4.189
N	3.495	4.444	5.184	5.965	5.809	5.856	5.999	5.656	5.480	5.302	5.370	5.500	5.961	5.725	5.741	6.404	6.194	6.429	6.043	6.234	5.342	4.168
O	2.992	3.977	5.175	5.778	6.188	6.324	5.818	6.237	6.159	5.969	5.967	5.579	6.097	5.955	6.278	6.581	5.938	6.618	6.211	6.046	5.054	3.941
P		3.663	4.495	5.557	5.629	6.038	6.217	6.423	6.227	6.432	6.379	6.321	6.166	6.388	6.553	6.560	6.158	6.200	6.249	5.645	4.287	
Q		3.527	4.299	4.879	5.541	6.021	5.940	6.198	6.534	6.584	6.447	6.147	5.931	6.411	6.225	6.181	5.998	6.049	5.501	5.048	4.031	
R			4.047	4.771	4.891	5.808	5.828	6.346	6.589	6.321	5.868	6.384	6.170	6.632	6.452	6.399	5.877	5.568	4.869	4.433		
S			3.141	4.189	4.898	5.612	5.736	6.673	6.946	6.865	6.178	6.402	6.507	6.792	6.183	6.227	5.308	4.984	4.064	3.503		
T				3.553	4.463	5.235	5.488	6.423	6.321	6.625	5.910	6.443	6.644	6.259	6.018	5.739	4.626	4.242	3.395			
U					3.442	4.327	5.085	5.823	6.188	6.258	6.076	5.882	6.071	6.032	5.594	4.953	4.114	3.225				
V						3.307	4.173	4.620	5.098	5.331	5.231	5.374	5.151	5.030	4.381	3.559	3.055					
W									3.948	4.136	4.165	4.204	4.018	3.701								

Figure 29. Branch Structure 1 (Top) vs. Branch Structure 2 (Bottom) Channel Powers

3.4.3.2. PARCS Cross Section Processing Verification

PARCS does not provide any way for the user to verify that the cross section input data (via the PMAX file), and TH/control rod data (via the .hst file for TH data and .lcr file for control rod positioning) are being processed correctly to produce the final cross sections that are applied to a given node (i.e., it would be beneficial if a user could request some nodal cross sections used in the diffusion calculation to be written to the output). This is of general concern when using PARCS, especially if there is no experimental or reference solution for a full core to compare to. Furthermore, given the PMAX/.hst file branch structure modifications described above, and the use of a Python script to perform the incremental cross section processing, it was decided that a method to verify the internal cross section processing was required. To this end, a modified version of the PARCS source code was created by Simon Younan, which prints out the nodewise cross sections that are used in the diffusion calculation to the output file. With this version of PARCS, simple tests could be performed to verify the code is performing the cross-section calculations as expected. For example, by setting the node-wise burnup distribution to a uniform value that corresponds to one of the PMAX burnup points (e.g. 0 burnup), and setting the TH values to the reference values, one can look at the effect of individual control rods. Additionally, by removing all control rods, and changing one TH parameter at a time, one can look at the effect of the branch coefficients.

Two sample tests are shown here. Both tests were performed with the specified cross section data. Results can be seen in Figure 30 and Figure 31.

3.4.3.2.1. Test 1 – Incremental Cross Sections

In the first test, all burnup values were set to 0.0 MW.days/kg(U), and all TH parameters were set to the reference values. From the PMAX File:

- 0 Burnup, Reference TH, Group 1 Absorption Cross Section = 1.731E-3 cm^{-1}
- Fully inserted, Adjuster Type 1, Group 1 Absorption Incremental = 3.0905E-5 cm^{-1}

The rod insertion fraction in column 5 = 0.5

- Predicted Final Cross Section = 1.731E-3 + 0.5*(3.0905E-5) = 1.7464525E-3

As shown below, the printed cross section = 1.746452E-3, which is identical to what was predicted.

3.4.3.2.2. Test 2 – TH Branch Partial Derivative Cross Sections

In the second test, all burnup values were again set to 0.0 MW/days/kg(U), all TH parameters were set to the reference values except for the coolant density, which was increased by 0.1 g/cm^3 relative to the reference value, and all control devices were removed. From the PMAX File:

- 0 Burnup, Reference TH, Group 1 Absorption Cross Section = 1.731E-3 cm^{-1}
- 0 Burnup, Coolant Density, Group 1 Absorption Co-efficient = 2.286E-4 cm^{-1}

Coolant Density Perturbation = 0.1 g/cm^3 (ref = 0.80623 g/cm^3, perturbation = 0.90623 g/cm^3)

- Predicted Final Cross Section = 1.731E-3 + 2.286E-4*(0.1) = 1.75386E-3
- Printed Final Cross Section = 1.753860E-3

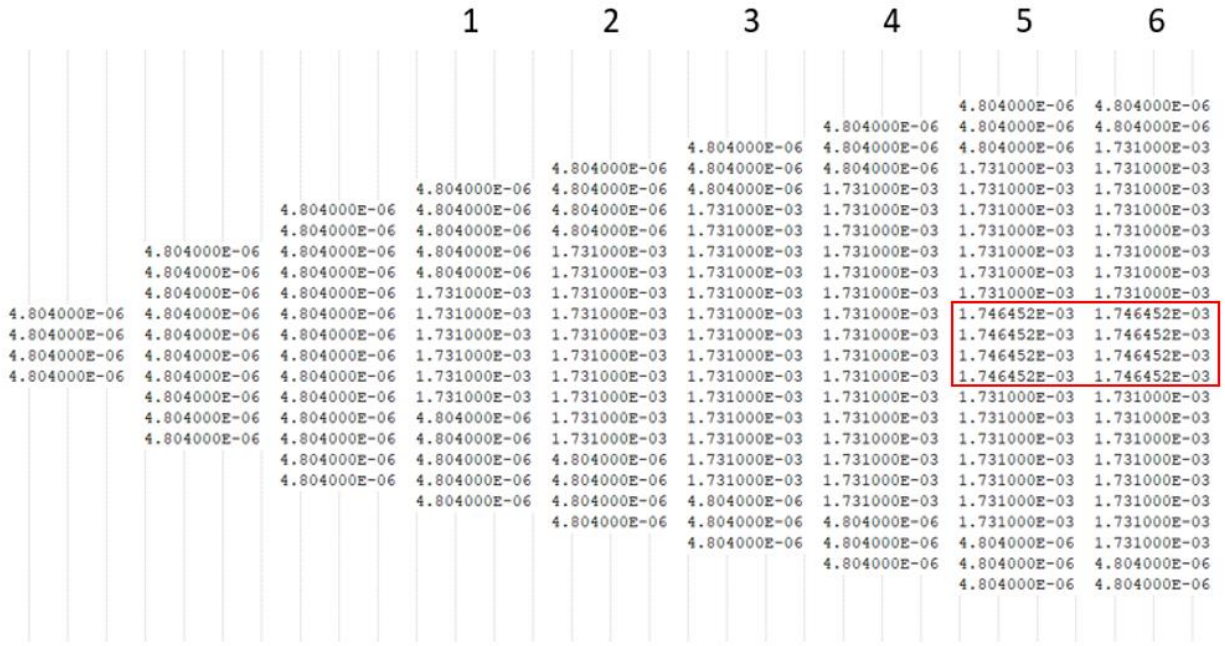

Figure 30. PARCS Cross Section Verification Test - Incremental Cross Section Processing

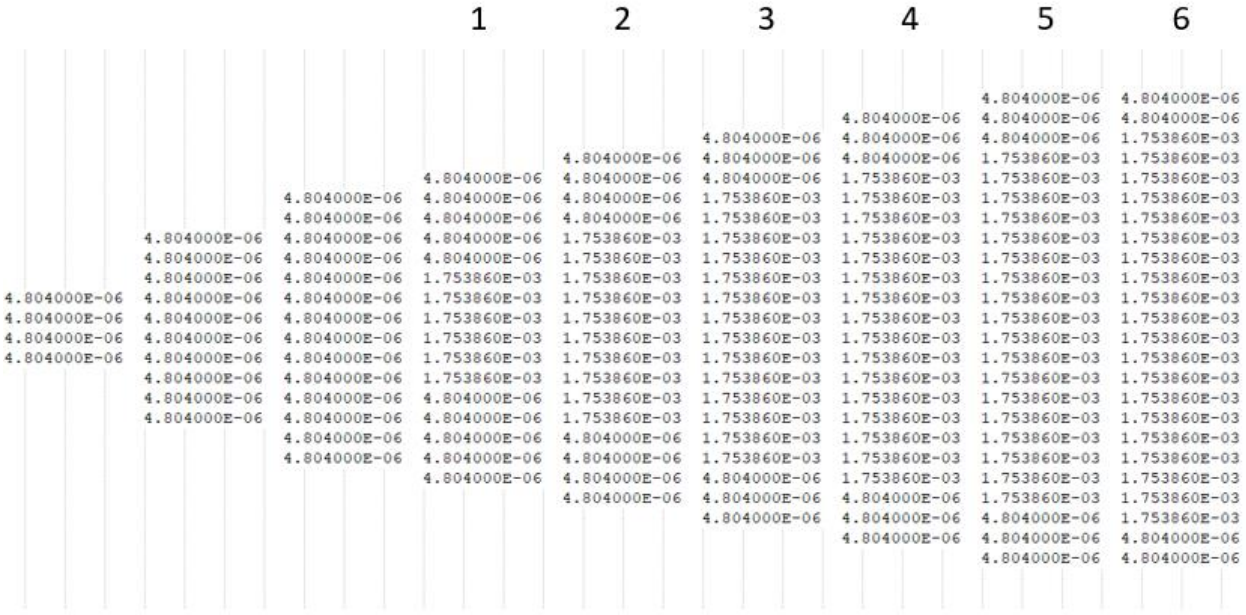

Figure 31. PARCS Cross Section Verification Test - TH Branch Partial Derivative Cross Section Coefficients

These tests show that PARCS is indeed processing the cross-section data as expected. However, these tests also resulted in a finding regarding the incremental cross section processing. For an unknown reason, PARCS does not return the correct final cross section when the incremental device cross sections are written to Control Rod Branch 1 (i.e. CR1). The values are close to what is expected, but there is always a small deviation. This could be due to control rod de-cusping calculations that can only be

performed on the first control rod branch incremental, but when this calculation option was turned off, the results were still inconsistent with expectation. As such, in all PMAX files used in this study, CR data is written to the first CR branch, but it is never actually used (CR1 and CR2 are identical). It is worth noting that this bug could only have been found through this type of verification, as the error in the cross section is too small to have an appreciable affect on the full core results.

3.5. Coupling Methodology

One way (or single physics/stand-alone transients) and two-way coupling methodologies were developed as part of the IAEA ICSP Benchmark work and forms a major component of this thesis. To facilitate stand-alone calculations, participants were provided with a set of channel powers and TH distributions for each transient as part of the final Specifications. The purpose of the stand-alone transients was to test each code separately, with realistic and consistent input parameters, to determine differences between participants models, and to help explain differences in two way coupled results. This type of approach allows the ICSP group to clearly see where there are differences in the single-physics models, as well as in multi-physics result. In this work, the data transfer and simulation restart mechanisms used in the stand-alone methodologies were retained in the two-way coupling methodology. As such, the stand-alone cases also provide high level verification of some aspects of the coupling methodology. Furthermore, all coupling was done externally, with data transfer, and code execution controlled by a series of Python scripts.

3.5.1. Stand-alone PARCS Transient Methodology

For the stand-alone diffusion calculations, thermal-hydraulics data were provided for each node in the 28 fuel channel groups, in 0.1 second intervals, for the duration of the transient. The format of the data provided is very similar to that shown in Figures B-2, B-3, and B-4. Plots of the core average TH parameters are shown in Figures B-8, B-9, and B-10 in Appendix B. In these plots, the TH parameters from all 12 nodes in all 28 fuel channel groups are averaged together, to give an idea of the overall trend of the data. As such, each participant was responsible for mapping the TH data to the correct neutronics channels, and writing this data in the appropriate input format, for each time step. In PARCS, the restart filename and time step number from the previous time step also had to be written to the input file. Unfortunately, there is no way to write all the TH data for the entire transient in one History file (.hst file) in PARCS and run the calculation without restarts, to verify the restart methodology. For the LOR and LOCA problems, the movement of the adjuster rods and initiation of the shutoff rods also had to be written to the input file. PARCS transient convergence and time-step parameters are shown in Table 5.

Table 5. PARCS Transient Convergence and Time-step Parameters

Parameter	Value
Time Step	0.01 s
K-effective Convergence	1×10^{-10}
Global Fission Source Convergence	1×10^{-10}
Local Fission Source Convergence	1×10^{-10}

The trends shown in the Appendix B plots are worth discussing here. First, it was realised sometime after the release of the Final Specifications that there was an issue with the ARIANT model that was

used to generate the stand-alone data. As such, the trends shown in Appendix C do not necessarily reflect the actual behaviour one would expect to see during coupled transients. However, the major trends are still present. For the LOCA case, shown in Figure C-8, there is a rapid decrease in coolant density as the system de-pressurizes, and a corresponding increase in coolant and fuel temperatures, which are terminated by reactor shutdown shortly after 1 second. The LOR and LOF cases, shown in Figure B-9 and B-10 respectively, there is a more gradual decrease in coolant density, and increase in coolant and fuel temperatures. The LOF case also shows unreasonably large changes in TH parameters by the end of the transient, which is a direct result of the ARIANT error mentioned above. In particular, the coolant density drops significantly, causing a large power transient. It was recognized that this behaviour would not be expected during coupled transients.

3.5.2. Stand-alone TRACE Transient Methodology

Similar to the stand-alone reactor-physics (diffusion) transients, the purpose of the stand-alone system thermal-hydraulics transients was to compare the predicted TH variables that would be passed to the diffusion code and the general system response between participants for the three accident scenarios. In this case, a set of 28 grouped channel powers as a function of time were provided for the duration of the transient, in 0.1 second intervals, and participants were responsible for formatting and writing these values into the system thermal-hydraulics code of choice. This is a slightly easier task compared to the stand-alone physics transients, as the channel grouping was performed by the Benchmark Team. For the header break and pump rundown problems, the opening of the header break valve and the pump trip also had to be considered. In TRACE, a full set of channel powers and axial channel power distribution data can be defined for the entire transient in a single input file and the case can be run without restarts, unlike PARCS. Conversely, the user can define the channel power and axial distribution data for a single time step, and restart from the end of the previous time step. The later method is necessary in coupled calculations, while the former method is less error prone and is compatible with the SNAP software, which allows the user to make animations of the TRACE run. Both methods were employed in this work. TRACE convergence and time-step parameters are shown in Table 6.

Plots of the total core power for each stand-alone transient can be seen in Figure A-4, in Appendix A. The trends shown in this Figure align with those described above for the stand-alone reactor physics transients, as the two sets of data were generated from the same coupled calculation performed by the Benchmark team. One can see the large power ramp in the LOF case, compared to the more moderate power pulse and power ramp in the LOCA and LOR cases, respectively.

Table 6. TRACE Transient Convergence and Time-step Parameters

Parameter	Value
Steady State Convergence Criteria	1×10^{-3}
Outer Pressure Iteration Convergence Criteria	1×10^{-3}
Minimum Time Step	1×10^{-7} s
Maximum Time Step	1×10^{-2} s

3.5.3. TRACE and PARCS Coupling Methodology

3.5.3.1. Steady State Picard Iterations

Before one can perform a coupled transient calculation, initial conditions must be obtained such that the total core power, channel power distribution and thermal-hydraulic conditions stay constant over time during a null transient run. In the context of this work, a null transient refers to a coupled transient calculation where no explicit changes to either model are made (i.e. turning of a valve, movement of a control device, etc.). Typically, these initial conditions can be achieved using a Reactor Regulating System (RRS) model, that would, for example, adjust liquid zone levels in response to changing core conditions, to maintain a constant core power. However, no RRS model is present in the IAEA ICSP Benchmark Specifications, so initial conditions must be obtained some other way. To this end, the method of steady state Picard iterations was selected by many participants. In this methodology, steady state iterations of both codes are performed, where information is exchanged between codes after every iteration, until a converged set of TH parameters and channel powers are obtained. In this work, it was found that as little as 3 iterations are required.

In the methodology used in this work, PARCS was run first, and TRACE was run second. This is an arbitrary choice when performing steady state Picard iterations, and the code order could be reversed without any change in output parameters. Both codes are run with the transient convergence and time-step parameters defined in Table 5 and Table 6. As discussed in Section 3.1.4, TRACE will never converge to these values during a steady state calculation, so a run time of 50 seconds is used, to allow TRACE to achieve a sufficient steady state. As such, TRACE is by far the limiting code in terms of run time.

The output of a steady state Picard iteration is a TRACE restart file (.tpr file at the end of a steady state run, which must be renamed to a .rst file to act as a restart file), which completely defines the state of the TRACE system at the end of the last steady state calculation, and a PARCS History (.hst) file, which contains the TH conditions from the last steady state TRACE calculation, and the Xenon/Samarium number densities from the last steady state PARCS calculation. These two files are required to initiate the coupled transients. On the TRACE side of the problem, the input file cannot include any components that have defined initial conditions (i.e. pipes, heat-structures, pumps etc.) when running a transient calculation from a restart file. As such, valve position tables and pump rundown curves must be defined in the steady state TRACE input file. This is the most basic way to define a transient and can be improved upon using TRACE signal variables, which can be adjusted in the transient input file.

3.5.3.2. Code to Code Information Exchange

The calculations and methods used to exchange information between PARCS and TRACE (TRACE passing TH distribution to PARCS, PARCS passing Channel Powers to TRACE) are identical in both the steady state Picard iterations and coupled runs, and are described in the Sections below.

3.5.3.2.1. PARCS Information Exchange

At the end of each run (steady state, or transient) PARCS outputs normalized bundle power distributions for each core plane. To convert these values into actual bundle powers with units of power (W, kW, MW), each normalized bundle power is multiplied by the core average bundle power at that time in the calculation, as shown in Equations 3-3 and 3-4.

$$P_{bundle,core\ average}(t) = \frac{P_{core,norm}(t) * 2000MW}{380 * 12} = \frac{P_{core,norm}(t) * 2000MW}{4560} \quad (3-3)$$

Where:

- $P_{bundle,core\ average}(t)$ is the core wide average bundle power at time t
- $P_{core,norm}(t)$ is the normalized total core power predicted by PARCS at time t
- $2000\ MW$ is the steady state core power defined by the IAEA ICSP Benchmark Specifications
- 380 is the number of fuel channels
- 12 is the number of fuel bundles per channel

$$P_{bundle_k} = P_{bundle,core\ average}(t) * P_{bundle,norm_k} \quad (3-4)$$

Where:

- P_{bundle_k} is the bundle power in MW in node k (where $k = 1$ to 4560)
- $P_{bundle,norm_k}$ is the normalized bundle power in node k, computed by PARCS

Once the actual bundle power distribution has been obtained, group averaged bundle powers for a TRACE fuel channel group are computed by averaging all the bundle powers in channels that belong to that group, as shown in Equation 3-5. The channels that belong to a given group are defined in the Channel Map shown in Figure A-1 in Appendix A.

$$P_{bundle,group\ ave_{g,n}} = \frac{\sum_{i=1}^{N_g} P_{bundle_{i,n}}}{N_g} \quad (3-5)$$

Where:

- $P_{bundle,group\ ave_{g,n}}$ is the average bundle power in TRACE group g, node, n, where n represents the bundle number between 1 and 12 and g represents channel groups 1 through 28
- $P_{bundle_{i,n}}$ is the bundle power for node n, from channel i in channel group g computed by PARCS
- N_g is the number of channels in channel group g, which varies between 11 and 17 channels

The group averaged bundle powers are then summed to determine a group averaged channel power, as shown in Equation 3-6.

$$P_{channel,group\ ave,g} = \sum_{n=1}^{12} P_{bundle,group\ ave_{g,n}} \quad (3-6)$$

Where:

- $P_{channel,group\ ave,g}$ is the channel power for group g that will be passed directly to TRACE

This group averaged channel power is then used to normalize the group averaged bundle power to obtain a channel power and normalized axial power distribution that can be passed to TRACE, as shown in Equation 3-7.

$$P_{bundle\ TRACE\ axial_{g,n}} = \frac{P_{bundle,group\ ave_{g,n}}}{P_{channel,group\ ave,g}} \quad (3-7)$$

Where:

- $P_{bundle\ TRACE\ axial_{g,n}}$ is the normalized axial bundle power for group g, node n that will be passed directly to TRACE

3.5.3.2.2. TRACE Information Exchange

At the end of each TRACE timestep, the thermal-hydraulic conditions throughout the system model are written to the output file. The coolant density, coolant temperature and Doppler fuel temperature in each fuel bundle node must be passed to PARCS. The Doppler fuel temperature is just the average fuel element temperature computed by TRACE, and the coolant density and coolant temperature are weighted sums of the liquid and gas densities and temperatures, where the void fraction is used to perform the weighting as described in Eqn. 3-9 and 3-10.

$$T_{F_{g,n}} = T_{F,ave,TRACE_{g,n}} \quad (3-8)$$

$$T_{C_{g,n}} = (1-\alpha)T_{C,liquid_{g,n}} + \alpha T_{C,vapour_{g,n}} \quad (3-9)$$

$$D_{C_{g,n}} = (1-\alpha)D_{C,liquid_{g,n}} + \alpha D_{C,vapour_{g,n}} \quad (3-10)$$

Where:

- $T_{F_{g,n}}$, $T_{C_{g,n}}$ and $D_{C_{g,n}}$ are the fuel temperature, coolant temperature and coolant density passed to PARCS for node n in all channels in channel group g
- $T_{C,liquid_{g,n}}$, $D_{C,liquid_{g,n}}$, $T_{C,vapour_{g,n}}$, $D_{C,vapour_{g,n}}$ are the liquid phase coolant temperature and density, and the vapour phase coolant temperature and density for node n in all channels in channel group g, respectively, computed by TRACE
- $T_{F,ave,TRACE_{g,n}}$ is the average fuel element temperature computed by TRACE
- α is the void fraction

This is a much simpler calculation that the PARCS bundle/channel power calculation, as no averaging needs to be performed. 28 axial distributions of coolant density, coolant temperature and fuel temperature are mapped directly to the corresponding PARCS channels, as per the Channel Map defined in Figure A-1, in Appendix A.

3.5.3.3. Coupled TRACE/PARCS Calculations

As described in Section 3.5.3.1, each coupled transient calculation is linked to the outputs of the steady state Picard iteration calculation. The final TRACE restart file generated during the steady state iterations defines the starting conditions for the TRACE side of the problem, and the PARC History file that was generated at the end of the steady state iterations defines the TH and Xe/Sm distributions for the first PARCS time step. The reason the steady state Xe/Sm distributions are required is that the equilibrium Xenon and Samarium calculation is slightly different between the steady state and transient calculation modes. As such, if the transient equilibrium Xenon/Samarium calculation is used to initialize the Xe/Sm concentrations at the start of the null transient, it will yield a core power distribution that is slightly different than the distribution obtained at the end of a steady state PARCS calculation. This will in turn cause small changes in the null transient TRACE system conditions and the TH variables passed to

PARCS, compared to those generated during the last steady state TRACE iteration. Since the effective core multiplication factor (K-effective) is set equal to 1.0 at the start of a PARCS transient, any change in TH parameters will lead to a small power excursion during a null transient. As such, during coupled calculations, the steady state Xe/Sm number densities from the last steady state PARCS iteration are read into PARCS only at time = 0.0 seconds and are then updated by the transient Xe/Sm solver for all other time steps.

In the coupling methodology used in this work, PARCS is the first code to run followed by TRACE. This is different than the traditional method used to couple system thermal-hydraulic and diffusion codes, where the system code is run first, and used to set the information transfer time. In this methodology, a fixed information transfer time is selected by the user (typically 0.1 to 0.001 seconds), so there is no benefit of running one code before the other. This type of coupling algorithm is called a "Marching Algorithm" in [30]. As the calculation proceeds, PARCS runs 1 time step equal to the length of the information transfer time, with a smaller internal calculation time step (must be less than or equal to the time step length, and typically, an internal time step 10x smaller is used). Channel power information is then passed to TRACE, which simulates the same time step, again with a smaller internal calculation time step, before passing updated TH information to PARCS for the next time step. Unlike PARCS, which uses a constant internal time step defined by the user, in TRACE, the user defines a range of internal time steps, and the code is allowed to explore the space depending on the rate of change of the state variables. TRACE contains a sophisticated algorithm to select the appropriate time step, and will always add small, additional time steps, if needed, to align the calculation with the end time defined by the user. The coupled calculations were performed using a Python script. In this script, the user has the option to set the information transfer time, and internal time steps of both codes. This algorithm is depicted in Figure 32.

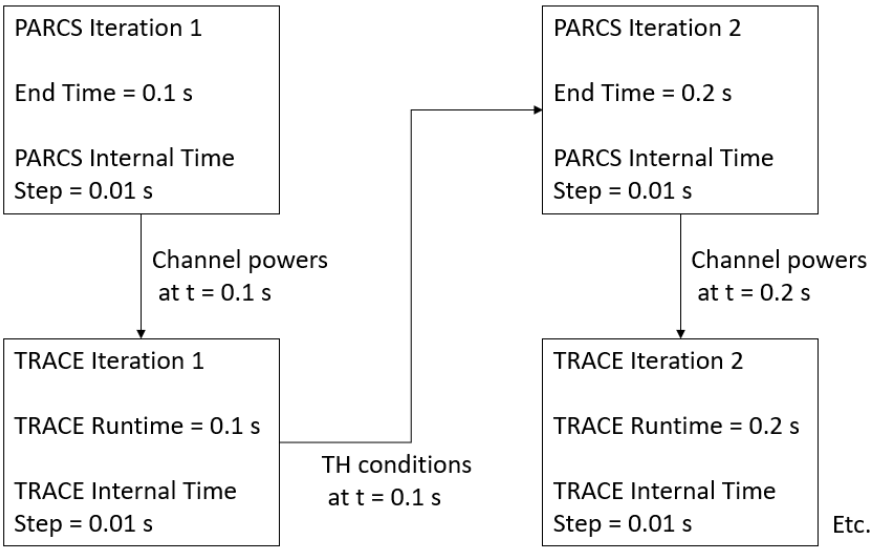

Figure 32. Illustration of the McMaster Coupling Methodology (Marching Algorithm)

4. Results

For all the results and discussion presented below, it must be recognized that the transients defined in the IAEA ICSP Benchmark are very stylized and do not represent the behaviour of an operating CANDU 6 reactor. For example, at the start of the transients the Specifications instruct the user to isolate the pressurizer boundary condition from the PHTS, which significantly alters the system behaviour and transient response. This specific example is discussed further below. Such instructions were included in the ICSP Specifications to remove any model differences that may result from pressurizer control features which were not included in the specification. Other changes of this type were also implemented in the Specifications to isolate only thermal-hydraulic and reactor physics phenomena.

4.1. Stand-alone Transient Results

In addition to the general disclaimer above, it is also worth noting that the input data used to run the stand-alone transients was generated through preliminary coupled calculations by CNL. When these transients were run, there was an unspecified error in CNL's system model (ARIANT) which lead to some issues with the data, particularly for the LOF case. As such, the stand-alone results may not accurately reflect the response obtained during coupled calculations. This error was subsequently fixed and is not present in any of the final CNL results included in this thesis.

4.1.1. Stand-alone Reactor Physics/Diffusion Results - PARCS

Normalized core power results predicted by PARCS during stand-alone calculations were compared with CNL and CNEA results generated using the specified cross section data. These plots are shown in Figure 33, Figure 34, and Figure 35. All cases were run with the specified cross section data, raw HELIOS cross section data, full branch SCALE cross section data and the reduced branch uncertainty propagation SCALE cross section data (SCALE UP, discussed in Section 3.2.3). While the results do not overlap perfectly, one can see that trends (the shape of the core power as a function of time) and magnitudes are comparable across all three transients, particularly when the PARCS results generated with the specified cross section input data are compared to the CNL and CNEA results. This provides additional confidence in the stand-alone PARCS transient methodology discussed in Section 3.5.1, and the PARCS model development, discussed in Section 3.4.

Across all cases, the two sets of SCALE cross section data (full branch SCALE vs. SCALE UP) consistently predict lower core powers than the two sets of HELIOS cross section data (full branch HELIOS and specified), which is to be expected given the lattice level CVR results shown in Figure 18 and the steady state full core coolant density perturbation results shown in Table 4, where in both cases, the SCALE data shows a smaller change in reactivity. This under prediction is most notable in the LOF/LOCA cases, which are thermal-hydraulic driven transients, and less noticeable in the LOR case, which is driven by the reactivity of the adjuster rods. However, comparing between the two sets of HELIOS data and the two sets of SCALE data across all three transients, one can see the results are very similar. This implies that the thermal-hydraulic reactivity feedback is nearly linear over the range of variation explored in these transients, since for both data sets, the multi-branch results are not markedly different from the single branch results.

These results are also consistent with the results of a larger TH perturbation study, shown in Table 7 and summarized in Table 8, that was performed with the TH distribution obtained from the last coupled

steady state Picard iteration, as opposed to the TH distribution provided in the Specifications, which was used to generate the results shown in Table 4. In general, the two sets of SCALE data tend to agree better, which can be most clearly seen in the LOF case. From Table 8, one can see that the HELIOS data yields less negative fuel temperature reactivity feedback when the fuel temperature increased, and more positive fuel temperature reactivity feedback when the fuel temperature is decreased, compared to the specified data. As such, regardless of the change in fuel temperature, the HELIOS data will result in higher core powers than the specified data, as there is no appreciable difference in coolant density or temperature feedback. A similar result is seen between the SCALE and SCALE UP data, with the SCALE UP data exhibiting stronger fuel temperature feedback. However, the SCALE UP data also shows more positive coolant density reactivity feedback at low coolant densities, less than 0.3 g/cc, which offsets the fuel temperature bias, and generally leads to slightly higher core powers than the full SCALE data.

With regards to the LOCA results, it is worth noting that the core power is very comparable between all three participants for the first second of the transient and the major difference is the time at which the power begins to decrease. The cause of this discrepancy is unclear, but the trend indicates that small differences in the SOR timing and drop profile may be responsible. In addition, for the LOF case, while the transient was defined for 25 seconds of run time, results were only available from CNEA for the first 15 seconds. Shortly after 15 seconds, the core power begins to increase very rapidly, and by 22.2 seconds, the CNL results show a core power of 114 733 %FP, or 229 466 000 MW, and the McMaster results show a core power of 4073.9 %FP.

Channel power distribution animations were generated for all stand-alone PARCS transients that used the specified cross section data. These animations are a convenient way to visualize the evolution of the spatial power distribution during the transients. The animations were also a very useful de-bugging tool during when communicating with other participants. The full animations can be found on the IAEA SharePoint site and some select frames are shown in Appendix D. For the LOR case shown in Figure D-1, one can see a gradual increase in power, with a peak on the right side of the core. This is to be expected, as the withdrawn adjuster (adjusters 7 and 14) are located on the right side of the core (see Figure B-6). For the LOF case, shown in Figure D-2, the core power at the end of the transient is so large that the initial channel power distribution appears uniform, when plotted on the same color scale. In this case, a large power peak can be seen in the lower left-hand side of the core, which corresponds to the location of the tripped pump (pump 2, see Figure 15). Finally, for the LOCA case, shown in Figure D-3, one can see the power pulse on the left side of the core, which again corresponds to the location of the broken header (inlet header 4, see Figure 15). Furthermore, one can see the progression of the shutoff rods as they move through the core, and the final shutdown state.

In addition to core power animations, channel averaged TH parameter distribution animations were also generated, and can be found on the SharePoint site. Due to space limitations, only a single snapshot of the three TH variables during the LOCA case are shown in Figure D-4, one second into the transient. The impact of channel grouping, bi-directional re-fuelling, and the two-loop design of the CANDU reactor can clearly be seen in this Figure. In both the coolant density and temperature snapshots, checkerboard voiding can clearly be seen on the left side of the core, with lower density fuel channels corresponding to those connected to the broken header. Furthermore, one can see the impact of fuel channel grouping, with one fuel channel group from the broken loop predicting a much smaller change in coolant density than the other 6 groups. Finally, one can see that the in-tact loop on the right side of the core is largely unaffected, with only a small change in TH parameters.

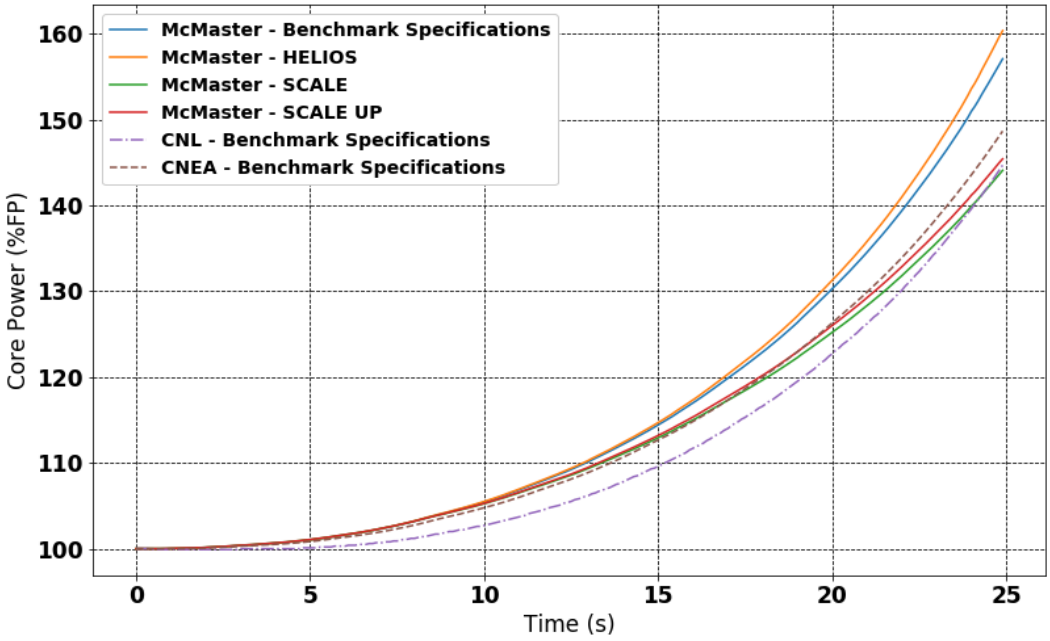

Figure 33. Stand-alone Diffusion Results– Adjuster Pull (LOR) Normalized Core Power

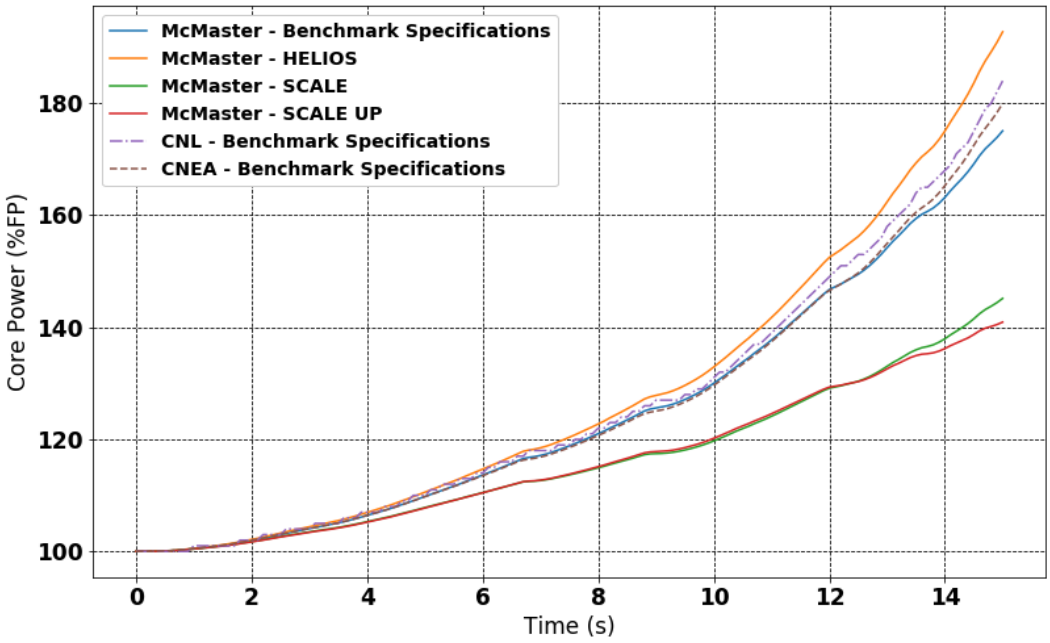

Figure 34. Stand-alone Diffusion Results– Pump Rundown (LOF) Normalized Core Power

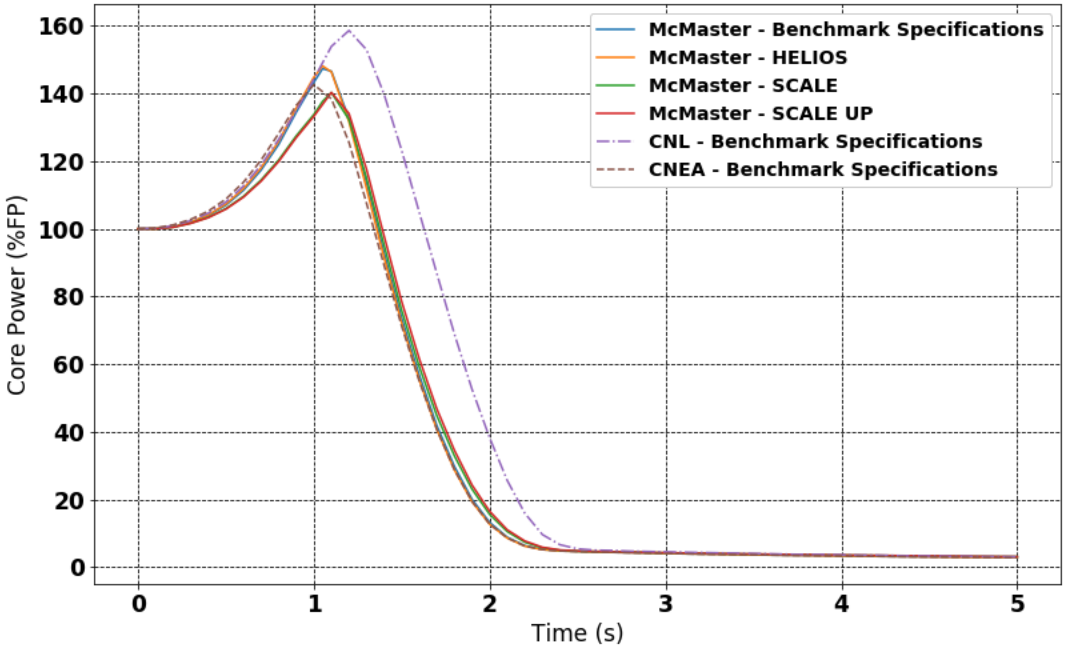

Figure 35. Stand-alone Diffusion Results– Loss of Coolant (LOCA) Normalized Core Power

4.1.2. Stand-alone System Thermal-hydraulics Results - TRACE

For all three cases, stand-alone TRACE transients were performed with the final and modified TRACE models (see Section 3.1.2.1). Unfortunately, participants channel averaged fuel temperature and coolant density/temperature results for the stand-alone transients were not available for comparison at the time of writing. These results would provide the best insight into the impact different system thermal-hydraulics models would have on coupled calculations, as they would provide a direct comparison of the variables passed to the reactor physics code. The core average TRACE results are shown in Figure 36, Figure 37, and Figure 38, for reference. As such, to perform a high-level verification with the CNL and CNEA results, other figures of merits had to be used. This can still provide confidence that the different system codes are predicting comparable values for key TH variables, but it is not as valuable as a direct comparison. For the purposes of this dissertation, the following figures of merit were compared:

- LOR: 1. Pressure and temperature of the header closest to the withdrawn adjusters (OHD7)
- LOF: 1. Pressure and temperature of the header connected to the broken pump (IHD4)
- LOCA: 1. Header break discharge mass flow rate, and 2. broken header pressure (IHD2)

These results can be seen in Figure 39, Figure 40, Figure 41, and Figure 42, respectively. For the LOR case, one can see that the TRACE outlet header 7 pressures (outlet header closest to pulled adjusters) compare very closely to the CNEA results, with the CNL pressure increasing at a slightly slower rate. In general, the system pressurization results from isolating the pressurizer boundary condition during the transients and the mismatch between core power and flow with no RRS action. The header temperature also increases in this case, again with CNL increasing at a slightly slower rate. Similar results are seen for the LOF transient, however, in this case, inlet header 2 (IHD2) is compared, as this is the header connected to the tripped pump. In this transient, the coolant temperature decreases in the inlet header, due to increased heat transfer in the steam generators that results from a lower flow rate. The pressure in the header also rises considerably in this case, to around 18 MPa, due to the large core power ramp shown in Figure A-4. The mass flow rate through the PHTS pumps is a major driver for this accident scenario, but unfortunately, results from other participants were not available. The results for the final TRACE model are shown in Figure 43.

The largest discrepancy in participants results is seen in the LOCA case. The magnitude of the power pulse in a LOCA is almost completely determined by the rate of de-pressurization of the broken loop in the first second of the transient (which drives the decrease in coolant density), and the timing of the shut-off rods. Furthermore, the de-pressurization of the broken loop is almost completely determined by the break discharge flow rate. From Figure 41, one can see that the McMaster, CNL, and CNEA inlet header 4 pressures (IHD4, the broken header) show major differences during the first second of the transient. This is supported by the break discharge results shown in Figure 42, with CNL having the largest discharge flow rate during the first second, CNEA having the smallest flow rate and McMaster in-between, but comparable to the CNL results. Also shown in Figure 42 are the results of a break discharge sensitivity study, where different K-factors were used to attempt to match various flow rates. One can see that the magnitude of the break discharge can be effectively tuned by varying the K-factor at the break plane. The rationale for the range of K-factors used is provided in [47] and [48]. Finally, comparing the inlet header temperatures, one can see that TRACE predicts a much larger increase in coolant temperature than ARIANT (CNL) or RELAP (CNEA). Despite this case showing a larger range of results

than the other two, the major trends are comparable between participants, and can be used to help explain differences in coupled results.

As mentioned in Section 3.5.2, the stand-alone system thermal-hydraulics runs were performed twice: once using restart features, like the coupled approach, and once using a single input file. The results discussed above were all generated using the restart approach. However, the single input file approach allows the transients to be loaded into SNAP where they can be visualized with animations. These animations were found to be extremely valuable in understanding the transient behaviour. The full animations can be found on the IAEA SharePoint site and some select frames can be seen in Appendix E. For the LOR case in Figure E-1, one can see the pressurization of the system, both from the header pressures shown numerically, and from the void collapse in the steam generator U-tubes on the left side of the core. This collapse is not seen on the right side of the core, due to the power peak that occurs there, shown in Figure D-1. Similar, but more drastic behaviour is seen in the LOF case, shown in Figure E-2, where after 10 seconds, all the void in the right hand side of the core has collapsed (the tripped pump is on the left side of the core in this case), and after 15 seconds, the entire core has gone solid, and all coolant is below the saturation temperature. Again, given the issue with the stand-alone data discussed previously, this is not be representative of the system response during the coupled runs.

From Figure E-3, one can see the LOCA behaviour is much different than the other two cases. The break opens completely during the first 0.1 seconds, and one can see the rapid de-pressurization of IHD2 (the broken header), a large decrease in flow rate in some fuel channels, and flow reversal in others. By 0.16 seconds, complete flow reversal is achieved in the broken pass. After 1.0 seconds, super heated steam can be seen in the broken pass and by 1.5 seconds, super heated steam is present in many fuel channels in the broken pass. As the transient progresses to 2.5 seconds, the void fraction in the steam generator increases again, and by 5.0 seconds, there is significant void present in every steam generator U-tube node, and flow has been completely lost in several fuel channels.

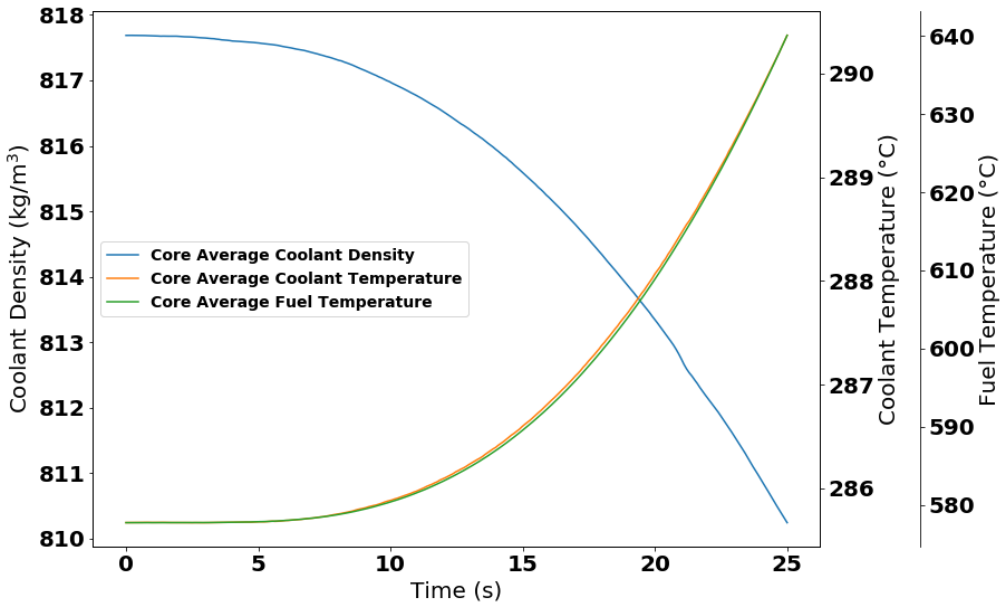

Figure 36. Stand-Alone TRACE LOR Results: Core Average Coolant Density, Fuel and Coolant Temperatures

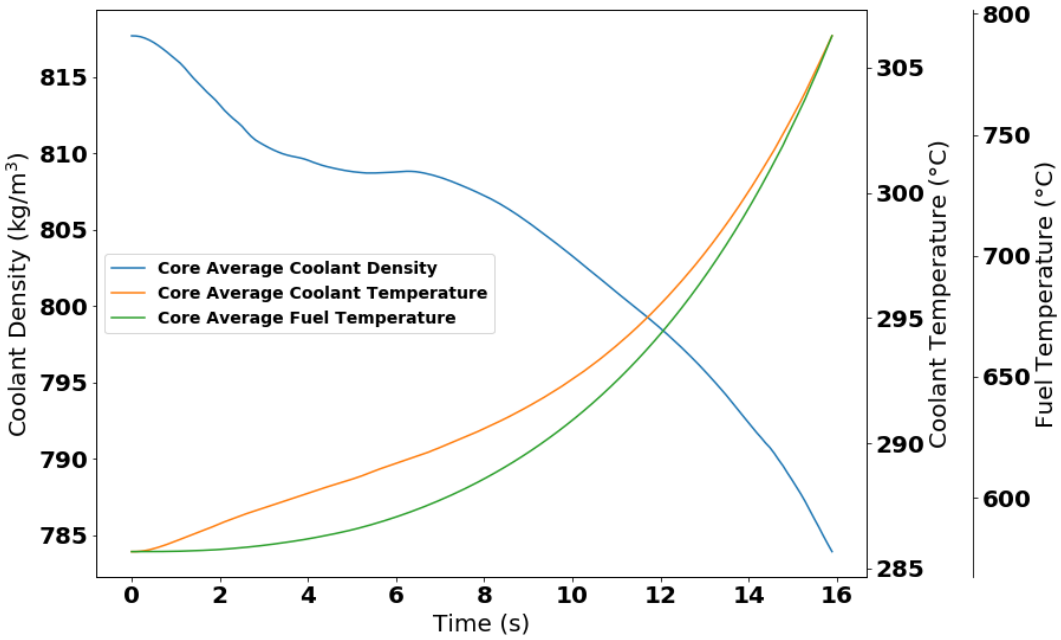

Figure 37. Stand-Alone TRACE LOF Results: Core Average Coolant Density, Fuel and Coolant Temperatures

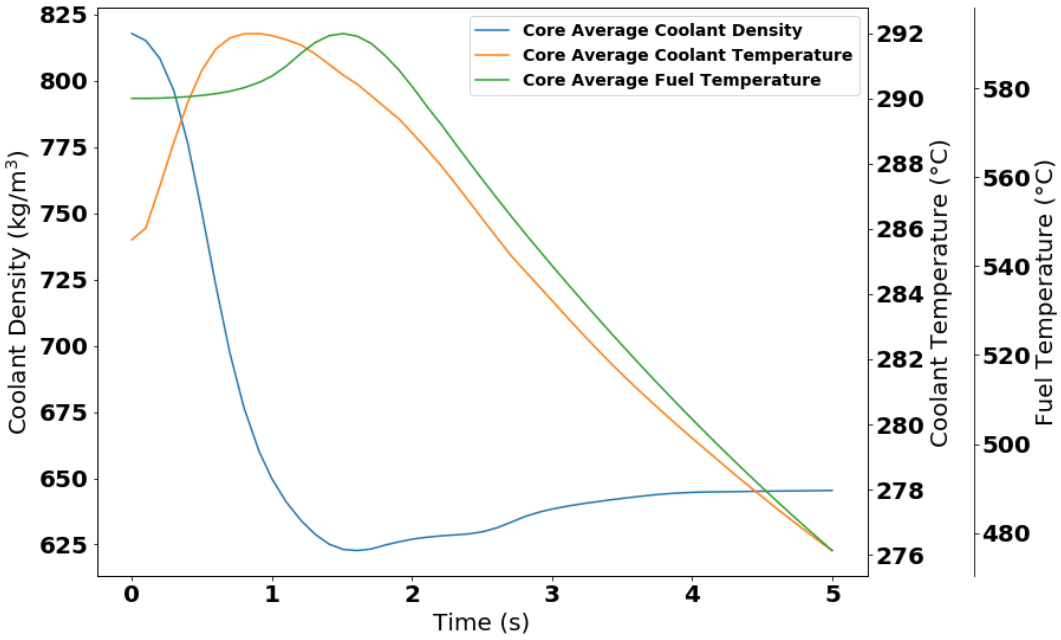

Figure 38. Stand-Alone TRACE LOCA Results: Core Average Coolant Density, Fuel and Coolant Temperatures

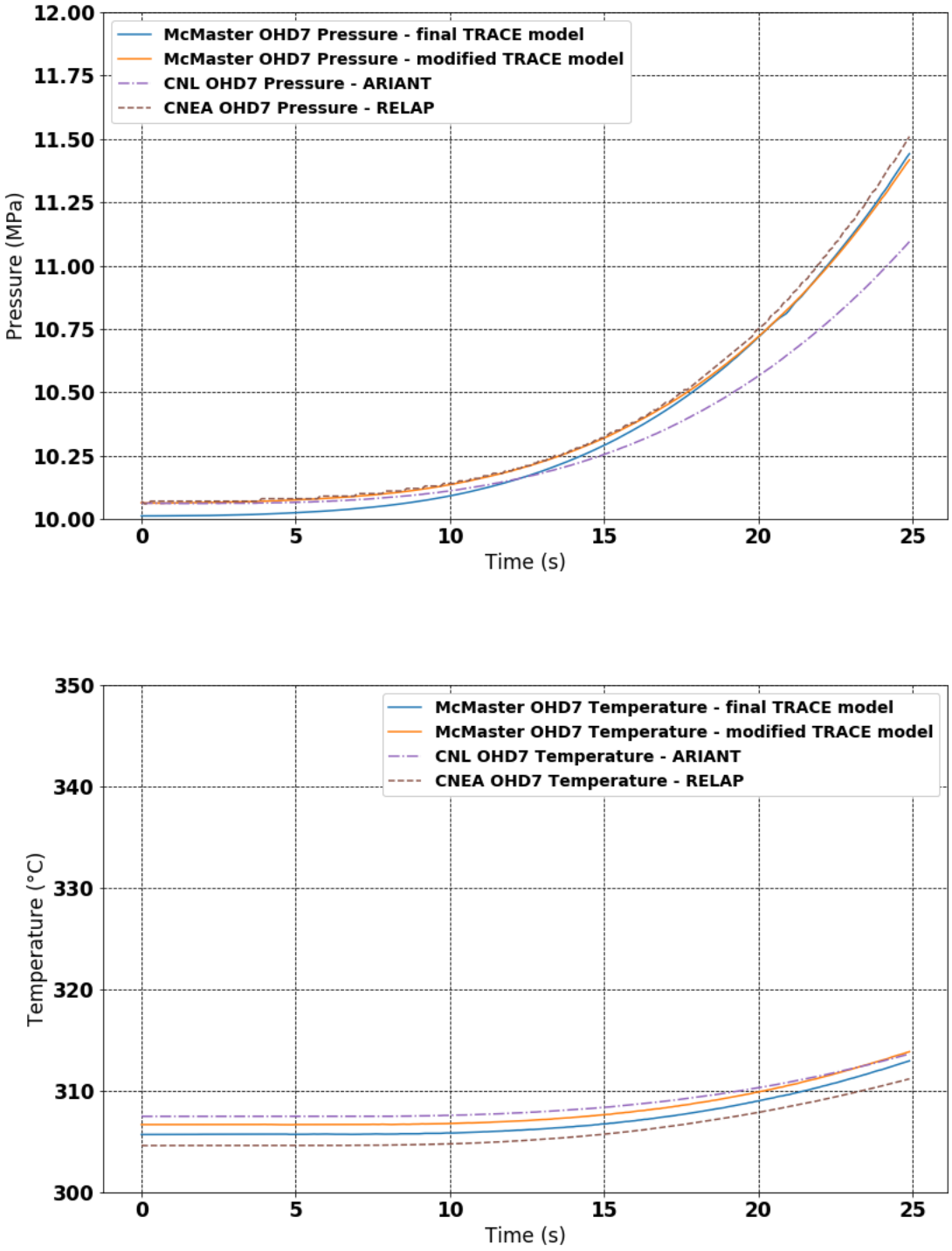

Figure 39. Stand-alone System Thermal-Hydraulics Results Comparison: LOR Top - OHD7 Pressure, Bottom - OHD7 Temperature

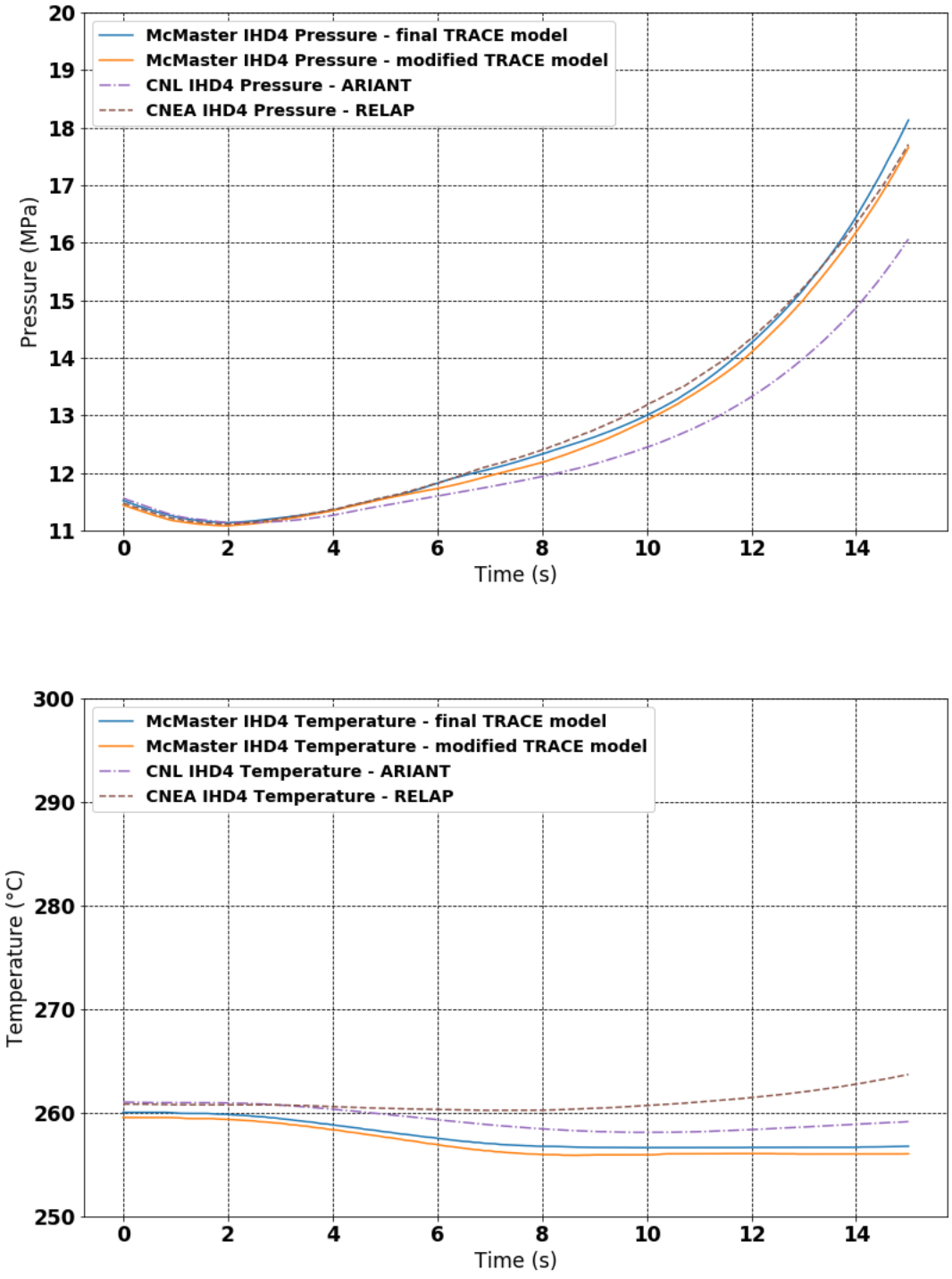

Figure 40. Stand-alone System Thermal-Hydraulics Results Comparison: LOF
Top – IHD4 Pressure, Bottom – IHD4 Temperature

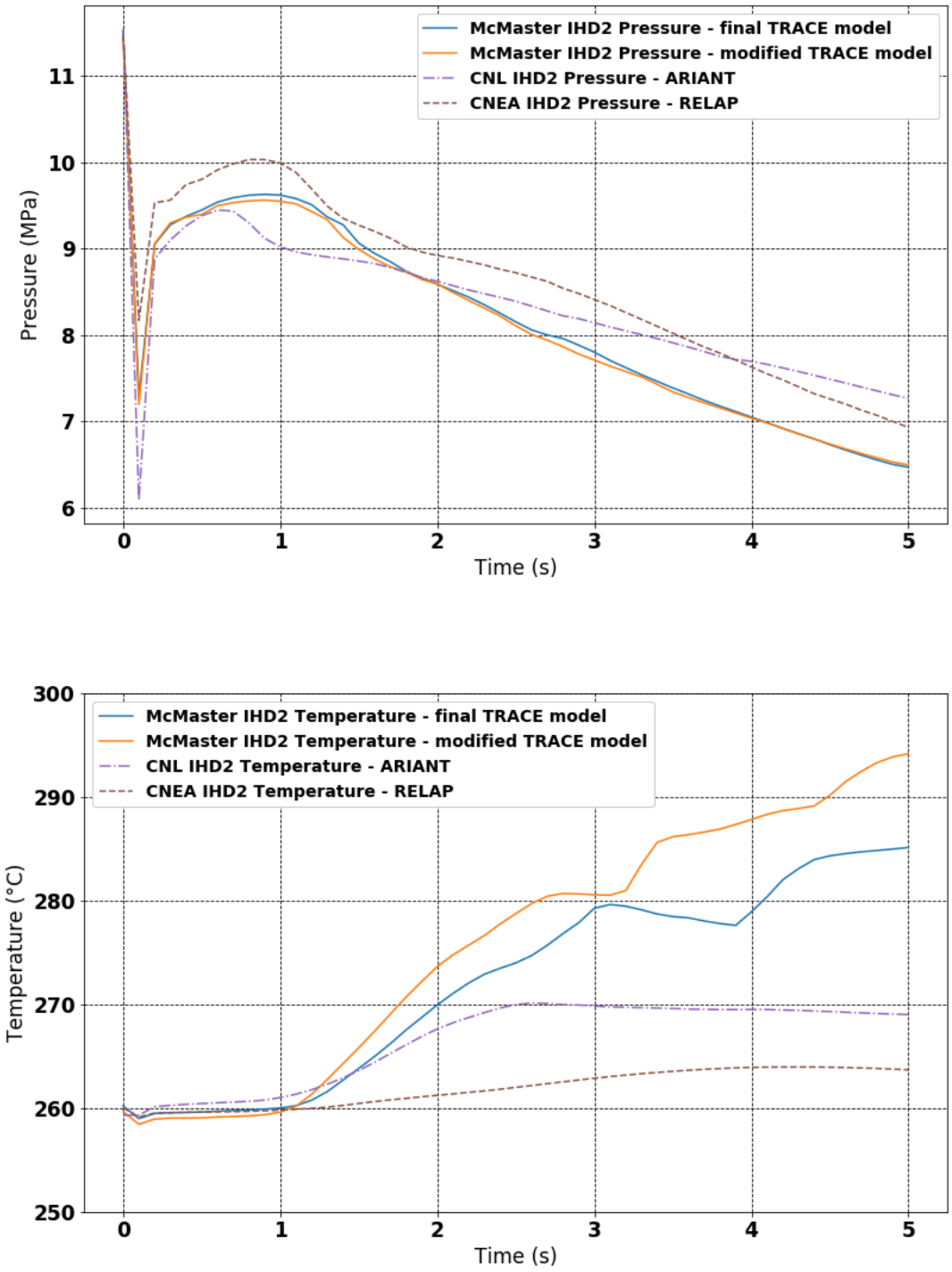

Figure 41. Stand-alone System Thermal-Hydraulics Results Comparison: LOCA
Top - OHD7 Pressure, Bottom - OHD7 Temperature

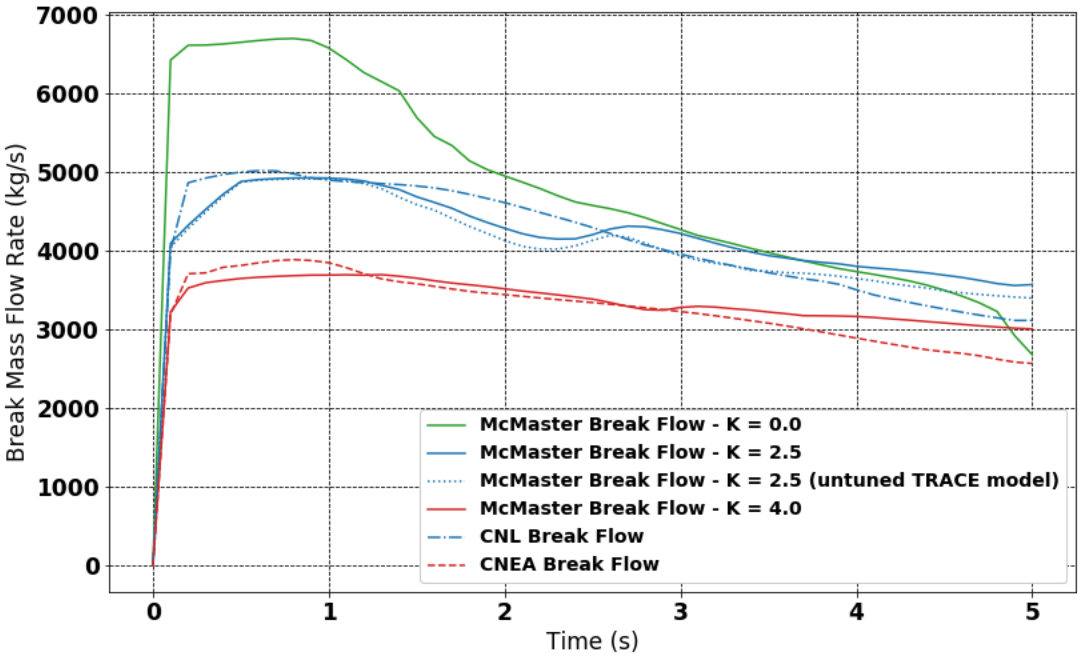

Figure 42. Stand-alone System Thermal-hydraulics Results Comparison: LOCA – Break Mass Flow Rate

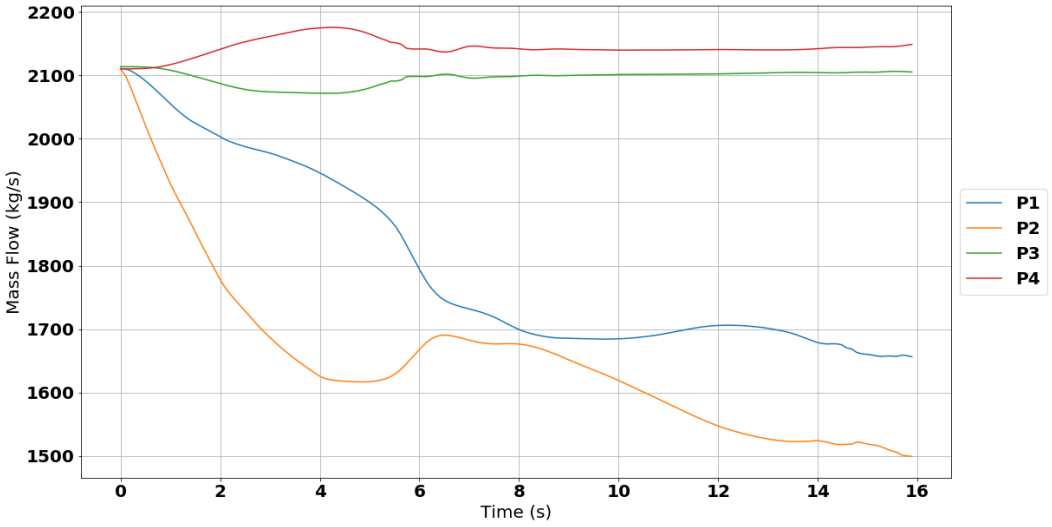

Figure 43. Stand-alone TRACE LOF Pump Mass Flow Rate (generated with the Final TRACE model)

4.2. Coupled Steady State Results

Coupled steady state initial condition results obtained through Picard iterations of TRACE and PARCS are presented here, for all 4 sets of cross section input data discussed in this work. The channel power distribution predicted by PARCS using the specified cross sections at the end of the steady state Picard iterations can be seen in Figure 44. Comparing to the channel power distributions generated with the specified TH distribution (shown in Figures B-2, B-3 and B-4), shown in Figure 28, one can see that the power distributions are very comparable. Furthermore, channel S9 is the highest-powered channel in all cases, with a power of ~6.9 MW, which is below the regulatory limit for a CANDU-6 reactor of 7.0 MW. While not shown, the highest-powered bundle was found to be bundle 7 in channel S9 for all cases, with a power of ~ 866.7 kW, which is below the regulatory limit of 880 kW.

TRACE fluid condition results obtained from the last steady state Picard iteration are shown in Figure 45. Comparing to the results shown in Figure 14 and Figure 15, which were generated using the power distributions shown Figure A-2 and A-3, one can see that the overall system results compare well. The coupled steady state results fall somewhere in between the results of Figure 14 and Figure 15, with significantly less void than the model that was run with the channel power distribution provided in the Final Specifications, but more void than the model run with the ideal power distribution. The results discussed here show that the method of steady state Picard Iterations yields realistic initial conditions for both codes, that are comparable to the steady state initial conditions defined in the Specifications.

Table 7 shows the core K-effective, device reactivity worth and the reactivity associated with various TH perturbations, for all 4 sets of cross sections. A summary of the results is provided in Table 8. From Table 7, there is a clear bias between the SCALE and HELIOS results, with SCALE predicting higher K-effective values, although all values are close to 1.0. Furthermore, one can see that the reactivity worth's compare well across all cases. In this perturbation study, the specified device incremental cross sections (DRAGON) are used with the HELIOS data, and the SERPENT generated device incremental cross sections are used with the SCALE data. Comparing back to Table 4, one can see the results are comparable to the perturbations performed with the specified TH distribution. In Table 8, for each TH perturbation, the total reactivity in mk is shown in the left-hand column, and the reactivity per unit change in TH parameter (i.e. mk/°C, mk/g/cm^3) is shown in the right-hand column. To generate the right-hand column results, an average fuel temperature, coolant temperature and coolant density were calculated from the TH distribution obtained at the end of the Picard iterations, and the difference between the perturbated value and the average value were used to normalize the results. This helps show the linearity of the perturbations; i.e. it helps answer questions such as, "if two TH perturbations are performed, one twice as large as the other, does the core reactivity change by more or less than a factor of 2?".

For the coolant density perturbations, one can that the results are very linear when the coolant density is increased, for all cases. When the coolant density is decreased, a small non-linearity can be seen, with larger relative reactivity changes at lower coolant densities, except for the full branch SCALE data which shows a significant change in behaviour at 0.1 g/cc. A clear bias can also be seen between the two sets of HELIOS data, and the two sets of SCALE data, with both sets of SCALE results showing a much smaller change in reactivity for all coolant density branches, consistent with the lattice level CVR results shown in Figure 18. For the fuel temperature perturbations, when the fuel temperature is decreased, non-linear behaviour can be seen across all cases, with smaller relative reactivity changes at lower fuel temperatures. When the fuel temperature is increased, the same trend can be seen for the multi-branch

data sets (SCALE and HELIOS), where the relative reactivity change is smaller for higher fuel temperatures, but this is not seen in the single branch cases (specified and SCALE UP). There is also a clear bias between the SCALE and HELIOS data, with both SCALE data sets predicting a stronger fuel temperature feedback in both directions. Finally, a quarter core vs. full core voiding case was considered. The purpose of this case is to see the impact of the flux tilt of reactivity perturbations. By voiding 1 quarter of the core (half of the channels on the left side of the reactor), the flux will tilt towards the voided half, and one would expect a reactivity change slightly greater than ¼ of the full core voiding reactivity change, which is what is shown in Table 7.

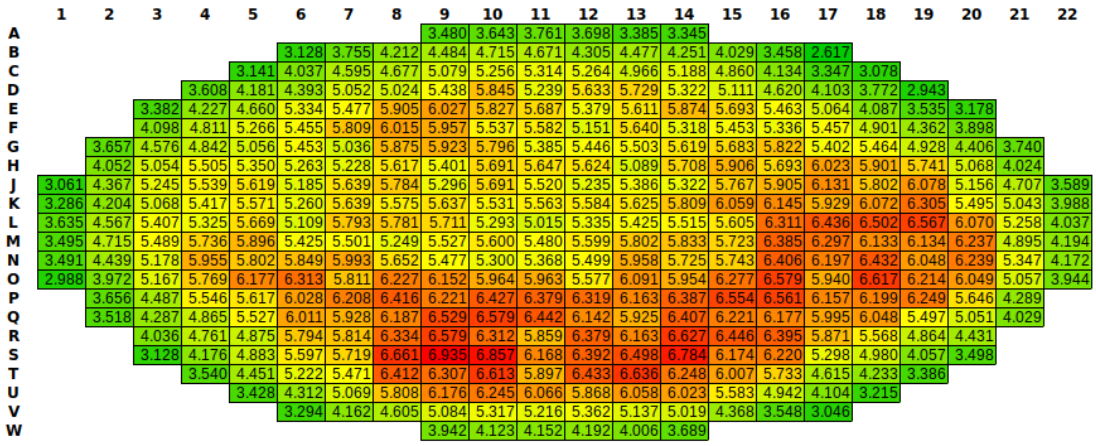

	1	2	3	4	5	6	7	8	9	10	11	12	13	14	15	16	17	18	19	20	21	22
A									3.480	3.643	3.761	3.698	3.385	3.345								
B						3.128	3.755	4.212	4.484	4.715	4.671	4.305	4.477	4.251	4.029	3.458	2.617					
C					3.141	4.037	4.595	4.677	5.079	5.256	5.314	5.264	4.966	5.188	4.860	4.134	3.347	3.078				
D				3.608	4.181	4.393	5.052	5.024	5.438	5.845	5.239	5.633	5.729	5.322	5.111	4.620	4.103	3.772	2.943			
E			3.382	4.227	4.660	5.334	5.477	5.905	6.027	5.827	5.687	5.379	5.611	5.874	5.693	5.463	5.064	4.087	3.535	3.178		
F			4.098	4.811	5.266	5.455	5.809	6.015	5.957	5.537	5.582	5.151	5.640	5.318	5.453	5.336	5.457	4.901	4.362	3.898		
G		3.657	4.576	4.842	5.056	5.453	5.036	5.875	5.923	5.796	5.385	5.446	5.503	5.619	5.683	5.822	5.402	5.464	4.928	4.406	3.740	
H		4.052	5.054	5.505	5.350	5.263	5.228	5.617	5.401	5.691	5.647	5.624	5.089	5.708	5.906	5.693	6.023	5.901	5.741	5.068	4.024	
J	3.061	4.367	5.245	5.539	5.619	5.185	5.639	5.784	5.296	5.691	5.520	5.235	5.386	5.322	5.767	5.905	6.131	5.802	6.078	5.156	4.707	3.589
K	3.286	4.204	5.068	5.417	5.571	5.260	5.639	5.575	5.637	5.531	5.563	5.584	5.625	5.809	6.059	6.145	5.929	6.072	6.305	5.495	5.043	3.988
L	3.635	4.567	5.407	5.325	5.669	5.109	5.793	5.781	5.711	5.293	5.015	5.335	5.425	5.515	5.605	6.311	6.436	6.502	6.567	6.070	5.258	4.037
M	3.495	4.715	5.489	5.736	5.896	5.425	5.501	5.249	5.527	5.600	5.480	5.599	5.802	5.833	5.723	6.385	6.297	6.133	6.134	6.237	4.895	4.194
N	3.491	4.439	5.178	5.955	5.802	5.849	5.993	5.652	5.477	5.300	5.368	5.499	5.958	5.725	5.743	6.406	6.197	6.432	6.048	6.239	5.347	4.172
O	2.988	3.972	5.167	5.769	6.177	6.313	5.811	6.227	6.152	5.964	5.963	5.577	6.091	5.954	6.277	6.579	5.940	6.617	6.214	6.049	5.057	3.944
P		3.656	4.487	5.546	5.617	6.028	6.208	6.416	6.221	6.427	6.379	6.319	6.163	6.387	6.554	6.561	6.157	6.199	6.249	5.646	4.289	
Q		3.518	4.287	4.865	5.527	6.011	5.928	6.187	6.529	6.579	6.442	6.142	5.925	6.407	6.221	6.177	5.995	6.048	5.497	5.051	4.029	
R			4.036	4.761	4.875	5.794	5.814	6.334	6.579	6.312	5.859	6.379	6.163	6.627	6.446	6.395	5.871	5.568	4.864	4.431		
S			3.128	4.176	4.883	5.597	5.719	6.661	6.935	6.857	6.168	6.392	6.498	6.784	6.174	6.220	5.298	4.980	4.057	3.498		
T				3.540	4.451	5.222	5.471	6.412	6.307	6.613	5.897	6.433	6.636	6.248	6.007	5.733	4.615	4.233	3.386			
U					3.428	4.312	5.069	5.808	6.176	6.245	6.066	5.868	6.058	6.023	5.583	4.942	4.104	3.215				
V						3.294	4.162	4.605	5.084	5.317	5.216	5.362	5.137	5.019	4.368	3.548	3.046					
W									3.942	4.123	4.152	4.192	4.006	3.689								

Figure 44. PARCS Channel Power Distribution after 3 Steady State Picard Iterations with the Specified Cross Section Input Data

Table 7. Results of Steady State Picard Iterations and TH Perturbations for 4 different Cross Section Sets (Average Reference Values: FT = 579.45 °C, CT = 285.79 °C, CD = 0.821 g/cc)

Case	Perturbation Reactivity or Device Worth							
	Specified Cross Sections and Incrementals		**HELIOS Cross Sections and Specified Incrementals**		**SCALE Cross Sections and SERPENT Incrementals**		**SCALE UP Cross Sections SERPENT Incrementals**	
Base K-effective	0.998177		0.99832		1.003839		1.00645	
Adjuster Worth	16.97		16.93		16.28		16.12	
Full Liquid Zone Worth	7.11		7.11		7.35		7.25	
Shut-off Rod Worth	79.24		79.14		77.72		76.96	
Full Core CT: 210 °C	-0.57	-0.0076	-0.95	-0.0125	-0.78	-0.0103	-0.86	-0.0113
Full Core CT: 350 °C	0.43	0.0067	0.76	0.0119	0.77	0.012	0.63	0.0098
Full Core FT: 100 °C	1.54	0.0032	2.91	0.0061	4.50	0.0094	2.38	0.005
Full Core FT: 500 °C	0.38	0.0048	0.51	0.0064	0.84	0.0105	0.60	0.0075
Full Core FT: 1000 °C	-0.68	-0.0016	-0.62	-0.0015	-0.99	-0.0023	-1.03	-0.0025
Full Core FT: 1500 °C	-1.53	-0.0017	-1.05	-0.0011	-1.50	-0.0016	-2.34	-0.0025
Full Core FT: 2000 °C	-2.26	-0.0016	-1.18	-0.0008	-1.67	-0.0012	-3.47	-0.0024
Full Core CD: 0.1 g/cm^3	14.52	20.14	14.62	20.27	10.81	14.99	11.55	16.02
Full Core CD: 0.3 g/cm^3	10.42	19.99	10.45	20.05	8.35	16.01	8.30	15.92
Full Core CD: 0.5 g/cm^3	6.38	19.86	6.38	19.88	5.22	16.24	5.09	15.84
Full Core CD: 0.9 g/cm^3	-1.53	-19.38	-1.53	-19.47	-1.27	-16.15	-1.22	-15.45
Full Core CD: 1.1 g/cm^3	-5.40	-19.37	-5.42	-19.45	-4.55	-16.31	-4.32	-15.49
Full Core CD: 1.3 g/cm^3	-9.22	-19.26	-9.26	-19.34	-7.83	-16.36	-7.39	-15.43
Full Core CD: 0.001 g/cm^3	16.58		16.73		12.67		13.18	
Quarter Core CD: 0.001 g/cm^3	4.96		5.03		3.62		3.78	

*for TH perturbations, left hand column is full reactivity in mk, and right-hand column is reactivity per unit change in TH variable, e.g. mk/°C or mk/g/cc.

Table 8. Summary of TH Perturbation Study

Case Comparison	Positive FT Perturbations (FT > Ref FT)	Negative FT Perturbations (FT < Ref FT)	Positive CD Perturbations (CD > Ref CD)	Negative CD Perturbations (CD < Ref CD)	Net result
Specified vs. HELIOS	Specified data yields more negative reactivity	Specified data yields less positive reactivity	No difference	No difference	Specified data yields larger reactivity feedback when FT is increased, and smaller reactivity feedback when FT is decreased. Net result is higher power from HELIOS data in all cases.
SCALE vs. SCALE UP	SCALE UP data yields more negative reactivity	SCALE UP data yields less positive reactivity	No difference	No difference until low density (< 0.3 g/cc) where SCALE UP data yields more positive reactivity	Same FT trend as Specified vs. HELIOS data, with SCALE data resulting in higher power. This is offset by the larger reactivity feedback in SCALE UP data when CD is decreased.
SCALE vs. HELIOS	SCALE data yields more negative reactivity	SCALE data yields more positive reactivity	SCALE data yields less negative reactivity	SCALE data yields less positive reactivity	SCALE data yields larger reactivity feedback in FT case, and smaller reactivity feedback in CD case

4.3. Coupled Null Transient Results

The purpose of the steady state Picard iterations is to obtain a set of channel powers and TH parameters that yield a constant core power during a coupled null transient. The steady state conditions can only be said to be "converged" if this condition is met. As such, it can be difficult to determine when the steady state iterations are complete, as even small changes in TH parameters can lead to a long-term change in core power with no RRS present. In the methodology developed in this work, 3 steady state iterations were performed, and while the change in conditions between iterations 2 and 3 were small, there were some differences. Trials were performed with a larger number of iterations (up to 6), but regardless of the number, some differences between the second last and last iteration were always present. As such, one can see that there would be little to no benefit in defining arbitrary steady state convergence criteria for various parameters, as they could yield constant core powers during null transients for some participants and not others. Despite this, many participants reported their steady state convergence criteria, with no null transient results. As such, there is no way to quantify any underlying transients that may be present in other participants results.

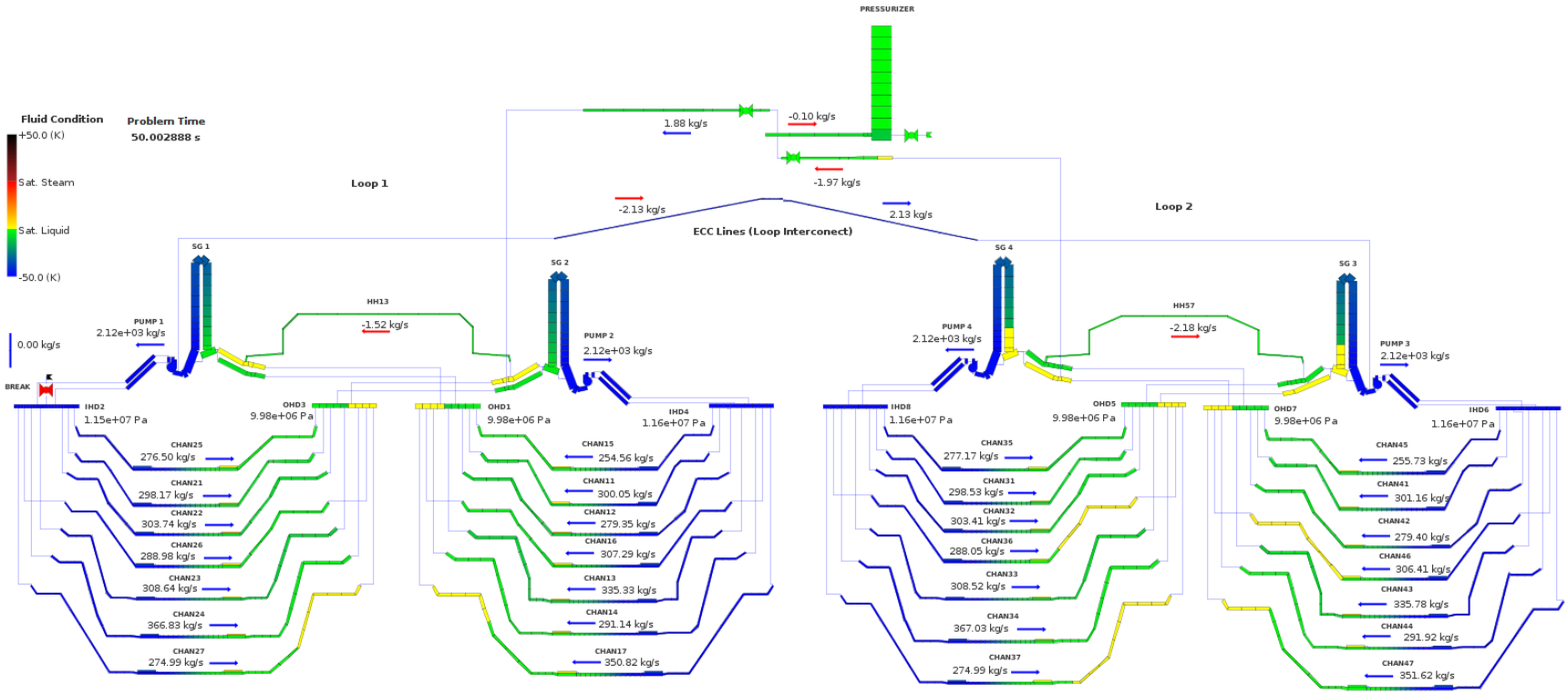

Figure 45. TRACE Fluid Condition Results after 3 Steady State Picard Iterations

The results of the coupled null transient simulations with all 4 cross section sets are shown in Figure 46. The core reactivity for the full branch SCALE case is shown in Figure 47. One can see that for all 4 sets of cross section input data, a constant core power is obtained for a duration of 50 seconds. When the HELIOS data was used, a small increase in core power to 100.01 %FP occurs shortly after 25 seconds. This shows the effectiveness of the steady state Picard Iterations approach used in this work to generate converged initial conditions for coupled transients, and that as little as 3 iterations are required.

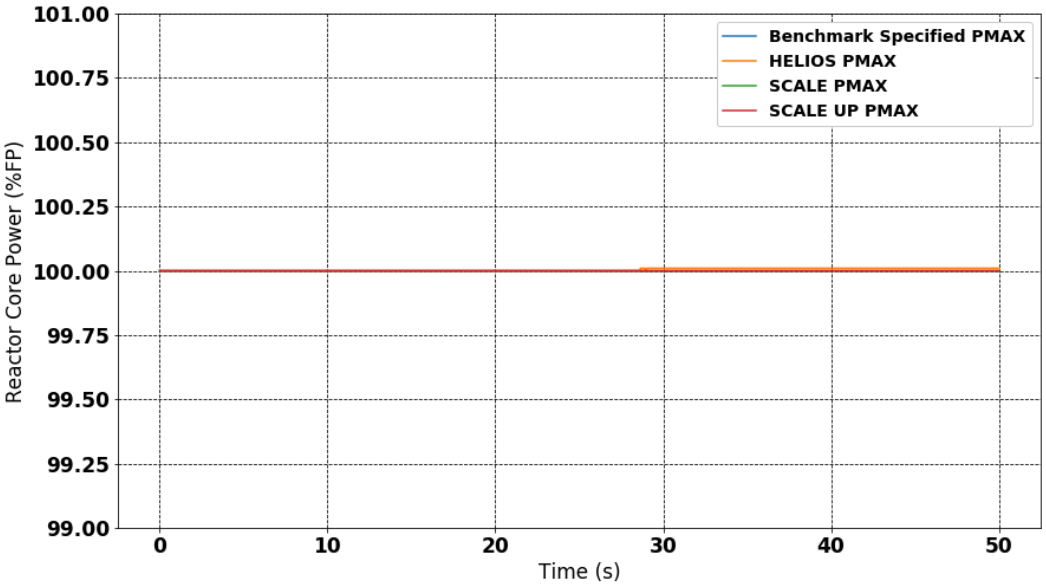

Figure 46. PARCS Transient Core Power During a Coupled Null Transient

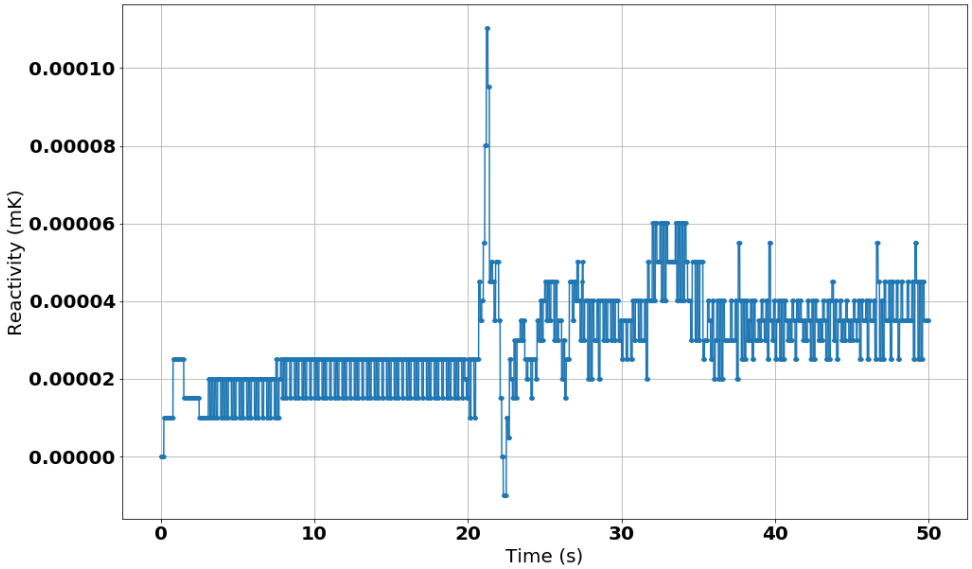

Figure 47. Core Reactivity During a Null Transient with SCALE Cross Section Data

4.4. Coupled Transient Results

Coupled core power results are shown for the three transients considered in the IAEA ICSP Benchmark in Figure 48, Figure 49, and Figure 52. The pump mass flow rates and inlet header 4 pressures are shown for the LOF transient, in Figure 50 and Figure 51, due to significant differences between the coupled and stand-alone results. All three transients were run with the 4 cross sections sets discussed in Section 3.2 and the final TRACE model discussed in Section 3.1.2.1. For the LOF and LOR cases, the information exchange time step was set to 0.1 seconds, and for the LOCA case, an information exchange time step was set to 0.05 seconds. These choices are justified in Section 4.4.1. Final CNL and CNEA results were also obtained for comparison purposes.

Starting with the LOR case, shown in Figure 48, one can that the McMaster results generated with the specified cross section data compare very well with the CNEA results generated with the same cross sections, while the CNL results show a slower power ramp. Comparing back to the stand-alone reactor physics results, shown in Figure 33, one can see the results are comparable, with similar core powers at the end of the transient. For the LOF case shown in Figure 49, again, there is good agreement between the CNEA and McMaster results generated with the specified cross section data, while CNL shows a much faster power ramp. This case was still being investigated by the Benchmark Team at the time of writing of this thesis in response to this discrepancy. Comparing back to the stand-alone reactor physics results shown in Figure 34, one can see the behaviour is entirely different, with the coupled transient yielding a much smaller increase in core power. Comparing the stand alone pump mass flow rates and header pressures shown in Figure 40 and Figure 43, to the coupled responses shown in Figure 50 and Figure 51, one can see that the coupled transient progresses at a slower rate, with a smaller increase in system pressure and a smaller decrease in pump mass flow rate. This discrepancy is due to an unspecified issue with the ARIANT system model that was used to generate the TH parameters for the stand-alone runs, with the coupled results showing more reasonable behaviour.

For both the LOR and LOF cases, it must again be recognized that the predicted core response is markedly different from what one would expect during a realistic accident scenario. As a result of isolating the pressurizer boundary condition at the start of the transients, the system pressure begins to increase almost immediately after the beginning of the transient, while in a realistic accident scenario, the pressurizer level control system would attempt to keep the reactor pressure at the set point (near 10 MPa) for some time, limiting the pressure rise in the core. In this realistic case, void generation is enhanced, and the core reactivity can become much larger. A sensitivity study was performed in response to this observation for the LOF case by keeping the pressurizer boundary condition connected to the system, to try and re-create a realistic transient response. These results are discussed in Section 4.4.3.

For the LOCA case shown Figure 52, the McMaster results generated with the specified cross sections lie in between the CNL and CNEA results generated with the same data, but are more comparable to the CNL results. CNL show a faster power rise and peak core power than any other case, while the CNEA results show a comparable power rise to the McMaster results, but a much smaller peak power. These results can be explained directly by the break flow results shown in Figure 42. For CNEA, the smaller power pulse results from a smaller mass flow rate predicted by RELAP, and in turn, a smaller de-pressurization of IHD2. For CNL, the break flow rates predicted by ARIANT are slightly higher than the TRACE flow rates for the first half second and are comparable from 0.5 to 1.0 seconds. Examining Figure

41, one can see that this leads to lower IHD2 pressures in ARIANT than in TRACE. This header pressure has a large impact on the voiding rate, and subsequent reactivity insertion and helps explain the faster power rise predicted by CNL. This case best highlights the impact of the user effect on transient results, as participants were free to model the break in any way they chose, leading to different break flow rates and system de-pressurization. Furthermore, while this case is still idealistic, it bears the closest resemblance to the expected response of an operating CANDU. This was a major driver for the selection of the LOCA case for additional sensitivity analysis, shown in Section 4.6.

Comparing the McMaster results generated with the 4 different cross section sets for all cases, one can see that the results are similar to those discussed for the stand-alone reactor physics transients, and are consistent with the coupled steady state perturbation study results shown in Table 7. As such all the discussion from Sections 4.1.1 and 4.2 apply here; the HELIOS data consistently predicts markedly higher powers than the specified data, the SCALE UP data consistently predicts slightly higher powers than the full branch SCALE data, and the two sets of SCALE data consistently predict smaller powers than the two sets of HELIOS data.

While differences are present between participant results in every case discussed here, one can see that the general behaviour of the transients are similar. This is a good result for the IAEA ICSP Benchmark in general, as this is the first time where comparable behaviour was seen for all participants. In the 4th technical meeting held in November 2019, which was intended to be the last meeting of the Benchmark, there were significant differences in the evolution of the LOF and LOCA power between participants. For the LOF case, some participants predicted large, coupled power ramps like that shown in Figure A-4, while others predicted smaller power ramps like those shown below. For the LOCA case, there was a large spread in both the magnitude and timing of the peak core power. As such, the results presented show that at minimum, the Specifications have been interpreted correctly, the models are predicting similar transient behaviour, and the coupling methods are comparable for the three participants discussed here.

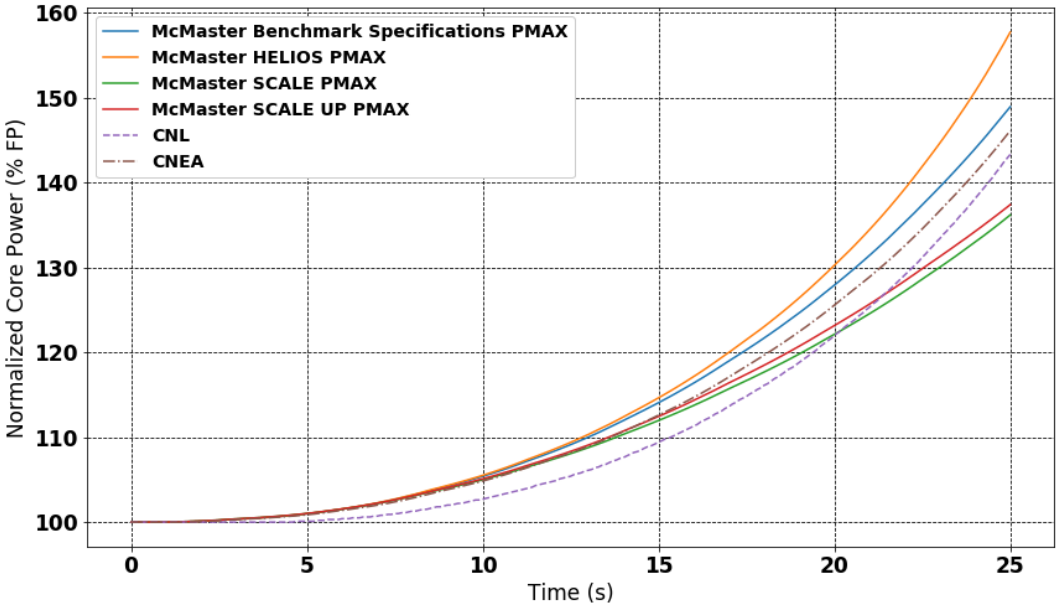

Figure 48. Coupled LOR Transient Core Power Comparison

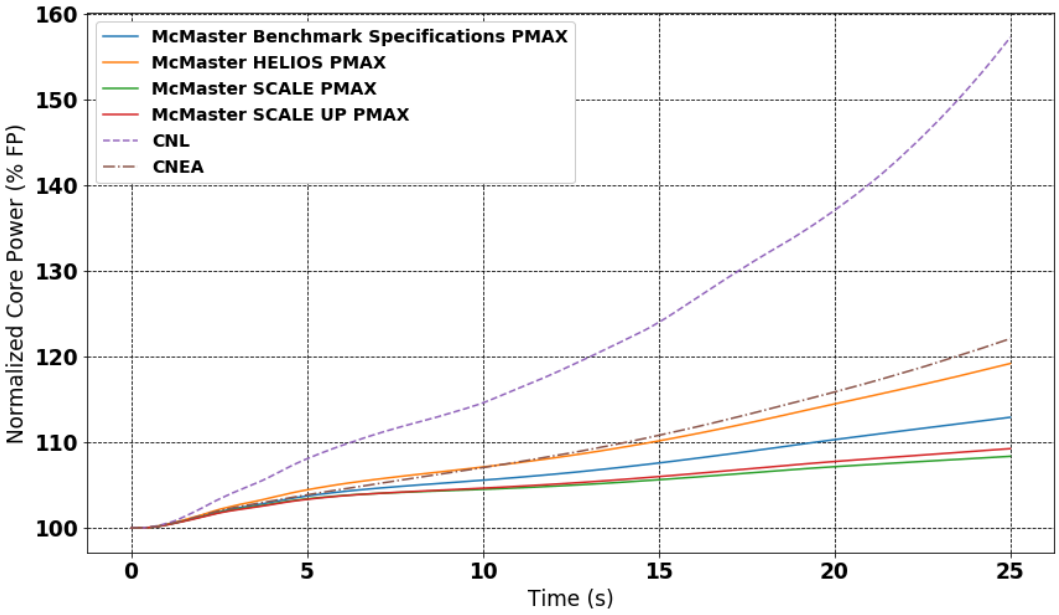

Figure 49. Coupled LOF Transient Core Power Comparison

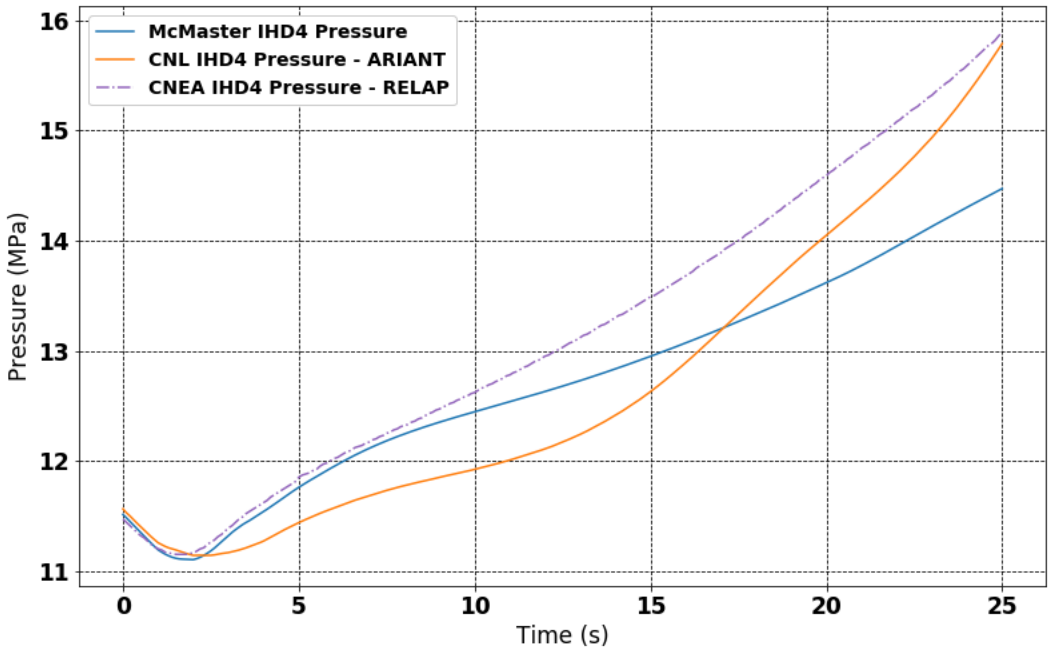

Figure 50. Coupled LOF Transient IHD4 Pressure Comparison

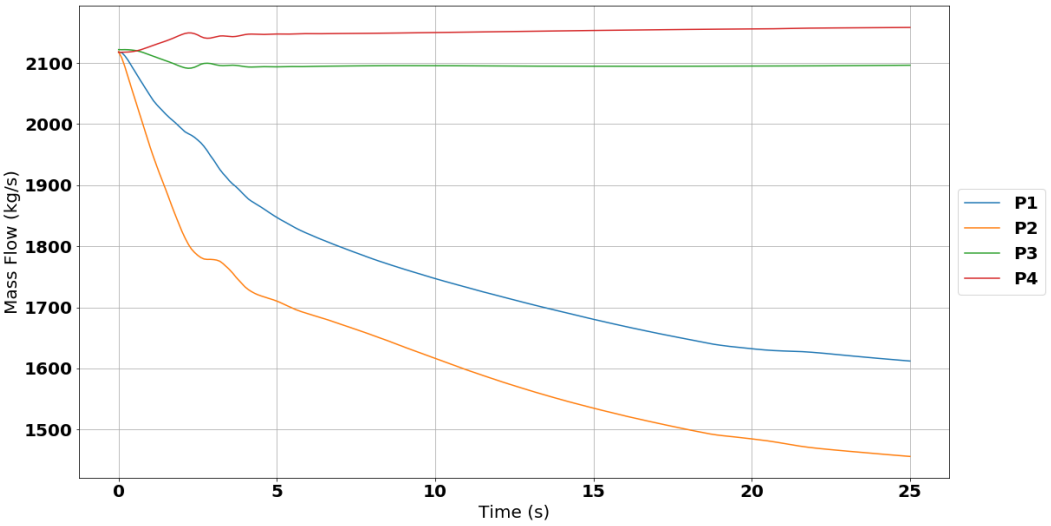

Figure 51. Coupled LOF Transient Pump Mass Flow Rates – McMaster Results

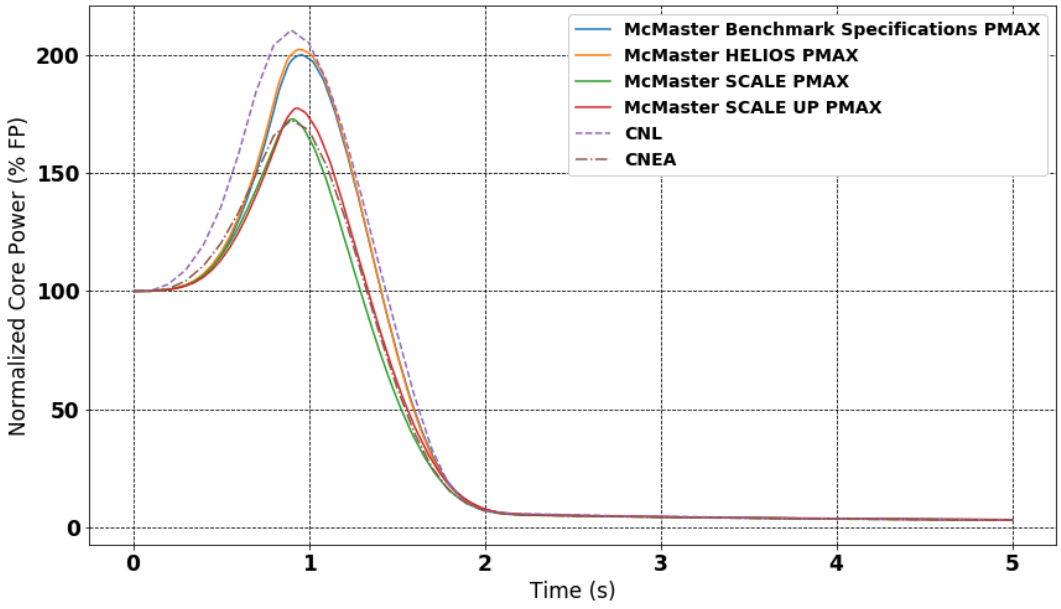

Figure 52. Coupled LOCA Transient Core Power Comparison

4.4.1. Information Exchange Time Step Sensitivity Study

As discussed in Section 3.5.3, the user must set the information exchange time step when running a coupled transient calculation using the methodology developed in this work. This information exchange time step defines how often information is passed between TRACE and PARCS. The impact of this parameter on the core power was investigated for the LOCA and LOF cases, and the results are shown in Figure 53 and Figure 54. For the LOCA case, with an information exchange time step of 0.1 seconds, one can see the piecewise nature of the solution in the first couple time steps of the transient. This behaviour disappears after reducing the exchange time step by a factor of 2, to 0.05 seconds. There is also a small shift in the magnitude and timing of the peak core power towards higher powers earlier in the transient. The difference between the 0.05 and 0.01 second cases are very small, which helps justify the 0.05 second result that was submitted to the IAEA. Beyond 0.01 seconds, the run times become excessively long, and the memory requirements become very large, so these cases were not investigated. Note that these transients were run with a break K-factor of 3.0, not 2.5, and therefore show a slightly smaller peak power than the results shown in Figure 52. For the LOF case, one can see there is no appreciable difference in the results between a 0.1 and a 0.05 information exchange time step, which justifies the 0.1 second result that was submitted to the IAEA. It is expected that these results would hold for the LOR case, as the transient progresses at a similar rate.

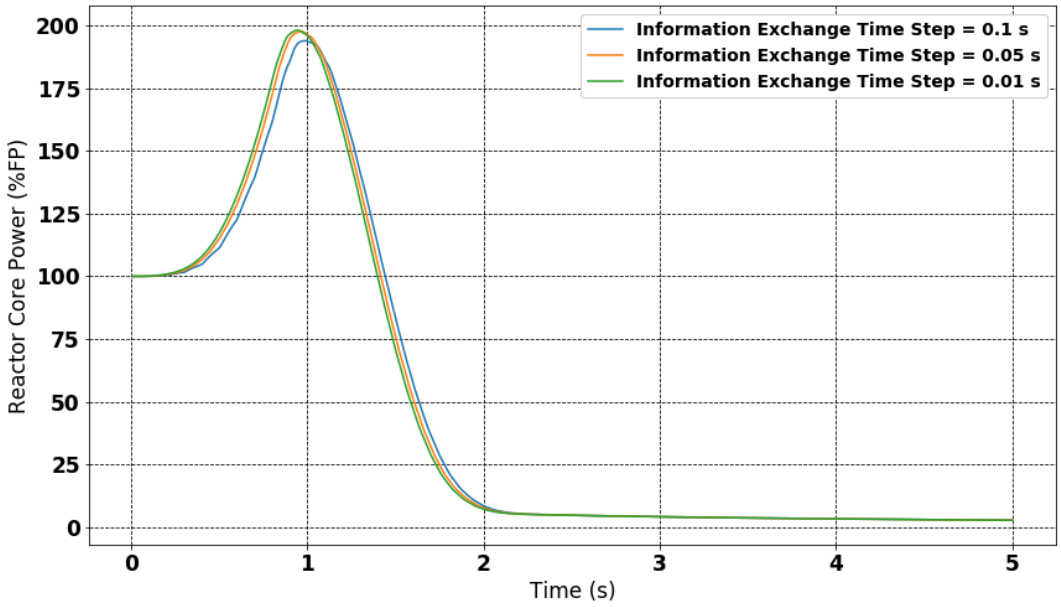

Figure 53. LOCA Time Step Sensitivity Study Core Powers

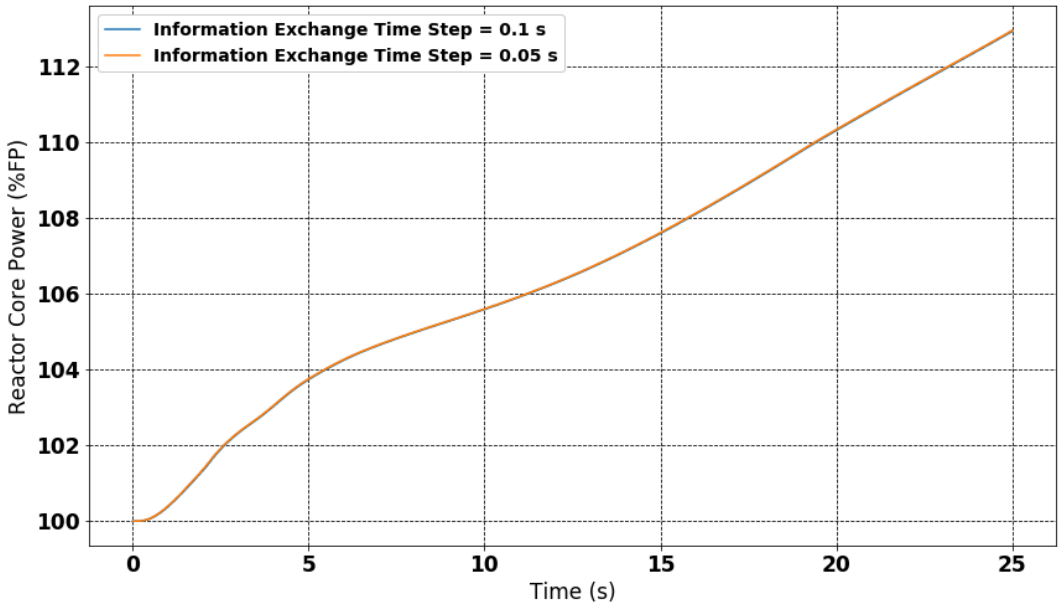

Figure 54. LOF Time Step Sensitivity Study Core Powers

4.4.2. Break K-Factor Sensitivity Study

Extending on the stand-alone break K-factor sensitivity study whose results are shown in Figure 42, a coupled break K-factor sensitivity study was performed to understand how different break flow rates

affect the power pulse magnitude and timing. The results are shown below in Figure 55. All cases were run with the specified cross section data. From inspection of Figure 55, one can see that the break K-factor, and in turn, the break flow rate, have a large impact on the magnitude and timing of the peak core power, with larger break flow rates leading to higher peak powers earlier in the transient. It is worth noting that when a K-factor of 0.0 and 5.0 are sued, the results start to compare well with the CNL and CNEA results, respectively. Given the uncertainty in the true value of the break K-factor [47] [48], additional research into this area may lead to better agreement between the McMaster results, and the CNL/CNEA results.

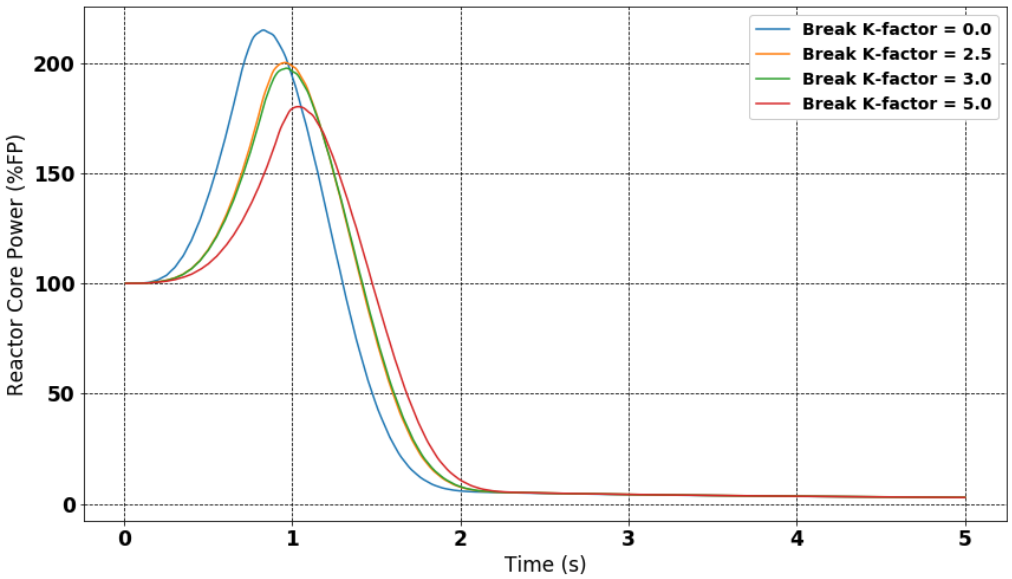

Figure 55. Break K-factor Sensitivity Study

4.4.3. Loss of Flow Sensitivity Study – Pressurizer Remains Connected to System

As mentioned previously, the transients defined in the IAEA ICSP Benchmark are highly stylized and simplified compared to realistic reactor accident scenarios. One major source of discrepancy from real life operation is the isolation of the pressurizer boundary condition from the rest of the system at the start of every transient. With this boundary condition isolated, there is nothing in the system that can help maintain system pressure, as no feed or bleed systems are present. In actual reactor operation, there is a complicated control system acting on the pressurizer that responds to changes in the pressurizer level and acts to keep the system pressure constant. This simplification leads to non-realistic accident progressions, particularly in the LOF case, where the reactor pressure climbs to around 15 MPa in the coupled case with a small increase in reactor power, and almost 20 MPa in the stand-alone case with a very large increase in reactor power. A more realistic accident progression can be obtained by simply leaving the pressurizer connected during the transient. This was investigated as a sensitivity case, and the normalized core power and inlet header 4 pressures are shown in Figure 56 and Figure 57 for the first 15 seconds of the transients. In this case, one can see that the reactor pressure stays low until the power starts to increase rapidly, as expected. TRACE crashes around 17 seconds, due to high

fuel/cladding temperatures, and at this point in the transient, the core power is almost 50, 000 %FP. As such, this transient configuration yields channel powers like those provided for the stand-alone case by the Benchmark Team, indicating that the error in the ARIANT model discussed earlier could be related to an un-isolated pressure boundary condition.

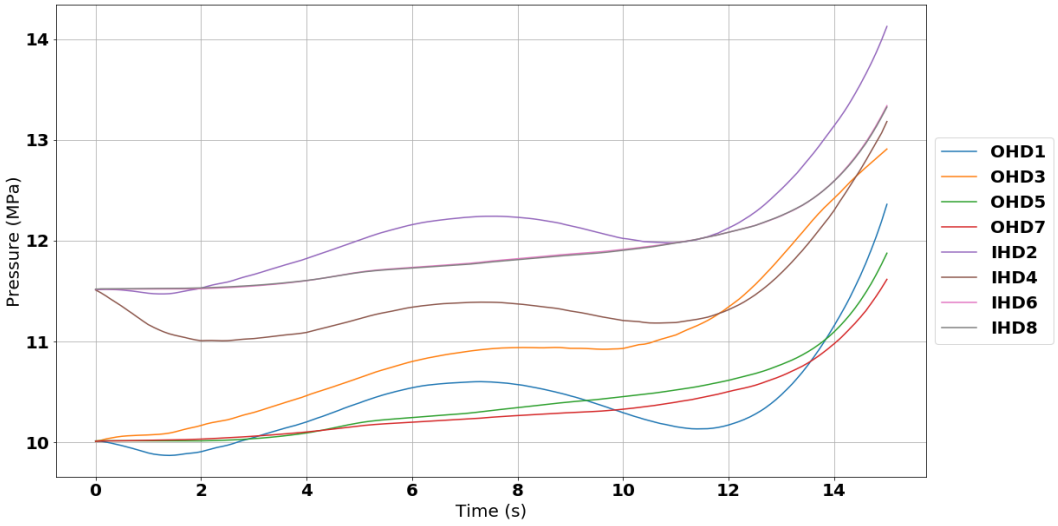

Figure 56. LOF Sensitivity Case (Pressurizer Connected to System) - Header Pressures

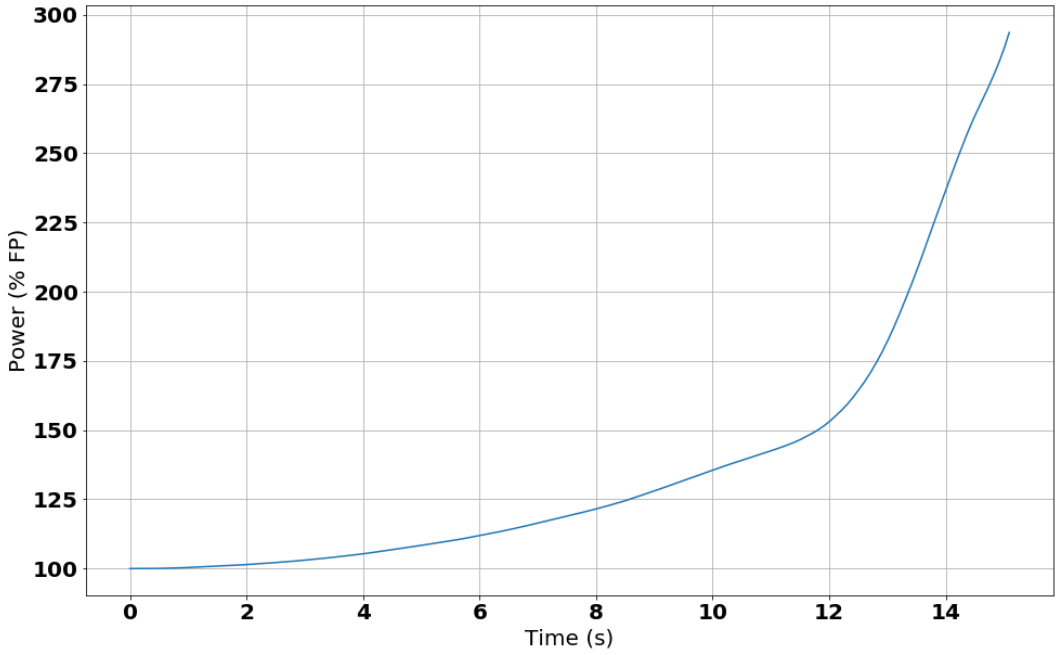

Figure 57. LOF Sensitivity Case (Pressurizer Connected to System) - Normalized Core Power

4.5. Uncertainty Propagation Results

The results of the lattice physics uncertainty propagation runs are described here. As discussed in Section 3.2.3, 59 sets of perturbed 2 group fuel cross sections were generated using the SAMPLER Module of SCALE. This corresponds to the minimum number of runs required to obtain a one sided 95/95 confidence interval for a single parameter, using Wilk's formula [35]. For each set of perturbed 2 group cross section data, steady state Picard Iterations were performed to generate converged initial conditions from which the transient could be initiated. This results in 60 different initial channel power distributions, TH parameter distributions and core reactivities. The mean channel power distribution and the standard deviation are shown in Figure 58 and Figure 59. One can see that the mean power distribution compares well with the other channel power distributions discussed in this dissertation (Figure 28 and Figure 44), as expected. This shows the large dependence of the channel power distribution on the burnup distribution, as different 2 group cross section data and TH distributions yield very similar channel power distributions, with all cases predicting, for example, the same location of the maximum channel power (S9). From Figure 59, one can see that the channel power uncertainty is largest near high powered regions of the core, and smaller near low powered regions. The maximum relative uncertainty in channel power is less than 2%. Figure 60 shows the K-effective distribution for the 60 cases. Comparing to Figure 25, one can see that the spread in the core wide K-effective value is much larger than the spread in the lattice level K-effective. This is expected, due to local variations in TH parameters and burnup, and shows the impact full core calculations have on K-effective uncertainty.

4.5.1. Steady State UP Results

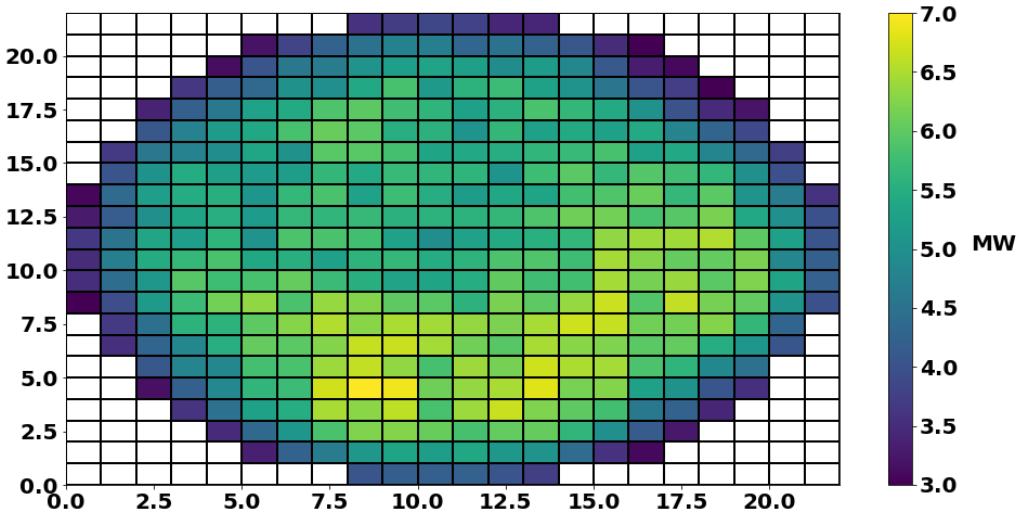

Figure 58. Mean Channel Power Distribution from 60 Converged Steady State PARCS Runs

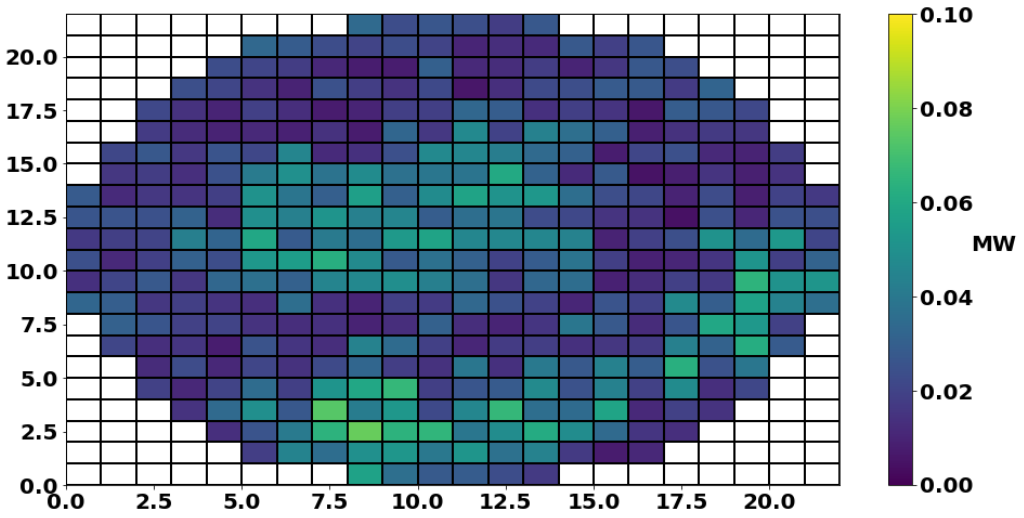

Figure 59. Power Distribution Standard Deviation from 60 Converged Steady State PARCS Runs

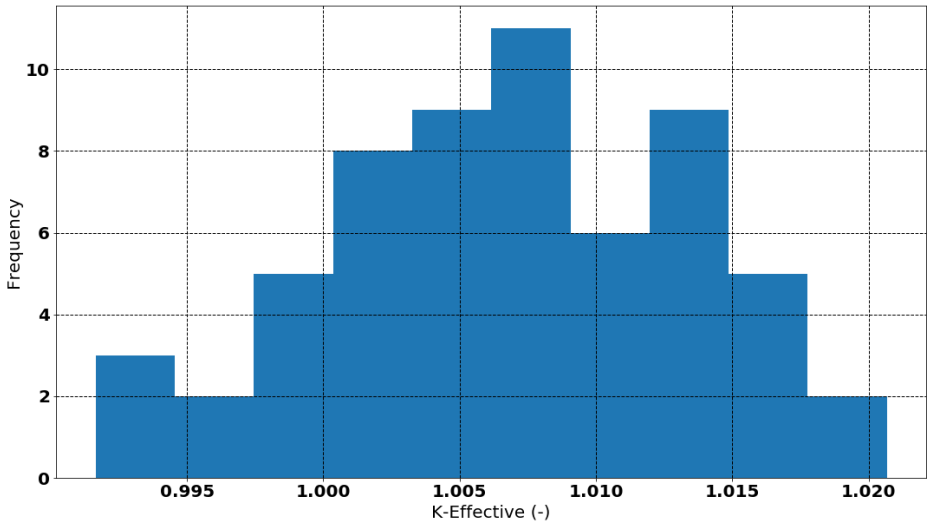

Figure 60. K-eff distribution for 60 Converged Steady State PARCS Runs

4.5.2. Transient UP Results

Core power results for all 60 runs are shown in Figure 61, Figure 62, and Figure 63, for the LOR, LOF and LOCA cases respectively. Figure 64 shows the results of a 30% inlet header break sensitivity study. For each case, the uncertainty in the follows parameters was determined:

1. Integrated Core Power
2. Magnitude and Timing of the Peak Core Power (timing only relevant for the LOCA cases)
3. Maximum Integrated Channel Power (i.e. the channel with the largest integrated power)

4. Magnitude and Timing of the Peak Channel Power

For parameter 1, the total core power in MW was integrated over the full transient, for all 60 cases, and the mean and standard deviation are reported. For parameter 2, the maximum core power and time at which this core power occurs was determined for all 60 cases, and again the mean and standard deviation are reported. For parameter 3, the channel power from all 380 channels was integrated for all 60 runs. The channel with the largest integrated power was then recorded. For all transients, it was found that all 60 runs yielded the same channel, and so the mean and standard deviation for the integrated channel power was computed and reported. Finally, for parameter 4, a search was performed to determine the channel with the highest power in all 60 cases. Again, it was found that for all transients, all runs predicted the same channel. As such, the mean and standard deviation of that channel power, as well as the time at which that power occurs, were computed, and reported. These results are shown in Table 9.

Comparing the peak core power uncertainty between cases, the relative uncertainty (standard deviation divided by the mean) was found to be 5.70%, 2.15%, 4.84%, and 1.60% for the LOR, LOF, 60% LOCA and 30% LOCA, respectively. This indicates that the largest relative spread in peak core power occurs for the LOR case. From inspection of Figure 61, and Figure 62, it is clear that the peak core power always occurs at the end of the transient, at time = 25.0 seconds, for the LOF and LOR cases. However, for the LOCA cases, the actuation of the shutdown system at 120 %FP leads to some uncertainty in the timing of the peak core power. Comparing Figure 63, and Figure 64, one can see that the spread in the time of the peak core power is much larger in the 30% header break case, and this is reflected in the results shown in Table 9, where the relative uncertainty is only 0.65% for the 60% header break case, and 6.77% for the 30% header break case. This suggests that for a LOCA type accident scenario, there is a trade-off between the size of the break, and the magnitude of the uncertainty associated with the peak core power and the timing of the peak core power; i.e. smaller breaks have smaller uncertainty in the peak core power magnitude, but larger uncertainty in when this peak power will occur, while the opposite is true for larger breaks.

Comparing the peak channel power uncertainty between cases, one can see that the results are similar to the peak core power case, with relative uncertainties of 6.12%, 2.75%, 7.84% and 3.02%, for the LOR, LOF, 60% header break LOCA and 30% header break LOCA, respectively. In all cases, the relative uncertainty in peak channel power magnitude is larger than the relative uncertainty in the peak core power magnitude. For the LOF, and 30% LOCA cases, channel S9, which is the highest-powered channel in steady state, was found to be the highest power channel in all transient runs. In these transients, reactivity is inserted asymmetrically on the left side of the core, so it is logical that channel S9 would be the highest power channel at the end of the transients. For the 60% LOCA case, surprisingly, channel S8 was found to have the largest peak channel power. For the LOR case, reactivity is inserted on the right side of the core, and the highest power channel was found to be L18, which corresponds to the location of a withdrawn adjuster rod. Comparing the uncertainty in the time of the peak channel power between the 30% and 60% header break cases, the relative uncertainties are found to be 1.78%, and 2.34%, respectively. For the 60% header break, the uncertainty in the time of the maximum channel power is much larger than the uncertainty in the time of the peak core power, while for the 30% header break problem, it is much smaller. As such, the finding stated above regarding the trade off in uncertainty for peak core power magnitude and timing is not true for the uncertainty in peak channel powers.

Looking at the maximum integrated channel power uncertainty, surprisingly, the channel with the maximum integrated power was not always the same as the channel with the maximum peak power. This can be clearly understood by comparing the S9 and S8 channel power plots for the 60% header break LOCA case, shown in Figure 65. While somewhat difficult to see, the S8 channel powers start the transient with consistently lower powers than channel S9 but have consistently larger peak channel powers. This behaviour can in tun be attributed to the channel grouping shown in Figure A-1, where channel S8 is part of channel group 24, which is connected directly to the broken header (IHD2), while channel S9 is part of channel group 14, which is connected to the intact header (IHD4) in the broken loop. From the stand-alone LOCA animation results, shown in Figures E-6 to E-12, one can see that there is significantly more vapour formation in the pass connected to the broken header.

Comparing the integrated core power, the relative uncertainties were found to be 1.86%, 1.02%, 2.09%, and 1.63% for the LOR, LOF, 60% header break LOCA and 30% header break LOCA, respectively. In general, the uncertainty in integrated core power is smaller than the uncertainty in the magnitude of the peak core power. A surprising result is the larger mean integrated core power in the 30% header break case than the 60 % header break case. Intuitively, one would expect that a transient which has a larger peak core power would also have a larger integrated core power. However, because the core power rises faster in the 60 % header break, shutoff rod actuation occurs sooner and the core is shutdown faster, with the core powers from all runs dropping below 10 %FP by around 2 seconds in the 60% header break case, and 2.5 seconds in the 30% header break case. The same behaviour can be seen in the maximum integrated channel power results, with the 30% header break case yielding higher integrated channel powers. This shows that from an integrated core power perspective, smaller break loss of coolant accidents can be more limiting from a safety analysis point of view than large break loss of coolant accidents.

Finally, for all cases, one can see that the mean core power is slightly higher than the unperturbed reference run. This implies a small bias towards higher core powers in the perturbed data sets. This difference could likely be attributed to the relatively small number of perturbed cross sections that were generated through the SAMPLER module, and it is expected that as more runs are performed, the difference between the mean and reference cases would shrink.

Table 9. Uncertainty Propagation Results: Integrated Core Power, Peak Core Power Magnitude and Timing, Maximum Integrated Channel Power, and Magnitude and Timing of Peak Channel Power Mean and Standard Deviation

Case	Integrated Core Power (MJ)	Peak Core Power (%FP)	Time of Peak Core Power (s)	Max Integrated Channel Power (MJ)	Peak Channel Power (MW)	Time of Peak Channel Power (s)
LOR	56 106 ± 1044	138.65 ± 7.90	25.0 ± 0.0	198.69 ± 4.62 (O18)	10.29 ± 0.63 (L18)	25.0 ± 0.0
LOF	52 713 ± 540	109.45 ± 2.35	25.0 ± 0.0	184.18 ± 2.81 (S9)	7.69 ± 0.20 (S9)	25.0 ± 0.0
LOCA – 60% break	4 244 ± 89	180.28 ± 8.72	0.920 ± 0.006	18.45 ± 0.69 (S9)	15.56 ± 1.22 (S8)	1.067 ± 0.025
LOCA – 30% break	4 607 ± 75	143.89 ± 2.3	1.404 ± 0.095	18.90 ± 0.39 (S9)	11.59 ± 0.35 (S9)	1.454 ± 0.026

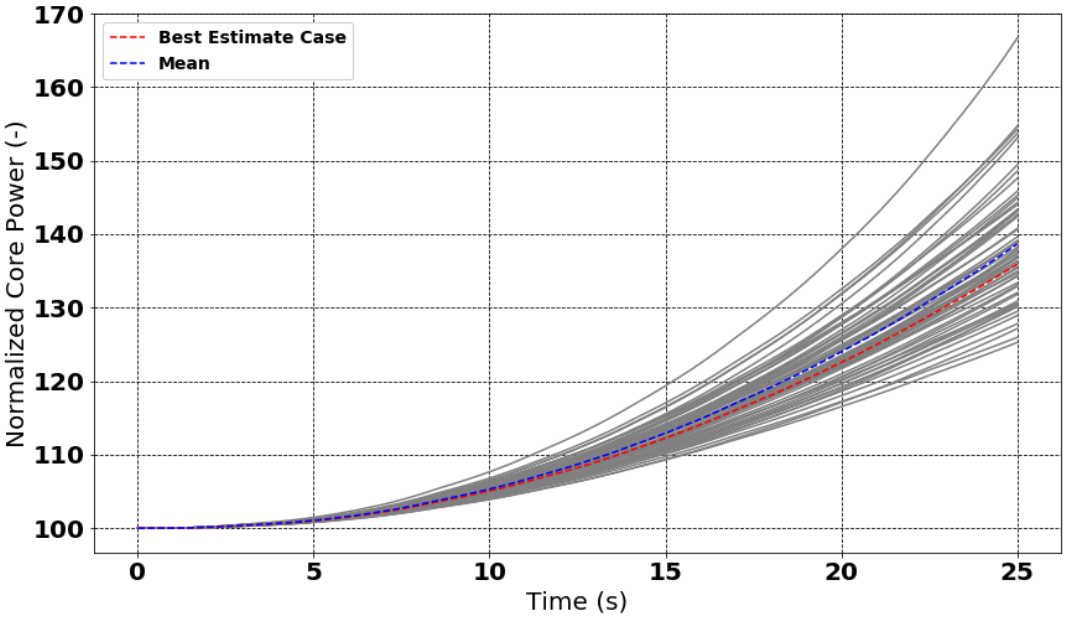

Figure 61. LOR Uncertainty Propagation Results - Core Power

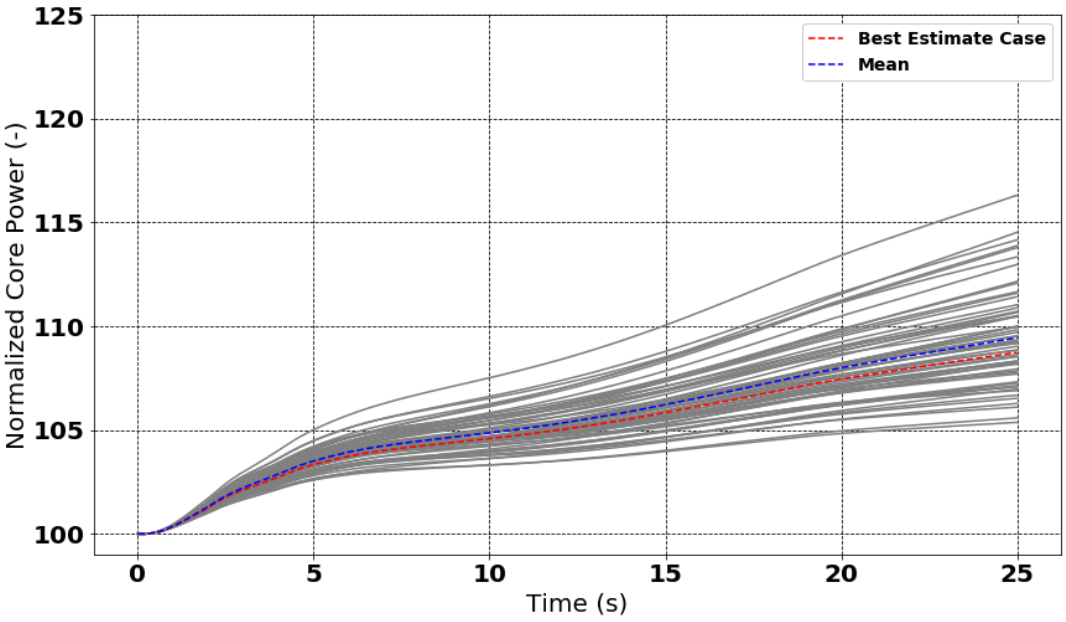

Figure 62. LOF Uncertainty Propagation Results - Core Power

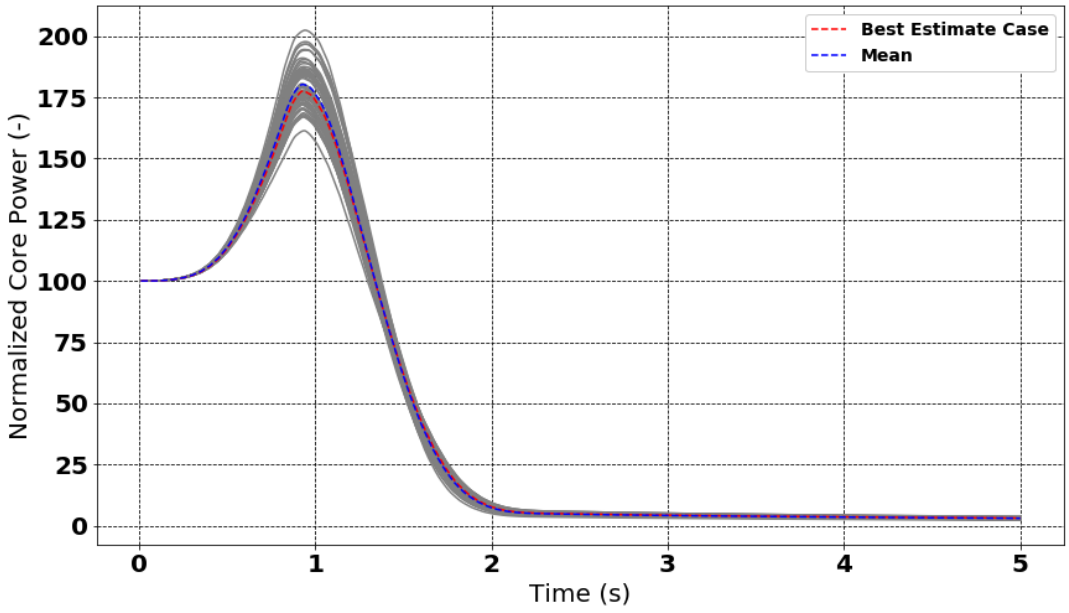

Figure 63. 60% Inlet Header Break LOCA Uncertainty Propagation Results - Core Power

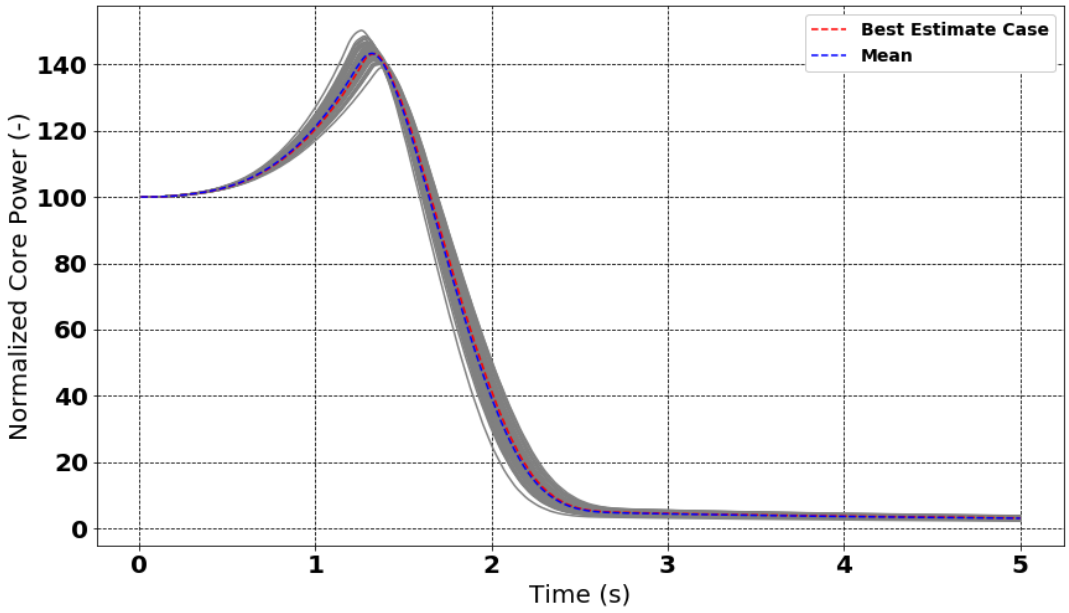

Figure 64. 30% Inlet Header Break LOCA Uncertainty Propagation Results - Core Power

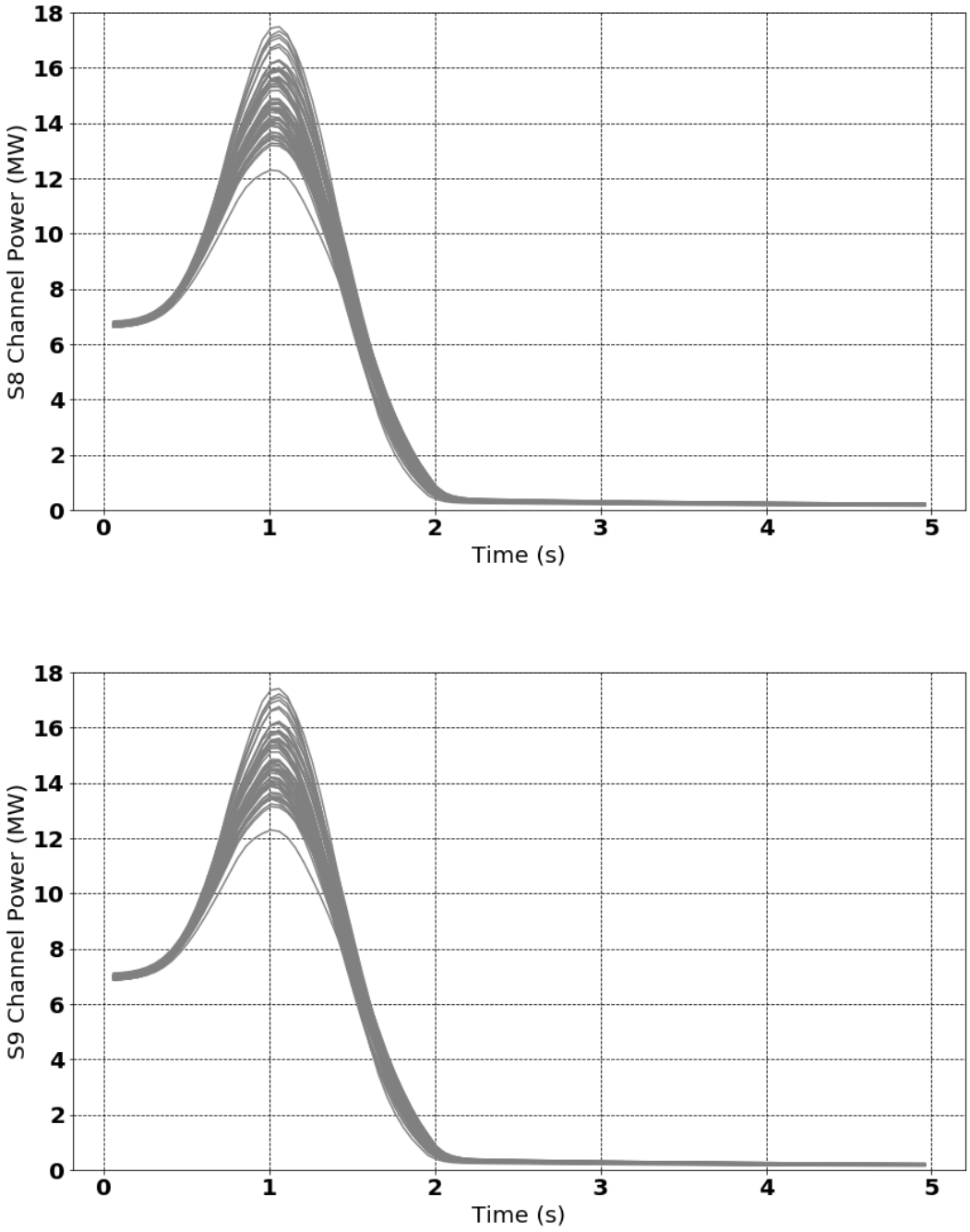

Figure 65. Channel S8 (top) and S9 (bottom) Powers from the 60% Inlet Header Break Uncertainty Propgoation Run

4.6. Sensitivity Study Results

Sensitivity studies were performed on the 60% inlet header break LOCA case with SCALE UP cross section data. While fundamental nuclear data uncertainty could only be propagated through lattice physics calculations for the SCALE UP cross section data, any of the cross section data sets discussed in this work could be used in the type of sensitivity study performed here. The SCALE UP data was chosen for consistency with the uncertainty propagation work. The goal of this sensitivity study was to produce a PKPIRT for the 60% inlet header break LOCA case considered in this work. The methodology that was selected to perform the sensitivity study is similar to the linear response method outlined in [37]. In this method, a Figure of Merit (FOM e.g. peak core power, integrated channel power, etc.) is chosen and an initial list of relevant phenomena and parameters are generated, typically from expert judgement. Several perturbations are then performed for each parameter or phenomena, the coupled accident scenario is run for each perturbation, and the FOM is computed. The expected result is a linear change in the FOM as a function of the change in the perturbed parameter. The slope of the FOM as a function of the perturbed parameter or phenomena then gives can indication of the sensitivity of the FOM to the parameter or phenomena, with slopes of larger magnitude showing higher sensitivity than slopes of smaller magnitude.

Some details of the study are provided in Table 10. The left-hand column shows the phenomena and parameters that were considered. This serves as the identification phase of the methodology outlined above. The plant parameters and relevant physical phenomena that are identified in Table 10 were selected through discussion with the Benchmark Team and Dr. Novog. The second column indicates the model parameter that was perturbed to capture the identified plant parameter or phenomena. The following 3 columns then indicate the reference value of the model parameter, the perturbed values, and the "perturbation factors". The perturbation factors were computed for all cases by equation 4-1.

$$Perturbation\ Factor = \frac{Perturbed\ Value - \ Reference\ Value}{Reference\ Value} \qquad (4-1)$$

The perturbation factors were used to normalize the results so that the slope of the FOM vs. the perturbation factor can be compared between cases. This in turn allows the parameters and phenomena to be ranked quantitatively.

In this work, two different FOMs were selected: 1. Integrated S9 channel power, and 2. Peak S9 channel power. These FOMs were a natural extension of the uncertainty propagation study discussed above. The majority of the S9 channel power results from the sensitivity study can be seen in Figure 66. The two cases which are not shown, coolant temperature and header pressure, have very little deviation from the reference solution, less so than the fuel temperature case shown in the bottom right.

The results of the sensitivity study shown in Figure 66 were then used to generate PKPIRTs for both FOMs. These can be seen in Table 11 and Table 12, respectively. The FOM is plotted against the perturbation factors in Figure 67 and Figure 68 for the same cases shown in Figure 66. In both PKPIRTs, parameters that relate to shutdown system actuation and effectiveness, as well as coolant density reactivity, rank near the top, while fuel temperature and coolant temperature feedback rank low. This is consistent both with initial expectation, and the results shown in [37], which ranks coolant void reactivity and timing of the first SOR gate, as the most sensitive and 7th most sensitive parameters/phenomena out of a list of over 40 for the hot bundle enthalpy during a large break loss of

coolant accident in a Pickering unit. An unexpected result is low ranking of the break K-factor and break size in the integrated S9 channel power FOM PKPIRT, and the high ranking in the peak S9 channel power PKPIRT. This result can be explained from examination of Figure 66. For both the break size and break K-factor perturbations, when the break flow rate increases (due to a smaller K-factor or larger break), the core power increases at a faster rate, leading to higher peak channel powers. However, this also leads to earlier shutoff rod actuation, and subsequent shutdown. These two effects effectively cancel each other such that the total integrated power is almost the exact same across all cases (similar to the above discussion on 30% vs. 60% header break loss of coolant accidents). In fact, for the break K-factor, the reference value of 2.5 yields the largest integrated power. This explanation is consistent with the results shown in Table 12, where these two parameters rank near the top.

Table 10. Sensitivity Study Perturbation Parameters and Values

Phenomena or Parameter	Perturbed Parameter	Reference Value(s)	Perturbed Value(s)	Perturbation Factors
CD, FT, and CT Feedback	2 group cross section PDCSCs	N/A	N/A	-0.5, -0.3, -0.2, -0.15, 0.15, 0.2, 0.3, 0.5
ADJ, LQZ and SOR Absorption	2 Group Incremental Cross Sections	N/A	N/A	-0.5, -0.3, -0.2, -0.15, 0.15, 0.2, 0.3, 0.5
SOR Delay	Delay in SOR movement after SCRAM power has been reached	0.25 s	0.2, 0.23, 0.27, 0.30 s	-0.2, -0.08, 0.08, 0.2
Break Size	Flow area (and hydraulic diameter) of the inlet header (IHD2) break	0.0645 m^2	0.05805, 0.061275, 0.067725, 0.07095 m^2	-0.1, -0.05, 0.0, 0.5, 0.1
Inlet Header Temperature	Secondary Side Pre-heater temperature	513.23 °K	508.23, 511.23, 515.23, 518.23 °K	-9.7466E-3, -3.8986E-3, 3.8986E-3, 9.7466E-3
Inlet Header Pressure	Pressurizer Pressure	9.925 MPa	9.5, 9.7, 10.3, 10.5 MPa	-0.04282, -0.02267, 0.03778, 0.0579
Break K-factor	Inlet header break K-factor	2.5	0.0, 1.5, 3.5, 5.0	-1, -0.4, 0.0, 0.4, 1
SCRAM Power	Reactor power which initiates the SCRAM signal	120%FP, or 2400 MW	115, 117, 119, 121, 123, 125 %FP	-0.05, -0.03, -0.01, 0.0, 0.01, 0.03, 0.05

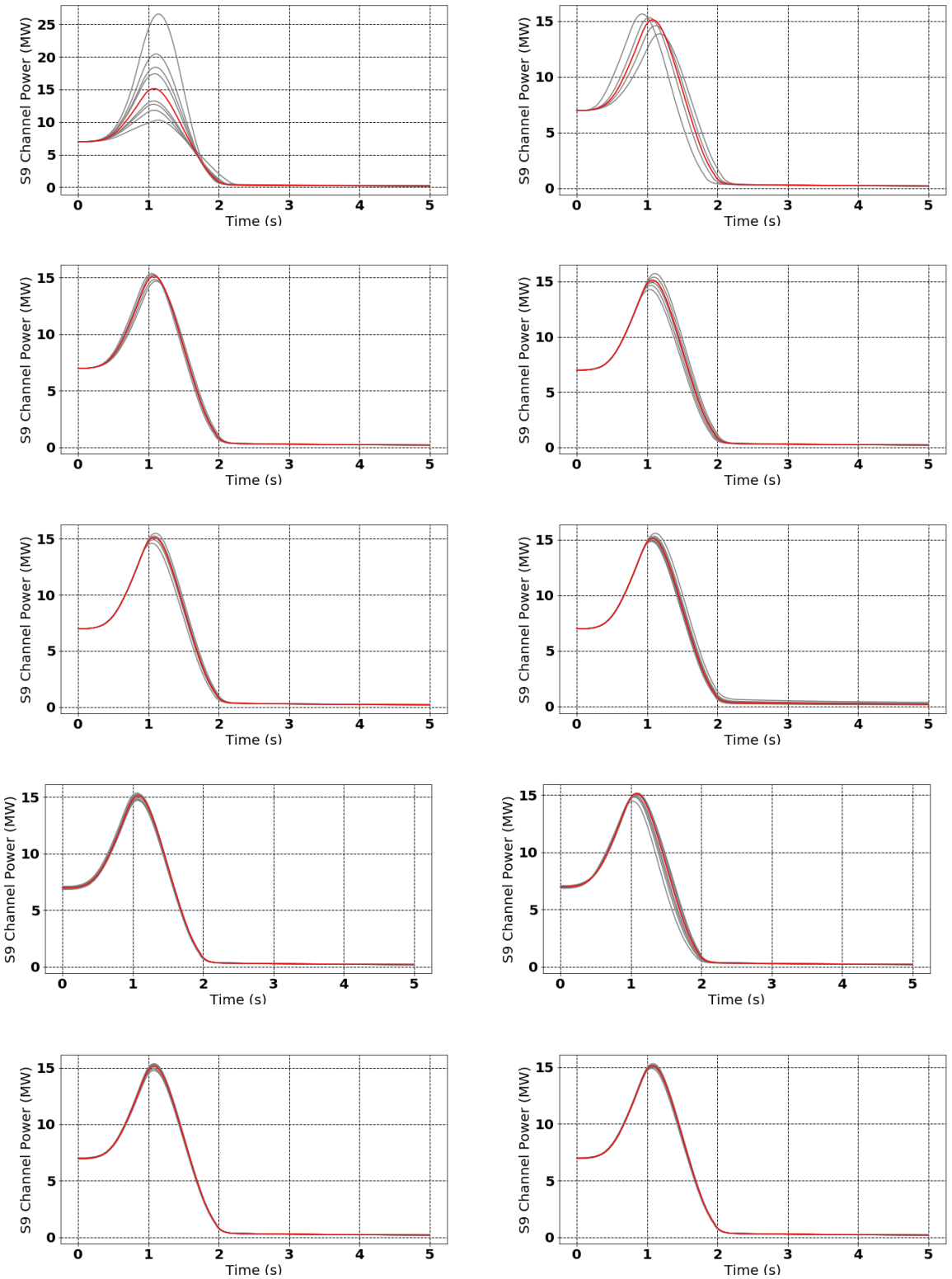

Figure 66. S9 Channel Power Results from Sensitivity Study Run: 1. Coolant Density, 2. Break K-Factor, 3. Break Size, 4. SCRAM Power, 5. SOR Delay, 6. SOR Incremental, 7. Initial Power, 8. ADJ Incremental, 9. LQZ Incremental and 10. Fuel Temperature

Table 11. LOCA Sensitivity Study Results for the S9 Integrated Channel Power FOM

Case	Mean Integrated Channel Enthalpy (MJ)	Channel Enthalpy Standard Deviation (MJ)	Slope (MJ/Fraction of Range)	Co-efficient of Determination	Rank
SCRAM Power	18.61	0.64	18.77	0.990	1
CD PDCSC	19.59	3.52	10.58	0.906	2
SOR Delay	18.65	0.47	3.05	0.990	3
SOR Incremental	18.83	0.73	-2.20	0.915	4
ADJ Incremental	18.49	0.67	2.02	0.918	5
Inlet Header Pressure	18.68	0.08	1.17	0.35	6
LQZ Incremental	18.68	0.22	0.67	0.949	7
Break Size	18.65	0.08	0.58	0.337	8
FT PDCSC	18.67	0.16	-0.47	0.911	9
Break K-factor	18.47	0.3	0.30	0.588	10
CT PDCSC	18.62	0.09	0.22	0.528	11

Table 12. LOCA Sensitivity Study Results for the S9 Peak Channel Power FOM

Case	Mean Maximum Channel Power (MW)	Maximum Channel Power Standard Deviation (MW)	Slope (MW/Fraction of Range)	Co-efficient of Determination	Rank
CD PDCSC	16.21	5.1	15.51	0.931	1
SCRAM Power	15.03	0.48	13.85	0.987	2
Break Size	15.03	0.29	3.59	0.959	3
SOR Delay	15.06	0.34	2.19	0.988	4
Break K-factor	14.91	0.70	-0.89	0.951	5
Inlet Header Pressure	15.11	0.07	0.83	0.230	6
SOR Incremental	15.11	0.24	-0.73	0.927	7
LQZ Incremental	15.08	0.21	0.66	0.971	8
ADJ Incremental	14.95	0.23	0.58	0.655	9
FT PDCSC	15.09	0.13	-0.39	0.954	10
CT PDCSC	15.04	0.12	0.35	0.829	11

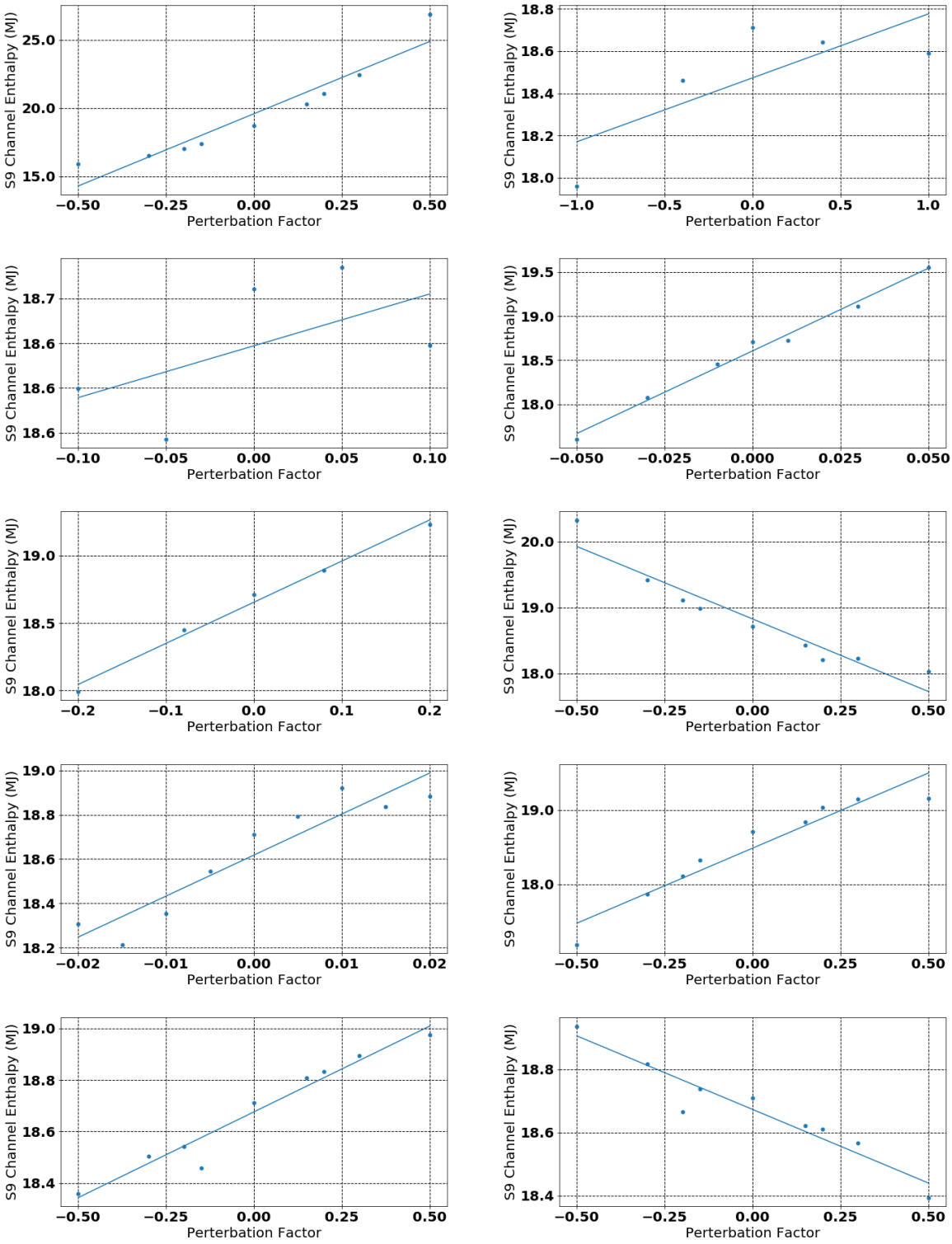

Figure 67. Sensitivity Case Results for the Integrated S9 Channel Power FOM: 1. Coolant Density, 2. Break K-Factor, 3. Break Size, 4. SCRAM Power, 5. SOR Delay, 6. SOR Incremental, 7. Initial Power, 8. ADJ Incremental, 9. LQZ Incremental and 10. Fuel Temperature

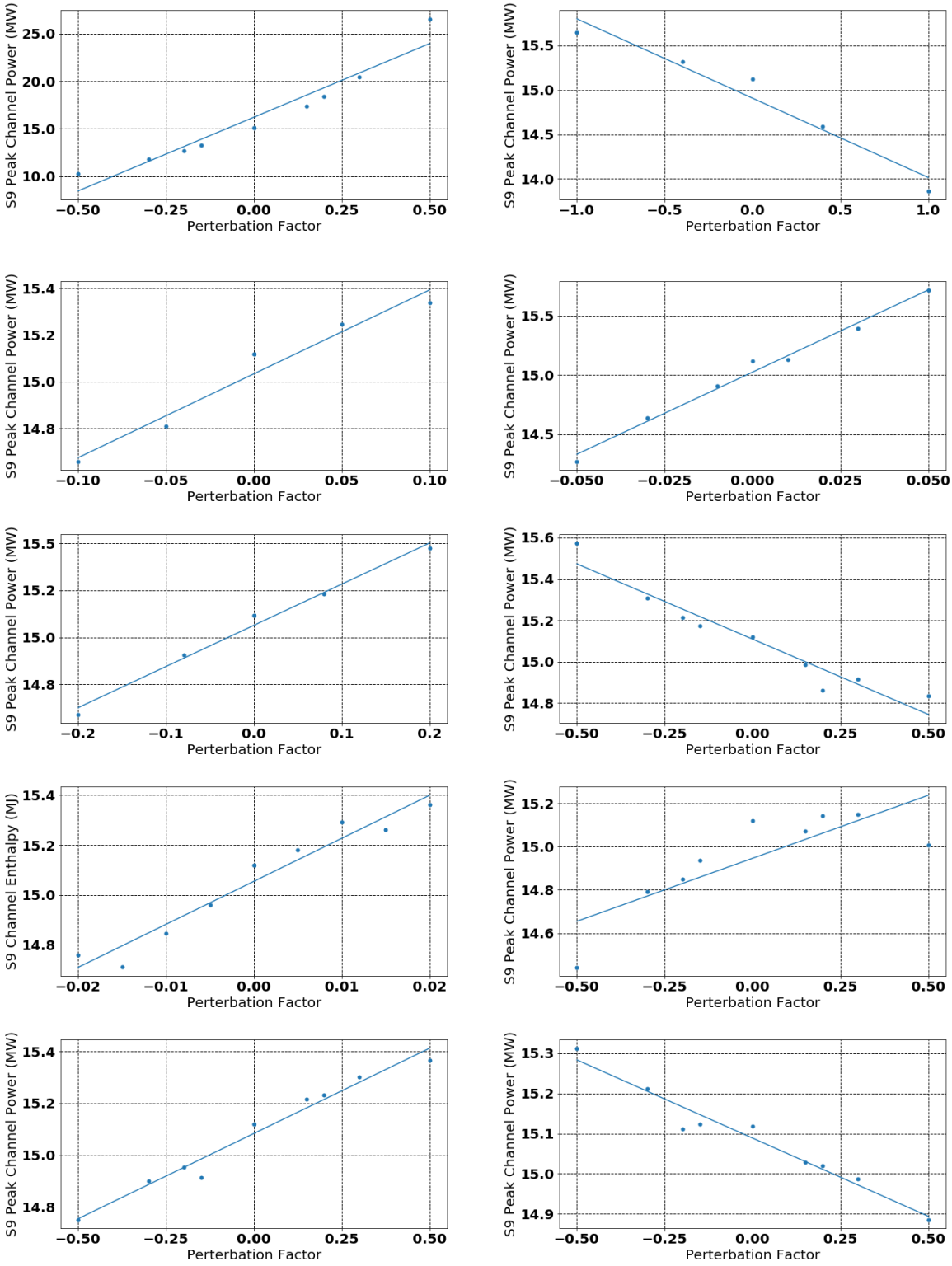

Figure 68. Sensitivity Case Results for the Peak S9 Channel Power FOM: 1. Coolant Density, 2. Break K-Factor, 3. Break Size, 4. SCRAM Power, 5. SOR Delay, 6. SOR Incremental, 7. Initial Power, 8. ADJ Incremental, 9. LQZ Incremental and 10. Fuel Temperature

5. Conclusions and Future Work

This thesis dissertation documents McMaster's contribution to the IAEA ICSP on Benchmarks for Multi-physics Simulation of PHWR Transients. Select results from 3 accident scenarios; loss of regulation (LOR – withdrawal of 2 adjuster rods), loss of forced flow (LOF - single pump trip), and loss of coolant (LOCA - 60% inlet header break), are presented for the coupled solutions and stand-alone physics tests, and are compared with the final results from 2 other participants (CNL and CNEA). In addition, propagation of fundamental nuclear data uncertainty through lattice physics calculations and coupled transients was performed and the uncertainty in the coupled PARCS/TRACE core power was presented. This phase of the work is beyond the scope of the current IAEA ICSP Benchmark, and provides preliminary results for potential follow up Benchmarks, which will investigate an integrated uncertainty analysis (including thermal-hydraulics and plant uncertainty, in addition to fundamental nuclear data uncertainty) for one or more of the above transients. Additional discussion on this point is provided below. This potential follow up Benchmark was also the driver for the sensitivity analysis, and PKPIRT development described in this dissertation, where the quantitative rankings could be used by the Benchmark Team to help determine which parameters require consideration in an integrated uncertainty analysis, and which parameters may be ignored. Further discussion on this is also provided below. The result of all the work performed in this thesis is a methodology that can be used to perform uncertainty and sensitivity analysis of coupled transients with the SCALE, PARCS and TRACE analysis tools. This methodology is summarized in Figure 69, which is a slightly modified version of the same figure that was included in a BEPU2020 submission [49]. In Figure 69, the step numbers are associated with following aspects of the methodology:

- Step 1 – 2 Group Cross Section Generation and Verification
- Step 2 - Reactor Physics (diffusion) and System Thermal-Hydraulics Model Preparation and Verification
- Step 3 – Generation of Coupled Steady State Initial Conditions
- Step 4 – Uncertainty Propagation or Sensitivity Analysis Transient Runs

5.1. Uncertainty and Sensitivity Analysis Discussion

5.1.1. Summary of Uncertainty and Sensitivity Analysis Results

Three important results were obtained through comparison of the mean and standard deviation in the figures of merit defined in Section 4.5.2:

1. The uncertainty in the magnitude of the peak core power is proportional to the size of the break, while the uncertainty in the time of the peak core power is inversely proportional with the size of the break, for large break loss of coolant accidents (see Section 2.3.3 for large break LOCA definition). Or in other words, smaller breaks have a smaller uncertainty in the peak core power magnitude, but a larger uncertainty in when this peak power will occur, while the opposite is true for larger breaks. However, this conclusion does not hold true for the peak channel power, with comparable uncertainties in the time of the break, for both the 30% and 60% header break cases.
2. The magnitude and uncertainty of the integrated core power and integrated channel powers are not sensitive to the size of the break. From Table 9, one can see the magnitude and uncertainty

of both the integrated core power, and maximum integrated channel power, are comparable between the 30% and 60% header break cases. While the 60% header break case has a much larger peak core power, it takes longer for the core power to reach its maximum value in the 30% header break case.

3. For all accident scenarios, the same channel location was predicted for the peak channel power, and the maximum integrated channel power, for all 60 runs. However, in the 30% LOCA and LOR cases, the channel locations were not the same. Or in other words, different FOMs can lead to different limiting channel locations, but for a given FOM, the same limiting channel location was always predicted.

These results are well known in industry but are not well documented in the open literature. Furthermore, the first two results show that counterintuitively, smaller break loss of coolant accidents can be more limiting than larger break loss of coolant accidents from a safety and licensing point of view, leading to a lower reactor power setpoint during normal operation.

The PKPIRTs shown in Table 11 and Table 12 extend on the LOCA uncertainty analysis work, and show that both the peak core power and maximum integrated channel power FOMs are most sensitive to coolant void reactivity, and parameters relating to shutoff rod effectiveness (drop delay, incremental cross section etc.). However, the results also show that parameters related to break mass flow rate only have a large impact on the peak core power and are less important when considering the maximum integrated channel power. This is due to a trade off between the magnitude of the peak core power, and the time at which the shutoff rods are actuated, as shown in Figure 55 and Figure 66, with smaller break mass flow rates resulting in lower peak core powers, but a longer transient. These results directly support the conclusions described above for loss of coolant accident uncertainty.

5.1.2. Uncertainty Propagation in a Benchmark Setting - Feasibility Study

While the uncertainty propagation work described in this dissertation is the first known attempt in academia to propagate fundamental nuclear data uncertainty through coupled PARCS/TRACE transients for CANDU safety analysis applications specifically, the approach that was used is not novel. There are many examples in literature ([50] and [51]) where perturbed 2 group cross sections are generated in SAMPLER and used to run a series of full core coupled calculations to generate an output uncertainty. However, the work presented here also shows the feasibility of performing this type of analysis in a Benchmark setting. One of the major challenges when performing coupled uncertainty analysis is the computational resources required. This is of concern in several areas of the problem: 1. SAMPLER Lattice physics calculations, 2. Steady state Picard iterations, and 3. Coupled transients. In all three areas, both run time and memory requirements are of concern, although the later is more easily mitigated. In terms of run time, SAMPLER lattice physics calculations are by far the most intensive, followed by Picard iterations and lastly coupled calculations. When running SAMPLER, a transport solution must be generated for each burnup step of each branch of each perturbed run. For 36 burnup steps, a minimum of 4 branches (reference, coolant density, coolant temperature and fuel temperature) and 59 perturbed sets of input cross section data, in addition to the reference calculation, a total of 8 496 transport calculation must be performed. In this work, a 32 CPU computer was used to run 30 cases in parallel, which required over 128 Gb of RAM, and approximately 5 days of run time, even after performing some minor optimization of the transport calculation. While this is not a great result, it is likely that this calculation would only be performed once, so all participants use the same set of perturbed cross

sections, and such a computation could reasonably be performed on a non-cluster machine. Regarding the computational resources for Picard iterations and coupled calculations, the steady state Picard iterations tend to dominate the runtime, due to the long TRACE steady state calculations discussed in Section 3.1.4. Even still, all 60 steady state and coupled calculations could be run in under 12 hours, on an 8-core machine. This shows the benefit of being able to obtain converged steady state initial conditions with only 3 iterations.

5.1.3. Follow-up Sensitivity Analysis

The PKPIRTs developed through sensitivity analysis are intended to provide a preliminary ranking of key phenomena and parameters that could be considered in an integrated uncertainty analysis. However, the analysis is far from all encompassing, and many important parameters were not considered due to time constraints, or an in-ability to effectively perturb the parameter or phenomena in question. Thermal-hydraulics perturbations were limited to break flow modelling, and system pressure, while the following parameters, at minimum, should be considered in an integrated uncertainty analysis:

- Pump operating characteristics (rated flow, rated head, homologous pump curves, etc.)
- Secondary side boundary conditions (secondary side heat transfer coefficients and temperature)
- Interfacial drag
- Interfacial heat transfer

The former two parameters were not considered due to time constraints, while the later two parameters could not be perturbed without performing source code modifications for each run, which was not possible at the time of the analysis. Furthermore, it is expected that most system-thermal hydraulics codes do not allow these phenomena to be perturbed directly from an input deck and will also require source code modification, making this a difficult parameter to include in a Benchmark setting. This is an unfortunate reality, as the sensitivity analysis performed in [37] for a loss of coolant accident in a Pickering NGS reactor ranked interfacial drag as the second most sensitive parameter for hot bundle enthalpy, which is closely related to the maximum integrated channel power.

On the reactor physics side of the problem, perturbations were limited to 2 group fuel cross sections, incremental cross section, partial derivative cross section coefficients, and shut-off rod timing. This is more inclusive list, but can still be extended upon by perturbing parameters such as:

- TH Invariant data (delayed neutron fractions and pre-curser decay rates, Xe-135 effective yield etc.)
- Burnup distribution
- Reflector cross sections
- Control rod positioning

Again, comparing to the results shown in [37], the total delayed neutron fraction was ranked as the 4th most sensitive parameter.

5.2. General Benchmark Recommendations - Specifications

Over the course of the Benchmark activities, experienced was gained interpreting and translating the Specifications, and some lessons learned are shared here. In the IAEA ICSP Benchmark, the Specifications were based directly on ARAINT and NESTLE-C input decks for the thermal-hydraulics and

diffusion side of the problem, respectively. It is the opinion of the author that this is a problematic approach for a Benchmark type setting, particularly for the thermal-hydraulics side of the problem, for the following reasons:

1. Given the significant differences in system thermal-hydraulics input requirements, and calculation methods, only participants with system thermal-hydraulics codes very similar to that used by the Benchmark Team can translate the Specifications directly without any additional modifications or calibration. The modifications and subsequent calibration (if necessary) are time consuming, but more importantly, lead to potential differences in system code input decks, which could be missed or hidden when only steady results are compared. A good example of a short coming in the Specifications is break flow modelling. Originally, the Benchmark Team wanted to prescribe a critical flow model to all participants. This was immediately problematic, as some participants system codes simply did not have the ARIANT specific correlation available. Furthermore, the Specifications defined inlet header geometries that were severely modified from realistic header dimensions (length reduced, and flow area increased by a factor of ~9). In this case the break flow modelling correlation used by ARIANT was not sensitive to the header geometry, but it was realised in the 4th technical meeting that the correlations used by other codes would be. These two issues were resolved by providing participants realistic header dimensions and allowing participants to use whatever critical flow correlation they felt was applicable. However, no information was provided on the break characteristics, other than the size of the break. At very minimum, there must be consistency in the location of the break, i.e. a side break or end break, and it is possible that there is still inconsistency between participants on this aspect of the header break problem, even in the final set of submitted results.
2. On the physics side of the problem, basing the Specifications on the NESTLE-C input deck was less problematic, and the only real issue was related to the 2 group cross section data provided to participants. Again, this data was formatted specifically for use in NESTLE-C, and it was found that there are some small differences between the input requirements of NESTLE-C, and PARCS. In this case, it is recommended that the raw 2 group cross sections produced by HELIOS be provided to participants instead. It is unclear why this wasn't done from the start, as the data was available for participants to use (it was obtained for the work discussed here), and contains a full set of branch partial derivative cross section coefficients, which would add accuracy to the problem without any considerable increase in runtime.
3. Providing Specifications based on an input deck is an error prone process. First, errors present in the input decks themselves may be missed and propagated to the Specifications. This occurred on the thermal-hydraulic side of the problem, where one ARIANT channel group had a volume 10x large than intended, and while the geometry defined in the Specifications did not contain this error, the pressure drop results that were used to modify and calibrate the system models were generated with this error. Second, errors may occur while translating the input deck into the Specifications. This happened on both side of the problem; an ARIANT component that played a major role in pump rundown transient was omitted from the Specifications entirely, and errors were present in the core shape (382 channels instead of 380 are still defined in the final Specifications) and control rod positions on the reactor physics side of the problem.
4. It is the opinion of the author that providing Specifications in this manor detracts from the overall applicability of the Benchmark to safety analysis methods used in industry, as the problem becomes more about matching the solution generated by the Benchmark Team , than

performing a rigorous safety analysis. Furthermore, as no experimental data was provided, it puts pressure on the Benchmark Team to provide an accurate solution for participants to compare against, at all levels of the problem. In this case, the Benchmark Team was new to coupled transient analysis, like many other participants, and this constant reliance on the Benchmark Team to make clarifications and updates lead to delays in the Benchmark progress.

As mentioned above, it is the opinion of the author that an improved approach would be to provide plant specific data, which could be used to generate the system thermal-hydraulics and diffusion input decks, and raw cross section data that could be processed directly by each participant. While this may seem like a very time consuming task, given the amount of re-work associated with any change to the Specifications, and the number of changes that were made to the Specifications over the course of the Benchmark, it is possible that both approaches could be similar in terms of participants time requirements. Furthermore, this would better align the IAEA ICSP Benchmark with industry practises, and best practises used in other Benchmarks, like the UAM or MPCMIV Benchmarks run through the OCED NEA.

5.3. SCALE Coolant Void Reactivity Discrepancy

As shown in Figure 18, when lattice physics calculations were performed using the NEWT and TRITON modules of the SCALE code package, the coolant void reactivity that was predicted was markedly smaller for every coolant density branch, than the corresponding HELIOS result. In response to this discrepancy, a literature review was performed to see if similar results were obtained by other researchers using NEWT/TRITON. To start, reference [45] provides a detailed overview of CANDU lattice physics calculations in NEWT/TRITON, SERPENT and HELIOS (the HELIOS cross section described in this reference are the same those mentioned throughout this work). Unfortunately, lattice level CVR results like those shown in Figure 18 were not reported in this work. However, full core diffusion based (NESTLE-C) CVR values were computed, like the perturbation study results shown in Table 4, and these results are shown in Table 40 in [45]. In this case, NEWT/TRITON predicted a higher CVR than HELIOS and SERPENT, around 17 mk vs. 16 mk. However, the coolant density perturbation was set to 0.001 g/cm^3 in this reference, where NEWT/TRITON predictions require careful application of the Dancoff factors within dan2pitch. There are no mentions of Dancoff factors in this report. Therefore, it is difficult to understand the differences between the CVRs in this thesis and that work.

Reference [52] presents lattice physics CVR results for a modified 37 element CANDU fuel bundle. The modification being referred to is a small change in the diameter of the central fuel element. This modification was introduced in an attempt to reduce linear element rating and resolve safety analysis issues and is not expected to have a large impact on CVR. In this work, WIMS-IST was used to perform lattice physics calculations, and CVRs of ~15.2, and 12.5 and 12.3 mk were obtained at 0 burnup, mid-burnup (3000 MW.days/tonne) and close to discharge burnup (6000 MW.days/tonne). In this case, the results are close to the 0.01 g/cm^3 branch results shown in Figure 18, with an ~1 mk bias relative to the NEWT/TRITON results, possibly because of differences in the underlying nuclear data. Unfortunately, it is unclear what coolant density perturbation was used in this work, and as a result, it is unclear whether like for like calculations are being compared.

Finally, Reference [53] compares the coolant void reactivity obtained using Polaris, KENO, and NEWT, with various self shielding options in SCALE. In this work, when NEWT was used with BONAMI, CVR

results similar to those shown in [52] were obtained, with a 0 burnup value of ~15 mk, and mid to end burnup values near 13 mk. Again, It is unclear what coolant density perturbation was used in this work, however, discussion with the author indicated that it was much less than 0.001 g/cm^3 and special treatment of the Dancoff factors was required to obtain reasonable results using dan2pitch at this density. The CVR results obtained with other codes such as KENO, matched more closely to the HELIOS results.

This literature review suggests that there may have been an error in the lattice physics calculations that were performed early in this work, perhaps in the Dancoff factor treatment or dan2pitch, leading to a 1-2 mk bais in the CVR compared to other NEWT calculations, and a 3-4 mk bias relative to HELIOS calculations. This is an important area of consideration and should be investigated in the future. Another finding from the literature review is that most studies on CVR are limited to a single coolant density perturbation at very low densities and often, only a couple of burnup points. This is a gap in the open literature, and there could be value in performing a rigorous comparison of the CVR predicted by several lattice physics codes, as a function of burnup, over a large range of coolant density perturbations, like what is shown Figure 18. The need to examine a larger range of coolant density perturbations is supported by the results of the LOCA case analyzed in this wok, where the minimum coolant density never dropped below 0.01 g/cm^3, and was typically on the order of 0.02 to 0.03 g/cm^3.

5.4. Areas for Future Work

Areas for future research were identified throughout this thesis dissertation. Often, these would be small issues with the TRACE or PARCS models that were developed. Of these, the most important issue is the discrepancy in the TRACE results for the LOF case. Some major areas for future research are listed here:

1. Internal TRACE/PARCS Coupling: TRACE and PARCS were originally designed to be natively coupled through the TRACE External Communications Command (ECC) Module. Here, the user defines a channel mapping, similar to what is shown in Figure A-1, in a MAPTAB file, and information is exchanged between codes through computer memory. The advantage of this approach is that the internal time steps of both codes, and the information exchange time step, are determined automatically. Research on internal coupling has already begun at McMaster, by Simon Younan, using the TRACE and PARCS models developed in this work.
2. There is no RRS (Reactor Regulating System) present in the models developed in this work. Any control rod movement that was performed during steady state verification was done manually by re-defining their position in the input deck. In the internal coupling work mentioned above, and RRS model is also being developed to model liquid zone and adjuster rod movement during steady state Picard iterations and during coupled transients.
3. The uncertainty propagation study that was performed only considered the propagation of fundamental nuclear data uncertainty through the coupled calculations. Future research could investigate an integrated uncertainty analysis, extending on the models and perturbed 2 group cross section data that was generated in this work. The PKPIRTs developed in the sensitivity analysis could be used as a starting point.
4. As mentioned above, the sensitivity analysis that was performed is far from all encompassing, and additional parameters and phenomena could easily be investigated by adding additional cases to the list defined in Table 10.

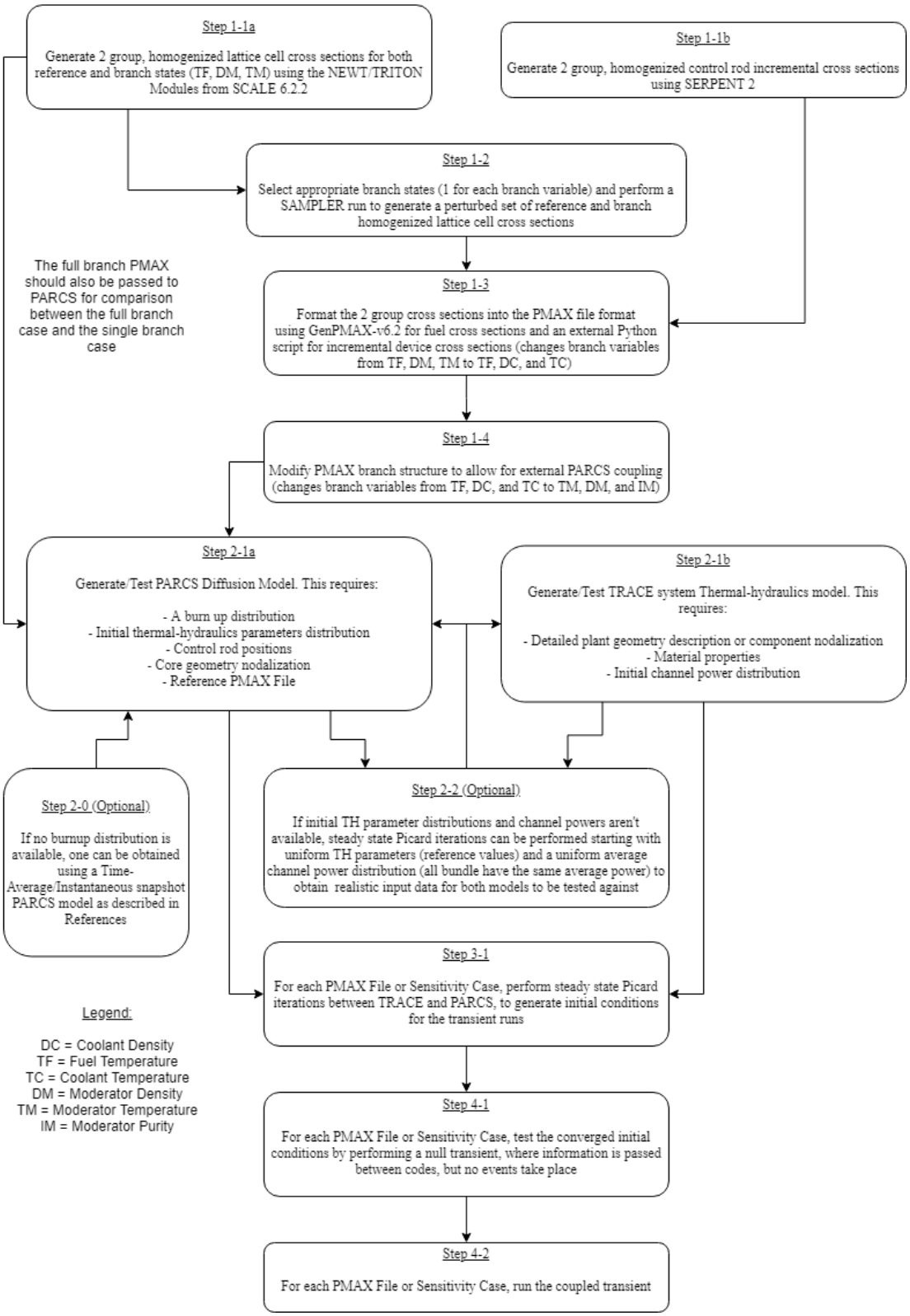

Figure 69. Overview of SCALE/TRACE/PARCS Transient Uncertainty Propagation and Sensitivity Analysis Methodology

6. Works Cited

[1] M. Krause and A. Trottier, "IAEA-TECDOC-XXXX - Numerical Benchmarks for Multiphysics Simulation of Pressurized Heavy Water Reactor Transients," International Atomic Energy Agency, XXXX, In Progress.

[2] K. Ivanov *et al.*, "Benchmarks for Uncertainty Analysis in Modelling (UAM) for the Design, Operation and Safety Analysis of LWRs - Volume 1: Specification and Support Data for Neutronics Cases (Phase 1)," OECD NEA, NEA/NSC/DOC(2013)7, Nov. 2013.

[3] K. Ivanov, T. Beam, and A. J. Baratta, "Pressurized Water Reactor Main Steam Line Break (MLSB) Benchmark - Volume 1: Final Specifications," OECD NEA, NEA/NSC/DOC(99)8, Apr. 1999.

[4] J. Solis, K. Ivanov, and B. Sarikaya, "Boiling Water Reactor Turbine Trip (TT) Benchmark - Volume 1: Final Specifications," OECD NEA, NEA/NSC/DOC(2001)1, Feb. 2001.

[5] B. Ivanov, K. Ivanov, P. Groudev, M. Pavlova, and V. Hadjiev, "VVER-1000 Coolant Transient Benchmark - Phase 1: Final Specifications," OECD NEA, NEA/NSC/DOC(2002)6, 2002.

[6] V. Snell, "Chapter 13 Reactor Safety/Safety Analysis," in *The Essental CANDU, a Textbook on the CANDU Nuclear Power Plant Technology*, University Network of Excellence in Nuclear Engineering (UNENE).

[7] D. Hummel, "Coupled Neutronic-Thermalhydraulic Transient Behaviour of a Pressure Tube Type Supercritical Water-cooled Reactor," Thesis, McMaster, 2015.

[8] F. Salaun, "Assessment and Optimization of the Canadian SCWR reactivity control systems through reactor physics and thermal-hydraulics coupling," Thesis, McMaster, 2018.

[9] A. C. Morreale, "Analysis of Transuranic Mixed Oxide Fuel in a CANDU Nuclear Reactor," Thesis, McMaster, 2013.

[10] A. Trottier, N. Aydemir, and A. Vasic, "ICSP on Numerical Benchmarks for Multiphysics Simulation of PHWR Transients - Draft Specifications for the Steady-State," Canadian Nuclear Laboratories, Dec. 2018.

[11] "High-Level Radioactive Waste," *Canadian Nuclear Safety Commission*, Jan. 15, 2020. http://nuclearsafety.gc.ca/eng/waste/high-level-waste/index.cfm (accessed Aug. 02, 2020).

[12] J. J. Duderstadt and L. J. Hamilton, *Nuclear Reactor Analysis*. New York; London; Sydney; Toronto John Wiley and Sons, Inc., 1976.

[13] D. G. Cacuci, Ed., *Handbook of Nuclear Engineering: Vol. 1: Nuclear Engineering Fundamentals; Vol. 2: Reactor Design; Vol. 3: Reactor Analysis; Vol. 4: Reactors of Generations III and IV; Vol. 5: Fuel Cycles, Decommissioning, Waste Disposal and Safeguards*, 2010 edition. New York ; London: Springer, 2010.

[14] M. A. Jessee and M. D. DeHart, "NEWT: A NEW Transport Algorithm for Two-Dimensional Discrete-Ordinates Analysis in Non-Orthogonal Geometries." Oak Ridge National Laboratory, Aug. 2016.

[15] M. A. Jessee *et al.*, "POLARIS - 2D Light Water Reactor Lattice Physics Module." Oak Ridge National Laboratory.

[16] B. T. Rearden and M. A. Jessee, "SCALE 6.2.2 Code System User's Manual." Oak Ridge National Laboratory, Feb. 2017.

[17] J. V. Donnelly, "WIMS-CRNL: A user's manual for the Chalk River version of WIMS," Atomic Energy of Canada Ltd., AECL--8955, 1986.

[18] G. Marleau, A. Hebert, and R. Roy, "A User Guide for DRAGON Version4." Ecole Polytechnique de Montreal, Aug. 26, 2016.

[19] A. Hébert, *Applied Reactor Physics*. Presses inter Polytechnique, 2009.

[20] J. Leppanen, "The Serpent Monte Carlo code: Status, development and applications in 2013," *Ann. Nucl. Energy*, vol. 82, pp. 142–150, Jun. 2015.

[21] X-5 Monte Carlo Team, "MCNP - A General Monte Carlo N-Particle Transport Code, Version 5 - Volume 1: Overview and Theory." Los Alamos National Laboratory, Apr. 24, 2003.
[22] L. M. Petrie *et al.*, "KENO: A Monte Carlo Criticality Program." Oak Ridge National Laboratory, Aug. 2016.
[23] T. Downar, D. Lee, Y. Xu, and T. Kozlowski, "PARCS v2.7 U.S. NRC Core Neutronics Simulator Theory Manual." Purdue University, School of Engineering.
[24] A. Ward, Y. Xu, and T. Downar, "GenPMAX - v6.2 User's Manual - Code for Generating the PARCS Cross Section Interface File PMAXS." University of Michigan, Jul. 2016.
[25] A. C. Morreale, M. R. Ball, D. R. Novog, and J. C. Luxat, "The effects of fuel burnup on incremental cross sections in actinide fuels in CANDU reactors,".
[26] M. Dahmani, G. Marleau, and E. Varin, "Effect of burnup on ACR-700 3-D reactivity devices cross sections," Jul. 2006.
[27] S. Bajorek, "TRACE V5.0 Patch 5 Theory Manual: Field Equations, Solution Methods and Physical Models." United States Nuclear Regulatory Commission, 2017.
[28] "RELAP5/MOD3.3 Code Manual Volume II: Input Requirements." Information Systems Laboratories, Mar. 2006.
[29] B. N. Hanna, "CATHENA: A thermalhydraulic code for CANDU analysis," *Nucl. Eng. Des.*, vol. 180, no. 2, pp. 113–131, Mar. 1998, doi: 10.1016/S0029-5493(97)00294-X.
[30] M. N. Avramova and K. N. Ivanov, "Verification, validation and uncertainty quantification in multi-physics modeling for nuclear reactor design and safety analysis," *Prog. Nucl. Energy*, vol. 52, no. 7, pp. 601–614, Sep. 2010, doi: 10.1016/j.pnucene.2010.03.009.
[31] J. Peltonen, T. Kozlowski, and D. Truc-Nam, "Spatial Coupling for Coupled Code Safety Analysis of BWR Design Basis Accidents," *Int. Conf. React. Phys. Nucl. Power Sustain. Resour.*, Jan. 2008, Accessed: Jun. 08, 2019.
[32] J. D. Hales *et al.*, "Advanced multiphysics coupling for LWR fuel performance analysis," *Ann. Nucl. Energy*, vol. 84, pp. 98–110, Oct. 2015, doi: 10.1016/j.anucene.2014.11.003.
[33] R. N. Bratton, M. Avramova, and K. Ivanov, "OECD/NEA BENCHMARK FOR UNCERTAINTY ANALYSIS IN MODELING (UAM) FOR LWRS – SUMMARY AND DISCUSSION OF NEUTRONICS CASES (PHASE I)," *Nucl. Eng. Technol.*, vol. 46, no. 3, pp. 313–342, Jun. 2014, doi: 10.5516/NET.01.2014.710.
[34] K. Ivanov, E. Sartori, E. Royer, S. Langenbuch, and K. Velkov, "Validation of Coupled Thermal-Hydraulic and Neutronics Codes for Safety Analysis by International Cooperations," *Nucl. Technol.*, vol. 157, no. 2, pp. 177–195, Feb. 2007, doi: 10.13182/NT07-A3811.
[35] F. D'Auria, H. Glaeser, S. Lee, J. Misak, M. Modro, and R. Shultz, "Safety Reports Series No. 52 - Best Estimate Safety Analysis for Nuclear Power Plants: Uncertainty Evaluation," International Atomic Energy Agency, 2008.
[36] G. E. Wilson and B. E. Boyack, "The role of the PIRT process in experiments, code development and code applications associated with reactor safety analysis," *Nucl. Eng. Des.*, vol. 186, no. 1, pp. 23–37, Nov. 1998, doi: 10.1016/S0029-5493(98)00216-7.
[37] L. Blake, G. Gavrus, J. Vecchiarelli, and J. Stoklosa, "Best Estimate Plus Uncertainty Analysis of LBLOCA for a Pickering B CANDU Reactor," Jan. 2010, pp. 1463–1472, doi: 10.1115/FEDSM-ICNMM2010-31018.
[38] D. R. Novog and F. Bao, "Phenomena Identification and Ranking for Loss of Forced Circulation Accidents in a CANDU Reactor," *12th Int. Meet. Nucl. React. Therm. Hyraulics*, 2007.
[39] K. Groves and D. R. Novog, "Preliminary TRACE Thermal-Hydraulic Results for the IAEA ICSP on Numerical Benchmarks for Multi-Physics Simulation of PHWR Transients," presented at the 43rd Annual Canadian Nuclear Society's/Canadian Nuclear Association's Student Conference, Jun. 2019.

[40] G. Bill, M. Tayal, and M. Gacesa, "The Essential CANDU, A Textbook on the CANDU Nuclear Power Plant Technology. Chapter 17 - Fuel," University Network of Excellence in Nuclear Engineering (UNENE).
[41] D. L. Hagrman and G. A. Reymann, "MATPRO-Version 11: a handbook of materials properties for use in the analysis of light water reactor fuel rod behavior," Idaho National Engineering Lab., Idaho Falls (USA), NUREG/CR-0497; TREE-1280, Feb. 1979. doi: 10.2172/6442256.
[42] S. Bajorek, "TRACE V5.0 Patch 5 User's Manual Volume 2: Modeling Guidelines." United States Nuclear Regulatory Commission, 2017.
[43] M. A. Jessee, D. Wiarda, K. T. Clarno, U. Mertyurek, and K. Bekar, "TRITON: A Multiprupose Transport, Depletion, and Sensitivity and Uncertainty Analysis Module." Oak Ridge National Laboratory, Feb. 2017.
[44] M. D. Tucker and D. R. Novog, "The Impact of Fueling Operations on Full Core Uncertainty Analysis in CANDU Reactors," *J. Nucl. Eng. Radiat. Sci.*, vol. 6, no. 3, Jul. 2020, doi: 10.1115/1.4045485.
[45] A. Trottier and H. S. Abdel-Khalik, "Multigroup Reference and Convariance Cross Section Data Libraries for NESTLE-C," Canadian Nuclear Safety Comission, CNSC Research Project R598.2, Sep. 2019.
[46] W. A. Wieselquist *et al.*, "SAMPLER: A Module for Statistical Uncertainty Analysis with SCALE Sequences." Oak Ridge National Laboratory, Aug. 2016.
[47] A. K. Majumdar, "Mathematical modelling of flows in dividing and combining flow manifold," *Appl. Math. Model.*, vol. 4, no. 6, pp. 424–432, Dec. 1980, doi: 10.1016/0307-904X(80)90174-2.
[48] A. W. Badar, R. Buchholz, Y. Lou, and F. Ziegler, "CFD based analysis of flow distribution in a coaxial vacuum tube solar collector with laminar flow conditions," *Int. J. Energy Environ. Eng.*, vol. 3, no. 1, p. 24, Sep. 2012, doi: 10.1186/2251-6832-3-24.
[49] K. Groves and D. Novog, "A TRACE/PARCS Transient Coupling and Nuclear Data Uncertainty Propogation Methodology for a Loss of Coolant Accident Scenario in a CANDU Style Reactor," *Best Estim. Plus Uncertain. Int. Conf.*, May 2020.
[50] D. Huang and H. S. Abdel-Khalik, "Application of Cross Sections Uncertainty Propagation Framework to Light and Heavy Water Reactor Systems," *J. Nucl. Eng. Radiat. Sci.*, vol. 6, no. 1, Jan. 2020, doi: 10.1115/1.4045032.
[51] K. Zeng, J. Hou, K. Ivanov, and M. A. Jessee, "Uncertainty Quantification and Propagation of Multiphysics Simulation of the Pressurized Water Reactor Core," *Nucl. Technol.*, vol. 205, no. 12, pp. 1618–1637, Dec. 2019, doi: 10.1080/00295450.2019.1580533.
[52] R. Pristavu and M. Rizoiu, "Reactor Physics Assessment of Modifed 37-element CANDU Fuel Bundle," RATEN Institute for Nuclear Research, Romania, 2016.
[53] S. Younan and D. Novog, "Extension and preliminary validation of the Polaris lattice physics code for CANDU analysis," *Nucl. Eng. Des.*, vol. 361, p. 110540, May 2020, doi: 10.1016/j.nucengdes.2020.110540.

Appendix A - IAEA ICSP Benchmark Thermal-Hydraulics Specifications

The numbers in the fuel channel map below correspond to the system-thermal hydraulics fuel channel groups. For example, Channel D11 belongs to fuel channel group CHAN11, and Channel A14 corresponds to fuel channel group CHAN35. The number of fuel channels were group varies between 11 and 19. The "Front order" and "Back order" labels refer to the direction of fuelling.

	1	2	3	4	5	6	7	8	9	10	11	12	13	14	15	16	17	18	19	20	21	22
A									25	15	25	35	45	35								
B						25	15	25	15	25	15	45	35	45	35	45	35					
C					25	15	25	15	25	15	25	35	45	35	45	35	45	35				
D				25	15	25	15	25	15	21	11	41	31	45	35	45	35	45	35			
E			25	15	25	15	25	11	21	11	21	31	41	31	41	35	45	35	45	35		
F			15	25	15	21	11	21	11	21	11	41	31	41	31	41	31	45	35	45		
G		16	26	16	26	11	21	11	21	11	21	31	41	31	41	31	41	36	46	36	46	
H		26	16	26	16	21	11	21	11	21	11	41	31	41	31	41	31	46	36	46	36	
J	26	16	26	16	22	12	22	12	22	12	22	32	42	32	42	32	42	32	46	36	46	36
K	16	26	16	22	12	22	12	22	12	22	12	42	32	42	32	42	32	42	32	46	36	46
L	26	16	26	12	22	12	22	12	22	12	22	32	42	32	42	32	42	32	42	36	46	36
M	16	26	16	23	13	23	13	23	13	23	13	43	33	43	33	43	33	43	33	46	36	46
N	26	16	26	13	23	13	23	13	23	13	23	33	43	33	43	33	43	33	43	36	46	36
O	16	26	16	26	13	23	13	23	13	23	13	43	33	43	33	43	33	43	36	46	36	46
P		16	26	16	24	14	24	14	24	14	24	34	44	34	44	34	44	34	46	36	46	
Q		27	17	27	17	24	14	24	14	24	14	44	34	44	34	44	34	47	37	47	37	
R			27	17	27	17	24	14	24	14	24	34	44	34	44	34	47	37	47	37		
S			17	27	17	27	17	24	14	24	14	44	34	44	34	47	37	47	37	47		
T				17	27	17	27	17	24	14	24	34	44	34	47	37	47	37	47			
U					17	27	17	27	17	27	17	47	37	47	37	47	37	47				
V						17	27	17	27	17	27	37	47	37	47	37	47					
W									17	27	17	47	37	47								

Front order
Back order

Figure A-1. Fuel Channel Grouping for the IAEA ICSP Benchmark

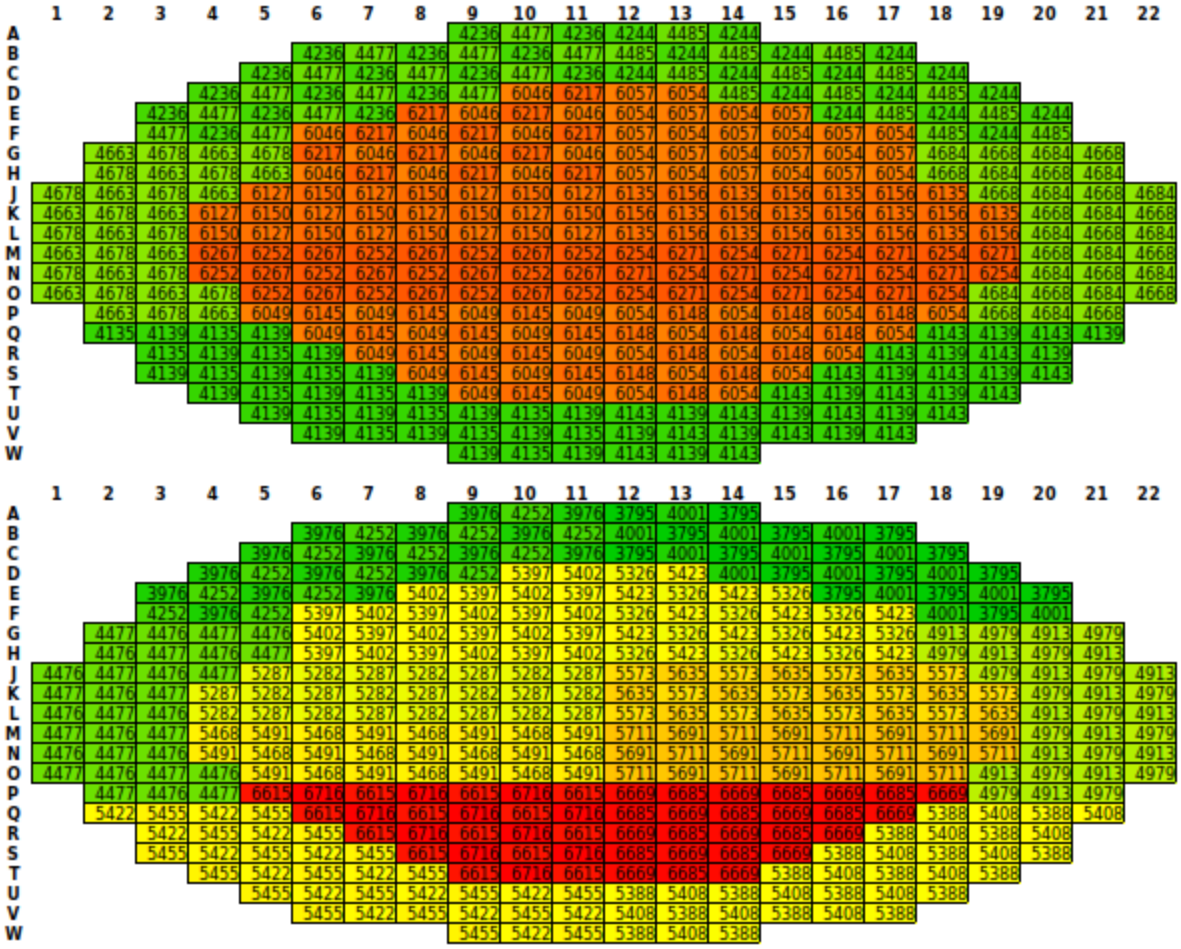

Figure A-2. IAEA ICSP Reference Channel Power Distribution (kW), Top - December 2018 Specifications, Bottom - Final Specifications

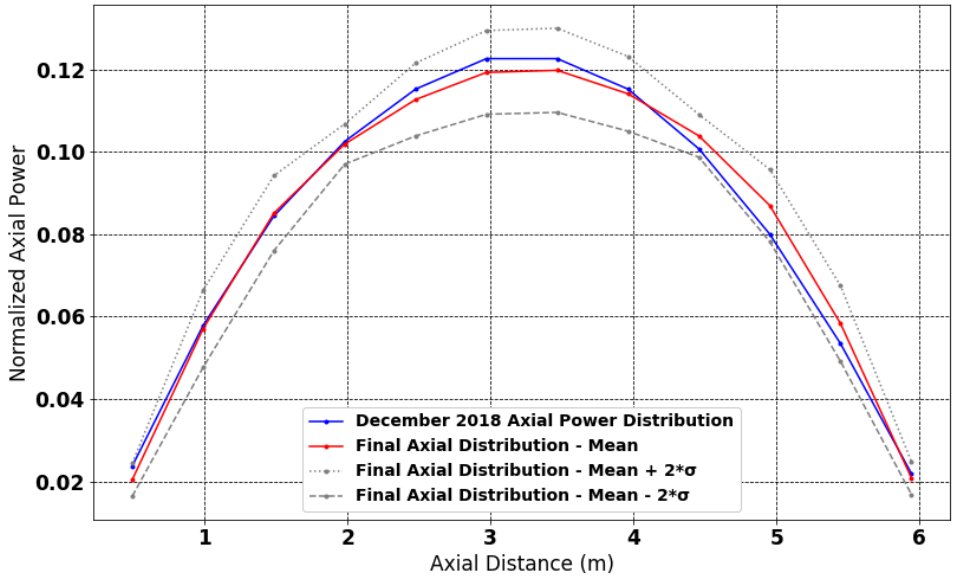

Figure A-3. IAEA ICSP Reference Axial Power Distributions

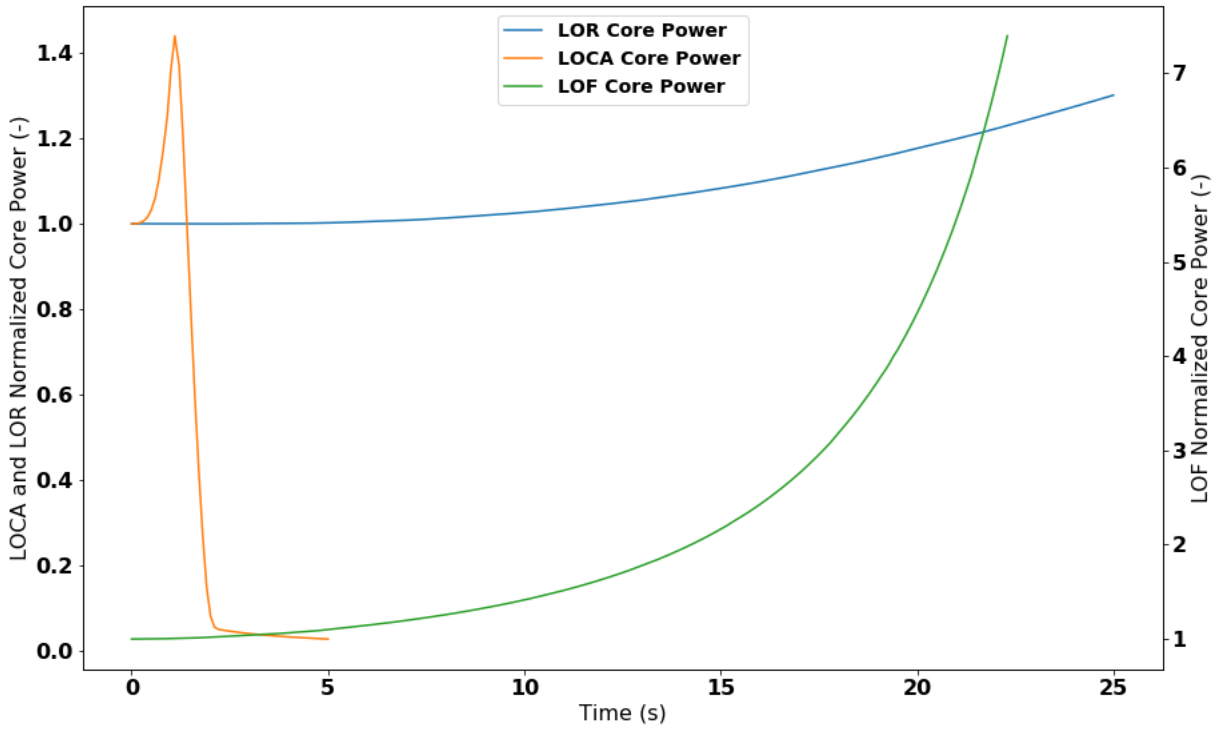

Figure A-4. IAEA ICSP Core Power Input Data for the Stand-alone System Thermal-hydraulics Calculations

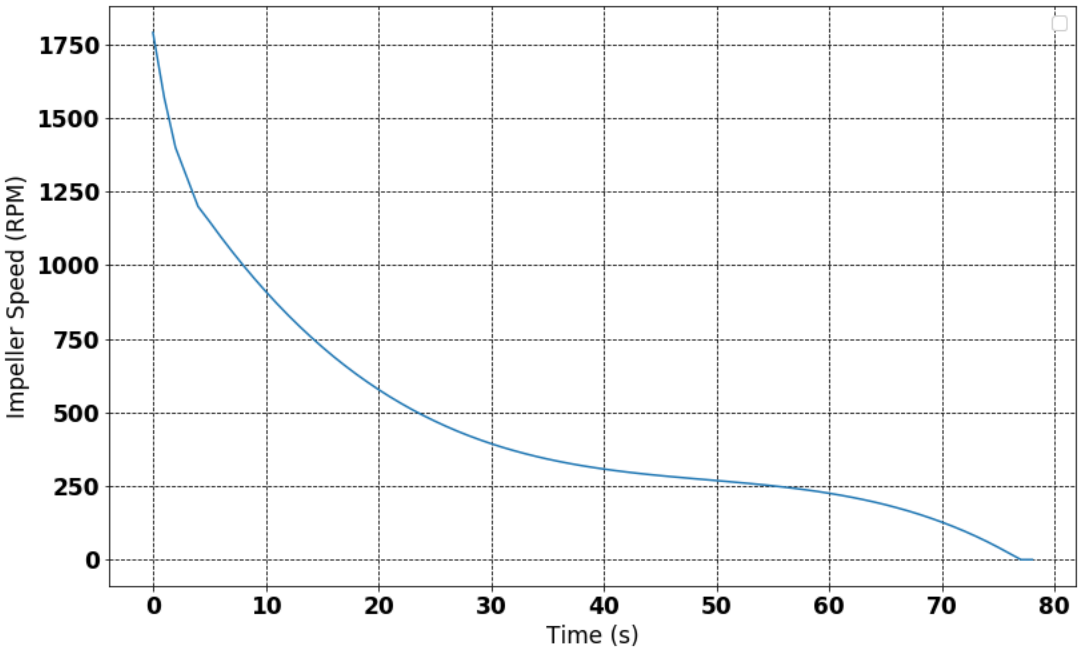

Figure A-5. Pump Rundown Curve for the LOF Case Defined in the IAEA ICSP Benchmark Specifications

Appendix B - IAEA ICSP Benchmark Reactor Physics Specifications

	1	2	3	4	5	6	7	8	9	10	11	12	13	14	15	16	17	18	19	20	21	22
A									1.616	3.771	2.454	1.598	4.793	1.697								
B						1.161	2.106	2.656	3.234	2.124	3.282	5.827	3.223	4.033	1.27	1.957	5.547					
C					6.048	1.774	2.616	5.342	4.393	4.54	1.48	3.07	5.892	1.881	2.507	4.37	6.28	2.634				
D				1.579	1.976	6.249	4.196	6.849	5.374	2.071	6.302	2.87	1.928	5.701	5.039	5.946	5.699	2.804	5.672			
E			4.049	3.16	5.011	1.836	4.832	3.474	2.896	4.585	3.689	5.468	5.048	2.617	3.598	2.598	2.529	6.571	6.133	1.487		
F			3.485	2.911	2.562	4.386	2.141	2.183	3.286	5.703	2.207	6.415	2.292	6.324	5.253	5.684	1.968	4.467	4.773	3.461		
G		3.977	1.369	5.582	5.434	3.552	8.077	1.639	2.591	3.103	5.749	4.505	4.219	3.986	4.762	2.64	5.837	1.5	5.174	4.333	2.943	
H		4.012	2.371	1.952	4.52	5.294	6.189	4.717	5.892	3.814	3.853	3.01	7.238	3.222	2.024	5.672	2.795	3.197	2.833	3.369	5.474	
J	5.796	1.976	1.874	4.058	3.015	6.202	3.708	2.656	6.457	2.426	4.567	6.316	4.888	6.535	4.95	4.93	1.712	5.522	2.895	5.937	2.613	4.081
K	4.965	5.712	4.961	5.038	1.776	5.383	4.259	5.145	3.79	4.321	1.79	2.905	3.678	2.328	3.23	4.017	5.349	4.326	3.416	5.696	3.381	2.739
L	2.757	4.36	2.571	6.349	3.624	7.558	2.099	3.486	2.776	5.554	6.863	4.81	5.374	5.56	6.7	3.632	2.612	2.927	1.859	3.729	1.611	4.51
M	4.873	2.689	3.272	4.553	2.846	6.116	5.735	7.196	4.662	2.134	3.465	3.083	2.195	3.897	6.228	2.053	4.721	5.706	5.796	2.436	6.713	3.249
N	1.99	4.127	5.136	1.744	4.964	4.882	3.374	5.674	5.88	6.607	5.584	5.146	2.599	5.552	6.653	3.831	5.28	3.899	6.239	1.976	2.815	1.496
O	5.921	5.428	3.081	4.268	2.927	2.52	6.429	1.954	2.578	4.301	4.042	6.653	1.615	5.404	4.535	2.396	7.465	1.875	5.13	2.786	3.33	3.001
P		5.596	5.929	1.39	5.294	4.32	3.89	3.104	4.911	2.799	1.797	3.039	4.484	3.402	1.643	3.239	4.823	4.542	2.12	3.016	6.188	
Q		3.415	4.333	5.625	3.705	1.859	5.437	5.313	1.593	2.51	3.446	5.257	6.278	3.745	5.63	5.13	4.883	2.771	4.861	1.488	3.992	
R			2.07	1.653	6.234	2.997	5.558	4.54	3.841	5.189	7.012	1.717	5.553	2.335	4.036	2.559	4.01	1.251	4.974	2.606		
S			5.85	3.466	3.289	2.632	6.08	3.122	2.789	1.724	5.523	4.44	4.951	2.86	5.668	3.031	5.087	1.525	5.428	3.888		
T				3.968	2.055	1.837	5.758	1.971	5.727	3.535	6.466	3.127	2.05	5.243	4.703	1.488	6.265	3.403	4.918			
U					5.439	3.986	3.735	2.711	2.24	3.271	2.149	4.557	3.816	2.405	2.739	3.12	3.721	5.984				
V						4.564	1.809	4.691	3.666	3.518	4.487	2.764	4.206	2.532	4.674	6.219	4.837					
W									1.02	3.493	3.989	3.46	3.603	4.208								

Figure B-1. IAEA ICSP Reference Burnup Distribution - all values in MW.days/kg(U)

Thermalhydraulics channel group	Coolant density (g/cc) Node 1	2	3	4	5	6	7	8	9	10	11	12
1	0.7773	0.7721	0.7645	0.7549	0.7439	0.7318	0.7192	0.7070	0.6959	0.6835	0.6730	0.6556
2	0.7774	0.7722	0.7645	0.7549	0.7438	0.7317	0.7191	0.7069	0.6958	0.6832	0.6726	0.6545
3	0.7773	0.7720	0.7641	0.7543	0.7430	0.7305	0.7176	0.7050	0.6935	0.6776	0.6585	0.6267
4	0.7773	0.7720	0.7642	0.7545	0.7432	0.7309	0.7181	0.7056	0.6943	0.6789	0.6639	0.6370
5	0.7768	0.7713	0.7631	0.7529	0.7412	0.7282	0.7148	0.7016	0.6807	0.6556	0.6008	0.5649
6	0.7769	0.7715	0.7636	0.7537	0.7423	0.7298	0.7167	0.7040	0.6925	0.6713	0.6360	0.6010
7	0.7769	0.7717	0.7639	0.7543	0.7431	0.7309	0.7182	0.7059	0.6947	0.6751	0.6565	0.6317
8	0.7780	0.7728	0.7652	0.7557	0.7447	0.7327	0.7202	0.7081	0.6971	0.6866	0.6766	0.6659
9	0.7780	0.7728	0.7652	0.7556	0.7446	0.7326	0.7200	0.7079	0.6968	0.6855	0.6754	0.6633
10	0.7780	0.7726	0.7648	0.7550	0.7437	0.7312	0.7183	0.7057	0.6943	0.6788	0.6631	0.6351
11	0.7779	0.7727	0.7649	0.7552	0.7440	0.7316	0.7189	0.7064	0.6952	0.6806	0.6679	0.6449
12	0.7773	0.7718	0.7636	0.7534	0.7416	0.7286	0.7152	0.7020	0.6806	0.6543	0.5999	0.5649
13	0.7775	0.7722	0.7642	0.7543	0.7428	0.7302	0.7172	0.7044	0.6929	0.6717	0.6380	0.6034
14	0.7775	0.7722	0.7644	0.7547	0.7435	0.7312	0.7184	0.7060	0.6947	0.6746	0.6536	0.6259
15	0.7777	0.7726	0.7649	0.7554	0.7444	0.7324	0.7199	0.7077	0.6967	0.6855	0.6755	0.6640
16	0.7777	0.7725	0.7649	0.7553	0.7443	0.7322	0.7197	0.7075	0.6965	0.6848	0.6747	0.6616
17	0.7777	0.7724	0.7645	0.7547	0.7434	0.7309	0.7180	0.7054	0.6940	0.6785	0.6623	0.6337
18	0.7777	0.7724	0.7646	0.7549	0.7437	0.7313	0.7186	0.7061	0.6948	0.6801	0.6670	0.6432
19	0.7771	0.7715	0.7633	0.7531	0.7413	0.7283	0.7148	0.7016	0.6792	0.6528	0.5970	0.5620
20	0.7772	0.7719	0.7639	0.7540	0.7425	0.7299	0.7169	0.7041	0.6925	0.6712	0.6362	0.6013
21	0.7772	0.7719	0.7641	0.7544	0.7432	0.7309	0.7181	0.7057	0.6944	0.6741	0.6522	0.6240
22	0.7788	0.7737	0.7660	0.7565	0.7455	0.7335	0.7210	0.7089	0.6979	0.6888	0.6790	0.6716
23	0.7789	0.7737	0.7660	0.7565	0.7455	0.7334	0.7209	0.7088	0.6977	0.6887	0.6788	0.6710
24	0.7788	0.7735	0.7657	0.7559	0.7447	0.7323	0.7194	0.7069	0.6956	0.6817	0.6701	0.6493
25	0.7788	0.7736	0.7658	0.7561	0.7449	0.7326	0.7199	0.7075	0.6963	0.6837	0.6732	0.6579
26	0.7783	0.7728	0.7646	0.7545	0.7428	0.7299	0.7165	0.7035	0.6889	0.6648	0.6192	0.5833
27	0.7784	0.7731	0.7652	0.7553	0.7440	0.7315	0.7185	0.7059	0.6945	0.6750	0.6522	0.6221
28	0.7784	0.7732	0.7655	0.7559	0.7448	0.7326	0.7200	0.7077	0.6966	0.6806	0.6673	0.6516

Figure B-2. IAEA ICSP Reference Coolant Density Distribution

Thermalhydraulics channel group	Coolant temperature (deg. C) Node											
	1	2	3	4	5	6	7	8	9	10	11	12
1	268.77	271.79	276.16	281.38	287.13	293.11	298.91	304.20	308.67	312.01	314.11	314.51
2	268.77	271.80	276.17	281.40	287.16	293.15	298.96	304.25	308.73	312.07	314.17	314.55
3	268.80	271.90	276.38	281.73	287.61	293.72	299.66	305.05	309.61	312.90	314.75	314.63
4	268.79	271.87	276.31	281.62	287.47	293.53	299.43	304.79	309.32	312.61	314.59	314.66
5	268.83	272.04	276.67	282.20	288.28	294.59	300.70	306.25	310.63	313.71	314.24	313.77
6	268.80	271.92	276.43	281.81	287.74	293.89	299.86	305.29	309.87	313.01	314.30	313.99
7	268.76	271.82	276.22	281.49	287.29	293.32	299.17	304.50	309.01	312.14	313.98	314.11
8	268.38	271.40	275.75	280.96	286.70	292.66	298.46	303.74	308.21	311.61	313.72	314.36
9	268.38	271.41	275.77	281.00	286.75	292.73	298.54	303.83	308.31	311.69	313.80	314.39
10	268.42	271.52	276.00	281.36	287.26	293.38	299.33	304.74	309.31	312.62	314.59	314.63
11	268.40	271.48	275.92	281.24	287.08	293.16	299.06	304.43	308.97	312.29	314.35	314.56
12	268.45	271.68	276.34	281.90	288.02	294.36	300.50	306.09	310.48	313.54	314.09	313.67
13	268.42	271.56	276.09	281.51	287.47	293.66	299.66	305.12	309.73	312.90	314.26	313.98
14	268.39	271.47	275.92	281.23	287.09	293.17	299.07	304.45	309.00	312.14	313.92	313.94
15	268.56	271.57	275.93	281.14	286.87	292.83	298.63	303.90	308.37	311.74	313.85	314.45
16	268.56	271.58	275.95	281.16	286.91	292.89	298.69	303.98	308.46	311.82	313.93	314.48
17	268.59	271.69	276.17	281.52	287.41	293.52	299.46	304.86	309.43	312.73	314.68	314.70
18	268.58	271.65	276.09	281.40	287.24	293.31	299.20	304.56	309.10	312.41	314.45	314.63
19	268.62	271.85	276.51	282.08	288.20	294.54	300.69	306.27	310.63	313.68	314.17	313.73
20	268.59	271.73	276.26	281.68	287.63	293.81	299.81	305.27	309.88	313.03	314.34	314.05
21	268.56	271.64	276.09	281.40	287.25	293.32	299.22	304.59	309.13	312.27	314.01	314.01
22	267.87	270.90	275.28	280.51	286.27	292.26	298.09	303.40	307.89	311.35	313.49	314.23
23	267.88	270.91	275.29	280.53	286.31	292.30	298.14	303.45	307.95	311.42	313.55	314.29
24	267.90	271.01	275.49	280.85	286.75	292.87	298.82	304.23	308.81	312.19	314.30	314.61
25	267.89	270.98	275.43	280.75	286.61	292.69	298.60	303.99	308.54	311.94	314.08	314.57
26	267.94	271.16	275.80	281.35	287.45	293.78	299.92	305.50	310.12	313.25	314.20	313.82
27	267.90	271.03	275.55	280.95	286.89	293.06	299.06	304.51	309.12	312.33	314.09	314.03
28	267.87	270.93	275.35	280.63	286.45	292.49	298.37	303.72	308.26	311.52	313.56	314.04

Figure B-3. IAEA ICSP Reference Coolant Temperature Distribution

Thermalhydraulics channel group	Fuel temperature (deg. C) Node											
	1	2	3	4	5	6	7	8	9	10	11	12
1	349.94	490.04	621.51	726.81	810.90	866.85	875.40	835.25	753.29	644.13	519.71	391.79
2	351.32	494.12	628.51	736.35	822.54	879.84	888.46	847.08	762.84	650.86	523.62	393.15
3	352.83	498.70	636.21	746.95	835.56	894.50	903.31	860.63	773.93	658.85	528.29	394.62
4	351.32	494.24	628.52	736.44	822.70	880.11	888.82	847.48	763.30	651.28	523.99	393.23
5	328.76	429.17	519.62	590.41	646.41	684.25	692.08	668.65	617.49	547.13	461.78	370.71
6	331.15	435.87	530.58	604.80	663.52	703.04	710.93	685.86	631.93	557.41	468.52	373.29
7	324.04	416.02	498.04	561.80	612.12	646.12	653.62	633.43	588.55	525.41	449.59	366.63
8	349.45	489.36	620.63	725.75	809.70	865.56	874.09	834.07	752.26	643.39	519.09	391.58
9	350.59	492.71	626.36	733.57	819.24	876.22	884.82	843.79	760.12	648.91	522.30	392.68
10	352.63	498.87	636.80	747.92	836.85	895.99	904.85	862.04	775.04	659.55	528.72	394.82
11	349.58	489.86	621.29	726.74	810.98	867.09	875.76	835.66	753.73	644.48	520.03	391.86
12	325.14	419.77	504.52	570.66	622.95	658.40	666.13	644.91	597.85	532.67	453.08	367.52
13	330.96	436.05	531.14	605.70	664.71	704.44	712.38	687.21	633.06	558.20	469.03	373.47
14	323.62	415.53	497.52	561.28	611.62	645.66	653.22	633.09	588.28	525.22	449.42	366.42
15	349.75	489.89	621.41	726.74	810.87	866.83	875.37	835.22	753.22	644.06	519.54	391.77
16	350.88	493.22	627.11	734.52	820.36	877.43	886.03	844.89	761.03	649.57	522.74	392.88
17	352.87	499.24	637.30	748.52	837.54	896.73	905.57	862.69	775.58	659.96	528.97	394.94
18	349.84	490.27	621.86	727.45	811.80	867.97	876.64	836.45	754.38	644.96	520.34	392.00
19	325.44	420.29	505.26	571.58	624.01	659.56	667.28	645.96	598.69	533.33	453.46	367.70
20	331.22	436.47	531.71	606.40	665.50	705.29	713.23	687.98	633.70	558.71	469.33	373.61
21	323.86	415.88	497.98	561.82	612.22	646.29	653.85	633.66	588.76	525.60	449.66	366.55
22	349.07	489.24	620.80	726.20	810.39	866.42	875.01	834.93	752.92	643.85	519.26	391.60
23	350.46	493.32	627.81	735.75	822.04	879.43	888.08	846.77	762.47	650.60	523.15	392.98
24	351.91	497.74	635.24	745.98	834.61	893.57	902.43	859.86	773.23	658.22	527.91	394.63
25	350.41	493.31	627.59	735.52	821.82	879.26	888.02	846.79	762.64	650.76	523.52	393.18
26	327.94	428.48	519.09	590.02	646.14	684.07	692.02	668.65	617.72	547.14	462.09	370.87
27	330.28	435.06	529.83	604.12	662.91	702.48	710.44	685.49	631.60	557.01	468.54	373.38
28	323.16	415.17	497.23	561.04	611.41	645.45	653.00	632.95	588.11	525.07	449.32	366.61

Figure B-4. IAEA ICSP Reference Fuel Temperature Distribution

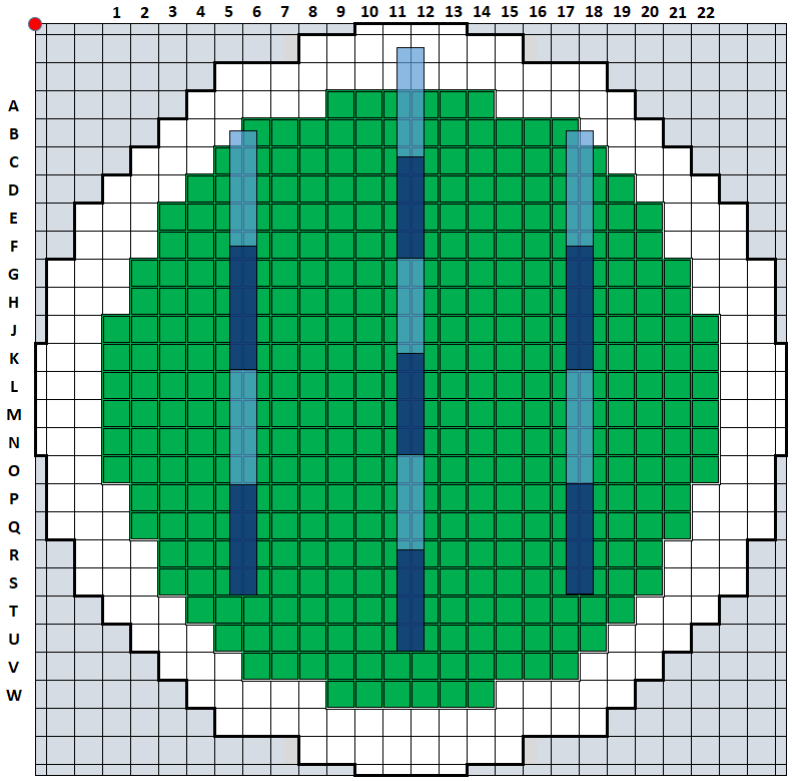

Figure B-5. Liquid Zone Controller X-Y Plane Locations - Dark Blue = Light Water, Light Blue = Air

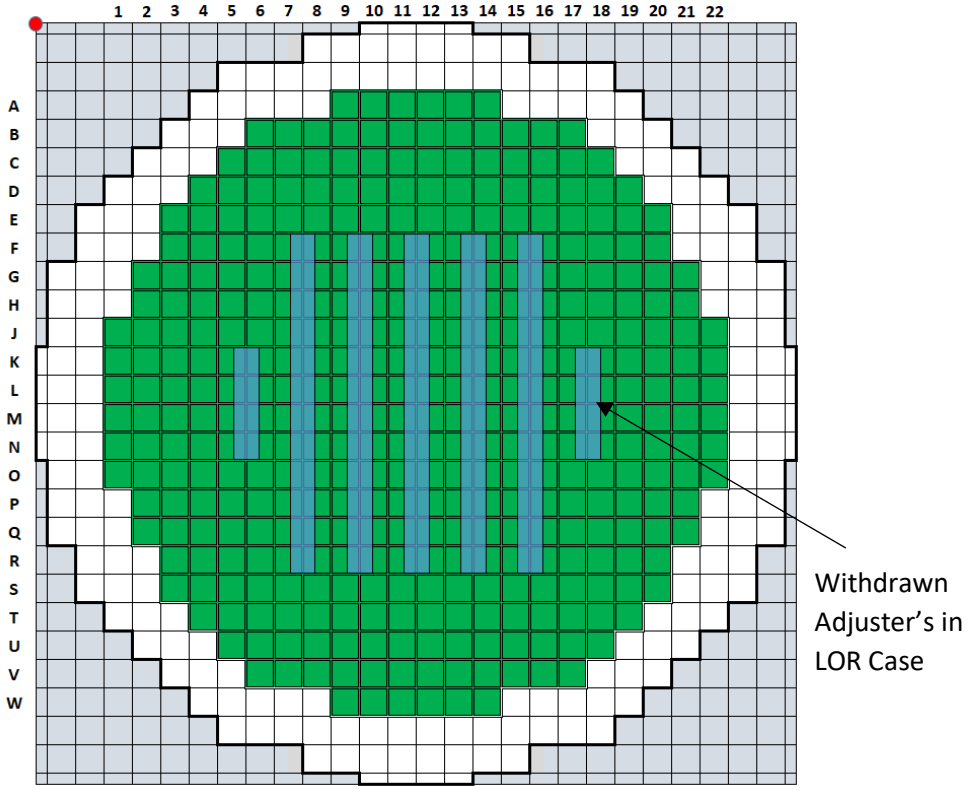

Figure B-6. Adjuster Rods X-Y Plane Locations

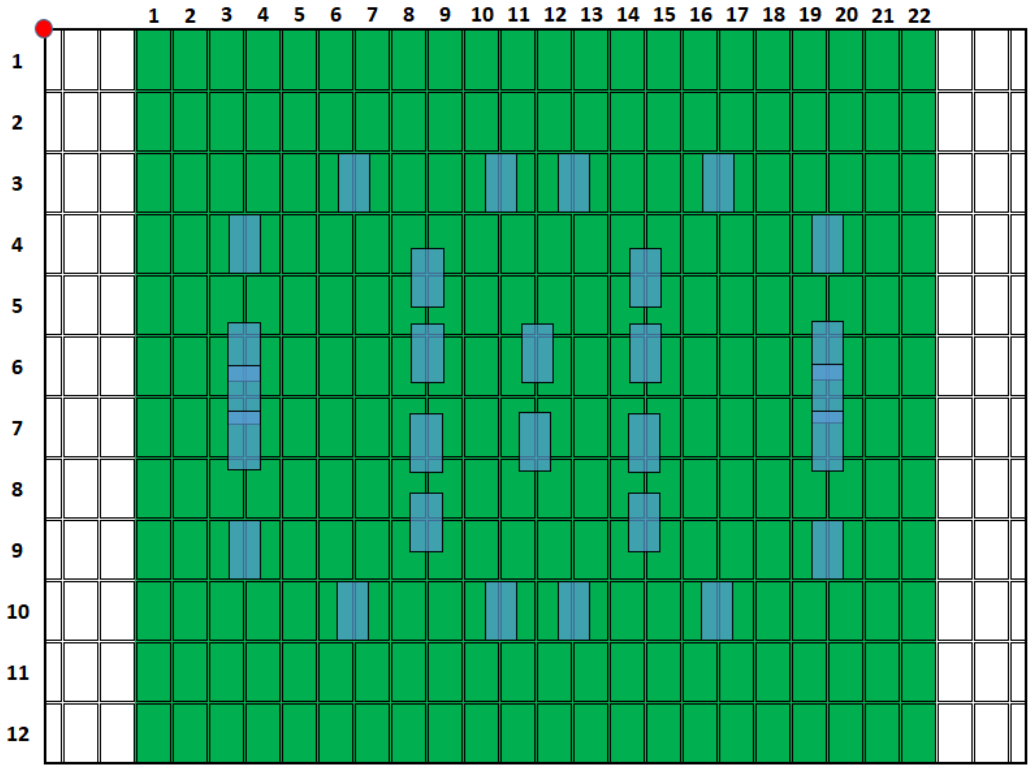

Figure B-7. Shutoff Rod X-Z Plane Locations

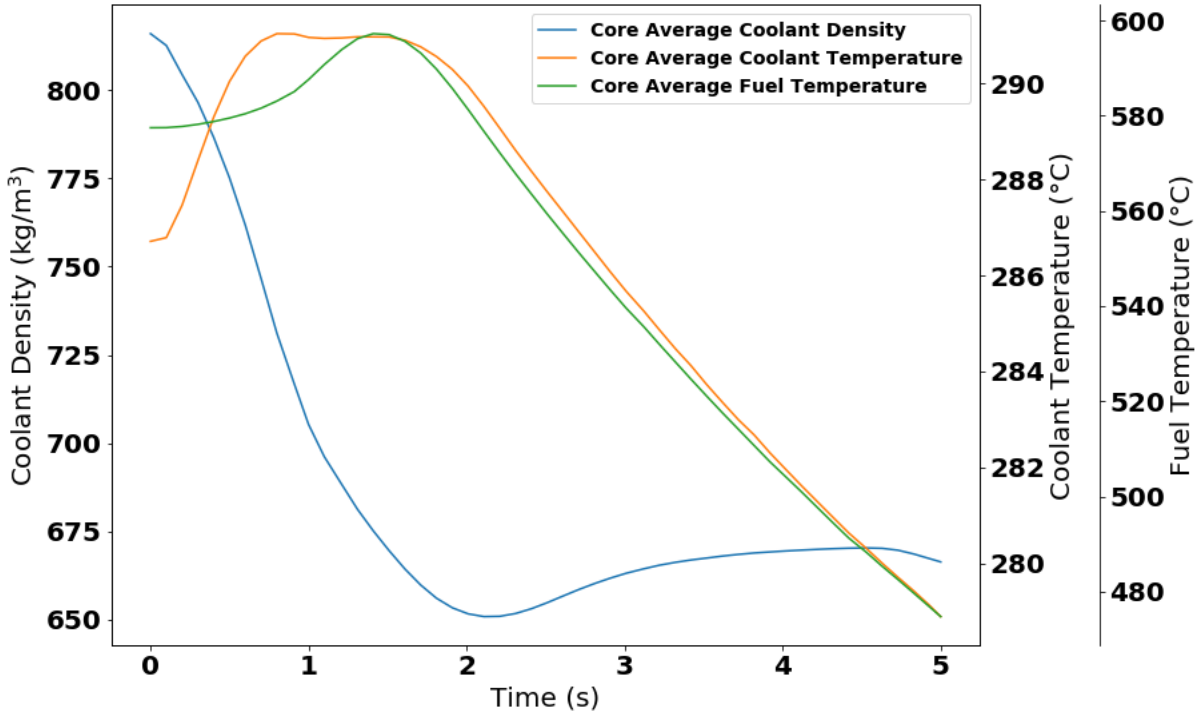

Figure B-8. Stand-alone LOCA Diffusion Calculation Inputs - Core Average Coolant Density, Fuel Temperature and Coolant Temperature

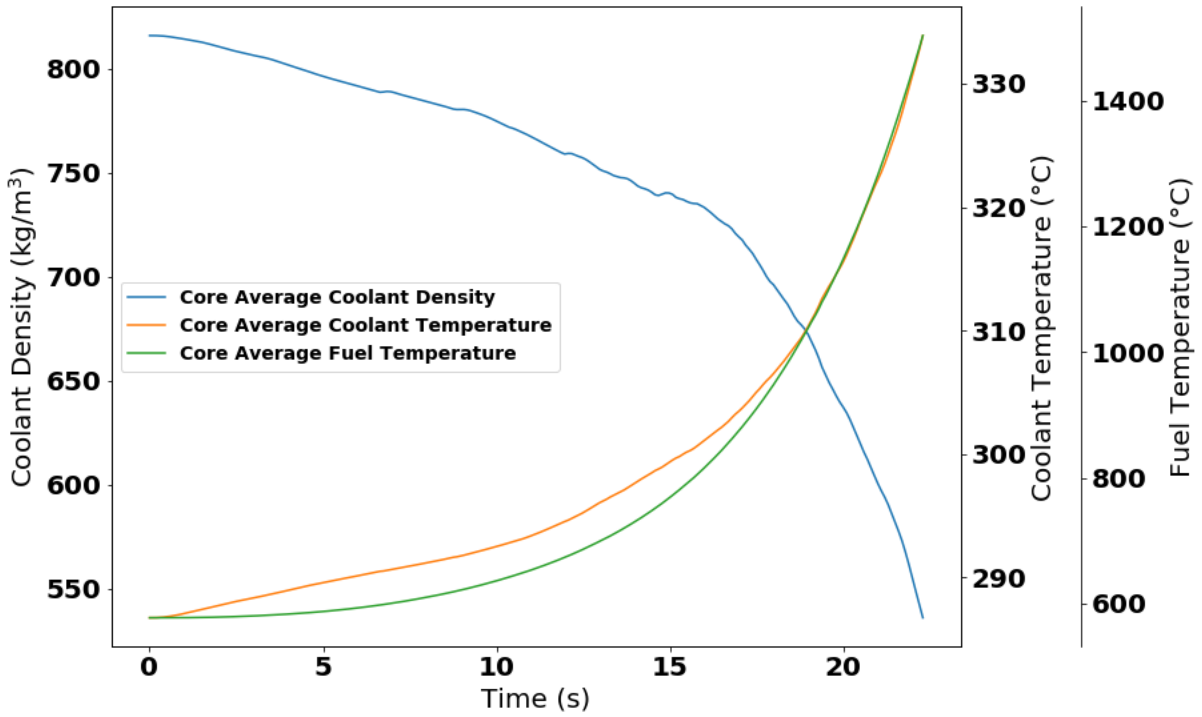

Figure B-9. Stand-alone Pump Trip Diffusion Calculation Inputs - Core Average Coolant Density, Fuel Temperature and Coolant Temperature

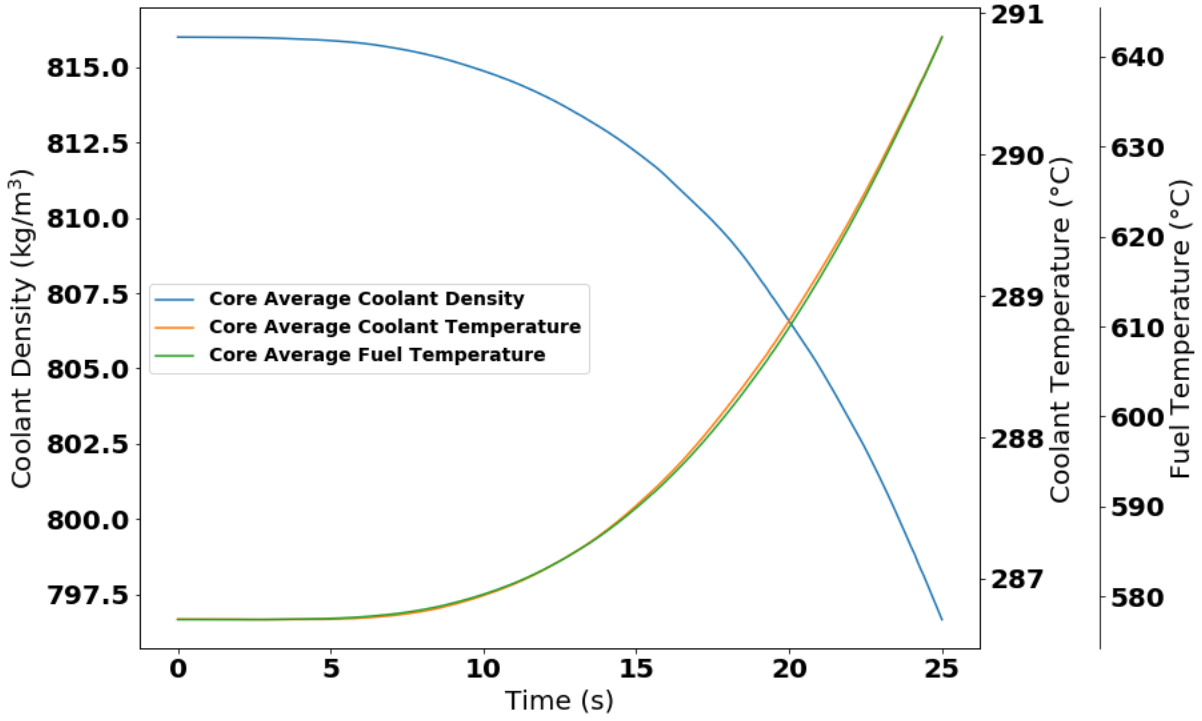

Figure B-10. Stand-alone Adjuster Pull Diffusion Calculation Inputs - Core Average Coolant Density, Fuel Temperature and Coolant Temperature

Appendix C - ARIANT to TRACE Nodalization Conversion Rules and Calibration Methods

Appendix C-1: General ARIANT to TRACE Conversion Rules

1. In TRACE, velocities, areas, hydraulic diameters and forward/reverse K-factors are cell edge quantities (meaning two values are given for every cell) and volume, length, elevation change, and initial pressures/temperatures are all cell centered quantities (meaning only one is given for each cell). In ARIANT/CATHENA, all quantities are cell centered. As such, any cell centered quantities defined in the Specifications were used directly without any modification. Rules for cell edge quantities are described below. A roughness parameter is also given for a pipe component but must be shared across all cells in that component. The number of pipes represented by the component must also be specified. For the fuel channel models, this ranges between 11 and 19. In this model, 380 fuel channels are grouped into 28 groups.

2. In ARIANT/CATHENA, a single value is given for K-factors, areas, and hydraulic diameters within a node. However, CATHENA/ARIANT can also add or over-write a K-factor at any given junction or link. As such rules must be developed for how to convert ARIANT/CATHENA Specifications into TRACE Specifications. The following rules were used:

    a. K factors:

$$K_{junction} = \frac{K_{component}}{N_{cells}} + K_{system\ model} \qquad (C-1)$$

    Where:

    - $K_{component}$ is the K-factor defined for a node, and is given in the Components tab of the TH Specifications
    - $K_{system\ model}$ is the additional ARIANT/CATHENA K-factor that can be written for a given junction, and is given in the System Model tab of the TH Specifications

    b. Areas and Hydraulic Diameters: When and area change occurs between two cells, the smaller area and hydraulic diameter is used.

    All initial velocities were set to 0. This seemed to have no impact on run time.

3. A pressure drop option must also be specified at every cell edge. There are 4 different pressure drop options available in TRACE:

    a. **nff = 1** – pressure drop due to friction, minor losses (K-factors), area change, and elevation change are all considered
    b. **nff = -1** – same as nff = 1, except an additional K-factor for abrupt area changes is added internally by TRACE
    c. **nff = 0** – pressure drop due to friction is not considered, and only minor losses, area change and elevation change are considered (no internal K-factor is calculated)

d. **nff = -100** – Same as 0, except the additional K-factor for abrupt area changes is calculated

Regardless of what option is selected, pressure drop due to area change and elevation change cannot be turned off. This is a significantly different than ARIANT/CATHENA, and unfortunately, this option is often used in the Specifications. It is because of this difference that significant changes to the fuel channel models had to be made, as described in further detail below. Both **nff = 1** and **nff = -1** were considered, but the final model corresponds to **nff = -1.**

4. Specific adjustments were made to improve the pressure drop agreement:
   - Increased all hydraulic diameters by 5 %.
   - When adjusting K factors (as described in detail below), in general, the following approach was used:

$$\Delta P_{fric} \sim KV^2 \text{ and } V \sim \frac{1}{A}$$

$$\Delta P_{fric} \sim K\frac{}{A}^2$$

Where:

- V is the velocity at a cell edge
- A is the cell edge area

If one makes a change from A_1 to A_2, then to keep the pressure change constant:

$$\Delta P_{fric} = \frac{K_1}{A_1^2} = \frac{K_2}{A_2^2}, \qquad K_2 = K_1\left(\frac{A_2^2}{A_1^2}\right) \qquad (C-2)$$

Appendix C-2: Model Adjustment - Method 2 Modifications

1. OUFDR Changes:
   - Adjusted the volume of the smaller diameter pipes, such that volume/dx is constant along the feeder and equal to the volume/dx value of the larger diameter pipes. This removes any pressure changes due to area changes (Bernoulli).
   - For cases with a double pressure drop in the first feeder component after the end fitting, the K-factor between OEF and OEFA (4.26/2 = 2.13) was added to the K factor for the second cell edge of the first feeder component, with no adjustment.
   - At the junction between OEFA and the first feeder component after the end fitting, the flow area and HD of OEFA (now equal to the flow area and HD of the CHAN/pressure tube) are used. For cases with a double pressure drop, the junction K-factor was modified as:

$$K_{jun} = \left(\frac{K_{OEFA}}{n_{cells,OEFA}+1}\right) * \left(\frac{A_{CHAN}^2}{A_{feeder}^2}\right) + \left(\frac{K_{feeder}}{n_{cells,feeder}+1}\right) * \left(\frac{A_{CHAN}^2}{A_{feeder}^2}\right) + K_{link} \qquad (C-3)$$

For FC11:

$$K_{jun} = \left(\frac{4.26}{2}\right) * \left(\frac{0.003517^2}{0.002734^2}\right) + \left(\frac{0.3635}{4}\right) * \left(\frac{0.003517^2}{0.002734^2}\right) + 0.08 = 0.3755123$$

For cases without a double pressure drop, the K factor was not modified, as shown below:

$$K_{jun} = \left(\frac{K_{OEFA}}{n_{cells,OEFA}}\right) + \left(\frac{K_{feeder}}{n_{cells,feeder}+1}\right) + K_{link} \qquad (C-4)$$

For FC13:

$$K_{jun} = \left(\frac{4.26}{2}\right) + \left(\frac{0.0703}{2}\right) + 0.08 = 2.24515$$

   - The double pressure drop refers to fuel channels which show a large, specified pressure drop between the first and second node of the first feeder component after the end fitting. While one would expect a large pressure drop between the end fitting and the first node of the feeder, it is unclear why such a large pressure drop would be seen between the first and second node, as this is just a normal section of piping. Furthermore, as described above, not all fuel channels had a double pressure drop in the Specifications.

2. OEF Changes:
   - Changed the area (0.003517 m^2), and hydraulic diameter (0.0076 m) to be equal to that of the CHAN/pressure tube. Adjusted the volume of the cells accordingly (volume = 0.003517*dx)
   - Removed K factor at the junction between OEF and OEFA
   - K factor at the junction between the CHAN/pressure tube and OEF was modified:

$$K_{jun} = \frac{K_{chan}}{2} * \left(\frac{A_{CHAN}^2}{A_{OEF}^2}\right) + K_{link} \qquad (C-5)$$

$$K_{jun} = \left(\frac{0.82474167}{2}\right) * \left(\frac{0.003517^2}{0.005545^2}\right) + 0.6113 = 0.77719357$$

3. CHAN (Pressure tube): No Changes

4. IEF:
   - Changed the area of both IEF and IEFA to be equal to that of the CHAN/pressure tube (0.003517 m^2).
   - Changed the hydraulic diameter of IEF to be equal to that of IEFA (0.00276 m). At the junction between IEF and the CHAN/pressure tube, this new hydraulic diameter is used.
   - The K factor at the junction between the CHAN/pressure tube and IEF was not modified, as the junction flow area was always equal to the pressure tube flow area:

$$K_{jun} = \frac{K_{chan}}{2} + K_{link} = \frac{0.82474167}{2} + 0.3893 = 0.80167083$$

   - The K factor at the junction between IEFA and IEF was modified as:

$$K_{jun} = \left(\frac{K_{IEFA}}{n_{cells,IEFA} + 1}\right) * \left(\frac{A_{CHAN}^2}{A_{IEF}^2}\right) \qquad (C-6)$$

For FC11:

$$K_{jun} = \left(\frac{3.89}{2}\right) * \left(\frac{0.003517^2}{0.005545^2}\right) = 0.782$$

   - At the junction between IEFA and the last inlet feeder component, the HD and area of the last inlet feeder component are used.
   - The K factor between the last feeder component and IEFA was modified as:

$$K_{jun} = \left(\frac{K_{IEFA}}{n_{cells,IEFA} + 1}\right) * \left(\frac{A_{CHAN}^2}{A_{IEF}^2}\right) + \left(\frac{K_{feeder}}{n_{feeder}}\right) + K_{link} \qquad (C-7)$$

For FC11:

$$K_{jun} = \left(\frac{3.89}{2}\right) * \left(\frac{0.003517^2}{0.005545^2}\right) + \left(\frac{0.2277}{4}\right) + 0.13 = 0.968925$$

5. INFDR:
   - Adjusted the volume of the smaller diameter pipes, such that volume/dx is constant along the feeder and equal to the volume/dx value of the larger diameter pipes. This removes any pressure changes due to area changes (Bernoulli).
   - Flow area and HD of larger diameter pipes used at the junction between the smaller diameter pipes and larger diameter pipes

- No K factor adjustments were made along the inlet feeders (other than junction between the last inlet feeder and IEFA, as described above)

6. Pump Models:
   - The TRACE pump component requires a single pipe component to be connected to the pump outlet. However, there are two discharge lines defined in the Specifications, as one would expect for a real CANDU plant, so the pump output was essentially divided into two components, each with half the length and volume, and no K-factor between them. This new pipe is labelled PxDIS1_tee and has both discharge lines connected as side junctions.

   - ARIANT Volume components (components with a volume but no length or area) are not possible in TRACE. The user can define SJCs (single junction components) in TRACE, which are components that have no volume, but in general, the purpose of the "Volumes" is to allow for cross flow connections, and SJCs do not allow for cross flow. As such, all Volume components were removed from the modified version. In the Benchmark Specifications, all pumps contain a volume component in one of the two discharge lines, PXDIS3V. It is unclear why this component was added, as there are no crossflow connections in the discharge lines. This was removed in all cases. What remains are two discharge lines PxDIS3U and PxDIS3D, which are identical to PxDIS2, when combined. As such, these components were combined to form PxDIS3, to make both discharge lines identical. Furthermore, in pumps 1 and 3, there is a Volume component in the pump suction line, PxINT, which serves as a cross flow connection for the loop isolation lines. This was removed as well, so that all four pump suction lines are identical. The loop isolation lines are connected to PxINB in the full system model. This simplifies the pump nodalization to:

$$\text{PxINA} \rightarrow \text{PxINB} \rightarrow \text{PxSUCT} \rightarrow \text{PxDIS1} \rightarrow \text{PxDIS1\_tee} \rightarrow \text{PxDIS2}$$
$$\rightarrow \text{PxDIS3}$$

   - While not a deviation from the Specifications, PxSUCT and PXDIS1 are combined into a single pump component in TRACE (Px). So, the final TRACE nodalization is:

$$\text{PxINA} \rightarrow \text{PxINB} \rightarrow \text{Px} \rightarrow \text{PxDIS1\_tee} \rightarrow \text{PxDIS2}$$
$$\rightarrow \text{PxDIS3}$$

All other aspects of the pump model are retained from the Benchmark Specifications (volume, flow area, length, etc.) so despite these differences, the modified model is considered a good analog to the ARIANT model provided in the Specifications.

7. Steam Generator Model

Notes on Naming Convention in IAEA ICSP Benchmark Specifications:

- The steam generator riser components are generally labelled as RISExVy, where x is the riser leg (either 1 or 2) and y is the steam generator number (1, 2, 3, or 4). This is opposite to what is typically done in the Benchmark Specifications.

- The riser legs are different lengths between the two loops. In loop 1 (SG 1 and 2), the short riser leg is labelled as riser 1, and is 4.5281 m long, while the longer riser leg is labelled as riser leg 2

and is 4.9659 m long (neglecting volume components in both cases). In all riser legs, the elevation change is 1.756 m.

- In loop 2 (SG 3 and 4), the short riser leg is labelled as riser 2, and is 4.5211 m, and the longer riser leg is labelled as riser leg 1 and is 4.9722 m. Again, for all riser legs, the elevation change is 1.756 m.

- All header balance line cross flow connections are done in the shorter riser leg, and all pressurizer cross flow connections are done in the longer riser leg:
    - RISE2V4A (SG4 - OHD7) is connected to the pressurizer
    - RISE2V5 (SG2 – OHD3) is connected to the pressurizer
    - RISE1V1 (SG1 – OHD1) is connected to RISE1V2 (SG2 – OHD3) via the loop balance line HH13Pxx
    - RISE2V3 (SG3 – OHD5) is connected to RISE2V4 (SG4 – OHD7) via the loop balance line HH57Pxx

General Steam Generator Modelling Notes:

- User defined material properties were used for all sections of the boiler, where wall heat transfer is modelled. The inlet and outlet plenums (BxIN and BxOUT) are made of carbon steel, the "TSU" components are made of stainless steel, and the remaining U-Tube components are made of Inconel.
- In the ARIANT Specifications, the BxIN -> BxOUT interconnects are modelled using valves. It is not possible to introduce valves between these components in TRACE, without also including some additional piping. Instead, an SJC (single junction component), a component with no length, or volume, but a flow area and hydraulic diameter, was used instead. The flow areas and hydraulic diameters are as follows:
    - SG1: FA = 0.0293*0.00853 = 0.00025 m^2, HD = 0.0178 m
    - SG2: FA = 0.0293*0.0144 = 0.00042 m^2, HD = 0.0232 m
    - SG3: FA = 0.0293*0.0 = 0.0 m^2, HD = 0.001 m (cannot be 0.0)
    - SG4: FA = 0.0293*0.0095 = 0.00028 m^2, HD = 0.0189 m
- The U-tube component are duplicated 3542 times using the npipes card. In general, the flow area, hydraulic diameter and volume are for a single U-tube, and these values are multiplied by npipes to get the total value. However, at a junction between a U-tube component and a boiler inlet or outlet plenum, the flow area and hydraulic diameters must be adjusted. The flow area value provided must equal the adjacent flow area when multiplied by npipes, but the hydraulic diameter value is the full hydraulic diameter of the adjacent component.
    - e.g. BxIN → BxTSU:

      BxIN right side – FA = 1.896 m^2, HD = 1.554 m
      BxTSU left side – FA = 5.3521E-4 m^2 (5.35291E-4*3542 = 1.8960007), HD = 1.554 m

Steam Generator K-factor Adjustments:

- The hydraulic diameter of the SG U-tube components was increased by a factor of 1.5.

SG 1/2:

- For SG1 BxTSD -> BxOUT, the K-factor was increased by 0.6 from (0.526, 0.390) to (1.126, 1.090)
- For SG2 BxTSD -> BxOUT, the K-factor was increased by 1.0 from (0.526, 0.390) to (1.526, 1.390)
- The RISE1UxB -> BxIN K-factor was increased by 0.8 from (0.29765, 0.15935) to (1.09765, 0.95935)
- The RISE1Vx -> RISExU1B K-factor was increased by 0.25 from (0.08765, 0.08765) to (0.33765, 0.33765)
- The RISE1Lx -> RISExU1A K-factor was increased by 0.3 from (0.0025502, 0.0021045) to (0.3025502, 0.3021045)
- The RISE2Ux -> BxIN K-factor was increased by 1.0 from (0.32755, 0.17185) to (1.32755, 1.17185)
- The RISE2LxC -> RISE2Ux K-factor was increased by 0.2 from (0.10154, 0.10103) to (0.30154, 0.30103)
- The RISE2LxB -> RISE2LxC K-factor was increased by 0.2 from (0.0, 0.0) to (0.2, 02)

SG 3/4:

- The BxTSD -> BxOUT K-factor was increased by 1.0 from (0.526, 0.390) to (1.526, 1.390)
- The RISE1Ux -> BxIN K-factor was increased by 1.6 from (0.3215, 0.1694) to (1.9215, 1.7694)
- The RISE1Lx ->RISE1Ux K-factor was decreased from (0.09905, 0.09860) to (0.0, 0.0
- The RISE2UxB -> BxIN K-factor was increased from (0.29765, 0.15935) to (1.32755, 1.17185)
- The RISE2LxC -> RISE2UxA K-factor was increased by 0.1 from (0.00289, 0.00238) to (0.10289, 0.10238)
- The RISE2LxB -> RISE2LxC K-factor was increased by 0.2 from (0.0 0.0) to (0.2, 0.2)

Appendix D - Additional Stand-alone Reactor Physics Results: Animations

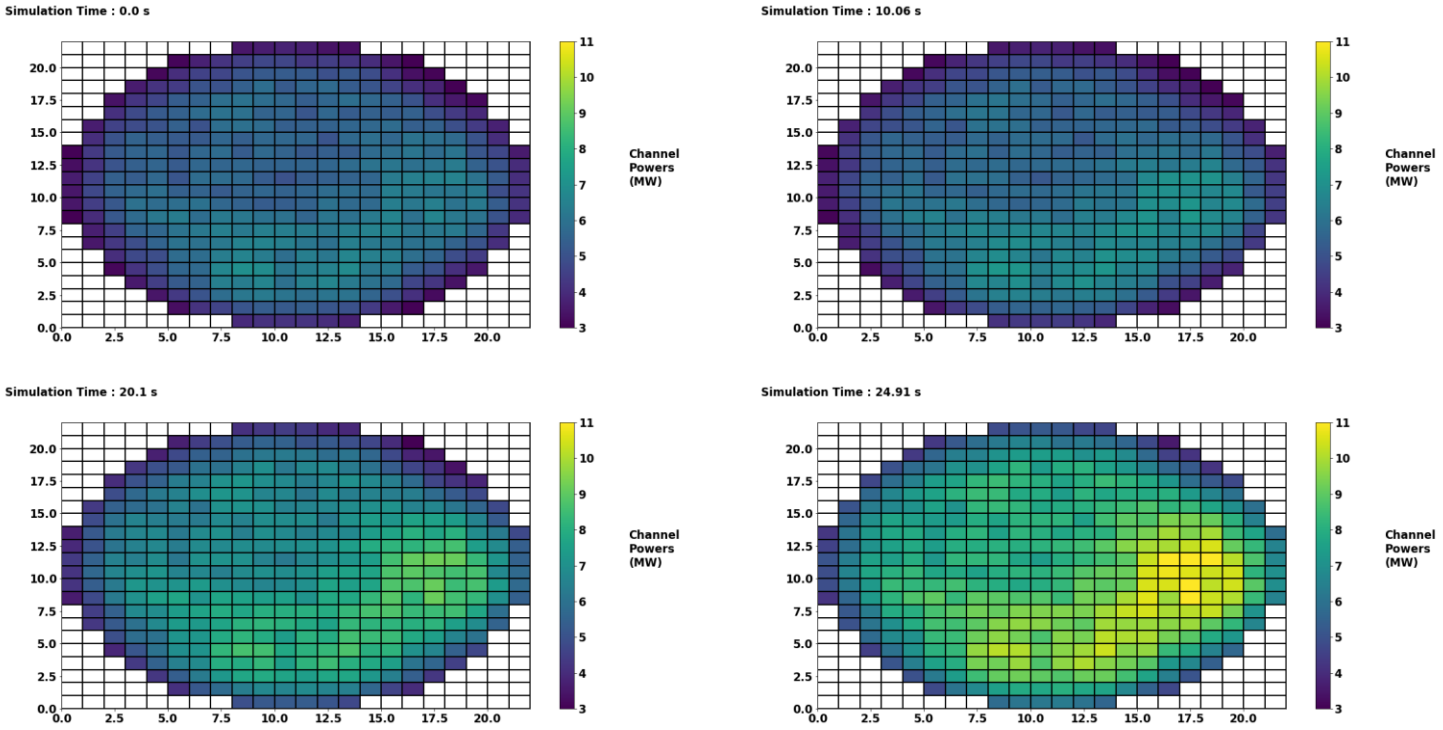

Figure D-1. Stand-alone Reactor Physics Results - LOR Core Power Evolution

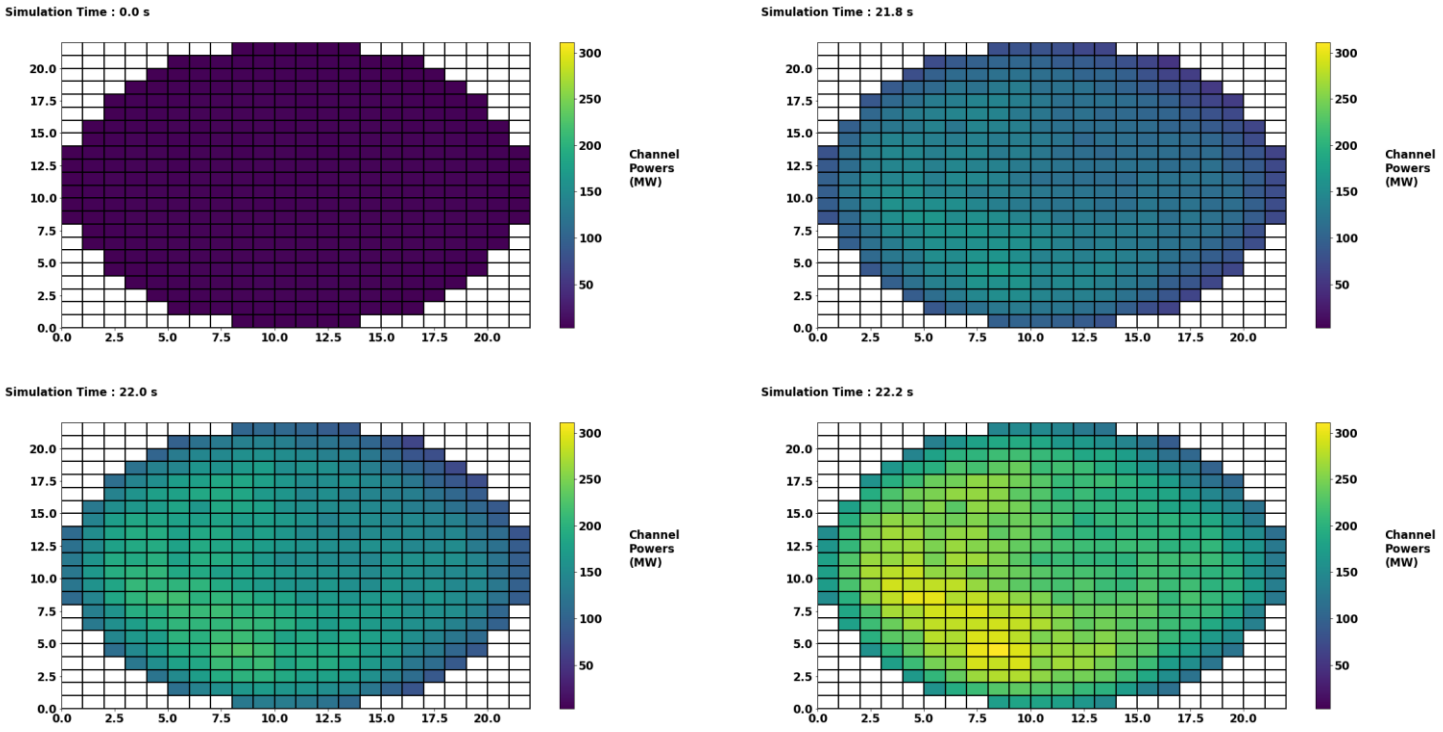

Figure D-2. Stand-alone Reactor Physics Results - LOF Core Power Evolution

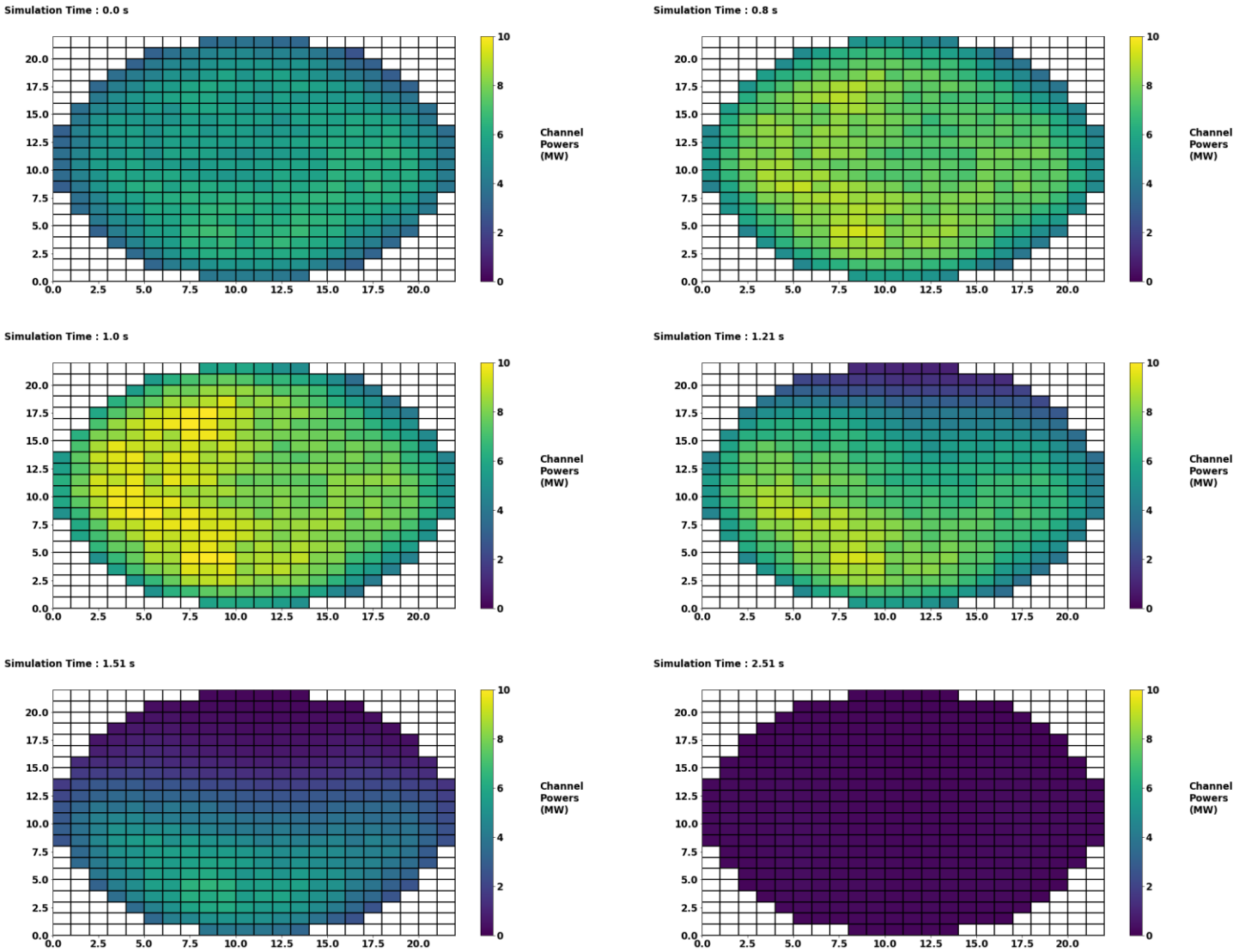

Figure D-2. Stand-alone Reactor Physics Results - LOCA Core Power Evolution

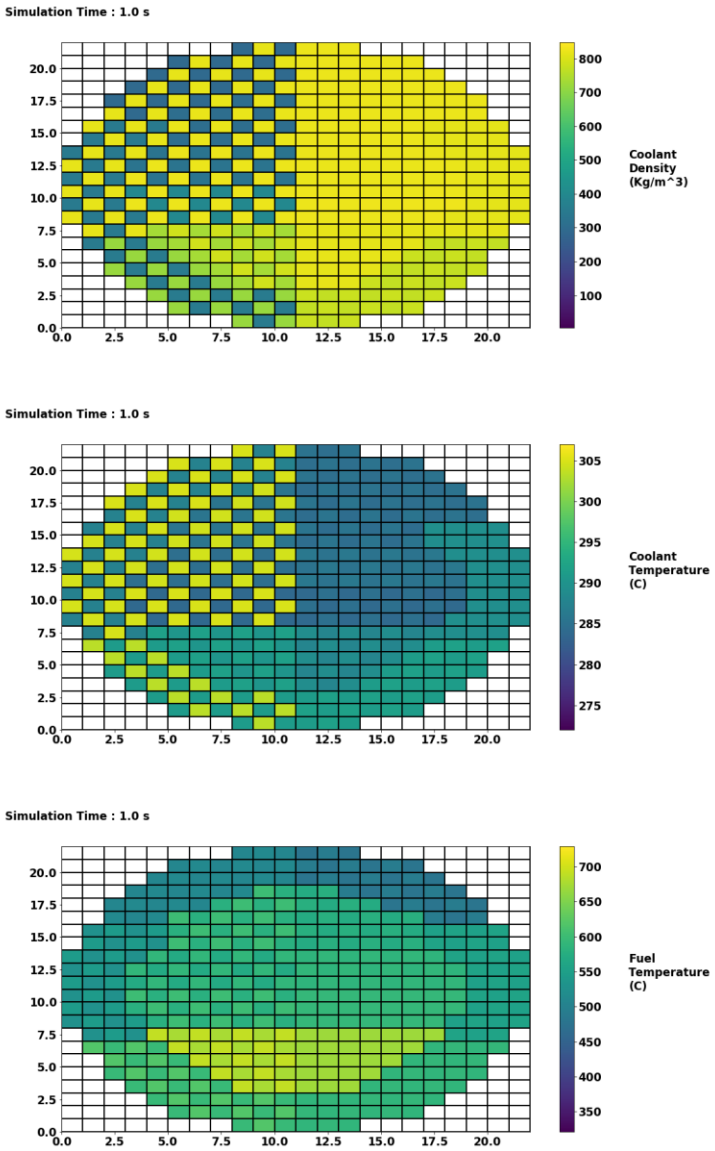

Figure D-4. Stand-alone Reactor Physics Results – TH parameter distribution 1 second into the LOCA transient

Appendix E - Additional Stand-alone System Thermal-Hydraulics Results: Animations

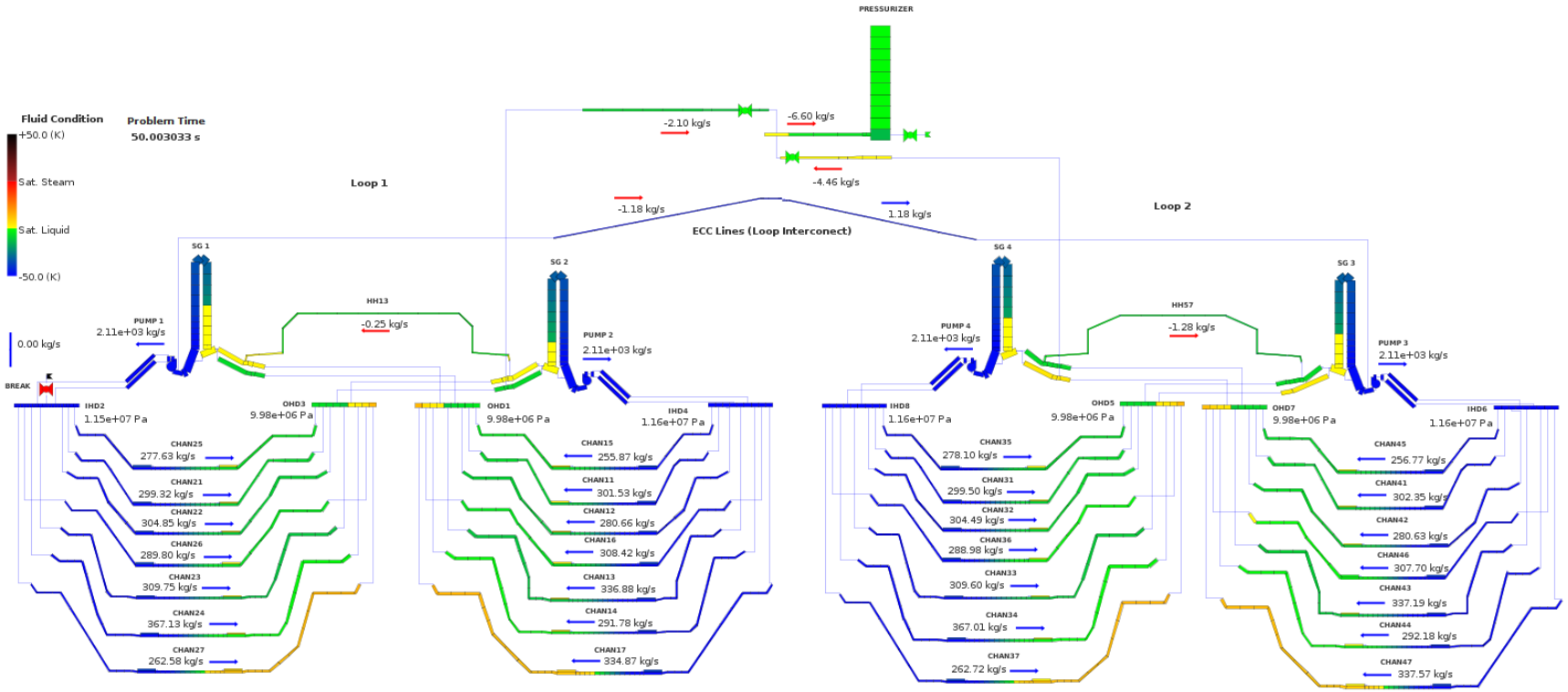

Figure E-1. Stand-alone Thermal-hydraulics Animation Results: All Transients - 0.0 seconds

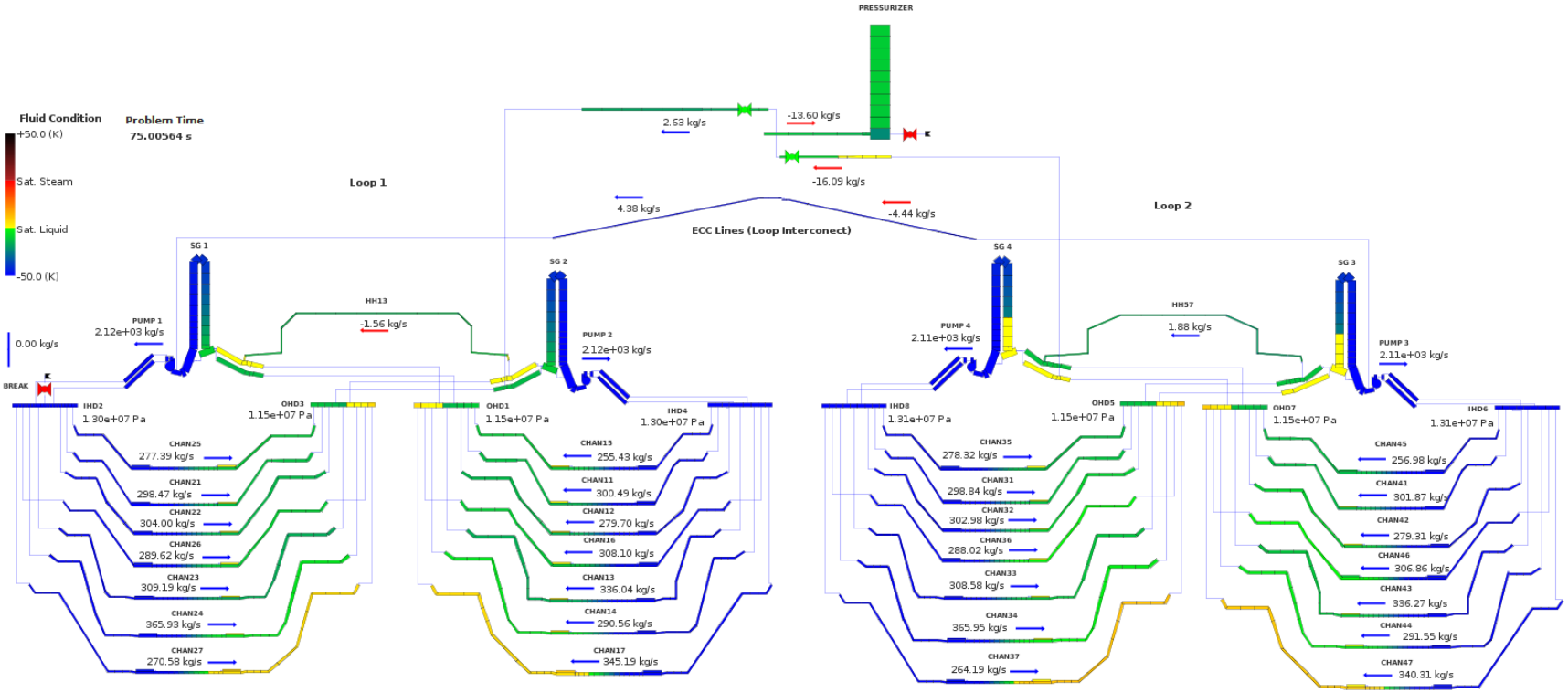

Figure E-2. Stand-alone Thermal-hydraulics Animation Results: LOR – 25.0 seconds

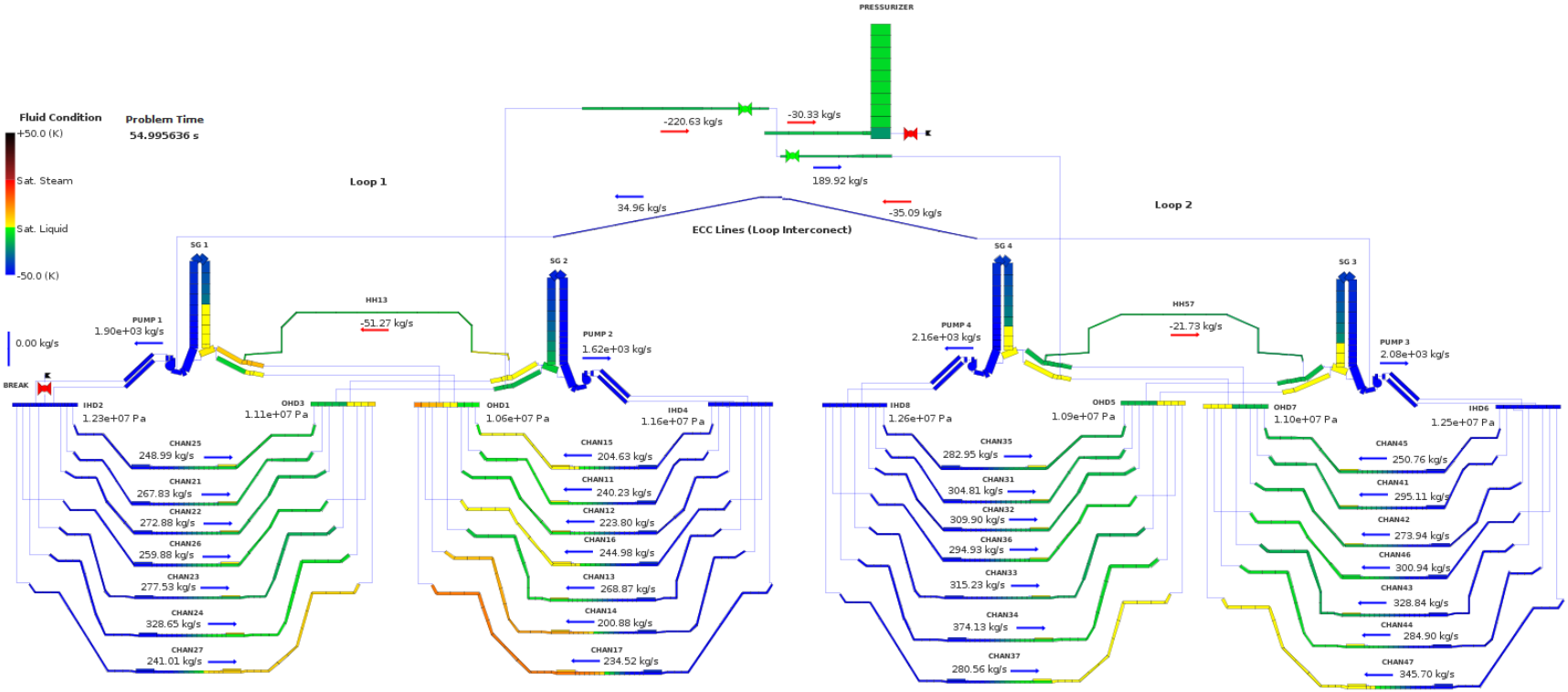

Figure E-3. Stand-alone Thermal-hydraulics Animation Results: LOF – 5.0 seconds

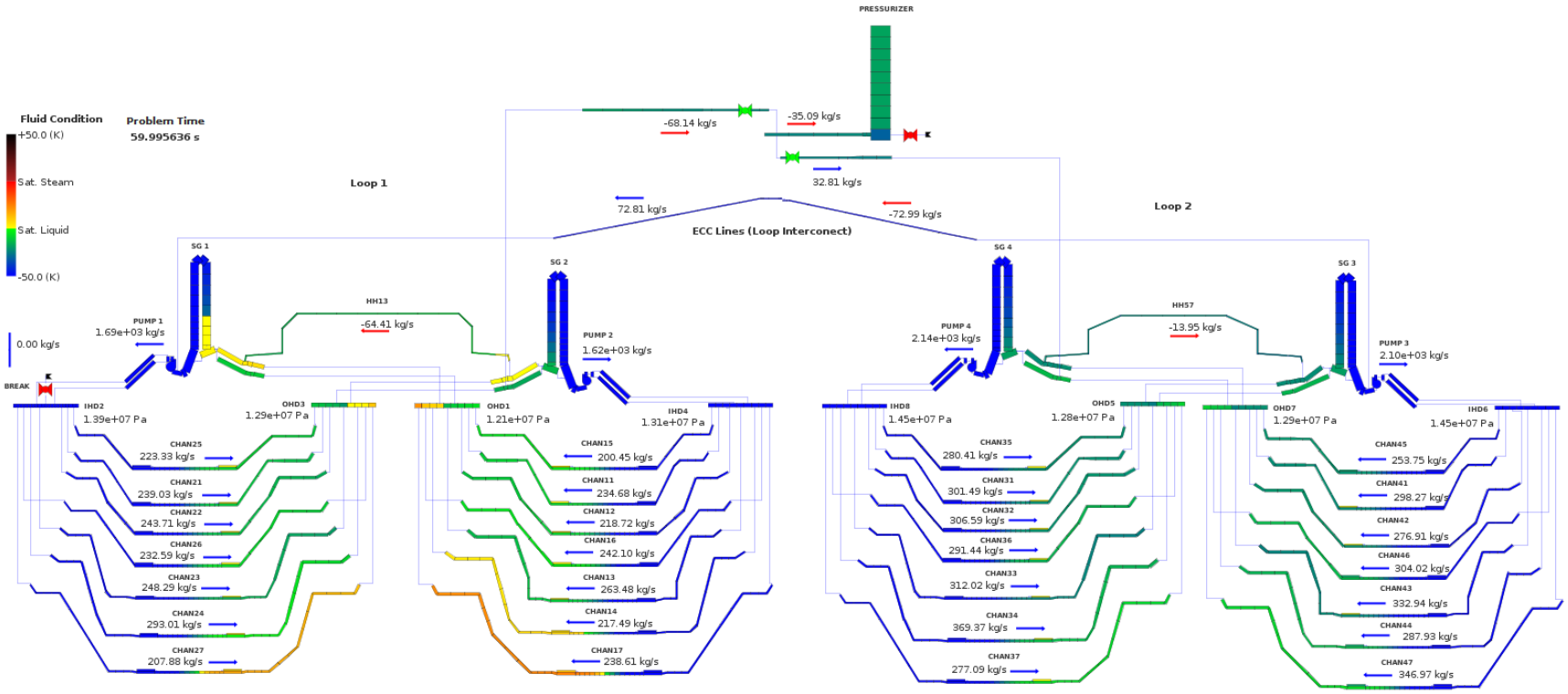

Figure E-4. Stand-alone Thermal-hydraulics Animation Results: LOF – 10.0 seconds

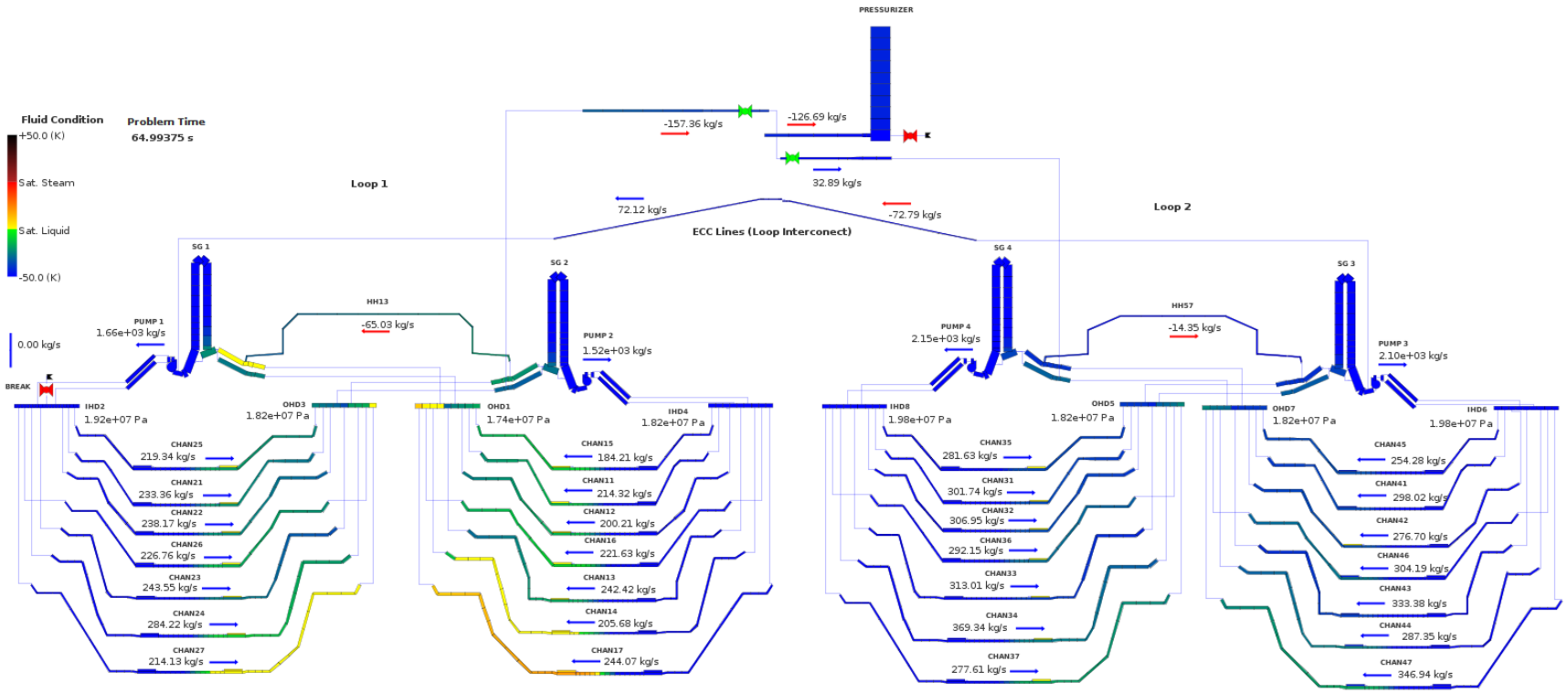

Figure E-5. Stand-alone Thermal-hydraulics Animation Results: LOF – 15.0 seconds

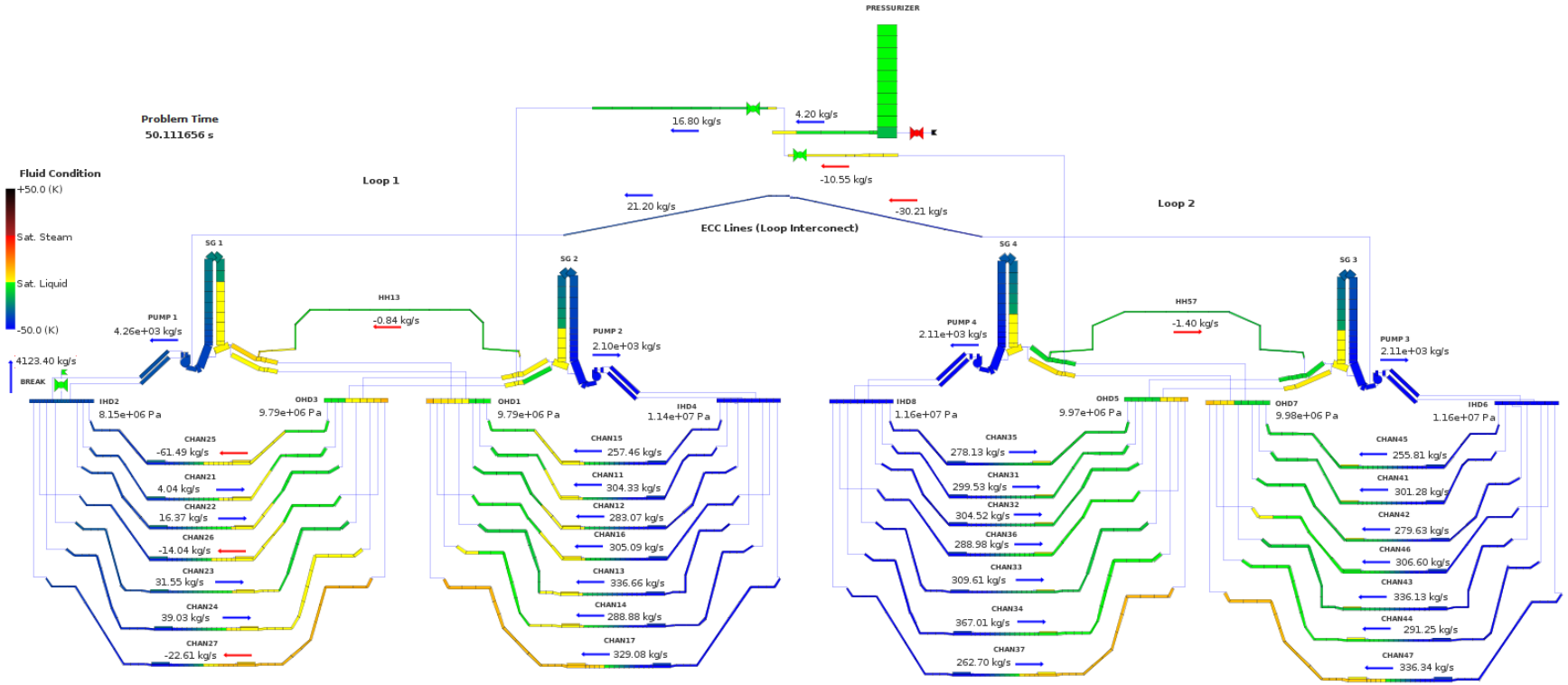

Figure E-6. Stand-alone Thermal-hydraulics Animation Results: LOCA – 0.11 seconds

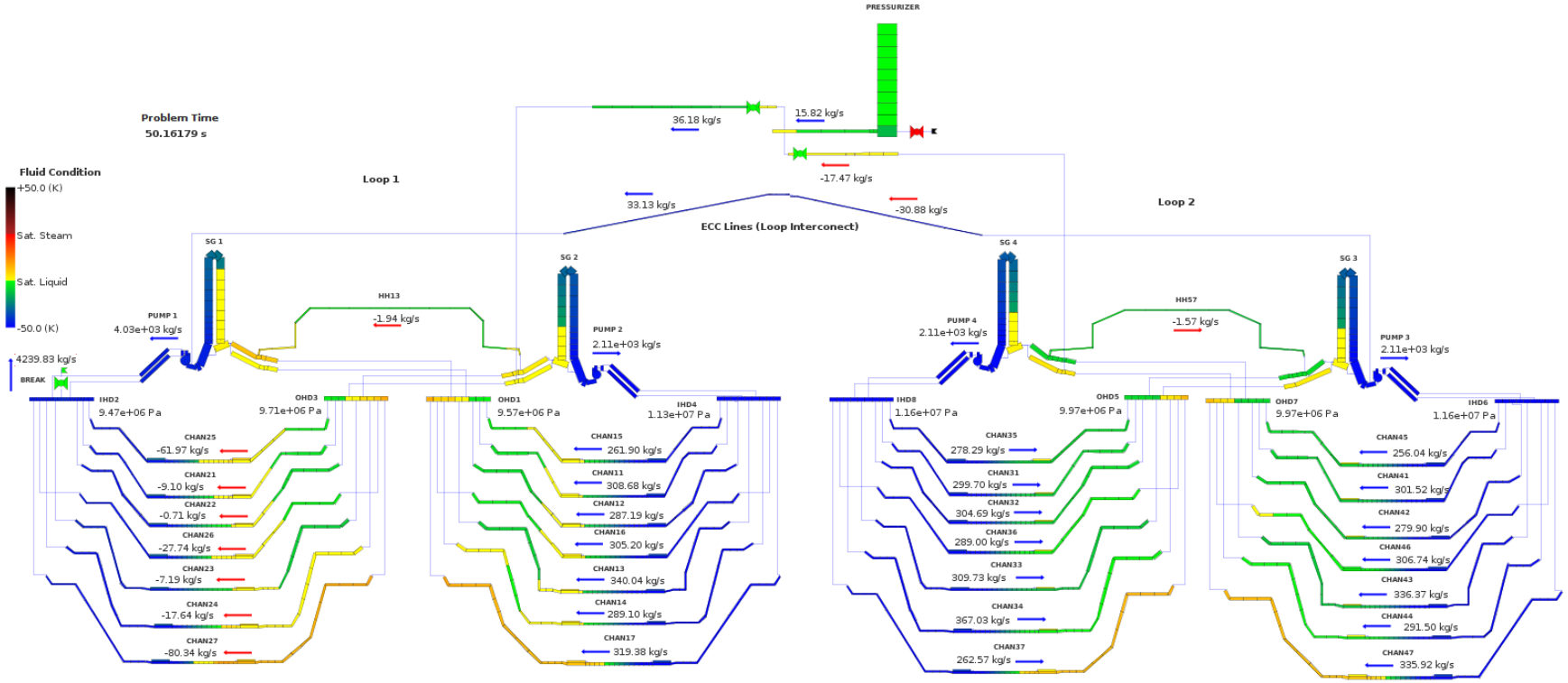

Figure E-7. Stand-alone Thermal-hydraulics Animation Results: LOCA – 0.16 seconds

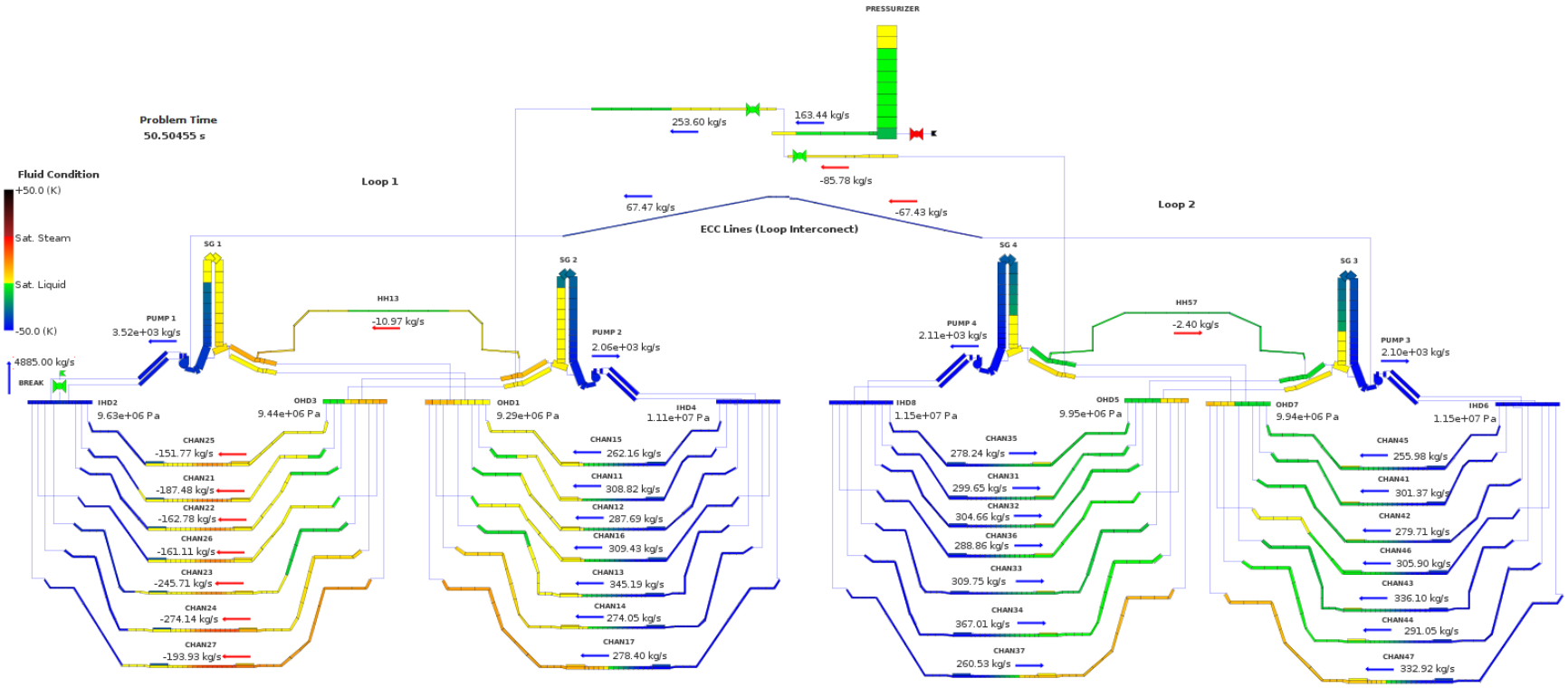

Figure E-8. Stand-alone Thermal-hydraulics Animation Results: LOCA – 0.5 seconds

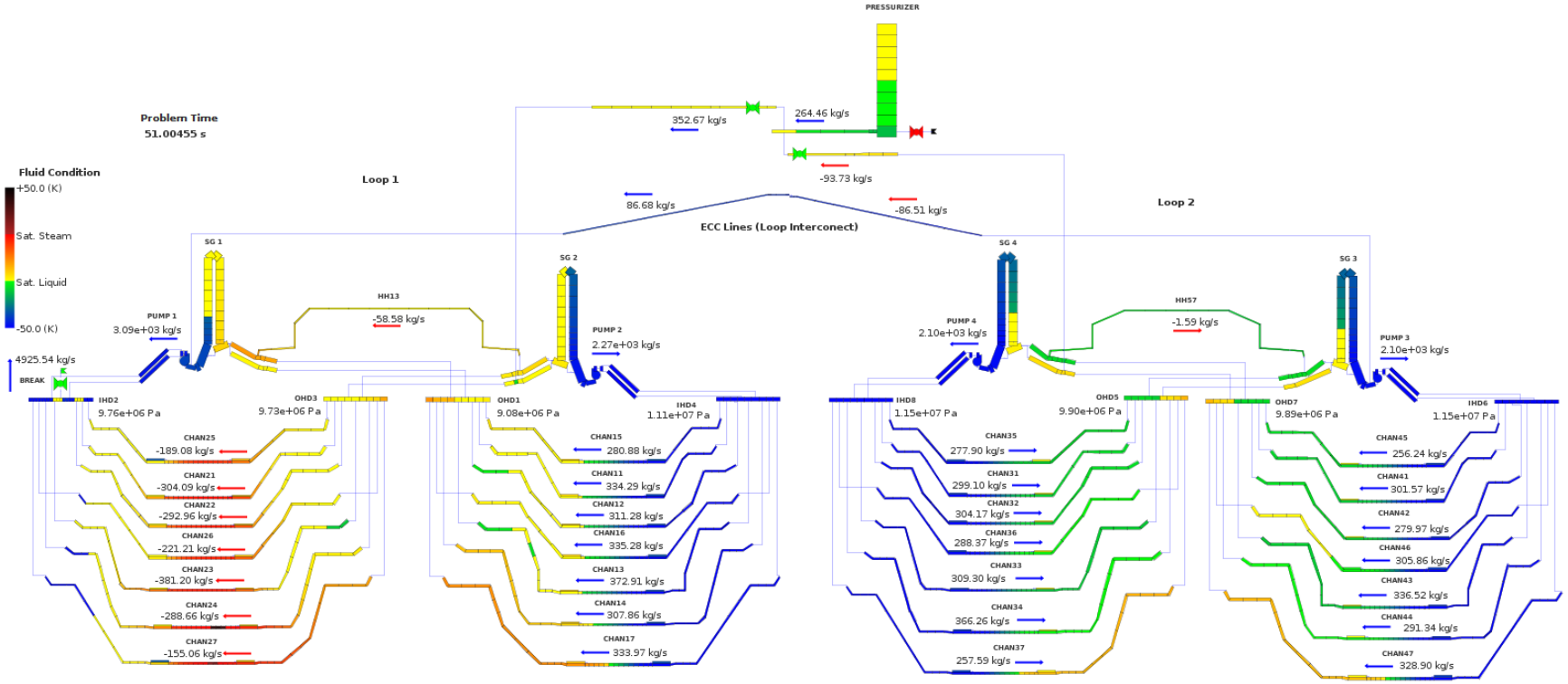

Figure E-9. Stand-alone Thermal-hydraulics Animation Results: LOCA – 1.0 seconds

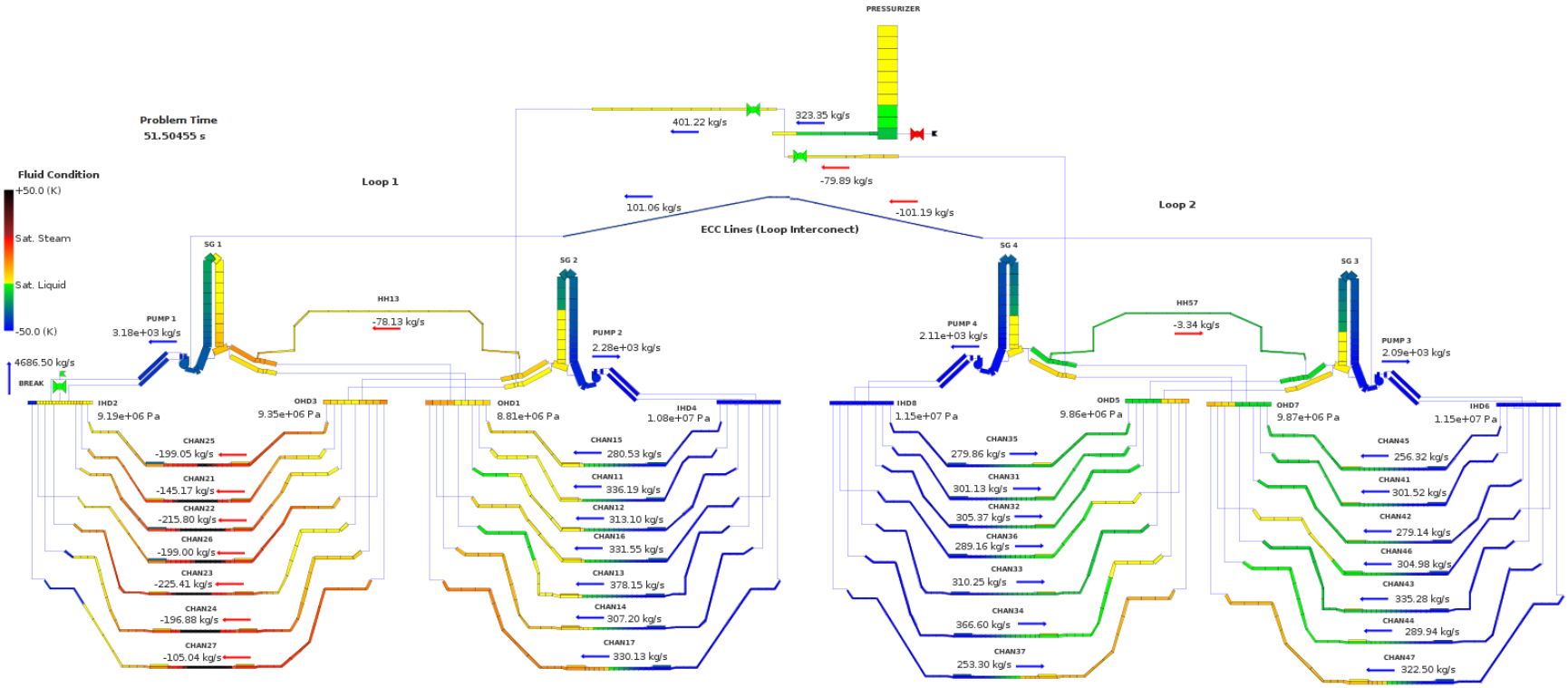

Figure E-10. Stand-alone Thermal-hydraulics Animation Results: LOCA – 1.5 seconds

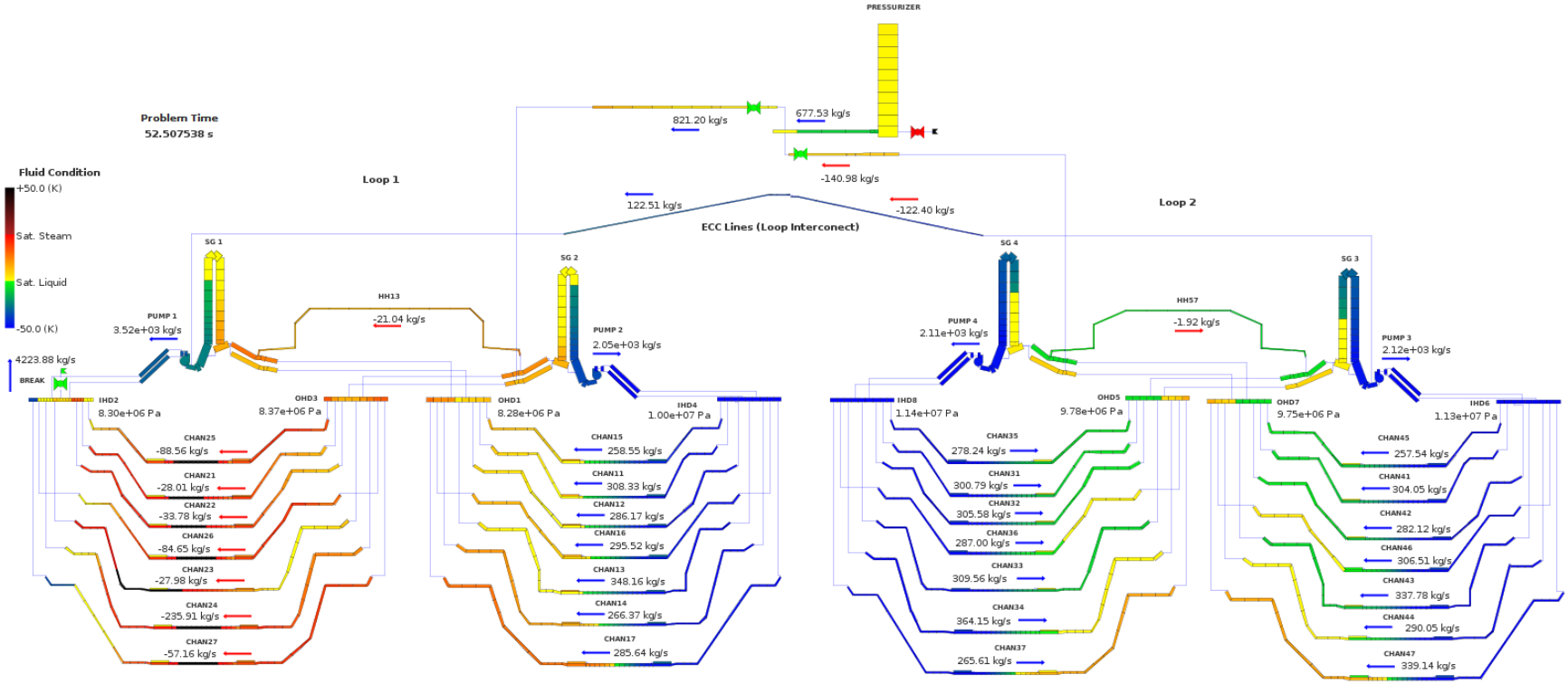

Figure E-11. Stand-alone Thermal-hydraulics Animation Results: LOCA – 2.5 seconds

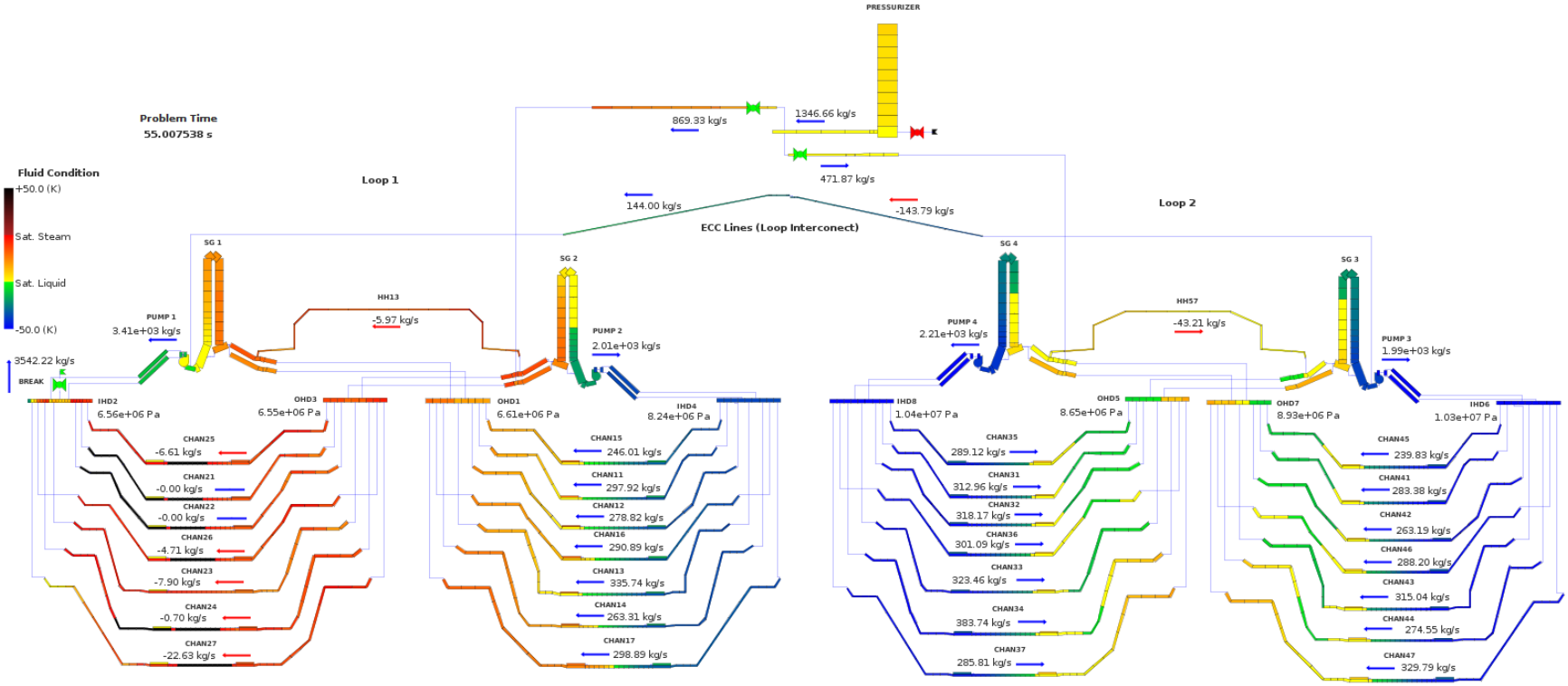

Figure E-12. Stand-alone Thermal-hydraulics Animation Results: LOCA – 5.0 seconds

Appendix F - Additional Lattice Physics Results

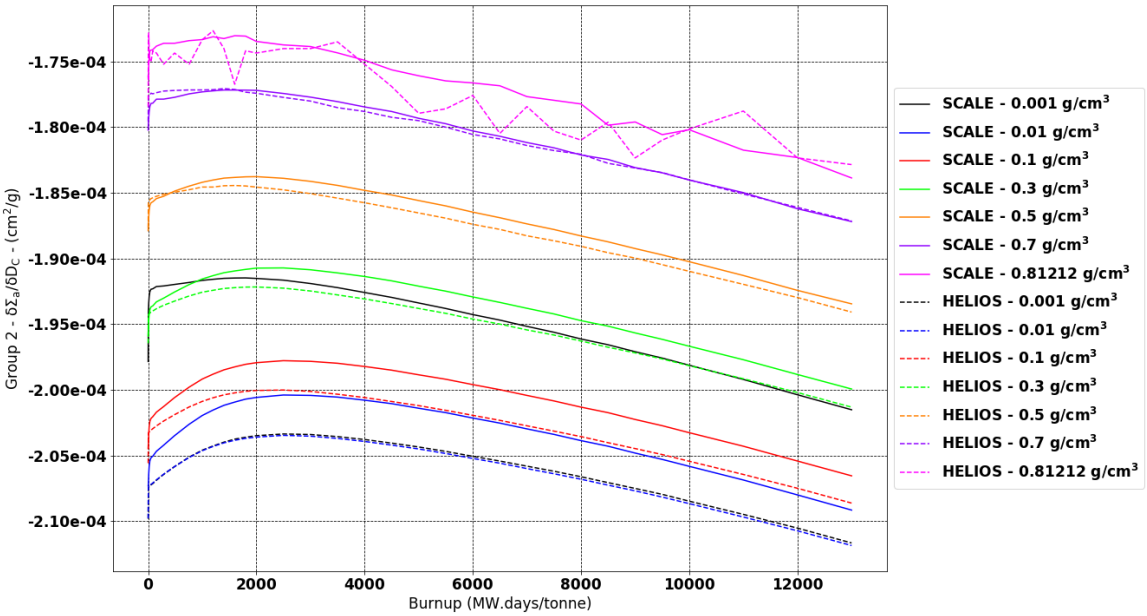

Figure F-1. SCALE vs. HELIOS Lattice Physics Comparison: Group 2 Absorption Coolant Density Partial Derivative Cross Section Co-efficient

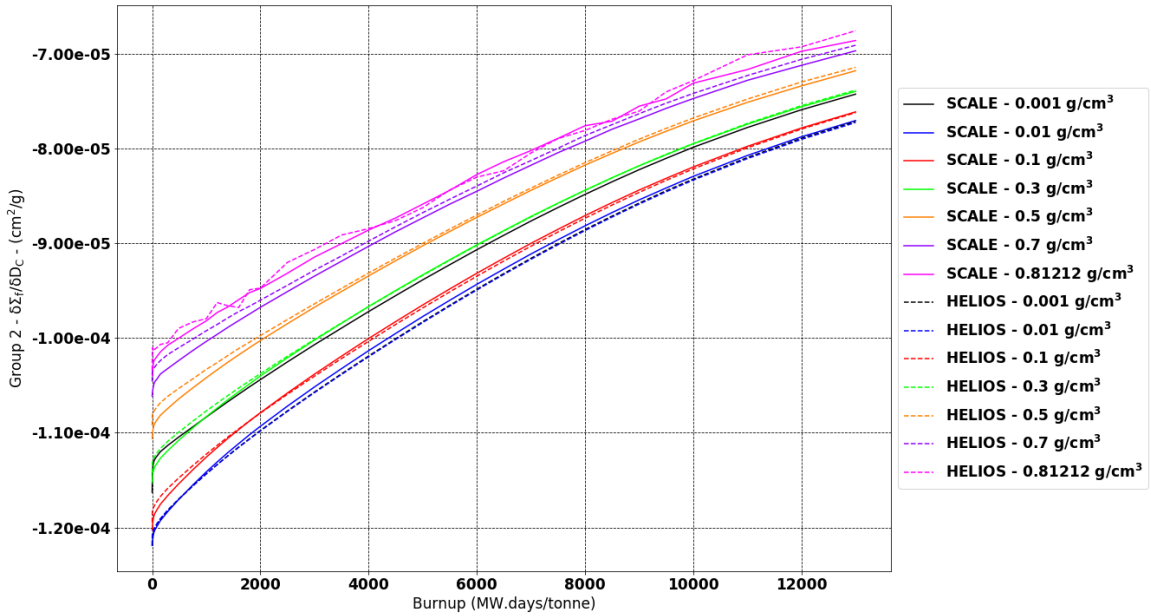

Figure F-2. SCALE vs. HELIOS Lattice Physics Comparison: Group 2 Fission Coolant Density Partial Derivative Cross Section Co-efficient

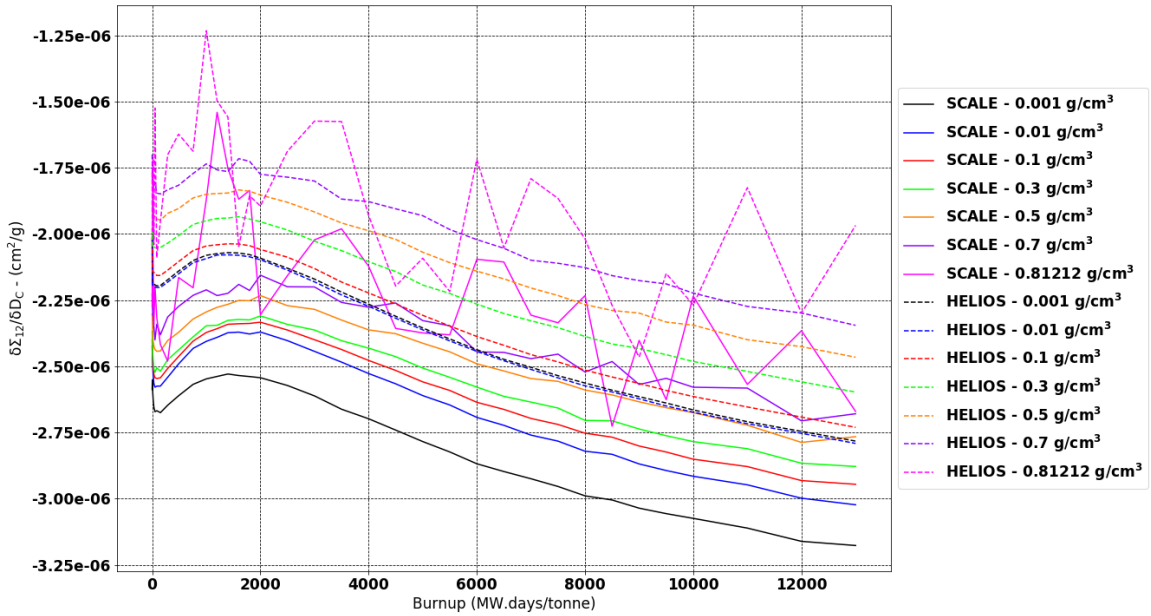

Figure F-3. SCALE vs. HELIOS Lattice Physics Comparison: Down scatter (Group 1 to 2) Coolant Density Partial Derivative Cross Section Co-efficient

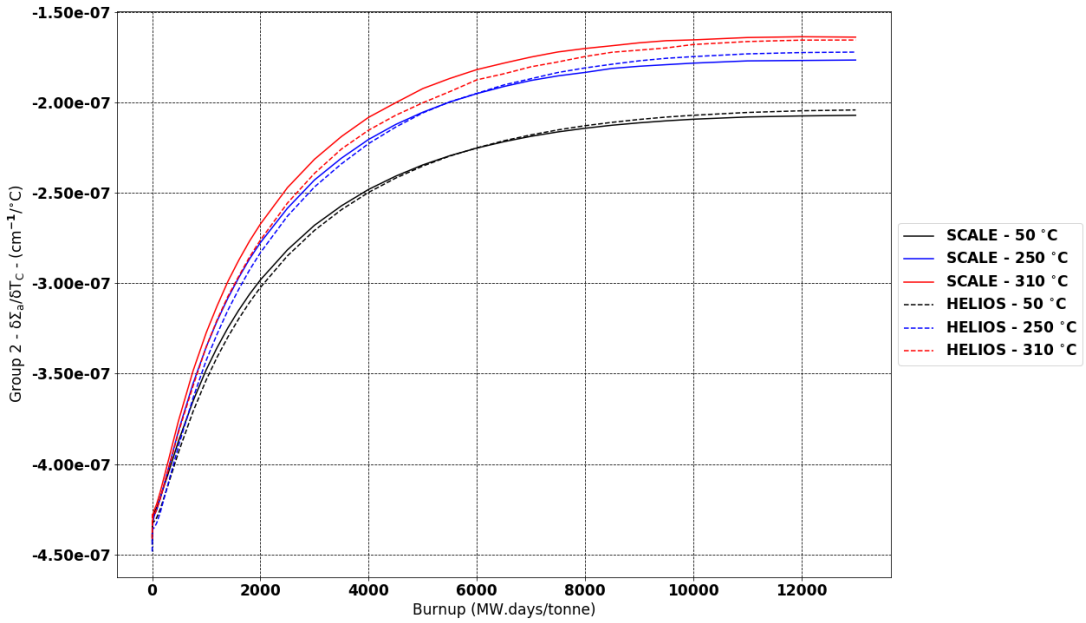

Figure F-4. SCALE vs. HELIOS Lattice Physics Comparison: Group 2 Absorption Coolant Temperature Partial Derivative Cross Section Co-efficient

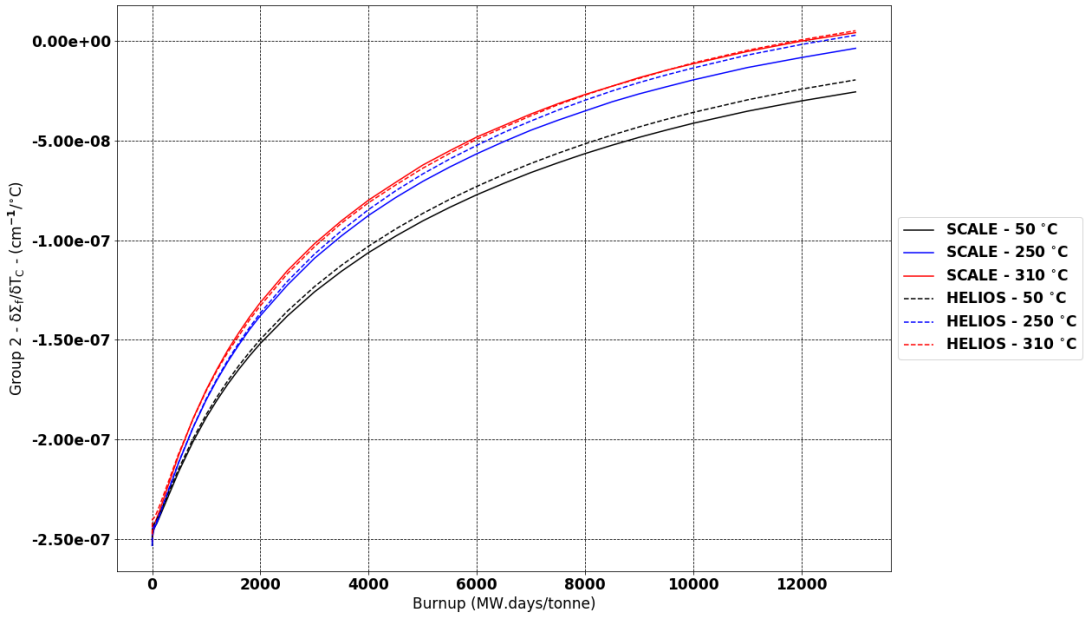

Figure F-5. SCALE vs. HELIOS Lattice Physics Comparison: Group 2 Fission Coolant Temperature Partial Derivative Cross Section Co-efficient

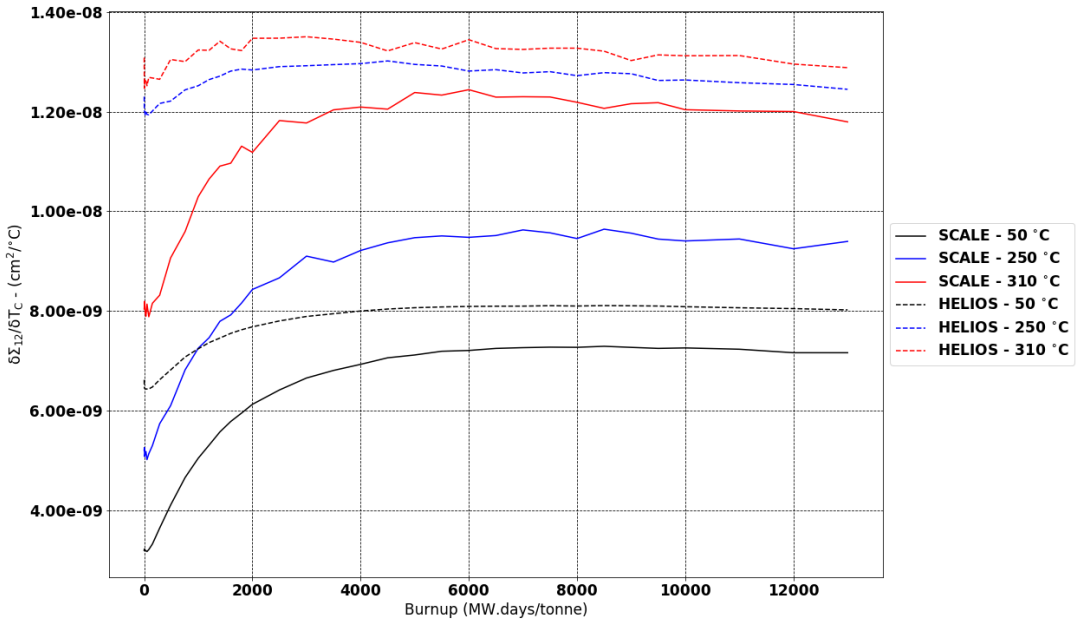

Figure F-6. SCALE vs. HELIOS Lattice Physics Comparison: Down Scatter Coolant Temperature Partial Derivative Cross Section Co-efficient

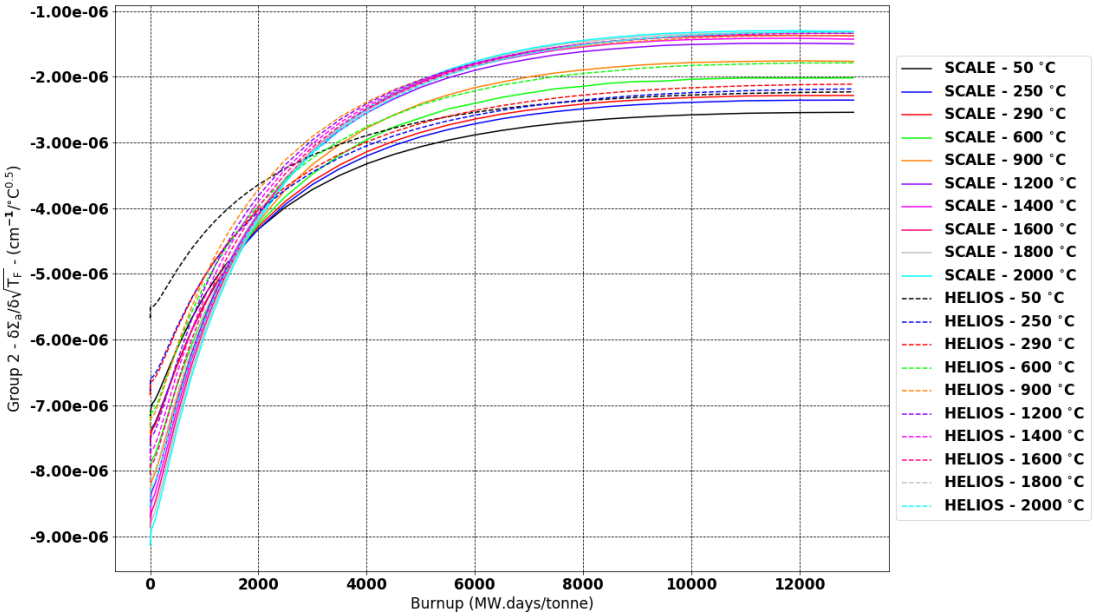

Figure F-7. SCALE vs. HELIOS Lattice Physics Comparison: Group 2 Absorption Fuel Temperature Partial Derivative Cross Section Co-efficient

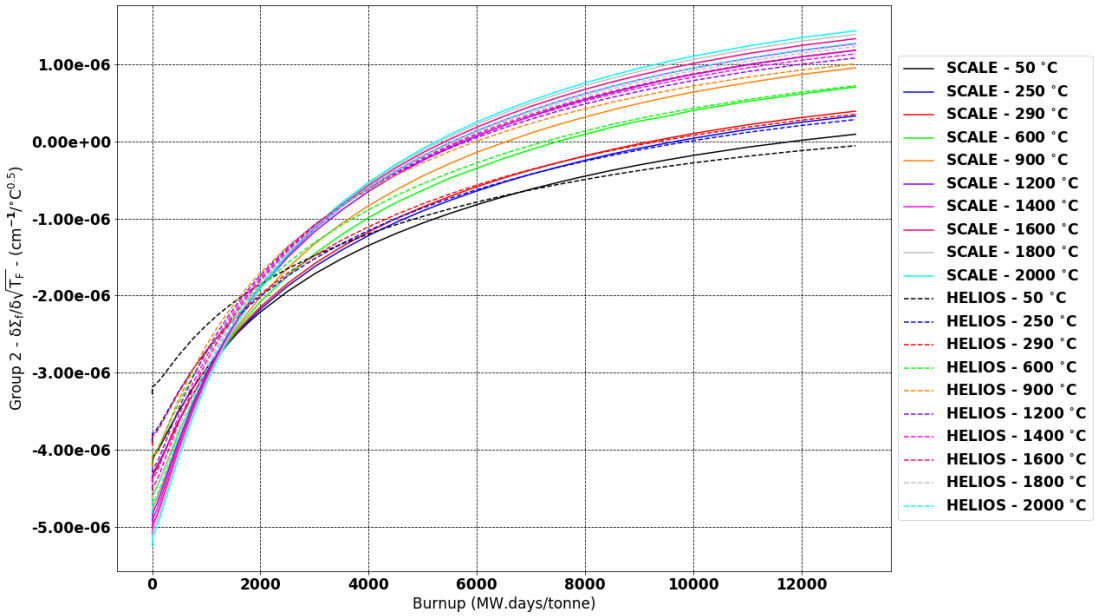

Figure F-8. SCALE vs. HELIOS Lattice Physics Comparison: Group 2 Fission Fuel Temperature Partial Derivative Cross Section Co-efficient

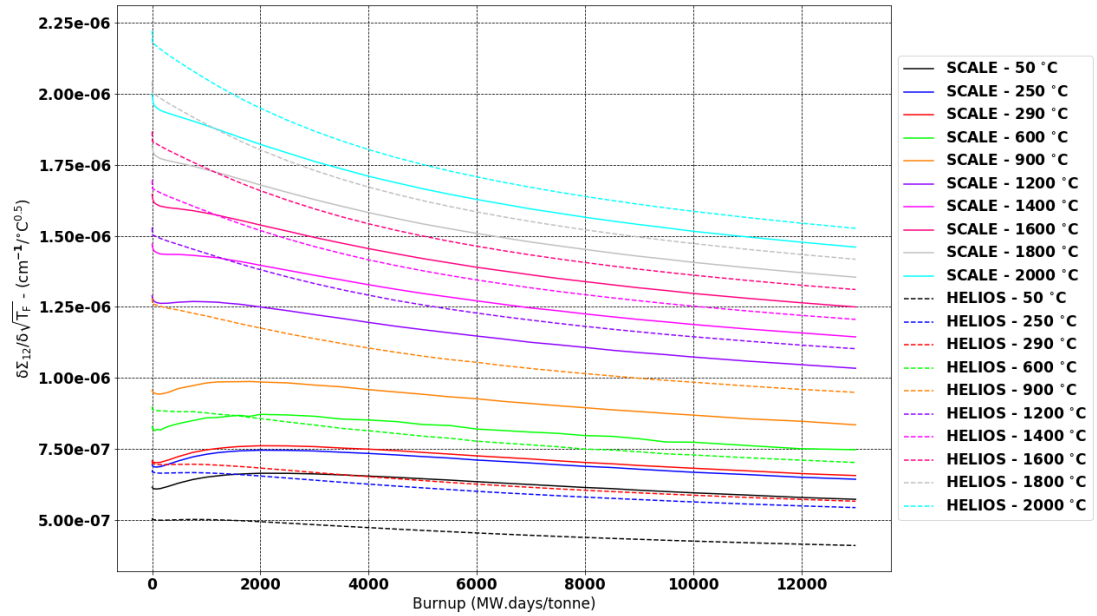

Figure F-9. SCALE vs. HELIOS Lattice Physics Comparison: Down Scatter (Group 1 to 2) Fuel Temperature Partial Derivative Cross Section Co-efficient